Collisional Transfer Between Excited Electronic States as a Mechanism for Sulfur Mass-Independent Fractionation

by

Alexander W. Hull

A.B. Chemistry
Colgate University, 2014

SUBMITTED TO THE DEPARTMENT OF CHEMISTRY IN PARTIAL REQUIREMENT FOR THE DEGREE OF

DOCTOR OF PHILOSOPHY
AT THE
MASSACHUSETTS INSTITUTE OF TECHNOLOGY

September 2020

Signature of Author: _____
Department of Chemistry
Date

Certified by: _____
Robert W. Field
Haslam and Dewey Professor of Chemistry
Thesis Supervisor

Accepted by: _____
Adam Willard
Associate Professor
Graduate Officer

This doctoral thesis has been examined by a Committee of the Department of Chemistry as follows:

Professor Mei Hong_____

Thesis Committee Chair
Professor of Chemistry

Professor Robert W. Field_____

Thesis Supervisor
Haslam and Dewey Professor of Chemistry

Professor Moungi Bawendi_____

Thesis Committee Member
Lester Wolfe Professor of Chemistry

Professor Brett McGuire_____

Thesis Committee Member
Assistant Professor of Chemistry

Abstract:

Excited Electronic State Collisional Transfer as a Possible Mechanism for Sulfur Mass-Independent Fractionation

Submitted to the Department of Chemistry on _____ in partial fulfillment of the requirements for the degree of Doctor of Philosophy

The Great Oxygenation Event, the introduction of O_2 into the Earth's atmosphere approximately 2.5 billion years ago, is a critical milestone in the development of life on Earth. The exact timing of this event is thought to be correlated with the disappearance of Archean sulfur isotopic anomalies, called Sulfur Mass -Independent Fractionation (S-MIF), in the rock record. This anomalous fractionation pattern can be described, generally, as an enrichment in the three rare isotopes: S-33 (0.75%), S-34 (4.25%) S-36 (0.01%), relative to the most abundant isotopologue S-32 (0.75%), However, the mechanism for the generation of S-MIF in a reducing atmosphere is still unknown.

I use the B-X UV transition ($\sim 31{,}000 - 36{,}000\ cm^{-1}$) in S_2 as a proxy for study of excited state collisional transfer as a possible mechanism for S-MIF. The short-lifetime B state (natural lifetime: 32 ns) state-mixes extensively with a longer-lifetime B" state (4200 ns). Furthermore, the most abundant isotopologue of S_2, ^{32}S-^{32}S has only half the number of rotational states compared to its asymmetric counterparts. In this work, I replicated Green and Western's effective Hamiltonian for the X, B, and B" states with additional considerations for mass-dependent vibrational level shifts and nuclear permutation effects.

I hypothesize that the collisional transfer between the B and B" states occurs differently for different isotopologues. This difference results in a different average excited state lifetimes, which, in turn, affects the relative rate at which they undergo chemical reactions and enter the rock record. Here, spectroscopic B/B" perturbations act as doorways through which population can exchange between the B and B" states. My model incorporates absorption, fluorescence, and predissociation, as described by Green and Western. It also includes the Gelbart-Freed model for electronically inelastic collisions and Brunner and Pritchard model for rotationally inelastic collisions. I calculate the amount of each isotopologue that enters the rock record by time-dependently solving a master equation kinetic model.

Results show that, generally, each region where a B vibronic state crosses a B" vibronic state behaves differently. However, the interactions display some systematic behavior. Because of the energy level patterns, lighter isotopologues are generally favored over the heavier ones (i.e. 32-36 < 32-34 < 32-33 < 32-32) in the absence of predissociation. When predissociation is present the trend reverses, but remains Mass-Dependent, and cannot explain the S-MIF signature in the rock record. The most important conclusion, however: the interactions with the smaller B/B" state-mixing showed the *larger* isotope effects.

To continue my analysis, therefore, I considered the same B/B" system where the perturbation matrix elements are 1% of their original Green and Western values, i.e. a "weak perturbation model". Here, I develop a statistical doorway model, which posits that doorway locations are somewhat random, and that the asymmetric isotopologues converge to a limiting, ensemble behavior at lower pressures than do symmetric species that are missing half of their rotational states. Results show that this statistical isotope effect is relevant to the weak perturbation model, and may help explain the anomalous isotope patterns in the rock record.

Further analysis shows that non-statistical effects may also play a critical role. These include transfer between B and B" states with very small state-mixing (as little as 0.005%) and non-statistical

doorway sampling. I conclude that a model that combines statistical and non-statistical isotope effects may explain Archean S-MIF.

Thesis Supervisor: Robert W. Field
Title: Haslam and Dewey Professor of Chemistry

Table of Contents

Acknowledgements

This project took a number of twists and turns, ups and downs, and a few stumbles down blind alleys before reaching the final project that you are (presumably) about to read. As such, there are many people, from both my academic and personal lives, that deserve mention here.

First is my advisor, Bob Field. Bob had to wear a number of different hats during his time as my advisor. He was patient and allowed me to explore this problem to the fullest, even though our original hypothesis (and several of my subsequent hypotheses) did not lead us anywhere. He pushed me forward when I was stubbornly stuck on an idea that wasn't leading anywhere. Most importantly, he was willing to invest a large amount of his own time and effort to understand a geological problem, and a methodology for exploring this problem, that was far outside our group's specialty. This would say a lot about any advisor, but I feel this is especially true considering that I am the final graduate student to graduate from Bob's lab. It's my hope that this work can, in some small way, connect Bob's beautiful ideas about small molecule spectroscopy to a very different problem. He also introduced me to the acapella group, *The Bob's*, and I can honestly say that my graduate experience has never been quite the same since.

Second, I must mention Professor Shuhei Ono, from MIT's Earth, Atmospheric, and Planetary Science Department. It was Shuhei, along with his graduate student, Andrew Whitehill that first introduced me to the Sulfur Mass-Independent Fractionation problem. He was an excellent guide, showing me the extensive body of previous research on S-MIF, as well as keeping me apprised of recent developments. He also showed a keen interest in the quantum mechanical aspect of the problem, and generously provided me partial funding during my time as a graduate student. Our afternoon discussions were always very enjoyable, and I look forward to having several more of them before I leave MIT.

Third is Colin Western, from the University of Bristol, U.K. I have only met him in person a handful of times at conferences, and, most memorably, during a visit to MIT in 2018. My work is based on his thorough, detailed deperturbation of the B/B" system in S_2, and I quite literally could not have done this work without him. During the times we corresponded he was very generous, sharing any and all data I asked him for, as well as answering whatever questions I had. He visited MIT during a critical juncture for my research, and asked a few key questions about the nature of collisional transfer that helped me to shape this project into the final product you see here.

At this point, I should mention my fellow members of the Bob Field group. Dr. Steve Coy was a constant source of knowledge and wisdom throughout my graduate career regarding kinetic models for collisional transfer. In particular, without our discussions of symmetry rules for inelastic collisions, this thesis would be missing a key component. Similarly, thank you to Professor John Muenter for all your visits to our group, all the way from Rochester. You usually sat next to my desk, and I always appreciated your insight, funny anecdotes, and career advice in equal parts. When I first joined the lab, Jun Jiang (J.J.), Carrie Womack, David Grimes, and Barratt Park all helped me get my sea legs, both as a spectroscopist and as a graduate student. Over the course in my time in the lab, I've had the pleasure of working with a number of people doing experimental spectroscopy in Bob's lab. In particular, I'd like to thank Matt Nava, Liz Foreman, and, most recently, Piyush Mishra. They are all talented scientists that I learned much from, and they were all very understanding when I needed time in the office to work on my thesis project. A special mention goes out to Tim Barnum and Trevor Erickson, who have been present with me during all of my 5.5 years as a graduate student in the Field group. They were always good sports when I constantly pestered them about where equipment was in the lab. Finally, I would like to thank David and Trevor for our daily crossword puzzles and their constant reminders of where and when free food was being served (I could never keep track).

On the personal side, the MIT curling club has been a large, and very positive, influence on my time in grad school. I was lucky enough to be a member for five years and a member of , and now their coach. Thanks to Andrea Dubin and Greg Dooley for welcoming me onto the team. Thanks to Cody Karcher and Nate Bailey, who, along with Greg and myself, had an awesome, memorable time as the second event winners at the 2016 Nationals in Chaska, Minnesota. More recently, thanks to Kelsey Becker, Kika Arias, Leanne Galanek, Kevin Wang, Diana Faust, Jacob Colbert, Tom Carotti, Rebecca Jones, Jerry Zhang, Steven Burcat, Christine Roth, and Declan Gaylo for making my later years as president and coach so enjoyable. Special thanks to Kika and Kelsey for stepping up and helping to run the club (as undergrads). Thanks to Tom and Leanne for letting me on your radio show (twice). Thanks to Kika, Kelsey and Nate for being great teammates and for taking home the bronze at 2019 nationals. Finally, thanks to the friends I've met from other schools, including Evan Mullaney, Jack Cordes, and Richard Whitaker. The sportsmanship and comradery make curling special, and I've been really, really lucky to have met so many awesome people.

There is also (sometimes) more to my life than research and curling. Thanks to my fellow physical chemistry grad students Dan Banks, Brian Michael, and Katie Shullenburger for being great Thirsty Ear trivia teammates and even better roommates. I've also been fortunate to have kept in touch with several friends from college over the course of my time at MIT. Thanks especially to Rachel Petersen for planning those hiking and camping trips. I'll never forget our hike on the Knife's Edge on Katahdin as long as I live, and I'm looking forward to finally hiking Mt. Mansfield when the quarantine is over. Thanks to Matt Feeney for all those times we went out for dinner, drinks, and/or to watch UConn beat Syracuse 52-50 at Madison Square Garden. And thanks to his now fiancée, Jenna Glat, for often joining us. Thanks to Brandon Triminio for all the good times in New York, both Queens and Hamilton. Finally, to Rich Grey. We've come a long way since we were 18-year-old freshman roommates at Colgate. I wouldn't be where I am now, academically, and especially personally, if we were assigned to different rooms. Acknowledging this fact will not stop me from constantly pointing out that you're technically not a doctor until you graduate next May.

But I also wouldn't be where I am, personally or academically, without my family. Thank you to all my aunts, uncles, cousins and grandparents for all of the fun and laughs on the Fourth of July, Thanksgiving and all the times in between. Most importantly, thank you to my mom, dad, and sister for being so supportive over the course of these six years. Most graduate students travel much farther to MIT, but I was fortunate enough to be able to come home to Connecticut for rest and home cooked meals every so often. Thanks to my sister Beth for making me go kayaking, apple picking, Christmas shopping and more while I was home. Thanks to my parents for everything from helping me repair my car to helping me to move between apartments. Most importantly, though, thanks to both of them for all the children's astronomy books, all the Magic School Bus computer games, all the classes at Mystic Aquarium. I hope that some of that sense of wonder you helped show me comes through in this work.

Alex Hull
Cambridge, MA
7/19/20

List of Figures

List of Tables

Chapter 1 : A Geological Introduction to Sulfur Mass-Independent Fractionation

Abstract:

The term "fractionation" describes processes where isotopes of an element partition into different chemical, physical, or biological phases within a natural system. For sulfur, fractionation is categorized one of two ways. Sulfur mass-dependent fractionation (S-MDF), describes simple, linear, easy-to-define relationships between sulfur's four stable isotopes. Sulfur mass-independent fractionation (S-MIF) describes any significant deviation from a mass-dependent relationship. S-MIF signatures in the rock record are thought to be correlated with an anoxic atmosphere during the Archean period (4.0 billion to ~2.4 billion years ago). Their disappearance is a key temporal marker of the Great Oxygenation Event, a critical milestone in the development of life on Earth. However, the mechanism that generates S-MIF in the anoxic atmosphere has remained unknown for approximately 20 years. Various spectroscopic studies have been performed on bands of SO_2, but none show the same S-MIF signature as in the rock record. Nuclear permutation symmetry restrictions cause missing rotational states in the most abundant isotopologue of S_2, ^{32}S-^{32}S, and such restrictions have been shown to generate S-MIF in ozone. A S-MIF mechanism that invokes nuclear permutation symmetry would be an appealing explanation for the Archean rock record because it may cause the three rare isotopes, ^{33}S, ^{34}S, and ^{36}S (which come, primarily, from heteronuclear isotopologues) to become enriched, relative to ^{32}S.

1.1. Introduction to Fractionation and Lowercase Delta Notation

In geology, the term *fractionation* refers to any process by which different isotopes of the same element partially separate into different phases within a natural system. In other words, we say a sample (a rock, ocean water, or biomaterial, for example) is *fractionated* when the relative amounts of isotopes contained within the sample differ significantly from their natural abundance ratios. Isotope fractionation is an important tool in the Earth and planetary sciences. These isotopic signatures serve as "fingerprints" that provide important clues to the physical [1, 2, 3], chemical [4, 5], and biological [6] environment of a planet, dating back millions or billions of years. For example, metabolic processes in photosynthesis slightly favor uptake of $^{12}CO_2$, compared to $^{13}CO_2$. Because the ^{12}C and ^{13}C isotopes are both stable, this signature is preserved in sediment and biomaterial, providing insight into the Earth's current and past carbon cycles [7, 8].

Mathematically, geologists and geochemists quantify light element (C, N, O, S, etc.) fractionation using *lowercase delta notation*. Consider an element with isotopes x, and y, where y is the most abundant isotope, and x is a different, less abundant (rare) isotope. The fractionation of rare isotope, x, is given as δ^x (pronounced: "delta x") in equation 1.1 below [9],

$$\delta^x = \frac{\left({}^{[x]}/_{[y]}\right)_{sample}}{\left({}^{[x]}/_{[y]}\right)_{ref}} - 1. \tag{1.1}$$

Here, $\left({}^{[x]}/_{[y]}\right)_{sample}$ is the ratio of isotope x to isotope y in the sample being analyzed. The parameter $\left({}^{[x]}/_{[y]}\right)_{ref}$ is the ratio of x to y in an agreed upon reference, chosen to closely reflect the natural abundance. In the case of sulfur, the subject of this work, the reference is a modified scale based upon the Canon Diablo Trilobyte meteorite (called the V-CDT scale) [10, 11]. Note that when δ^x is positive, the sample is enriched in isotope x. When δ^x is negative, the sample is depleted in isotope x, relative to the chosen reference.

1.2. Mass Dependent Fractionation

Isotope fractionation patterns fall into one of two categories: Mass-*Dependent* Fractionation (MDF) and Mass-*Independent* Fractionation (MIF) [9]. In general, MDF describes ubiquitous, easy-to-define relationships between the rare sulfur isotopes (and their corresponding δ values), caused by the small differences in the isotopes' respective masses. However, there are several different MDF mechanisms (kinetic, thermodynamic, etc.), which may be more relevant for some elements than for others. Therefore, the exact mathematical definition of the MDF will be different for different elements. In this section, I derive the MDF relationships observed in sulfur (termed S-MDF). Sulfur has four stable isotopes: the most abundant, ^{32}S (94.99%), and three rare isotopes, ^{33}S (0.75%), ^{34}S (4.25%), and ^{36}S (0.01%) [12]. There are, therefore, three δ parameters: δ^{33}, δ^{34}, and δ^{36}, as defined in Equation 1.1. S-MDF defines simple, linear relationships between these three δ parameters.

In sulfur, mass-dependent fractionation is specifically defined to be a thermodynamic process, termed "equilibrium mass-dependent fractionation". For S-MDF, we consider a sulfur isotope exchange reaction, where S-R represents a sulfur compound that will permanently store its sulfur in the rock record and S-X represents a compound (or set of compounds) that will not. For sulfur-32 and sulfur-33, we have Equation 1.2,

$$^{33}SX + {}^{32}SR \leftrightharpoons {}^{32}SX + {}^{33}SR. \tag{1.2}$$

The chemical equilibrium constant for this reaction is given by Equation 1.3,

$$K_{32\leftrightarrow 33} = e^{-\frac{\Delta E_{32\leftrightarrow 33}}{kT}} = \frac{[^{32}SX][^{33}SR]}{[^{33}SX][^{32}SR]}. \tag{1.3}$$

Likewise, we can imagine an identical reaction for sulfur-34 exchanging with sulfur-32, with the associated chemical equilibrium constant given by Equation 1.4,

$$K_{32\leftrightarrow 34} = e^{-\frac{\Delta E_{32\leftrightarrow 34}}{kT}} = \frac{[^{32}SX][^{34}SR]}{[^{34}SX][^{32}SR]}. \tag{1.4}$$

Combining Equations 1.3 and 1.4, we obtain (Equation 1.5) [13]:

$$\frac{\Delta E_{32\leftrightarrow 33}}{\Delta E_{32\leftrightarrow 34}} ln\frac{[^{32}SX][^{34}SR]}{[^{34}SX][^{32}SR]} = ln\frac{[^{32}SX][^{33}SR]}{[^{33}SX][^{32}SR]}. \tag{1.5}$$

We assume that the largest contributor to $\Delta E_{a\leftrightarrow b}$ is the difference in vibrational frequency between reactants and products, i.e. $\Delta E_{a\leftrightarrow b}\ \alpha\ \frac{1}{\sqrt{m_a}} - \frac{1}{\sqrt{m_b}}$, where m is the isotope mass. Because $m_{32} \approx m_{33}$ and $m_{32} \approx m_{34}$, we can write Equation 1.6 [9],

$$\frac{\Delta E_{32\leftrightarrow 33}}{\Delta E_{32\leftrightarrow 34}} \approx \frac{\frac{1}{m_{32}} - \frac{1}{m_{33}}}{\frac{1}{m_{32}} - \frac{1}{m_{34}}} = 0.515. \tag{1.6}$$

I can now rewrite Equation 1.5 in a suggestive way (Equation 1.7):

$$0.515 \ln\left(\frac{{}^{[34}SR]/_{[32}SR]}{{}^{[34}SX]/_{[32}SX]}\right) = \ln\left(\frac{{}^{[33}SR]/_{[32}SR]}{{}^{[33}SX]/_{[32}SX]}\right). \quad (1.7)$$

Because the ratio ${}^{[34}SR]/_{[32}SR]$ is preserved in the rock record, I borrow notation from Equation 1.1 and write ${}^{[x}SR]/_{[32}SR] = ({}^{[x]}/_{[32]})_{sample}$. Likewise, if we assume that the equilibrium concentration of $[SX]$ is large compared to that of $[SR]$, it follows that ${}^{[x}SX]/_{[32}SX] \approx ({}^{[x]}/_{[32]})_{ref}$. Using the definition of δ^x given in Equation 1.1, I have Equation 1.8a, which leads trivially to Equation 1.8b,

$$0.515 \ln(\delta^{34} + 1) = \ln(\delta^{33} + 1) \quad (1.8a)$$

$$(\delta^{34} + 1)^{0.515} = (\delta^{33} + 1). \quad (1.8b)$$

Equation 1.8b is the general expression for sulfur-33 mass dependent fractionation. However, Equation 1.8a reveals an additional simplification. Specifically, I employ a property of logarithms, where $\ln(1 + \in) \approx \in$ for small values of $\in$. (In practice, δ^x is generally quite small and measured in parts per thousand). This leads to Equation 1.9,

$$\delta^{33} \approx 0.515 * \delta^{34}. \quad (1.9)$$

An identical analysis for sulfur-36 gives the following expression for sulfur-36 MDF (Equation 1.10),

$$\delta^{36} \approx 1.90 * \delta^{34}. \quad (1.10)$$

Equations 1.9 and 1.10 will serve as my definitions for sulfur mass-dependent fractionation (S-MDF) for the remainder of this text. Observe that three different isotopes (32, 34 and either 33 or 36) define each MDF relationship. That is, each δ^x is defined in terms of a rare isotope and S-32, and there are two such δ^x's that make up each MDF equation. Moreover, because sulfur has *four* stable, naturally occurring isotopes, it can have *two* such MDF relationships. This makes sulfur fractionation an especially useful

fingerprint, compared to other common elements like oxygen (three stable isotopes), carbon (two), and nitrogen (two). Its fractionation patterns encode a larger amount of information.

Finally, a word of clarification: mass dependent fractionation generally describes simple relationships between the isotope quantities in a sample, where the pattern is directly related to the isotopes' relative masses. However, that definition is specific to each element, chosen to reflect common patterns observed in a wide array of rock samples. Other types of MDF exist, such as "kinetic MDF" for *irreversible* reactions. In sulfur, however, the geochemical community defines S-MDF as the *equilibrium* isotope-exchange process described above.

1.3. Sulfur Mass-Independent Fractionation

In contrast with S-MDF, sulfur mass independent fractionation (S-MIF) is easier to *define*, but its physical origins are often much more complex. In words, sulfur mass independent fractionation is defined as any *significant deviation* (greater than ~ 0.5 parts per million) from mass dependent fractionation. Mathematically, we define *capital delta notation* as follows (Equations 1.11a and 1.11b)

$$\Delta^{33} = \delta^{33} - 0.515\delta^{34} \qquad (1.11a)$$

$$\Delta^{36} = \delta^{36} - 1.90\delta^{34}. \qquad (1.11b)$$

Sulfur-33 MIF is defined, therefore, as the difference between the δ^{33} actually observed in the sample, and the value δ^{33} predicted from δ^{34}, using the mass dependent relationship given in Equation 1.9.

(Likewise for sulfur-36 MIF). Figure 1-1 illustrates the difference between a hypothetical set of rock samples showing S-MDF and one showing S-MIF.

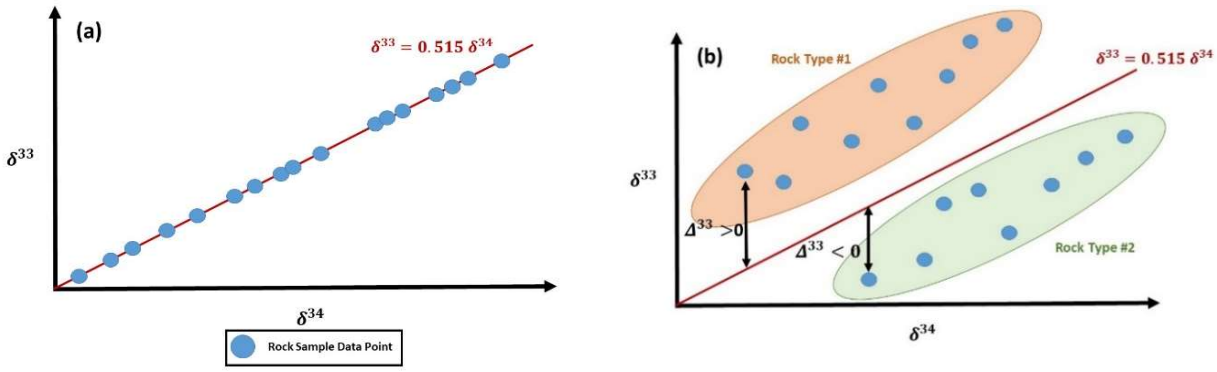

Figure 1-1: Illustrates the differences between a hypothetical series of rock samples that display MDF and a hypothetical series of samples that display MIF. The MDF series follows the linear relationship shown in **Figure 1a** and described in section 1.2. A hypothetical series exhibiting MIF is shown in **Figure 1b**. This series of samples deviates significantly from the linear relationship. Note that MIF generally requires two separate chemical or physical phases, such as two different types of rocks. One type of rock, orange in this example, will exhibit positive deviations from MDF ($\Delta^{33} > 0$). Another, green, will exhibit negative deviations ($\Delta^{33} < 0$).

The physical origins of mass-independent fractionation are often quite obscure, and I will explore possible mechanisms for S-MIF more thoroughly later on in this chapter. Here, I should comment that the terms "mass-independent fractionation" and "mass-dependent fractionation" may seem somewhat misleading to those outside the geochemical community. As mentioned in the previous section, we define S-MDF using the specific equilibrium isotope-exchange process. S-MIF, by contrast, describes *any* fractionation significantly different from this *one specific* S-MDF process. Often, S-MIF effects are caused, at least in part, by differences in isotope mass. For example, mass shifts can cause shifts in vibrational band frequencies in spectroscopy. Muskatel, et al. demonstrated this phenomenon to be a possible source of MIF in N_2 UV absorption [14]. In such cases, the S-MIF mechanism "depends on the mass", but it is *not* "mass-dependent fractionation".

Sulfur mass-independent fractionation acts as an important historical tracer of the atmosphere's oxidation state. It is generally accepted that sulfur fractionation patterns in the rock record are strongly correlated with oxygen levels in the Earth's atmosphere.

1.4 The Great Oxygenation Event and its Relevance to Sulfur Fractionation

The >4.0 billion year history of atmospheric oxygen is divided into two distinct periods. The earlier Archean period, ~4.0 to 2.3 billion years ago, was characterized by extremely low atmospheric oxygen levels. Modeling of the Archaen atmosphere, using SO_2 photolysis as the origin of S-MIF[1], suggests O_2 concentrations $>10^{-5}$ times larger than those of present atmospheric levels (PAL) [15]. The more recent period (2.45 billion years ago to present) is characterized by oxygen concentrations rapidly rising to their modern day values. The transition ~2.3 billion years ago is called the Great Oxygenation Event (GoE) [16].

The GoE was triggered primarily by the emergence of photosynthetic cyanobacteria in the Earth's oceans, and it had a massive impact on the Earth's climate and ecosystem. For example, rising oxygen levels triggered the Huronian Ice age from ~2.4-2.1 billion years ago, due to oxidation of methane, a very strong greenhouse gas, to carbon dioxide and water [17, 18]. In this same period, the toxicity of oxygen to the then-predominant organisms triggered a mass extinction event. On a longer timescale, however, high oxygen levels are linked to the evolution of eukaryotic organisms [19], and the greater chemical energy content of a more oxygenated environment may have helped drive increasing biodiversity [20], which culminated in the Cambrian explosion ~540 million years ago [21]. As such, the GoE is a critical milestone in the development of life on Earth, and understanding the exact timing of the GoE, as well as its influence on the ecological trajectory of the planet, has significant implications for the emerging field of astrobiology.

As previously mentioned, sulfur fractionation in the rock record provides the best indicator for the timing of the GoE. In 2000, James Farquhar and coworkers [22] reported a surprising discovery: the

[1] As I will discuss, SO_2 may not be the origin of the S-MIF signature in the Archean atmosphere. However, the mechanism by which rising oxygen levels eliminate S-MIF in the rock record should be *relatively* agnostic as to the chemical/photochemical origin of the fractionation. In this context, the 10^{-5} PAL number should be taken as a baseline estimate and not an exact value.

existence of significant S-MIF signatures in rock samples *older* than ~2.45 billion years, S-MDF in rock samples *younger* than 2.09 billion years, with a comparatively short transition period in between [23]. Moreover, Farquhar, et. al. concluded that this S-MIF pattern was strong evidence of gas phase chemistry and photochemistry being influential in the Earth's Archean sulfur cycle . Figures 2a-b illustrate their reasoning, using information adapted from works by Pavlov and Kasting (2002) [15] and by Lyons (2009) [24].

As seen in Figure 1-2, volcanic sulfur enters the atmosphere primarily as H_2S and SO_2. While in the atmosphere, these species can undergo a wide range of chemical and photochemical processes. In the Archean atmosphere (2a) sulfur is removed by one of two sinks. The first sink involves reduced, elemental sulfur wherein S_2 polymerizes to S_3, S_4 and S_8. The S_8 molecules clump together and

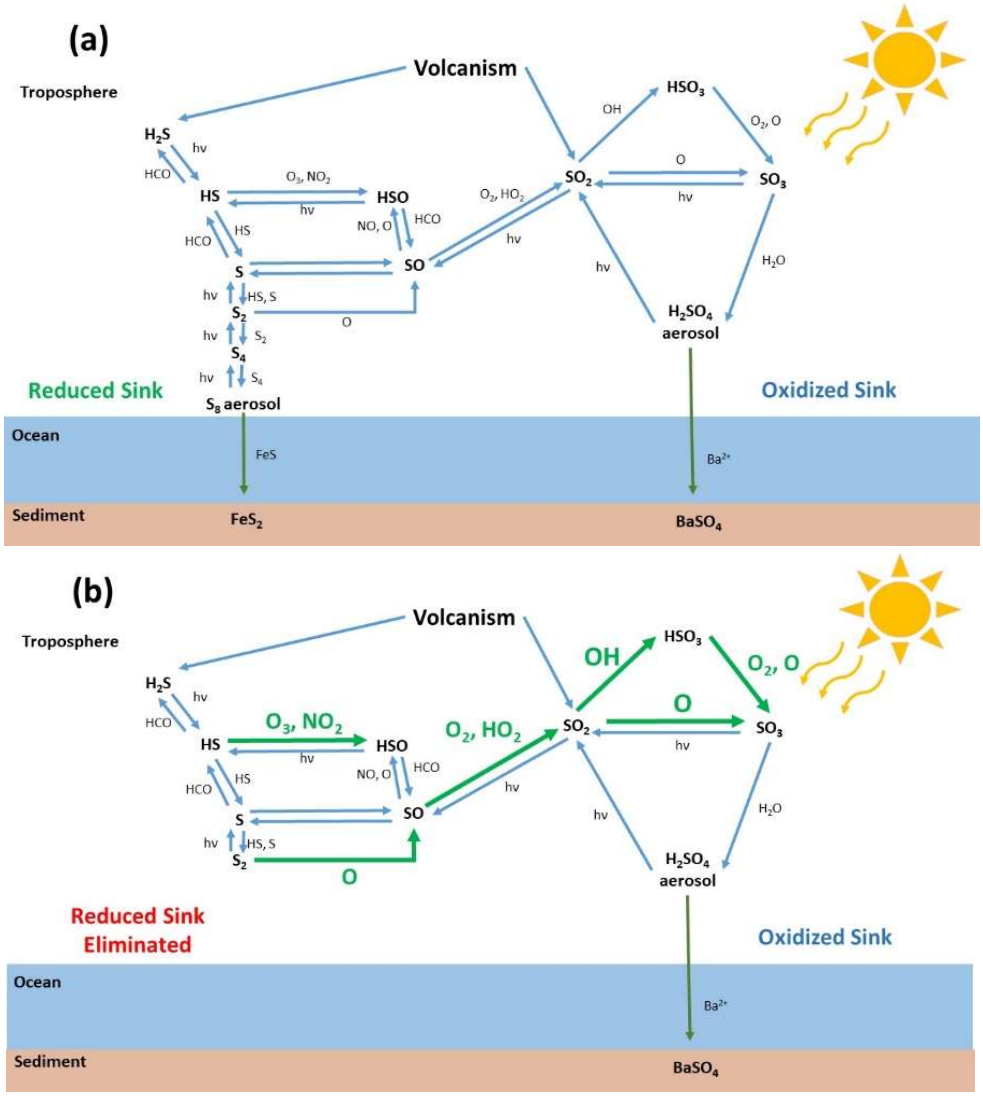

Figure 1-2: shows the major gas-phase chemical and photochemical processes involved in the Earth's sulfur cycle. In the Archean atmosphere **(2a)**, sulfur enters the atmosphere as H_2S or SO_2. It leaves via one of two sinks: a reduced sink as elemental sulfur aerosols, and an oxidized sink as H_2SO_4. If any chemical or photochemical process generate an S-MIF signature, it can be preserved in the rock record with the positive S-MIF stored in one sink and the negative S-MIF stored in the other. In the modern atmosphere **(2b)**, the high levels of oxygen drive chemistry to the oxidized sink (green arrows). The sulfur cycle is no longer capable of separating isotopes, and the S-MIF signature is lost.

precipitate out of the atmosphere as solid aerosol particles [25]. The second sink involves oxidized H_2SO_4, which rains out of the atmosphere as an aqueous solution. Out of the atmosphere, reduced sulfur enters the rock record as, for example, pyrite (FeS_2), whereas oxidized sulfur enters the rock record as different compounds, such as barite ($BaSO_4$) [15]. This two-sink system, by which sulfur can exit the atmosphere and enter the rock record in two different chemical forms, allows for preservation of any S-MIF generated by atmospheric processes (recall Figure 1-1). If such S-MIF is generated, we could expect

rock record sulfur compounds generated through one sink to exhibit a positive isotopic anomaly ($\Delta^x > 0$), while sulfur compounds generated through the other exhibit a negative anomaly ($\Delta^x < 0$).

In the Archean atmosphere (Figure 1-2a) the chemical processes that move sulfur toward the oxidized sink involve a variety of reactions with atomic oxygen, O_2, and other oxygen containing compounds. While we estimate Archean oxygen levels to be many orders of magnitude lower than those of the present, atmospheric oxygen was still present due to processes such as photolysis of CO_2. By contrast, processes that move sulfur toward the reduced sink generally involve UV photolysis. In a modern, oxidizing atmosphere (Figure 1-2b), high concentrations of oxygen, and absorption of UV light by ozone, effectively shut off the reduced sink [25]. Therefore, atmospheric processes that generate S-MIF are irrelevant to the rock record. Sulfur isotopes cannot be separated permanently, as they eventually exit the atmosphere through the same channel.

1.5. S-MIF Patterns in the Archean Rock Record

While the disappearance of S-MIF from the rock record ~2.3 billion years ago is widely accepted evidence of the Great Oxygenation Event, the identities of the gas-phase chemical or photochemical processes that produced the S-MIF signature in the Archean atmosphere remain unknown. In this section, I briefly summarize the primary features of S-MIF in the Archean rock record, and highlight those that any proposed fractionation mechanism must be able to account for.

Figure 1-3 shows data from the Neoarchean period, ~2.8-2.5 billion years ago, reproduced from Ono 2017 [26], so chosen because the period shows the largest magnitude and most distinct S-MIF signature. Comparisons between different Archean eras are somewhat fraught, as there is a very limited number of Archean rock formations from which to gather samples, and Neoarchean (~2.8-2.5 billion years ago) rock formations are noted by Ono [26] to be exceptionally well preserved.

Figure 1-3a displays the correlation between δ^{34} and Δ^{33}, while figure 1-3b displays the correlation between Δ^{33} and Δ^{36}. Three major features of these data are as follows:

1. A strong, relatively (but not entirely) linear correlation between δ^{34} and Δ^{33}, as well as between Δ^{33} and Δ^{36}. These relationships are defined by the geochemical community as $\Delta^{33} \approx 0.9\delta^{34}$ and $\Delta^{36} \approx -0.9\Delta^{33}$ *or* $\Delta^{36} \approx -1.5\Delta^{33}$. And collectively, these equations are referred to as the *Archean Reference Array* [26, 27, 28]. Any likely mechanism for S-MIF in the Archean atmosphere should feature similar correlation patterns.
2. A maximum value for Δ^{33} and Δ^{36} of about 15 parts per thousand. Any proposed mechanism would ideally produce an even larger S-MIF than this, as some chemical mixing of the reduced and oxidized sulfur likely occurs in the oceans, prior to entering the sediment (Figure 4) [26, 29]. This mixing would result in a reduced value of the S-MIF.
3. Pyrite (reduced) samples show $\Delta^{33} > 0$, while sulfate (oxidized) samples show $\Delta^{33} < 0$ (and vice versa for Δ^{36}). However, $|\Delta^{33}|$ is significantly smaller for the sulfate samples than for the pyrite samples. This asymmetry is hypothesized to be the result of bacterial sulfate reduction processes in the Earth's oceans [26]. However, atmospheric processes may also play a role.

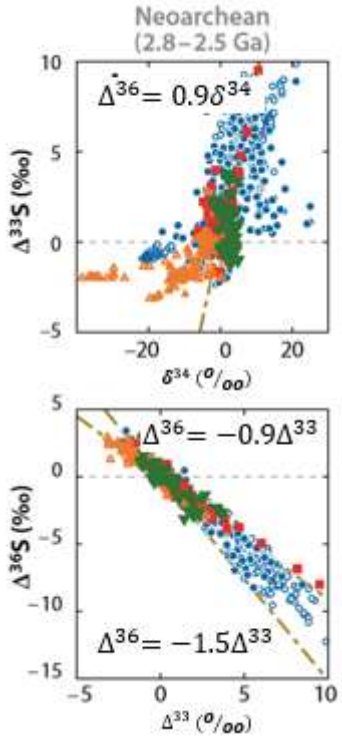

Figure 1-3: Reproduced from Ono (2017) *[26]*, these two plots show the correlations between the various fractionation parameters that define the Archean Reference Array. The top plot (1-3a) shows δ^{34}versus Δ^{33}, while the bottom plot (1-3b) shows Δ^{33} versus Δ^{36}. The different colored data points represent different rock samples. See Reference *[26]*.

1.6. SO_2: Use of Spectroscopy to Explain Sulfur Fractionation Patterns in the Archean Rock Record

The atmospheric process with the largest body of research assessing its relevance to the both the generation of S-MIF and the replication of the Archean Reference Array is the ultraviolet absorption of SO_2. The UV spectrum of SO_2 is characterized by absorption to one of three different electronic states from the electronic ground state ($\tilde{X}\ ^1A_1$). 1) The first involves a weak, spin-forbidden transition ($\tilde{a}\ ^3B_1 - \tilde{X}\ ^1A_1$) from ~400-350 nm. The second involves a stronger transition to two bound, coupled electronic states ($\tilde{A}\ ^1A_2/\tilde{B}\ ^1B_1 - \tilde{X}\ ^1A_1$) from ~350-250 nm [30]. The third involves a still stronger transition to a bound electronic state ($\tilde{C}\ ^1B_2 - \tilde{X}\ ^1A_1$) for wavelengths <240 nm [31]. However, the $\tilde{C}$ state predissociates to SO ($^1\Delta$) + O (^{1}D) at wavelengths <220 nm.

Over the past 20 years, a number of experiments and models have demonstrated significant quantities of SO_2 S-MIF, produced via a variety of mechanisms. For example, Lyons (2007) [32] used atmospheric modeling to propose *isotopologue self-shielding* in $\tilde{C}$ state photolysis from 190 nm to 220 nm. For SO_2, isotopologue self-shielding is caused by small isotopologue-dependent shifts in the transition frequency of vibrational bands in the UV absorption spectrum [33]. For molecules with high concentrations in the atmosphere (e.g. SO_2 during periods of volcanic activity) with strongly absorbing electronic states (such as the $\tilde{C}$ state), the transitions of the most abundant isotopologue ($^{32}SO_2$) will saturate. Therefore, light at $^{32}SO_2$ absorption frequencies cannot reach lower levels of the atmosphere. For rare isotopologues (e.g. $^{34}SO_2$,), however, the transition does not saturate and the frequency shifts in their absorption spectra exposes rare isotopologues to light at lower altitudes. A photochemical process that exhibits self-shielding occurs at a higher total rate for rare isotopologues than for the most abundant isotopologue, thereby generating a significant S-MIF signature.

Lyons observed that the sulfur contained in the SO resulting from the modeled photolysis process displayed $\Delta^{33} > 0$ and $\Delta^{36} < 0$, matching the reduced sulfur in the Archean reference array. However, the ratio $\Delta^{33}/\Delta^{36} \approx 2-3$ was about 2 to 3 times larger than that found in the rock record. Using a broadband light source combined with a bandpass filter, Whitehill and Ono [34] performed experiments on the predissociating 190-220 nm UV band of SO_2 by irradiating pure SO_2 gas and analyzing the solid elemental sulfur and residual SO_2. They reported a fractionation trend of $\Delta^{33}/\Delta^{36} \approx -1.90$, similar to Lyons's prediction and indicative of an isotopologue self-shielding MIF mechanism in the 190-220 nm absorption region. However, this pattern substantially differs from Archean reference array and cannot, by itself, explain those trends in the rock record [35].

A second proposed mechanism for S-MIF in UV absorption of SO_2 is a collision-induced intersystem crossing from the singlet, strongly absorbing $\tilde{A}\ ^1A_2/\tilde{B}\ ^1B_1$ to a long-lifetime triplet state (likely either $\tilde{a}\ ^3B_1$ or $\tilde{b}\ ^3A_2$). Experiments from Whitehill, et. al. [36] were performed by broadband excitation of SO_2 in N_2 by an Xe arc lamp. A very large S-MIF effect (up to 10 % for Δ^{36}) was observed.

It has been theorized that this large MIF effect is due to coincidental degeneracies between the singlet and triplet vibrational states, facilitating collisional transfer [36]. However, Δ^{36} and Δ^{33} were positively instead of negatively correlated (as in the rock record), with $\Delta^{36}/\Delta^{33} \approx 1.12 - 2.25$. Furthermore, Lyons (2009) [24] has argued against the singlet/triplet collision-induced intersystem crossing mechanism. He observed that the reaction that would preserve the isotopic signature (Equation 1.12a) had a smaller rate constant compared to the rate of singlet state collisional deactivation (Equation 1.12b)

$$^1SO_2 + SO_2 \rightarrow SO + SO_3 \qquad (1.12a)$$

$$^1SO_2 + M \rightarrow SO_2 + M. \qquad (1.12a)$$

In Equation 1.12a, $^1SO_2$ represents singlet state SO_2 and has associated rate constant $\sim 4 \times 10^{-1}\ cm^3\ s^{-1}$. For Equation 1.12b, M represents a generic molecule that carries away the excess energy, and has associated rate constant $\sim 1 \times 10^{-1}\ cm^3\ s^{-1}$.

1.7. The Ozone Eta Effect: Nuclear Permutation Symmetry as a Mechanism for MIF

The term *nuclear permutation symmetry* generally describes rules that a molecule's total wavefunction must follow upon the exchange of two *identical nuclei.* I will illustrate this effect in more detail in Chapter 2. Here, I summarize the results. For molecules with two indistinguishable bosons with zero nuclear spin (e.g. sulfur in ^{32}S-^{32}S, oxygen in ^{16}O-^{32}S-^{16}O), half of all rotational states (all states with either an odd or even rotational quantum number) do not exist. This purely quantum mechanical phenomenon has been used famously to explain MIF in the formation of ozone.

This idea, originally introduced by Hawthorn and Marcus [37, 38], was brought to prominence in seminal papers by Gao and Marcus [39, 40]. Specifically, they reported that nuclear permutation symmetry may play a role in the rates of the O_2 isotope exchange reaction given by Equation 1.13:

$$^aO - ^bO + ^cO \leftrightarrow ^aO + ^bO - ^cO \qquad (1.13)$$

Where a, b, c may or may not refer to the same oxygen isotope. The authors employed statistical RRKM theory, assuming that the rate of the reaction was proportional to the number of reactant quantum states (N^+) that could access the "ozone" transition state(${}^aO - {}^bO - {}^cO$) [40].

I now compare. two different forms of this exchange reaction. These are Equations 1.14a and 1.14b, where the X's represent the oxygen atoms with the same mass number, and so on for Y's and Z's

$$X - Y \; + \; X \leftrightarrow X \; + \; Y - X \tag{1.14a}$$

$$X - Y \; + \; Z \leftrightarrow Z \; + \; Y - X. \tag{1.14b}$$

For the reaction shown in Equation 1.14a, the ozone transition state, X-Y-X, is subject to nuclear permutation symmetry restrictions, with half of its total quantum energy levels missing compared to the "asymmetric" case. We label the number of O_2 states with access to the symmetric transition state as N_{sym}^+. Equation 1.14b is an example of a reaction with an asymmetric transition state (X-Y-Z) that is not subject to symmetry restrictions. Because the ozone transition state has double the rotational states, Gao and Marcus reasoned that $N_{asym}^+ > N_{sym}^+$, with $\frac{N_{asym}^+}{N_{sym}^+} = \eta$. Therefore, the total rate of exchange is greater for Equation 1.14a than for Equation 1.14b. This is the so-called "eta-effect" in ozone. Though it is easy to describe the eta effect qualitatively, quantitative descriptions are computationally expensive. Gao and Marcus observed that, though there are twice the number of quantum transition states in the asymmetric case compared to the symmetric case, their modeling best matched meteorite oxygen fractionation data with only $\eta \approx 1.18$. Marcus [41] has shown that this value of η is in rough agreement with classical dynamics calculations.[2] However, a precise understanding of this phenomenon in ozone remains elusive.

[2] For a more detailed explanation, consider an excited, unstable, O_3^* transition state, in quasi-equilibrium with O_2 + O. A certain subset of the O_3^* quantum states exhibit quasiperiodic motion, and cannot dissociate because dissociation is an aperiodic process. Resonances between a dissociating a non-dissociating O_3* states are more likely in asymmetric O_3 than in symmetric O_3, as the asymmetric case has more rotational quantum states. Therefore, the asymmetric O_3* molecule more readily samples the non-dissociating quasiperiodic states and is consequently stabilized. It has been estimated that about 10-15% of all states in O_3* are quasiperiodic, in rough agreement with $\eta = 1.18$. [41].

1.8. The Appeal of Symmetry Effects as Mechanisms for S-MIF.

As in the case of oxygen, nuclear permutation symmetry will be a relevant consideration in any molecule containing multiple sulfur atoms. As an example, consider S_2, the simplest case. Due to the high relative abundance of ^{32}S, the molecule that predominantly carries sulfur-32 into the rock record is ^{32}S-^{32}S (see Figure 1-2), which is subject to symmetry restrictions. Conversely, the molecules that primarily carry sulfur 33, 34, and 36 into the rock record are $^{33,34,36}S$-^{32}S, which are asymmetric and therefore not subject to the same restrictions. I now consider a chemical/photochemical process whose isotope effect is entirely determined by symmetry effects. Using notation from equation 1, I write: $[32]_{sample} < [33]_{sample} = [34]_{sample} = [36]_{sample}$, meaning that $[36]_s/[32]_s = [34]_s/[32]_s = [33]_s/[32]_s$. Plugging into equations 12a and 12b, we obtain $\frac{\Delta^{33}}{\Delta^{36}} = -1.8$, and $\frac{\Delta^{33}}{\delta^{34}} = 0.5$. Both relationships are similar to the Archean reference array values of $\frac{\Delta^{33}}{\Delta^{36}} = -1.5$ and $\frac{\Delta^{33}}{\delta^{34}} = 0.9$. Moreover, compounds with multiple sulfur atoms (S_2, S_4, etc.) are reduced, i.e. do not contain oxygen. If these reduced compounds are enriched in rare isotopes, we have $\Delta^{33} > 0$ and $\Delta^{36} < 0$, which also matches the rock record.

However, for an entirely symmetry-driven fractionation effect, the relationships still differ significantly from the reference array. Furthermore, the eta-effect cannot be employed in the same way in sulfur chemistry as it is in oxygen chemistry. As Babikov [42] notes, sulfur polymerizes to S_8, whereas oxygen cannot polymerize beyond O_3. This means that a comparable eta-effect involving atom exchange in S_2 (involving an S_3 transition state) is likely undone by fast atom exchange in S_3 (involving an S_4 transition state). Babikov instead proposed a unique mechanism, involving conformers of S_4, as the mechanism for S-MIF, but the effect has been neither computationally nor experimentally verified. It also predicts $\Delta^{33} < 0$ and $\Delta^{36} > 0$ for reduced sulfur in the rock record, the opposite of the expected pattern. Finally, Babikov's argument rests on the idea that the symmetric ^{32}S-^{32}S-^{32}S-^{32}S has extra conformational quantum states compared to an isotopically substituted S_4 (e.g. ^{32}S-^{32}S-^{33}S-^{32}S), but Gao and Marcus's

original nuclear permutation symmetry argument related to missing rotational, not conformational states, making Babikov's proposed connection between the two ideas seem tenuous.

1.9. Summary of our Current Understanding of S-MIF Processes

In summary, sulfur mass-dependent fractionation describes a specific isotope effect: shifts in the equilibrium of an isotope exchange reaction, as a function of isotope, caused by differences in vibrational zero point energy. S-MDF patterns are very commonly observed in the rock record. Less commonly observed, any significant deviation from the S-MDF pattern is termed sulfur mass independent fractionation (S-MIF). Large S-MIF signatures are observed in rock samples formed during the Earth's Archean period (~4.0-2.4 billion years ago), with younger rocks exhibiting a mass-dependent pattern. It is thought that S-MIF directly correlates with oxygen levels in the Earth's atmosphere. In a low oxygen, reducing atmosphere, sulfur can exit the atmosphere via one of two channels (sinks): 1) a reduced sink, whereby S_2 polymerizes to S_8, forming solid elemental sulfur aerosol particles and 2) an oxidized sink where sulfur rains out of the atmosphere at H_2SO_4. Because there are two exit channels, any S-MIF generated by chemical or photochemical processes can be preserved in the rock record. In a more modern, oxygenated atmosphere, the reduced sink is shut down, and the S-MIF signature cannot be preserved.

Many attempts have been made to explain sulfur mass independent fractionation in the Archean rock record, with limited success. 1) Shifts in the vibrational spectrum of SO_2 have been shown both empirically and theoretically, to produce large S-MIF signatures via an isotopologue self-shielding, dissociation mechanism. However, the fractionation pattern does not match the rock record well. 2) Collisional transfer from a bound, strongly absorbing singlet SO_2 electronic state to a longer lifetime triplet electronic state. This mechanism also produces large S-MIF signatures, possibly due to coincidental degeneracies between the singlet and triplet quantum energy levels. But these patterns also do not match the rock record, and the chemical reaction that preserves this S-MIF signature is slow compared to the collisional deactivation of the singlet state. 3) Nuclear permutation symmetry, wherein molecules with identical ^{32}S nuclei, such as ^{32}S-^{32}S, have half their rotational states missing relative to

asymmetric molecules like ^{33}S-^{32}S. This could generate S-MIF signatures that closely resemble those in the rock record. However, the most well-known isotope symmetry effect, the eta-effect in oxygen, cannot be readily applied in the case of sulfur, due to the latter's more complex atmospheric chemistry.

1.10. Gaps in our Current Understanding of S-MIF Processes

Thus far, attempts to explain Archean S-MIF are characterized by two types of basic mechanisms. First, is the effect of vibrational energy level shifts. These can impact both spectroscopy (isotopologue self-shielding in C state predissociation) and may create accidental degeneracies between energy levels of two different electronic states, which can facilitate transfer between the them (singlet/triplet transfer in bound SO_2). Second is the concept of nuclear permutation symmetry. The oxygen eta effect is rooted in a statistical model of connections between reactant quantum states and transition quantum states. This number, as noted by Gao and Marcus, is larger for asymmetric transition states than for symmetric transition states.

Many proposed S-MIF mechanisms rely heavily on the idea of vibrational energy level shifts and nuclear permutation symmetry affecting population transfer, either between one electronic state to another, or between one chemical state or another. However, the only evidence of this process (isotope fractionation data) is quite indirect. There has never been a full, state-by-state analysis of the mechanisms by which population may move between electronic states. This leaves many unanswered questions. For example, how do missing rotational states in symmetric molecules affect the transfer process, if at all? Is the overall rotation/vibration energy level structure of the two electronic states important? And can that overall structure be used to predict S-MIF effects in other systems and molecules? Or, is the transfer process more random, determined by coincidental energy level degeneracies between the two states? Is this process affected by the strength or character of the perturbations between the two states? Do the answers to these questions change for non-equilibrium, unidirectional processes versus equilibrium ones?

To address these questions, this thesis describes a complete state-by-state analysis of the ultraviolet B-X electronic state transition in S_2, including a full treatment of collisional transfer between the B excited state, and a nearby perturbing B" state. It attempts to assess whether this exact system, or a similar system could be the origin of S-MIF in the rock record. There many features of S_2 that merit a detailed analysis, including nuclear permutation symmetry, the systematic nature of the B/B" perturbations, and the onset of predissociation at higher vibrational levels that allows for analysis of nonequilibrium processes.

1.11 General Outline of this Work

The general spectroscopic features of the B and B" states of S_2, as well as their UV transitions to and from the X state will be explored in detail in Chapter 2. Chapter 3 details a novel collisional transfer model that combines a well known model for rotationally inelastic transfer with a doorway/perturbation based model for collisional transfer between the B/B" states, providing both intuition and a detailed description of the theory that is supplemented by Appendix A. Chapter 4 describes a Master Equation model that completely accounts for all radiative and collisional transfer processes in the B/B"-X system. This model can be solved both at steady state, and in a time dependent manner, a feature that will be important for the analysis in the final four chapters. The model solves for the fraction of population in the excited state, for each isotopologue. By assuming that excited state S_2 reacts at a much higher rate than does ground state, I hypothesize that the excited state population can be considered a fractionation parameter.

The final four chapters contain results and discussion. Chapter 5 explores the B/B" model in two ways: once at steady state (not predissociating), and once time dependently, when including predissociation at energy levels greater than 36,000. In both cases, the fractionation approximates a S-MDF relationship. The fractionation mechanisms are explored in detail, providing insight into the influence of energy level patterns on collisional transfer. I conclude that the B/B" state-mixing is too large, and therefore too systematic, to generate significant S-MIF. Chapter 6 explores whether or not

weaker perturbations could be the origin of S-MIF. Specifically, it develops a statistical model using small, random perturbations, and demonstrates that such a model can behave differently due to nuclear permutation symmetry (under certain conditions). It then compares the results of the statistical model to the output of the master equation model with the B/B" state-mixing matrix elements set to 1% of their original vales; it concludes that there is evidence of statistical behavior. Chapter 7 explores the impact of non-statistical effects on the results of the weakly state mixed model introduced in Chapter 6. This analysis, supplemented by Appendix B, reveals the possibility for very small state mixings, on the order of 0.002%, to have a significant impact on isotope fractionation, which greatly expands the number of possible S_2 electronic state interactions, beyond the B/B" system that could cause fractionation. The conclusion in Chapter 8 supplements this analysis with more calculations and suggests future areas of study.

Chapter 2 : Spectroscopy of the B/B”-X System in S_2

Abstract:

The goal of this work is to analyze the ability of collisional transfer between excited electronic states to generate S-MIF. The B/B”-X system (bound states: ~31,000 - ~36,000 cm^{-1}) in S_2 has a number of features that make it especially worthy of analysis. First, it has been extensively characterized in a variety of studies. Second, the bound vibrational levels of the short-lifetime (~32 ns) B states are extensively perturbed by the longer-lifetime (~4200 ns) B” state. This system has been deperturbed by Green and Western, which allows for a very detailed state-by-state analysis of fractionation mechanisms. Third, the most abundant isotopologue of S_2, 32-32, is subject to nuclear permutation symmetry restrictions that only allow for (-) parity rotational states. Fourth, the B/B” states predissociate above 35,999 cm^{-1}, which creates opportunities to study time-dependent, as opposed to equilibrium processes. Finally, the nature of the bound B/B” state vibronic level crossings change systematically over the extent of the band. This gives a number of different level crossing patterns to be analyzed. My spectroscopic model incorporates Green and Western’s effective Hamiltonian, detailed Franck-Condon calculations, nuclear permutation symmetry restrictions, predissociation, and mass-dependent vibrational level shifts.

2.1. Introduction

This work analyzes collisional transfer between the strongly interacting B and B” excited electronic states in S_2, where the excited states are populated via UV transitions from the X state, to assess the ability of rotationally/electronically inelastic transfer processes to create S-MIF in the rock record. A number of features of the B/B”-X state make it an especially good test case. For example, the bound levels of the short-lifetime B state are perturbed extensively by a longer-lifetime B” state, and these interactions have been extensively characterized. The nature of these interactions change systematically over the course of the band, which allows me to analyze a variety of different interactions. The most abundant isotopologue of S_2, 32-32, has half of its rotational levels missing due to nuclear permutation symmetry. Also, the B/B” system predissociates above ~36,000 cm^{-1}, which allows us to analyze time-dependent, as opposed to equilibrium processes.

In this chapter, I detail the properties of the B and B” states themselves, their perturbations, as well as the properties of their transitions to and from the X state. In the next chapter, I will detail the collisional transfer model. This chapter has two main parts. In the first, I overview a number of key

features of the S_2 B/B"-X band. The second portion details both the energy level and radiative calculations for the X and B/B" states.

2.2 The B/B"-X UV band of S_2: An overview

The complete B/B"-X system in S_2 is shown in Figure 1 [43]. The B state has molecular term symbol $^3\Sigma_u^-$, and the bound vibrational levels of the B state (v_B = 0-9) stretch from ~31000 cm^{-1} (323 nm) to a predissociation limit at ~35999 cm^{-1} (277 nm). This B state is perturbed over the entirety of this range, primarily via spin-orbit interactions by a B" state ($v_{B"} = 0 - 21$, term symbol: $^3\Pi_u$). It is important to note that the B and the B" state have different dissociation limits. The B state dissociates to a S (^{3}P) + S (^{1}D) limit at $\sim 42{,}000\ cm^{-1}$, and the B" state dissociates to a lower energy state, S (^{3}P) + S (^{3}P), at $35{,}5621\ cm^{-1}$. Because the B" state is approaching its dissociation limit at the upper end of this range, its vibrational levels become closely spaced. This is why the B" state has double the number of vibrational levels in the same energy range. The onset of predissociation around $v_B = 10/v_{B"} = 22$ is due to spin-orbit interactions with a repulsive, Hund's case (c) 1_u state that correlates to a $^1\Pi_u$ Hund's case

(a) state [44],[3], as has been detailed by Ricks and Barrow [45], Green and Western [46], Lewis, et. al. [47], and Stark, et. al. [48]. This repulsive 1_u state is also shown in Figure 1.

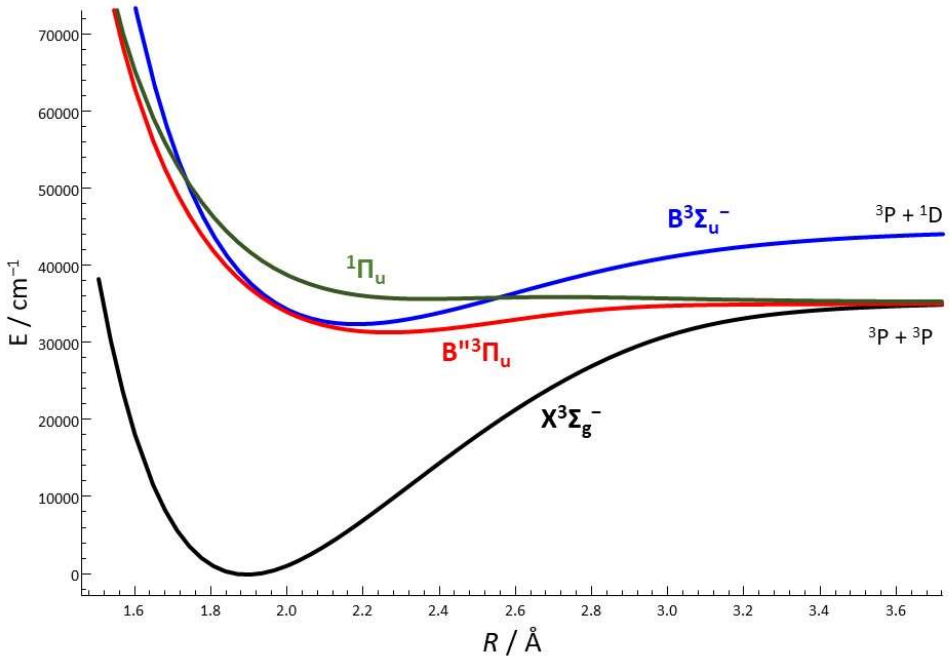

Figure 2-1: The relevant potential energy curves, as a function of internuclear distance, R. Note that the B" state dissociation limit is lower than the B state, creating a shallower potential energy curve. The repulsive $^1\Pi_u$ state crosses the B state at approximately $v = 9$.

2.1.1. Previous Studies of the B/B"-X System

The large body of extensive, detailed research on the B/B"-X system makes it a particularly excellent candidate for a state-by-state analysis of population transfer. Foundational research on B/B" state spectroscopy was undertaken by Meakin and Barrow [49]; Patino and Barrow [50]; Heaven, Miller, and Bondybey [51], among others. However, the seminal work on the topic was performed by Green and Western [52, 46]. Green and Western noted that previous attempts to deperturb the B/B" system were localized to specific avoided crossings and completely ignored long-range interactions. To fully describe the system, they performed two separate "global deperturbations" (first on $v_B = 0 - 6$ and $v_{B"} = 2 - 12$

[3] For a full overview of Hund's cases, see Lefebvre-Brion and Field (2004), Chapter 3.

[52] and then on $v_B = 7 - 9$ and $v_{B''} = 13 - 21$ [46]). In these "global deperturbations", all relevant B state spectroscopic parameters, B" state parameters, and B/B" interactions were floated simultaneously, in order to best fit the data. The authors also found it necessary to include small, long-range B/B" interactions that were not directly observed in their spectroscopic data. Additionally, they calculated the intrinsic lifetime of the B state as 32 ns, and the intrinsic lifetime of the B" state as 4160 ns. I will use these two values extensively in this work.

The widespread perturbations here are analogous to the $\tilde{A}/\tilde{B}$ band in SO_2, which, as I noted in chapter 1, has been shown to generate a S-MIF signature, presumably via collisional transfer to perturbing, long-lifetime, weakly-absorbing triplet states.[4] The advantage here, however, is that Green and Western provide a *largely complete*, *accurate* description of *all* bound states of *both* the strongly absorbing, spectroscopically "bright" B state, and its perturber: the weakly absorbing, spectroscopically "dark" B" state. This allows for a far more detailed, rotationally-resolved, state-by-state analysis of the mechanisms by which collisional population transfer can generate an S-MIF signature. While I am investigating whether the B/B" interaction is, itself, the cause of S-MIF, this level of detailed analysis may give general principles that can guide future studies of the topic.

2.1.2. The effect of isotope shifts on the B/B" system

In this work, I employ a modified version of Green and Western's original model. The simplest modification I make is to include the effect of small changes in mass for different S_2 isotopologues (Green and Western only observed lines for the most abundant isotopologue- ^{32}S-^{32}S). To do so, I assume that the vibrational frequency simply scales as the square root of the reduced mass (μ), i.e. Equation 2.1

$$\omega = \sqrt{\frac{k}{\mu}}. \tag{2.1}$$

[4] This, however, has not been proven.

where k is the spring constant, which is a function of the shape of the electronic state potential energy surface. If I assume this shape is independent of isotopologue, I can relate the known 32-32 frequency ω_{32-32}, determined by Green and Western, to the frequency of any other isotopologue, using the simple relationship given by Equation 2.2:

$$\frac{\omega_x}{\omega_{32-32}} = \sqrt{\frac{\mu_{32-32}}{\mu_x}}. \tag{2.2}$$

The rotational constant, B, is also related to the reduced mass, as shown in Equation 2.3

$$B = \frac{\hbar^2}{\mu {r_{eq}}^2}. \tag{2.3}$$

Here, $\hbar = {h}/{2\pi}$, where h is Planck's constant. The term r_{eq} is the equilibrium internuclear distance, which should also be independent of isotopologue. Therefore, I have Equation 2.4

$$\frac{B_x}{B_{32-3}} = \frac{\mu_{32-3}}{\mu_x}. \tag{2.4}$$

In a simplistic, but instructive, sense, I think of the bound B state energy level pattern as a series of vibrational origins, $E_B(v)$, where v is an integer from 0-9, and, likewise, we have the $E_{B"}(v)$, where $v = 0 - 21$. Within each vibrational level, there is a series of rotational levels that (roughly) scale as $B(v) * (X) * (X + 1)$, where X is the pattern forming rotational quantum number (X is a different quantum number for the B state and the B" state, as I will discuss). The rotational constant, B, is also a function of the vibrational quantum number, v. Figure 2-2 shows the rotational constants for the B and the B" states, as a function of their respective vibrational energies. Though they start with similar values, the rotational constants for the B" state begin to sharply decrease around 34,000 cm^{-1}. This reflects a softening of the potential energy curve and an increase in the equilibrium bond length (Equation 2.3) as the B" state approaches its dissociation limit (Figure 2-1). In addition, the shift in vibrational frequency as a function of mass causes larger energy level shifts at higher energy.

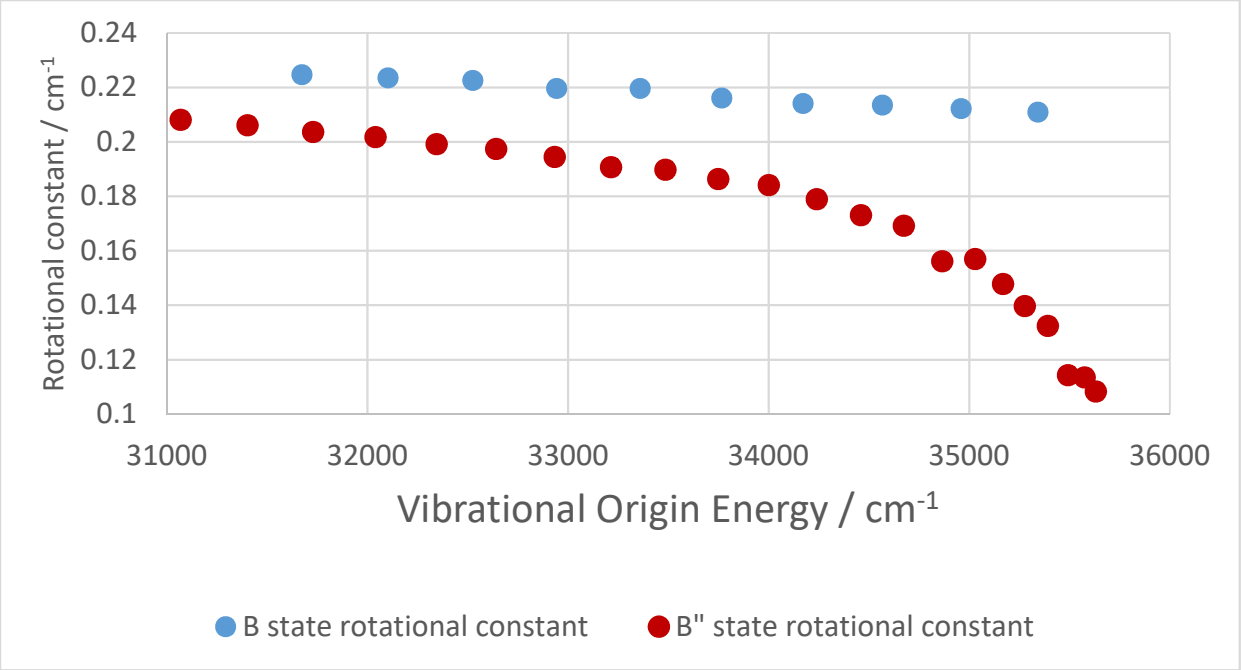

Figure 2-2: Rotational constants for the B and B" states as a function of vibrational energy. The B state rotational constants remain relatively constant, while the B" state constants begin to sharply decline around 34,000 cm^{-1}, as the B" state approaches its dissociation limit.

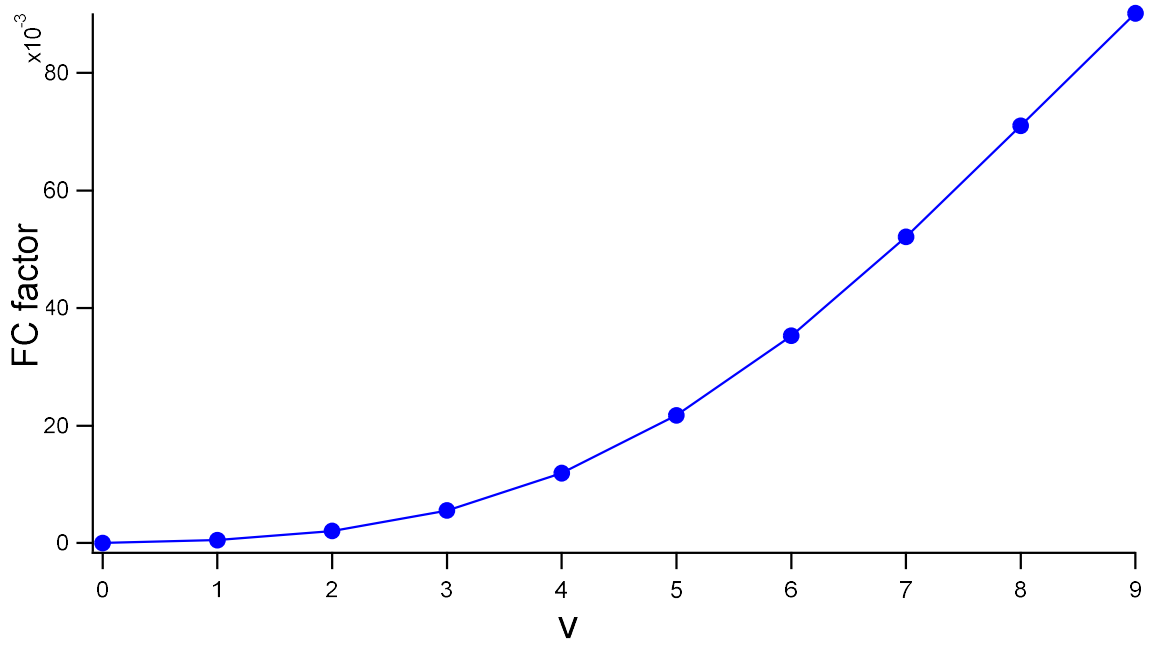

Figure 2-3: The B state Franck Condon progression from $v_x = 0$ to $v_B = 0 - 9$. Above $v_B = 9$, the B state predissociates.

These differences in behavior between the upper vibrational levels and the lower vibrational levels are especially relevant for the B/B"-X UV system, due to the Franck-Condon factors between the X

state and the B state and the B" states. **For the purposes of this discussion, I will use the B state as an example, but a similar discussion applies to the B" state. For more on the B" Franck Condon distribution, and its effects on isotope fractionation, see sections 2.8 and 5.4.**

To begin, the transition intensity between an X state vibrational level to the B state vibrational level is proportional to $q(v_B, v_X)$, where $q(v_B, v_X)$ is the Franck Condon factor, the overlap integral between the B state and the X state vibrational wavefunctions. Figure 2-3 shows the Franck Condon progression for $v_x = 0$ (which contains ~96% of the equilibrium population) to $v_B = x$, with x= 0 to 9. In Figure 2-3, the B state Franck Condon factors are much larger for higher v's than for lower v's. Figure 2-4 compares curve crossings between the B and B" electronic states with low vibrational quantum numbers and crossings between those with high vibrational quantum numbers. Figure 2-4a shows a crossing between a B state with $v = 2$, and a B" state with $v = 5$ for both $^{32}S - {}^{32}S$ and $^{32}S - {}^{36}S$. The interaction region is long because the rotational constants are similar, and the effect of the isotope shift is minimal. Figure 2-4b shows a crossing between B state, $v = 9$ and B" state, $v = 18$. The interaction is short because of the rotational constant disparity and effect of the isotope shift is much larger. Due to the Franck Condon weighting, these short interactions may have a greater influence on the overall behavior of the system than do the longer ones.

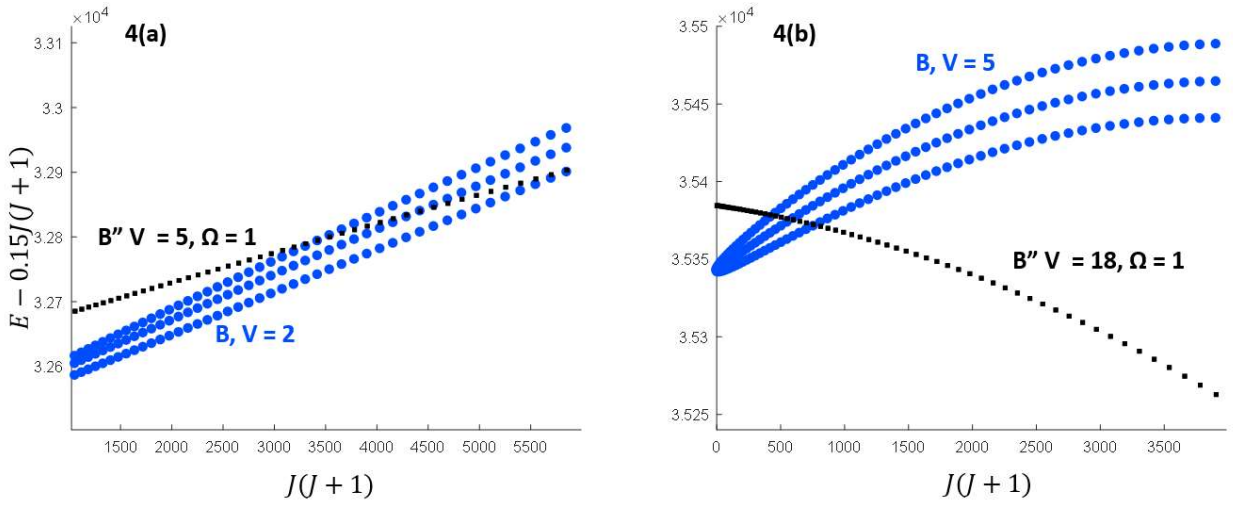

Figure 2-4: (a) shows the level crossing between the B, v = 2 state and the B" v = 5, $\Omega = 1$ state. **Figure 4(b)** shows the level crossing between the B, v = 9 state and the B" v = 18, $\Omega = 1$ state. The independent axis is "the reduced term value," where $0.15\mathrm{J(J+1)}$ is subtracted from each energy value, to achieve scale expansion and make the interaction easier to visualize. This is why the B" v = 18 state appears to "decrease" in energy as the rotational quantum number increases. The interaction is much more protracted, i.e. occurs over a much longer range of J, for the lower vibrational levels (left) than the higher ones (right).

2.3. Nuclear Spin Statistics and Missing Energy Levels in Symmetric Isotopologues

The symmetric isotopologues, 32-32, 34-34, and 36-36, have two identical nuclei with zero nuclear spin ($I = 0$). Therefore, any wavefunction (Ψ_{total}) that completely describes the system must obey Bose-Einstein statistics, i.e. the total wavefunction must be symmetric with respect to the exchange of the two identical nuclei ($\Psi(1,2) = \Psi(2,1)$, where 1 and 2 represent the set of nuclear coordinates for atom 1 and atom 2, respectively). Due to this quantum mechanical effect, half of all rotational states are missing in symmetric S_2, compared to asymmetric S_2. In this section, I fully derive this effect by analyzing the total molecular wavefunctions for the *X* state, the *B* state, and the *B"* state individually.

2.3.1. Introduction:

I begin by expressing the total wavefunction as a product of translational, vibrational, rotational, electronic, and nuclear spin wavefunctions (Equation 2.5)

$$\Psi_{total} = \psi_{trans}\psi_{vib}\psi_{rot}\psi_{elec}\psi_{nuc}. \tag{2.5}$$

In Equation 2.5, the translational and vibrational components of the total wavefunction depend only on the center of mass coordinate and internuclear distance, respectively, and are, therefore, always symmetric with respect to the exchange of nuclei. Because $I = 0$, the nuclear spin wavefunction must always be, likewise, symmetric. Both ψ_{elec} and ψ_{rot}, however, can be either symmetric or asymmetric with respect to exchange. Therefore, I consider ψ_{elec} and ψ_{rot} in turn for the X, B, and B" states.

2.3.2. X state, ($^3\Sigma_g^-$):

Because ψ_{rot} follows the Hund's case (b) angular momentum coupling pattern [44], the rotational pattern forming quantum number is N, where N is the total angular momentum (J), exclusive of spin (S), i.e. $\vec{N} = \vec{J} - \vec{S}$. Under the nuclear exchange operation, wavefunctions with $N = 0,2,4\ldots$ are symmetric ($\Psi_{rot}(1,2) = \Psi_{rot}(2,1)$) while wavefunctions with $N = 1,3,5\ldots$ are antisymmetric ($\Psi_{rot}(1,2) = -\Psi_{rot}(2,1)$) [53].

To determine the symmetry of the electronic wavefunction with respect to nuclear exchange, I begin with the electron configuration of the X state: $\ldots 5\sigma_g^2 2\pi_u^4 2\pi_g^2$. Electrons are fermions (spin ½), and their electronic wavefunction must obey Fermi-Dirac statistics. That is, ψ_{elec} must be **antisymmetric** with respect to electron exchange. The antisymmetry condition is given by Equation 6, where 1_e and 2_e represent the coordinates of the first and second *electron (not nucleus),* respectively

$$\psi_{elec}(1_e, 2_e) = -\psi_{elec}(2_e, 1_e). \tag{2.6}$$

I now consider ψ_{elec} as the product of an orbital wavefunction and a spin wavefunction, as in Equation 2.7

$$\psi_{elec}(1_e, 2_e) = \psi_{orbit}(1_e, 2_e)\psi_{spin}(1_e, 2_e). \tag{2.7}$$

For spin wavefunctions, I define α and β as the wavefunctions associated with $\sigma = \pm 1$, respectively. Here, the parameter σ is the projection of a single electron's *spin* angular momentum along the bond axis. The wavefunction α is associated with $\sigma = +1$ and β is associated with $\sigma = -1$.

For the X state, with two electrons in an open shell, there are four possible spin wavefunctions. They are: $\alpha(1_e)\alpha(2_e)$, $\beta(1_e)\beta(2_e)$, $\frac{1}{\sqrt{2}}[\alpha(1)\beta(2)+\alpha(2)\beta(1)]$, and $\frac{1}{\sqrt{2}}[\alpha(1)\beta(2)-\alpha(2)\beta(1)]$. The first three spin wave functions are all symmetric with respect to electron exchange, and therefore associated with the triplet X state. This gives Equation 2.8

$$\psi_{spin}(1_e,2_e)=\begin{cases}\alpha(1_e)\alpha(2_e)\\ \frac{1}{\sqrt{2}}[\alpha(1_e)\beta(2_e)+\beta(1_e)\alpha(2_e)]\\ \beta(1_e)\beta(2_e).\end{cases} \tag{2.8}$$

Because the triplet spin wavefunction must be *symmetric* with respect to electron exchange, we must have the orbital wavefunction antisymmetric with respect to electron exchange ($symmetric\ x\ antisymmetric\ =\ antisymmetric$). For the orbital wavefunctions, I now define π_+ as a pi electron orbital associated with $\lambda=+1$. The parameter λ is the molecular frame projection of a single electron's orbital angular momentum along the bond axis. The π_- orbital is defined, likewise, as the pi orbital associated with λ = -1. The required antisymmetric orbital wavefunction is given by Equation 2.9

$$\psi_{orbit}(1_e,2_e)=\frac{1}{\sqrt{2}}\left[\pi_{+,g}(1_e)\pi_{-,g}(2_e)-\pi_{-,g}(1_e)\pi_{+,g}(2_e)\right]. \tag{2.9}$$

Having ensured that ψ_{elec} satisfies Fermi-Dirac statistics with respect to **electron** exchange, I now asses the behavior of ψ_{elec} with respect to **nuclear** exchange. In electronic coordinates, the symmetry operator corresponding to the exchange of nuclei is $\hat{\imath}\times\hat{\sigma}$ [54]. Here, $\hat{\imath}$ is the inversion operator, which transforms the electronic coordinates of the orbital wave function from (x,y,z) to $(-x,-y,-z)$. The spin wavefunction is not a function of spacial coordinates and is therefore symmetric with respect to $\hat{\imath}$. For the orbital wavefunctions, we label their symmetric/antisymmetric behavior under the inversion operator as g/u ("gerade"/"ungerade"). For the X state, the π states are symmetric (g) states.

The $\hat{\sigma}$ operator is a reflection through a plane containing the internuclear axis, which transforms π_+ to π_-.[5] As with $\hat{\imath}$, it does not affect the spin wavefunction. Therefore, ψ_{spin} is symmetric with respect to electron exchange. Applying the complete $\hat{\imath} \times \hat{\sigma}$ operator shows that ψ_{orbit} is antisymmetric with respect to exchange. This makes the overall ψ_{elec} antisymmetric. Because ψ_{elec} is antisymmetric, and all other portions of the wavefunction ($\psi_{trans}\psi_{vib}\psi_{nuc}$) are symmetric, ψ_{rot} must be antisymmetric. Therefore, only odd N's exist for the X state.

However, my calculations are carried out using a Hund's case (a) basis set, where J, the total angular momentum, is the rotational quantum number, instead of N. Therefore, we briefly consider the consequences of nuclear spin statistics on J. For a case (b) electronic state, the total spin vector S couples to N to yield J. For a triplet state, projections of S can equal -1,0, or 1. Therefore, there are three possibilities: J = N + 1 (which has e rotationless symmetry), J = N (f rotationless symmetry), or J = N-1 (e rotationless symmetry). The N quantum number can only be odd, so J is even for e symmetry states and odd for f symmetry. The total parity of these states is (-).

2.3.3. B state ($^3\Sigma_u^-$):

The B state electron configuration is $\ldots 5\sigma_g^2 2\pi_u^3 2\pi_g^3$ The analysis is nearly identical to that for the X state, except the electron orbital wavefunction is antisymmetric with respect to inversion, $\hat{\imath}$, making the overall electronic wavefunction symmetric with respect to nuclear exchange. Therefore, the allowed N's are even, and the allowed J's are odd for e symmetry and even for f symmetry. The total parity is again, (-).

2.3.4. B" state ($^3\Pi_u$):

[5] Classically, we think of the +/- designation as representing either a clockwise or a counterclockwise rotation around the bond axis. The reflection operation described by σ reverses the direction of that rotation [55].

The B" state follows a Hund's case (a) coupling pattern. The rotational pattern forming quantum number is J, the total angular momentum. Therefore, the rotational wavefunction is symmetric with respect to nuclear exchange for even J, and antisymmetric with respect to nuclear exchange for odd J.

Analysis of the symmetry properties of the electronic wavefunction is more complex than that for the X or B states, but it follows a similar logical path. The electron configuration of the B" state is $\ldots 5\sigma_g^2 2\pi_u^4 2\pi_g^1 5\sigma_u^1$. Like the X state, the B" state is a triplet, so we have the same three symmetric spin wavefunctions (see Equation 2.8). Unlike the X state, however, there are not one, but two antisymmetric orbital wavefunctions allowed by Fermi-Dirac statistics. They are given by Equations 2.10a-b:

$$\psi_{orbit,+} = \frac{1}{\sqrt{2}}\left[\pi_{u+}(1)\sigma_g(2) - \pi_{u+}(2)\sigma_g(1)\right] \tag{2.10a}$$

$$\psi_{orbit,-} = \frac{1}{\sqrt{2}}\left[\pi_{u-}(1)\sigma_g(2) - \pi_{u-}(2)\sigma_g(1)\right]. \tag{2.10b}$$

Equation 2.10a has $\lambda = +1$, and Equation 2.10b has $\lambda = -1$. Note that neither wavefunction has a definite symmetry with respect to the $\hat{\sigma}$ operator, so we create symmetrized wavefunctions, as follows (Equations 2.11a-b)

$$\psi_{orbit,e} = \frac{1}{\sqrt{2}}[|\psi_{orbit+}> + |\psi_{orbi}\quad>] \tag{2.11a}$$

$$\psi_{orbit,f} = \frac{1}{\sqrt{2}}[|\psi_{orbit}\quad> - |\psi_{orbit-}>]. \tag{2.11b}$$

Here e and f denote the rotationless symmetry [44]. Applying the $\hat{\imath} \times \hat{\sigma}$ operator (nuclear exchange in electronic coordinates) shows that $|\psi_{orbit}\quad e>$ is antisymmetric, and $|\psi_{orbit+}\, f>$ is symmetric, with respect to exchange of nuclei. Therefore, both even-J and odd-J states exist, with the even J's having f symmetry, and the odd J's having e symmetry.

2.4: Introduction to the Green and Western Hamiltonian

In this study, I implement an effective Hamiltonian model for energy levels in the X, B, and B'' states, similar to that used by Green and Western. The principle differences are the vibrational/rotational level shifts and the inclusion of extra states in asymmetric S_2, described in Section 2.2. There are, additionally, a few small terms included in the Green and Western model that are excluded in my model, as they only affect high-J states that will be irrelevant to my collisional transfer model.

In the manner of Green and Western, I split the Hamiltonian in two. The larger terms are contained in $\widehat{H}_{major}$ (Equation 2.12a) and the smaller terms are contained within $\widehat{H}_{minor}$ (Equation 2.12b)

$$\widehat{H}_{major} = B\left[J(J+1) + S(S+1) - \hat{J}_z^2 - \hat{L}_z^2 - \hat{S}_z^2\right] + B\left[\hat{J}_+\hat{L}_- + \hat{J}_+\hat{L}_-\right] + B\left[\hat{J}_+\hat{S}_- + \hat{J}_+\hat{S}_-\right] + B\left[\hat{J}_+\hat{L}_- + \hat{J}_+\hat{L}_-\right] \quad (2.12a)$$

$$\widehat{H}_{minor} = -D\hat{R}^4 + \frac{2}{3}\lambda\left(3\hat{S}_z^2 - \hat{S}^2\right) + \gamma\widehat{N}\cdot\hat{S} - \frac{1}{2}o\left(\hat{S}_+^2 e^{-2i\phi} + \hat{S}_-^2 e^{2i\phi}\right). \quad (2.12b)$$

Here, L, S, R, and J represent the orbital, spin, rotational, and total angular momentum quantum numbers, respectively, with their angular momentum projection operators (e.g. $\hat{L}_z$) and the raising and lowering operators (e.g. $\hat{J}_{+/-}$) defined as in Levebre-Brion and Field [44]. Likewise, A is the spin orbit constant, and B is the rotational constant. Note that the raising and lowering operators are defined in the molecular reference frame, so $\hat{J}_-$ functions as a raising operator and $\hat{J}_+$ functions as a lowering operator (i.e. $\langle\Omega+1|\hat{J}_-|\Omega\rangle \neq 0$, and $\langle\Omega-1|\hat{J}_+|\Omega\rangle \neq 0$, where Ω is the projection of J along the bond axis). For more details, see Zare (1988) [55]. The terms in the minor Hamiltonian represent centrifugal distortion, spin-spin coupling, spin-rotation coupling, and "o-type" lambda doubling, with associated constants: D, λ, γ, and o. My model incorporates rotational quantum levels with $J = 0 - 100$. For vibrational levels, I include $v = 0 - 1$ for the X state (these two states account for >99% of the equilibrium vibrational population), $v = 0 - 9$ in the B state, and $v = 0 - 21$ in the B" state. Again, this accounts for all *bound* upper states in the B/B" system.

2.5: Constructing the Effective Hamiltonian

In this section, I detail every matrix element included in the effective Hamiltonian used in this study. To begin, I construct the effective Hamiltonians in the Hund's case (a) basis set. Hund's case (a) basis states are written in terms of their "good quantum numbers", i.e quantum numbers that represent quantum states with relatively small off-diagonal matrix elements in the case (a) angular momentum coupling scheme. I write these basis states as $|J\ \Omega\ S\ \Sigma\ \Lambda\ v>$, where Ω is the projection of the total angular momentum, Σ is the spin projection, Λ is the orbital angular momentum projection, and v is the vibrational quantum number.

It is also convenient to define a symmetrized basis set, as follows in Equations 2.13a-b, where e and f denote the rotationless symmetry (similar to section 2.3.4). We do so because the Hamiltonian does not connect states of opposite symmetry (i.e. $< e|\widehat{H}|f >= 0$, always)

$$|e> = \frac{1}{\sqrt{2}}(|J\ \Omega\ S\ \Sigma\ \Lambda\ v> + |J\ (-\Omega)\ S\ (-\Sigma)\ (-\Lambda)\ v>) \quad (2.13a)$$

$$|f> = \frac{1}{\sqrt{2}}(|J\ \Omega\ S\ \Sigma\ \Lambda\ v> - |J\ (-\Omega) S\ (-\Sigma)(-\Lambda) v>). \quad (2.13b)$$

The only exceptions are the $\Omega = 0$ components of the X and B $^3\Sigma^-$ states. For these components, $\Omega = \Sigma = \Lambda = 0$. Therefore, the basis states ($|J\ 0\ S\ 0\ 0\ v>$) have e symmetry, intrinsically.

I now list all matrix elements included in my effective Hamiltonian model. I begin with the X and B states, as they both correspond to the $^3\Sigma^-$ electronic term symbol. The diagonal matrix elements for the X and B states, sorted by their corresponding term in the Hamiltonian given in equations 2.12a-b, are listed in Table 2-I. The values of the molecular constants are those presented in Green and Western, with the exception of the isotopologue shifts described in the previous section. These matrix elements apply to both e symmetry and f symmetry states.

Table 2-I: $^3\Sigma^-$ (X and B state) Diagonal Matrix Elements

Hamiltonian Term	Diagonal Matrix Element
$<^3\Sigma^-_{\Omega}\| J^2 + S^2 - L_z^2 - S_z^2 - J_z^2 \|^3\Sigma^-_{\Omega}>$	$B (J (J+1) + S(S + 1) - \Omega^2 - \Sigma^2)$
$<^3\Sigma^-_{0}\| -DR^4 \|^3\Sigma^-_{0}>$	$-D[(J (J + 1))^2 + 8 J (J+1) + 4]$
$<^3\Sigma^-_{1}\| -DR^4 \|^3\Sigma^-_{1}>$	$-D[(J (J+1))^2 + 2J (J + 1)]$
$<^3\Sigma^-_{\Omega}\| 2/3\lambda(3S^2_z - S^2) \|^3\Sigma^-_{\Omega}>$	$2/3\lambda[3 \Sigma^2 - S(S + 1)]$
$<^3\Sigma^-_{\Omega}\|\gamma NS\|^3\Sigma^-_{\Omega}>$	$\gamma[\Sigma \Omega - S(S + 1)]$

Table 2-II displays the off-diagonal matrix elements within the $^3\Sigma^-$ states, between different spin orbit components (i.e. $\Omega = 0$ and $\Omega = 1$). For Σ^- states, $\Omega = 0$ components have exclusively e rotationless symmetry. Therefore, all off-diagonal matrix elements must be between two states with e symmetry.

Table 2-II: Off-Diagonal Matrix Elements for $^3\Sigma^-$ (X, B)

Hamiltonian Term	Matrix Element
$<^3\Sigma^-_{1}\, e\|-B(J_-S_+ + J_+S_-) \|^3\Sigma^-_{0}\, e>$	$-2B(J (J + 1))^{1/2}$
$<^3\Sigma^-_{1}\, e\| -DR^4 \|^3\Sigma^-_{0}\, e>$	$4D[(J (J + 1))^{3/2} + (J (J + 1))^{1/2}]$
$<^3\Sigma^-_{1}\, e\|\gamma NS\|^3\Sigma^-_{0}\, e>$	$\gamma(J (J + 1))^{1/2}$

Table 2-III shows the diagonal matrix elements for the B" $^3\Pi_u$ state. Note that the last two terms show a discrepancy in the behavior between e and f symmetry components, due to o-type ($\Omega = 0$) lambda doubling.

Table 2-III: Off-Diagonal Matrix Elements for $^3\Sigma^-$ (X, B)

Hamiltonian Term	Matrix Element
$<^3\Pi_{\Omega} \| J^2 + S^2 - L_z^2 - S_z^2 - J_z^2 \|^3\Pi_{\Omega}>$	$B[J(J + 1) + S(S + 1) - \Omega^2 - \Sigma^2 - 1$
$<^3\Pi_{\Omega} \| AL_zS_z \|^3\Pi_{\Omega}>$	$A \Sigma$
$<^3\Pi_{0} \| -DR^4 \|^3\Pi_{0}>$	$-D[(J (J+1))^2 - 2 J (J+1)]$

$<^3\Pi_1 \mid -DR^4 \mid ^3\Pi_1>$	$-D[\ (J(J+1))^2 + 4J(J+1) - 4]$
$<^3\Pi_2 \mid -DR^4 \mid ^3\Pi_2>$	$-D[\ (J(J+1))^2 + 6J(J+1) + 12]$
$<^3\Pi_\Omega \mid 2/3\lambda(3S^2_z - S^2) \mid ^3\Pi_\Omega>$	$2/3\lambda[3\ \Sigma^2 - S(S+1)]$
$<^3\Pi_\Omega \mid \gamma NS \mid ^3\Pi_\Omega>$	$\gamma[\Sigma\ \Omega - S(S+1)]$
$<^3\Pi_\Omega\ \Omega = 0, e\mid -1/2o(S_+^2e^{-2\phi} + S_+^2e^{+2\phi}) \mid ^3\Pi_\Omega\ \Omega = 0, e>$	o
$<^3\Pi_\Omega\ \Omega = 0, f\mid -1/2o(S_+^2e^{-2\phi} + S_+^2e^{+2\phi}) \mid ^3\Pi_\Omega\ \Omega = 0, f>$	-o

Table 2-IV gives the off-diagonal matrix elements within the B" $^3\Pi$ state. All nonzero matrix elements are between two states with the same rotationless symmetry.

Table 2-IV: Off-Diagonal Matrix Elements for $^3\Sigma^-$ (X, B)

Hamiltonian Term	**Matrix Element**
$<^3\Pi_1\ e/f\mid -B(J_-S_+ + J_+S_-) \mid ^3\Pi_0\ e/f>$	$-B[\ J\ (J+1)]^{1/2}$
$<^3\Pi_1\ e/f\mid -DR^4 \mid ^3\Pi_0\ e/f>$	$-2^{3/2}D(\ J\ (J+1))^{2/3}$
$<^3\Pi_1\ e/f\mid \gamma NS \mid ^3\Pi_0\ e/f>$	$\gamma/2(J(J+1))^{1/2}$
$<^3\Pi_2\ e/f\mid -B(J_-S_+ + J_+S_-) \mid ^3\Pi_1\ e/f>$	$B(2J(J+1) - 4)^{1/2}$
$<^3\Pi_2\ e/f\mid -DR^4 \mid ^3\Pi_1\ e/f>$	$-2^{3/2}D(2J(J+1) - 4)(2(J(J+1)-4)^{1/2}$
$<^3\Pi_2\ e/f\mid \gamma NS \mid ^3\Pi_1\ e/f>$	$\gamma/2(2J(J+1) - 4)^{1/2}$
$<^3\Pi_2\ e/f\mid -DR^4 \mid ^3\Pi_0\ e/f>$	$-2D((J(J+1) - 2)(J(J+1))^{1/2})^{1/2}$

Thus far, I have only listed off-diagonal elements within a given electronic state. For perturbations *between* electronic states, Green and Western define the parameters α and β, as in Equations 2.14a-b

$$\alpha = < B", v_{B"} \mid \left(\frac{1}{2}A + B\right)\hat{L}_+ \mid B, v_B > \qquad (2.14a)$$

$$\beta = < B", v_{B"} \mid B\hat{L}_+ \mid B, v_B >. \qquad (2.14b)$$

Green and Western list α and β as a function of v_B and $v_{B"}$.

Equations 2.15a-e give the B/B" state perturbations in terms of α and β

$$< {}^3\Pi_0 e \left| \hat{H} \right| {}^3\Sigma_0^- e > = \alpha + \beta \tag{2.15a}$$

$$< {}^3\Pi_1 e \left| \hat{H} \right| {}^3\Sigma_0^- e > = -\frac{1}{2}(J(J+1))^{1/2}\beta \tag{2.15b}$$

$$< {}^3\Pi_1 e/f \left| \hat{H} \right| {}^3\Sigma_1^- e/f > = 2^{\frac{1}{2}}(\alpha + \beta) \tag{2.15c}$$

$$< {}^3\Pi_0 e/f \left| \hat{H} \right| {}^3\Sigma_1^- e/f > = \mp 2^{\frac{1}{2}}(J(J+1))^{\frac{1}{2}}\beta \tag{2.15d}$$

$$< {}^3\Pi_2 e/f \left| \hat{H} \right| {}^3\Sigma_1^- e/f > = -[J(J+1) - 2]^{\frac{1}{2}}\beta. \tag{2.15e}$$

I assume these perturbations are identical for all isotopologues. This is equivalent to assuming that the Franck Condon factors are independent of isotopologue.

At this stage in the calculation, I have two Hamiltonians for each isotopologue: one for the X state and one for the B/B" system. Each Hamiltonian is then diagonalized in Matlab version 2017a [56], producing a set of eigenvalues and their corresponding eigenvectors. An algorithm then assigns an eigenstate (|eig>) to a zeroth order, Hund's case (a) basis state (|J Ω S Σ Λ v>). It finds the basis state that maximizes | <J S Ω Σ Λ|eig > |^2 and then stores the index for future use. In the next section, the assigned case (a) basis states are used to determine spectroscopic selection rules, while the complete eigenstate is used to calculate absorption intensity.

2.6: UV absorption spectroscopy calculations

The next component of the program calculates the absorption cross-section (σ) for every transition allowed by the case (a) selection rules. These rules are: $\Delta J = \pm 1$ for $e \rightarrow e$ or $f \rightarrow f$ transitions, and $\Delta J = 0$ for $e \rightarrow f$ or $f \rightarrow g$ transitions. Additionally, $\Delta \Omega = 0, \pm 1$.

In this section, I represent the initial and final eigenstates in the case (a) basis, as in Equation 2.16.

$$|eig> = \sum_i c_i |J_i\ \Omega_i> |S_i \Sigma_i \Lambda_i> |v_i>. \tag{2.16}$$

In Equation 2.16, the sum is over all case (a) basis states, and the c_i's are the coefficients, determined by the diagonalization procedure defined above. I have also separated the basis state into rotational, electronic, and vibrational parts, respectively. Using this construction, the absorption cross-section for a given transition (σ) given by Equation 2.17

$$\sigma = \frac{2\pi^2 \nu}{3\epsilon_0 hc(2J"+1)} \left| \sum_i c_i <J_i\ \Omega_i| <S_i \Sigma_i \Lambda_i| <v_i|\ \hat{\boldsymbol{\mu}} \sum_j c_j |J_j\ \Omega_j> |S_j \Sigma_j \Lambda_j> |v_j>\ \right|^2, \tag{2.17}$$

where ν is the transition frequency, ϵ_0 is the permittivity of free space, h is Planck's constant, c is the speed of light, and *J"* is the initial state total angular momentum quantum number. Most importantly for this section, $\hat{\boldsymbol{\mu}}$ is the electric dipole moment operator. The dipole moment operator is, here, associated with the UV sunlight that drives transitions from the X state to the B/B" state. The term <eig|$\hat{\mu}$|eig> is called the *transition dipole moment.* Note that $\hat{\boldsymbol{\mu}}$ operates on the rotational and electronic parts separately. The notation for the rotational and electronic components is given by Equations 2.18a-b

$$|<J_i\ \Omega_i|\hat{\boldsymbol{\mu}}|J_j\ \Omega_j>|^2 = S_{J_i \Omega_i, J_j, \Omega_j} \tag{2.18a}$$

$$|<S_i \Sigma_i \Lambda_i|\hat{\boldsymbol{\mu}}|S_j \Sigma_j \Lambda_j>|^2 = |R_e|^2. \tag{2.18b}$$

The term $S_{J_i \Omega_i, J_j, \Omega_j}$ is the *rotational linestrength,* and it must be calculated for each value of J and Ω (see: next section). By contrast, the term $|R_e|^2$, the *electronic transition dipole moment*, is assumed constant for the entire electronic state. In separating the electronic wavefunction from the vibrational one, I have assumed that the electronic transition dipole moment is independent of the internuclear distance. Therefore, the vibrational wavefunction (which is only a function of the internuclear distance) can be factored out, as in Equation 2.19

$$\left|<v_j| <S_i \Sigma_i \Lambda_i|\hat{\boldsymbol{\mu}}|S_j \Sigma_j \Lambda_j> |v_j>\right|^2 = |<v_i|v_j>|^2 \left| <S_i \Sigma_i \Lambda_i|\hat{\boldsymbol{\mu}}|S_j \Sigma_j \Lambda_j>\right|^2. \tag{2.19}$$

This factored term is the *Franck Condon* factor, i.e. $q(v_B, v_x) = |< v_i|v_j >|^2$. I consider the rotational linestrength, the electronic transition dipole moment, and the Franck Condon factors in the sections below.

2.7: Electronic Transition Dipole Moment and Rotational Linestrengths

To evaluate $S_{J_iJ_j}$, I first consider the dipole moment operator itself ($\hat{\boldsymbol{\mu}}$). The operator is a vector quantity that can be written in one of two coordinate systems: (1) a "molecule-fixed" coordinate system, with Cartesian coordinates (x, y, z), where z is the internuclear axis between the two sulfur atoms. (2) A so-called "laboratory" coordinate system, with coordinates (X, Y, Z) that is not defined relative to the molecule.

We write the dipole operator in the "lab frame" as follows in Equation 2.20, where $\hat{\imath}$, $\hat{\jmath}$, and $\hat{k}$ are unit vectors in the X, Y, and Z directions, respectively

$$\hat{\boldsymbol{\mu}} = \mu_X\hat{\imath} + \mu_Y\hat{\jmath} + \mu_Z\hat{k}. \tag{2.20}$$

The $\hat{\boldsymbol{\mu}}$ operator is associated with the radiation field that drives transitions from the X state to the B/B" electronic states, i.e. UV radiation from the sun. We can assume this light is isotropic, which gives Equation 2.21

$$\hat{\mu} = 3\hat{\mu}_Z. \tag{2.21}$$

I am interested in the effect of the radiation field on the molecule itself, so I now must transform the dipole moment operator from the laboratory frame to the molecular frame. In other words, I express $\hat{\mu}_Z$ (lab frame) as a linear combination of $\hat{\mu}_x$, $\hat{\mu}_y$, $\hat{\mu}_z$ (molecular frame), with associated coefficents α_{Zx}, α_{Zy}, α_{Zz}. The linear combination is given by Equation 2.22

$$\hat{\mu} = 3\left(\alpha_{Zx}\hat{\mu}_x + \alpha_{Zy}\hat{\mu}_y + \alpha_{Zz}\hat{\mu}_z\right). \tag{2.22}$$

I now rewrite the above equation in a particular way to yield Equation 2.23

$$\hat{\mu} = \frac{3}{2}(\alpha_{Zx} - i\alpha_{Zy})(\hat{\mu}_x + i\hat{\mu}_y) + \frac{3}{2}(\alpha_{Zx} + i\alpha_{Zy})(\hat{\mu}_x - i\hat{\mu}_y) + 3\alpha_{Zz}\hat{\mu}_z). \quad (2.23)$$

Equation 2.23 is so written because $(\hat{\mu}_x + i\hat{\mu}_y)$, $(\hat{\mu}_x - i\hat{\mu}_y)$, and $\hat{\mu}_z$ have a very limited set of nonzero matrix elements when operating on the electronic part of the wavefunction (|SΣΛ>). Here, as previously, I will write the electronic wavefunction as the direct product of an orbital wavefunction (|Λ>) and a spin wavefunction (|SΣ>). Noting that the dipole only operates on the orbital wavefunction, the nonzero matrix elements are given by Equations 2.24a-c

$$< \Lambda + 1 | (\hat{\mu}_x + i\hat{\mu}_y) | \Lambda > \quad (2.24a)$$

$$< \Lambda - 1 | (\hat{\mu}_x - i\hat{\mu}_y) | \Lambda > \quad (2.24b)$$

$$< \Lambda | \hat{\mu}_z | \Lambda >. \quad (2.24c)$$

Note that $\Omega = \Sigma + \Lambda$, whrere Σ is the total spin projection quantum number. Because Σ is unchanged, the nonzero matrix elements for Ω are identical. I can now define R_e^+, R_e^0, and R_e^-, as shown in Equations 2.25a-c

$$R_e^+ = < \Omega + 1 \left| \frac{1}{\sqrt{2}} (\hat{\mu}_x + i\hat{\mu}_y) \right| \Omega > \quad (2.25a)$$

$$R_e^- = < \Omega - 1 \left| \frac{1}{\sqrt{2}} (\hat{\mu}_x - i\hat{\mu}_y) \right| \Omega > \quad (2.25b)$$

$$R_e^0 = < \Omega | \hat{\mu}_z | \Omega >. \quad (2.25c)$$

For a transition with $\Delta S = 0$, it can be shown using symmetry relations that the magnitudes of R_e^+, R_e^-, R_e^0 are identical [57]. Therefore, I can define the familiar electronic TDM, $|R_e|^2$, as in Equation 2.26

$$|R_e|^2 = |R_e^+|^2 = |R_e^0|^2 = |R_e^-|^2. \quad (2.26)$$

This allows me to rewrite $< J_i\ \Omega_i | < S\ \Sigma_i\ \Lambda_i | \hat{\boldsymbol{\mu}} | J_i\ \Omega_i > | S\ \Sigma_i\ \Lambda_i >$, as in equation 2.27

$$< J_i\ \Omega_i | < S\ \Sigma_i\ \Lambda_i | \hat{\boldsymbol{\mu}} | J_i\ \Omega_i > | S\ \Sigma_i\ \Lambda_i > = |R_e|^2 || < J_i\ \Omega_i | \boldsymbol{\alpha} | J_i\ \Omega_i > |^2, \quad (2.27)$$

where $\boldsymbol{\alpha} = \frac{3}{2}(\alpha_{Zx} - i\alpha_{Zy})$, if $\Delta\Omega = 0$; $\boldsymbol{\alpha} = \frac{3}{2}(\alpha_{Zx} + i\alpha_{Zy})$, if $\Delta\Omega = -1$; and $\boldsymbol{\alpha} = 3\alpha_{Zz}$, if , $\Delta\Omega = 0$.

This conditional definition of $\boldsymbol{\alpha}$ constitutes the so-called "cosine-alpha" matrix. It has nonzero matrix elements for $\Delta\Omega = 0, -1, 1$ and $\Delta J = -1,0,1$. These values are tabulated in Whitting and Nicholls [57], and in Hougen [58].

2.8: Calculation of Franck Condon Factors

Recalling my expression for the total transition dipole moment (Equation 2.28):

$$|< J_i\ \Omega_i|< S\ \Sigma_i\ \Lambda_i|\ < v_i|\hat{\boldsymbol{\mu}}\ |v_i> |S\ \Sigma_i\ \Lambda_i> |J_i\ \Omega_i> |^2\ = |R_e|^2 S_{J_i,\Omega_i\, J_j,\Omega_j} q(v_{j,} v_i). \qquad (2.28)$$

The term $q(v_{j,} v_i)$ in Equation 28 is the Franck Condon (FC) factor. In matrix notation, the FC factor is $|< v_j|v_i> |2$, but it is perhaps more intuitive in integral form, as in Equation 2.29

$$|\int \psi_{v_j}\psi_{v_i}\, d\tau|^2. \qquad (2.29)$$

Here, ψ_{v_j} and $\psi_{v_i}$are the upper state and ground state vibrational wavefunctions, respectively, and the integral $d\tau$ is over all space. In words, the Franck Condon factor is the spacial overlap between the ground state and excited state vibrational wavefunctions.

To calculate the FC factors for all bound vibrational levels in the X, B, and B" states, I use LeRoy's RKR [59] and LEVEL [60] programs. The first program, RKR, uses a modification of the semiclassical WKB approximation, which is often used to approximate quantum energy levels (in this case, vibrational levels) given a potential energy curve [61]. The RKR procedure inverts this process. Given a set of rotational/vibrational levels, the program outputs a series of classical turning points that, taken together, form the potential energy curves.

For this study, I input the rotational and vibrational energy levels as constants from a low-order Dunham expansion. A Dunham expansion is a simple power expression of the rotational-vibrational energy in terms of $\left(v+\frac{1}{2}\right)$ and $J(J+1)$, as in Equation 2.30

$$E(v,J)=\sum_{j}\sum_{k}Y_{j,k}(v+\frac{1}{2})^{j}(J(J+1))^{k}. \tag{2.30}$$

To determine the $Y_{j,0}$ and $Y_{0,k}$ constants, I performed a least squares fit using the energy levels provided by Green and Western for ^{32}S-^{32}S. The results of this fit for the X and B states are shown in Table V.

Table 2-V: Least squares fit for Dunham Expansion Constants of X state and B state

Electronic State	$Y_{k,l}$	Least Squares Fit / cm^{-1}
X	$Y_{1,0}$	725.7
X	$Y_{2,0}$	-0.2850
X	$Y_{0,0}$	0.2955
X	$Y_{0,1}$	$-1.633*10^{-3}$
B	$Y_{1,0}$	435.6
B	$Y_{2,0}$	-3.636
B	$Y_{3,0}$	0.2191
B	$Y_{4,0}$	-0.01377
B	$Y_{0,0}$	0.228
B	$Y_{0,1}$	$-2.552*10^{-3}$
B	$Y_{0,2}$	$7.916*10^{-5}$

In Table 2-V, the X state and the B state have power expansions of different size. The size of the fit was chosen to be as large as possible, while avoiding an "overfit" scenario. I considered the curve overfit when the inner classical turning points began to increase with increasing energy, which is clearly nonphysical behavior.

Next, I use LeRoy's LEVEL program to calculate the vibrational wavefunctions and Franck Condon factors. I used a 12 point piecewise polynomial interpolation [60] to determine the potential energy function, V(r), from the classical turning points input from the RKR procedure. LEVEL then uses the interpolated V(r) to solve the Schrödinger equation. It does so by choosing a trial energy and numerically integrating the Schrödinger equation, beginning at both the inner and outer turning points. It then evaluates the discontinuity between the inner and outer solutions, chooses a new trial energy, and repeats until the solution converges. Finally, LEVEL uses the converged vibrational wavefunctions to calculate the Franck Condon factor, as in Equation 2.29.

The calculated B-X Franck Condon factors, displayed in Table VI, are used in my line intensity calculation.

Table 2-VI: Calculated Franck Condon factors for v_B = 0-9 and v_X= 0-1

$v_B \setminus v_X$	**0**	**1**
0	8.53e-05	9.45816e-04
1	5.80e-04	5.21e-03
2	2.13e-03	1.53e-02
3	5.62e-03	3.16e-02
4	1.19e-02	5.15e-02
5	2.18e-02	6.96e-02
6	3.53e-02	8.00e-02
7	5.21e-02	7.85e-02
8	7.10e-02	6.45e-02
9	9.01e-02	4.16e-02

My calculations compare favorably with Franck Condon factors empirically determined by Anderson and Crosley [62].

I also include the B" state Franck-Condon factors. While the absorption to the B" state is about two orders of magnitude weaker, the fluorescence is also, correspondingly, approximately two orders of magnitude weaker. Therefore, at steady state, the B" states will have similar populations to the B state. The least squares fit Dunham parameters (i.e. $Y_{j,0}$ and $Y_{0,k}$ constants) that were input into RKR are included in Table 2-VII.

Table 2-VII: Least squares fit for Dunham Expansion Constants of X state and B" state

Electronic State	$Y_{k,l}$	Least Squares Fit / cm^{-1}
B"	$Y_{1,0}$	391.5
B"	$Y_{2,0}$	-7.042
B"	$Y_{0,0}$	0.2049
B"	$Y_{0,1}$	$5.3*10^{-4}$
B"	$Y_{0,2}$	$-2.2*10^{-4}$

The calculated B"-X Franck Condon factors are displayed in Table 2-VIII.

Table 2-VIII: Calculated Franck Condon factors for $v_{B"}$ = 0-21 and v_x = 0-1

$v_{B"} \setminus v_X$	0	1
0	4.53e-07	6.51e-06
1	6.25e-06	7.71e-05
2	4.45e-05	0.00047
3	0.00022	0.0019
4	0.00082	0.00584
5	0.0025	0.0143
6	0.0064	0.029
7	0.014	0.048
8	0.026	0.067
9	0.044	0.078
10	0.064	0.075
11	0.084	0.057
12	0.010	0.032
13	0.11	0.011
14	0.11	0.000467
15	0.098	0.0032
16	0.084	0.015
17	0.067	0.029
18	0.050	0.039
19	0.035	0.042
20	0.022	0.035
21	0.0078	0.015

2.9: The Electronic Transition Dipole Moments

The final components needed to determine the absolute absorption cross section (Equation 2.17) are the electronic transition dipole moments for the B-X transition ($|R_e|_B^2$) and the B"-X transition ($|R_e|_{B"}^2$). I begin with $|R_e|_B^2$. To determine this quantity, I consider a hypothetical "pure" B rovibrational state with no perturbations from the B" state. I assume that the this upper state, U, has vibrational quantum number v_u, total angular momentum quantum number J_u, etc. Per Green and Western [52, 46], the empirically determined excited state lifetime of the B state is 32 ns. Therefore the fluorescence rate constant, termed the "Einstein A coefficient" (A_u) is simply 1/32 ns^{-1}.

The Einstein A coefficient is related to the transition dipole moment, as shown in Equation 2.31

$$A_u = \frac{1}{32}\, ns^{-1} = \frac{16\pi^3}{3\varepsilon_0 hc^3(2J_u+1)} \sum_i \nu_{ui}{}^3 q(v_u, v_i) |R_e|^2 S_{J_u J_i}. \tag{2.31}$$

In Equation 2.31, the sum is over all possible rotation/vibration states within the X electronic state that the B state can fluoresce to.

To evaluate this sum, I break it in two (Equation 2.32)

$$\sum_g \nu_{ug}{}^3 q(v_u, v_g) |R_e|^2 S_{J_u,\Omega_u\, J_g \Omega_g} = \sum_{v_g} (\nu_{v_u v_g})^3 q(v_u, v_g) \sum_{e_g,\, J_g} |R_e|^2 S_{J_u J_g}. \tag{2.32}$$

The first summation is over ground state vibrational quantum numbers, v_g, and the second one is over the ground state rotational and electronic quantum numbers, e_g and J_g. I write $\nu_{ug}{}^3$ as $(\nu_{v_u v_g})^3$, approximating the transition frequency using the difference in vibrational origin energy between the upper state and the ground state. This is an especially good approximation at low J.

Equation 2.33 gives the sum over rotational and electronic states is given by, where the factor of 3 is due to the triplet character of the electronic states

$$\sum_{v_g} (\nu_{v_u v_g})^3 q(v_u, v_g) \sum_{e_g,\, J_g} |R_e|^2 S_{J_u,\Omega_u\, J_g \Omega_g} = 3(2J_u + 1)|R_e|^2. \quad (33)$$

Plugging Equation 2.33 into Equation 2.31 gives Equation 2.34, which can be solved for $|R_e|^2$.

$$\frac{1}{32}\, ns^{-1} = \frac{16\pi^3}{\varepsilon_0 hc^3} |R_e|^2{}_{B"} \sum_{v_g} (\nu_{v_u v_g})^3 q(v_u, v_g) \quad (34)$$

I use Green and Western's vibrational origin energies and calculate Franck Condon factors. I obtain $|R_e|^2{}_{\boldsymbol{B}} \approx 1.97\ Debye$. I perform a nearly identical procedure for the B" electronic states with the exception of the larger lifetime and correspondingly smaller Einstein A coefficient (i.e $A_u = \frac{1}{4200}\, ns^{-1}$). This gives $|R_e|^2{}_{\boldsymbol{B"}} \approx 0.24\ Debye$.

2.10: The Structure of the Intensity Calculation

My Matlab code loops over all possible case (a) basis states for the X electronic state. For each basis state, it determines the case (a) basis states for the B/B" electronic states that are allowed by the transition dipole moment selection rules. It then accesses the eigenstate associated with each X and B/B" state, and passes these eigenvectors to a separate function. This function then calculates $\sum_i \sum_j c_i\, c_j S_{J_i,\Omega_i\, J_j,\Omega_j}$ given the "cosine-alpha" matrix elements detailed in section 2.7. The electronic transition dipole moments, $|R_e|^2{}_B$, $|R_e|^2{}_{B"}$ are calculated. Finally, the absorption cross-section, σ, is determined, as shown in Equation 2.17.

This concludes my discussion of the energy levels and transition intensity for the B/B"-X system. In Chapter 3, I will turn my attention to collisional transfer within the B and B" states.

Chapter 3 : A Simple, Robust Model for Rotationally and Electronically Inelastic Collisional Transfer

Abstract: My kinetic model incorporates both electronically and rotationally inelastic collisions between excited S_2 and inert species in the atmosphere, primarily N_2. The electronically and rotationally inelastic collisions act together to transfer population back and forth between the B and B" states. Rotationally inelastic collisions are considered for diabatic vibronic states in the Hund's case (a) basis set. I model them with a simplified version of Brunner and Pritchard's energy gap law, which contains two adjustable parameters that are simple to estimate. This model is hybridized with Gelbart and Freed's model for electronically inelastic collisions. In the Gelbart-Freed model, collisional interactions are considered in the short-duration limit, where the collisions themselves do not perturb the system. Instead, the spectroscopic perturbations, described in Chapter 2 serve as "doorways" between the electronic states. This process is called "doorway-mediated transfer". The Gelbart-Freed model involves the B/B" mixing coefficients, so simple phase conventions must be chosen, such that the model produces physically plausible results.

3.1. Introduction

In chapter 2, I described, in detail, the fundamental spectroscopy of population transfer between the X and B/B" electronic states of S_2. In this chapter, I consider collisional population transfer **within** the excited, B/B" states, induced by collisions with chemically inert species in the atmosphere, primarily N_2. In general, collisions can readily transfer population between rotational states (via "rotationally inelastic collisions"). In some cases, they can also efficiently transfer population between electronic states (via "electronically inelastic collisions"). However, collisional transfer between vibrational states is generally several orders of magnitude less efficient than rotational/electronic transfer, and I will not consider such collisions in this thesis. In this strongly perturbed S_2 system, however, population can move between vibrational levels indirectly[6] via the B/B" spectroscopic perturbations described in Chapter 2.

Here, I describe a novel collisional transfer model that completely describes rotationally inelastic transfer using the Power Gap (PG) model [63] and simultaneously describes the perturbation-based model for electronic transfer, originally proposed by Gelbart and Freed (G-F) [64]. This hybrid PG + G-F model

[6] Population can theoretically move between two B state vibrational levels if there is a B" state vibrational level that perturbs both of them.

is especially notable for its simplicity and broad applicability, as it requires only a few pieces of information:

(1) The B/B" mixed state probability amplitudes for the initial and final states involved in the collisional transfer. This information is easily attainable using the Hamiltonian diagonalization procedure detailed in Chapter 2.

(2) Estimates of two adjustable parameters in the PG model. One parameter is a function of the intermolecular potential energy between the excited state B/B" S_2 and its N_2 collision partner. The other is primarily a function the S_2*/N_2 collision frequency, which is itself a function of the temperature and pressure of the atmosphere. Both parameters are simple to estimate.

Another important feature of this model: it ignores purely electronically inelastic collisions (i.e. collisions that change electronic state quantum numbers but not rotational ones). Instead, **rotationally inelastic collisions facilitate electronically inelastic collisions.** This gives my model tremendous utility, as it is agnostic to the different properties of the two Born-Oppenheimer electronic states involved, and only depends on the extent of *mixing* between them. Therefore, I can indiscriminately apply this model to all 16210 rovibrational states included in my asymmetric B/B" Hamiltonian, as diagonalized in Chapter 2. This greatly simplifies any calculation.

I now discuss the Power Gap (PG) model for rotationally inelastic transfer and the Gelbart-Freed (G-F) model for electronically inelastic transfer in turn, before describing their hybridization.

3.2. The Power Gap Law for Rotationally Inelastic Transfer

Consider a pure, unperturbed vibronic state. This state has a manifold of rotational states ($i's$), with angular momentum quantum numbers, J_i, and energies, $E(J_i)$. I begin with Brunner and Pritchards's statistical power gap (SPG) law [65, 66], which is a more complex version of the power gap (PG) law that I will introduce later. Equation 1 gives the first-order rate constant ($k_{1\to2}$) for transfer *within* this rotational state manifold from rotational state 1 to rotational state 2

$$k_{1\to 2} = a|\frac{\Delta E}{B}|^{-\alpha} N_\lambda(J_1, J_2) R(\Delta E). \tag{3.1}$$

In equation 3.1, a is a proportionality constant with the same dimensions as the rate constant (first order, in our case). The parameter $|\Delta E|$ is the absolute difference in energy between the final state and the initial state, i.e. $|\Delta E| = |E_2 - E_1|$. B is the rotational constant for this particular vibronic state. The parameter α is a positive number, generally 1.2 ± 0.2. $N_\lambda(J_1, J_2)$ is a statistical factor that accounts for ΔM selection rules in the collisional transfer process. Here, M is the projection of the total angular momentum along the laboratory frame fixed axis, and λ is an integer, fit to empirical data, such that all allowed collisions have $\Delta M \leq \lambda$. Typically, λ is quite large. In the limit where all ΔM collisions are allowed with equal probability, $N_\lambda(J_1, J_2) = 2J_1 + 1$. In the opposite limit, where only $\Delta M = 0$ collisions are allowed, we have equation 3.2 [66]

$$N_\lambda(J_a, J_b) = \frac{(2J_- + 1)}{(2J_a + 1)}. \tag{3.2}$$

Here, J_- is the smaller of J_a and J_b. Finally, $R(\Delta E)$ accounts for the difference in translational density of states before and after the collision. For transitions where $\Delta E < k_B T$, $R(\Delta E)$ is approximately unity. If I assume $\Delta E < k_B T$, and ignore the statistical factor (which will be reincorporated in Chapter 4). I can write a simplified rotational transfer rate constant given by Equation 3.3

$$k_{a\to b} = a|\frac{\Delta E}{B}|^{-\alpha}. \tag{3.3}$$

I will refer to this simplified expression in Equation 3 as the power gap (PG) law. The PG law is, primarily, an experimental fitting law. However, using classical mechanics, Brunner and Pritchard derived an expression, very similar to Equation 3, which shows that $k_{a\to b}$ ought to follow an energy gap power law (i.e. $|\Delta E|^{-\alpha}$) [63, 67]. For the purposes of this discussion, there are two important assumptions in Brunner and Pritchard's classical derivation. The first is the sudden approximation, i.e. τ, the time of the interaction is small enough to ignore. Or, in other words, the derivation is performed in the limit

where $\tau \to 0$. If we assume that this is the case, then the molecule does not rotate during the collision. Consequently, Brunner and Pritchard derive an expression for $k_{0\to l}$, where l is the classical angular momentum. The second assumption: the long-range intermolecular potential energy $V(r)$ is proportional to r^{-n}, where n is a positive number and r is the intermolecular distance between S_2* and N_2.

Equation 3.4 shows a simplified equation based on Brunner and Pritchard's classical derivation

$$k_{0\to l} = a_n(T)[l(l+1)]^{-\frac{n}{n-1}}. \tag{3.4}$$

Here, the proportionality constant, $a_n(T)$, is a function of the thermally averaged relative velocity of the two molecules, which is itself a function of the temperature, T. The constant is also parameterized by the power, n, in the power law dependence of the intermolecular potential energy surface. Note also that if the initial state is $l = 0$ and the rotational energy scales as $Bl(l+1)$, then $l(l+1) = \frac{\Delta E}{B}$, identical to the expression in Equation 3. This expression also allows us to determine a reasonable estimate for α. If n = 6, for example, (van der Waals interaction) then $\alpha = \frac{6}{6-1} = 1.2$. The PG model has been utilized as a model for rotationally inelastic transfer in a variety of molecules, such as Li_2* [68], LiH [69], and Na_2* [70], with a variety of collision partners including He [71] and Ne [72]. In these models, the empirically fitted values for α generally range from ~1-1.4 [65]. In this model, therefore, I choose $\alpha = 1.2$.

The PG model has a few limitations. First, as mentioned, the model is most appropriate in the limiting case where the N_2/S_2* collision is short in duration relative to the rotational period of the molecule. For longer-duration interactions, the ability of the N_2 to perturb the B/B" system and alter its energy level structure must be taken into account. An energy corrected sudden scaling (ECS) model was developed to account for this effect, which has been extremely successful in describing a large range of collisional transfer phenomena. However, this model requires one additional parameter[7] that is difficult to

[7] This parameter is l_c, the length (in units of distance) of the interaction between the N_2 and S_2 molecule. The duration of the collision, τ_d, is equal to l_c/v, where v is the relative velocity of the two molecules.

estimate *a priori* and therefore must be fit to experimental data. A second shortcoming is that the SPG model tends to overestimate $k_{a\to b}$ for transitions with large ΔJ [73], because the real intermolecular potential, V(r), becomes repulsive at small values of r.[8,] [74] Pritchard, et. al. corrected this deficiency of the PG model by introducing a parameter, J^*, that represents the maximum allowed change in ΔJ for a single transition. They scale the rate constant $k_{J\to 0}$[9] by the factor listed in Equation 3.5

$$k_{J\to 0}\ \alpha\ e^{-\frac{J(J+1)}{J*(J*+1)}}. \tag{3.5}$$

The value of this J* factor, however, is also generally fitted to empirical data.

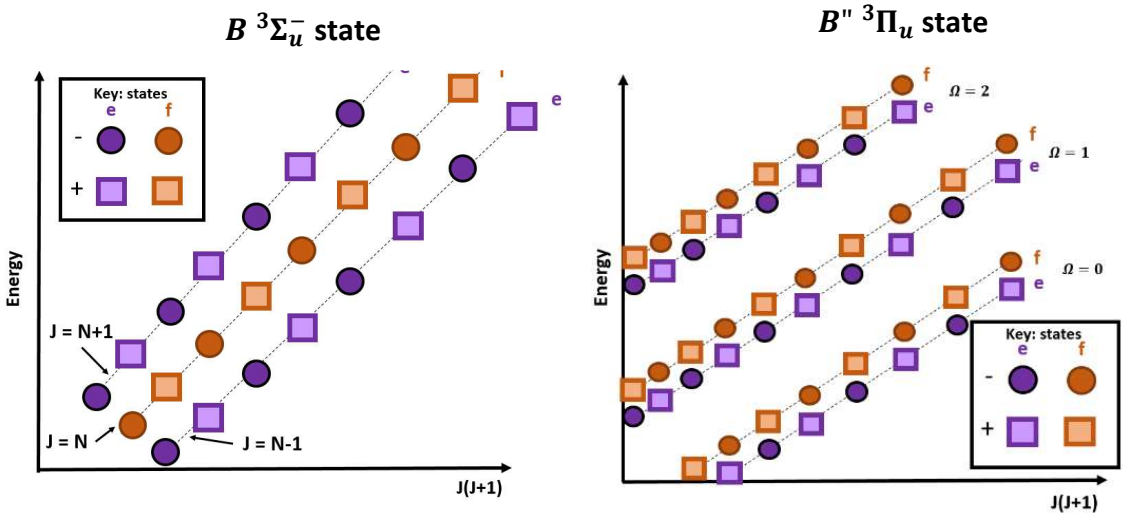

Figure 3-1: The general energy level structures for asymmetric, e.g. ^{32}S-^{33}S, B-state vibronic states (**1a** – left), and B"-state vibronic states (**1b**-right). Each state has e/f (orange/purple) symmetry manifolds. Within each manifold, the total +/- parity alternates (hollow/filled). Note that the structure of the B state is fundamentally different than of the B" state. For the B state, the two e-symmetry, spin-orbit states are strongly mixed by the S-uncoupling portion of the rotational Hamiltonian, whereas the B" state consists of 3 separate, relatively pure spin-orbit (Ω) states. In the B state, the three different manifolds correspond to different couplings between $\vec{N}$ and $\vec{S}$ ($J = N + 1, J = N,$ and $J = N - 1$).

[8] For detailed information as to why a repulsive potential leads to a limitation in single-collision ΔJ, see discussion in S.L. Dexheimer, et. al. [74]

[9] This rate constant is related to the usual $k_{1\to 2}$ by the ECS scaling law. This also requires fitting l_c, giving the model four fit parameters in total.

Because these corrections and improvements of the PG fitting law require additional fit parameters that are sensitive to the particular characteristics each system, and are difficult to estimate without empirical collisional transfer data, I have chosen not to use them in this work. This allows me to preserve the generality of my calculation, while still using a scheme for rotationally inelastic collision that has been quite successful in modeling a diverse array of experimental results.

3.3. Symmetry Restrictions for Rotational Transfer: Homonuclear Propensity

Figure 3-1(left) shows the energy level structure for the B $^3\Sigma_u^-$ state, while Figure 3-1(right) shows the energy level structure of the B" $^3\Pi_u$ state. While each manifold of states has a J-independent e/f symmetry, the *total* parity (+ or −), within an e or f symmetry manifold, alternates with rotational quantum number. (In Figure 3-1, + parity states are squares and – parity states are circles). In the most general sense, collisions do not preserve either e/f symmetry or +/- parity, as the presence of the collision partner destroys the symmetry of the molecule.

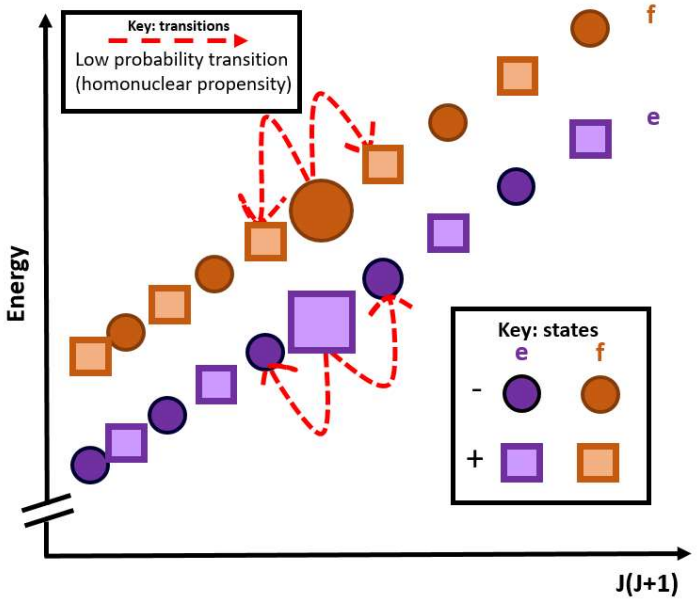

Figure 3-2: shows, for a B" spin-orbit state, the +/- parity switching $\Delta J = 1, e \leftrightarrow e$ or $f \leftrightarrow f$ transitions (dashed red arrows), that **would be** high probabilty, if not for the homonuclear propensity rule. These collisions violate the homonuclear propensity rule are actually of low probability.

In symmetric isotopologues (e.g. ^{32}S-^{32}S), collisions must preserve +/- parity, as the (+) parity states do not exist (see: Chapter 2). However, asymmetric isotpologues of homonuclear diatomic

molecules, such as ^{33}S-^{32}S or ^{36}S-^{32}S, there is nearly always a strong propensity for collisions to preserve total (+/-) parity, even though the opposite parity states *do* exist. If collisions do not induce transfer from the (+) parity manifold to the (-) parity manifold, then the collisional selection rules are identical to those in the symmetric molecule, with half of total the population in each of the two collisionally unconnected manifolds. Therefore, the tendency for collisions to preserve +/- parity is termed the "homonuclear propensity rule".

To illustrate the importance of the homonuclear propensity rule, consider a hypothetical scenario where +/- changing collisions are completely allowed. In such a scenario, based on the PG law, we could naively predict a much larger overall rotational transfer rate for heteronuclear S_2, due to the addition of strong-propensity, $\Delta J = 1, e \leftrightarrow e \; or \; f \leftrightarrow f$ collision-induced transitions that do not exist in homonuclear S_2. These transitions are shown for a B" state as dashed arrows in Figure 3-2. These forbidden $\Delta J = 1$ transitions would be strong because they have the smallest energy gap between initial state and final state (Recall that the PG rate constant is approximately proportional to $|\Delta E|^{-1.2}$).

However, in practice, larger net rotational transfer is not observed when comparing asymmetric to symmetric diatomic molecules. For example, Yang et. al. [75] measured line-broadening parameters for O_2 colliding with N_2, where the extent of the broadening reflected the magnitude of the rotationally inelastic collision rate. The measured broadening parameters for the heteronuclear ^{16}O-^{18}O isotopologue were identical (within experimental error) to those for the homonuclear ^{18}O-^{18}O and ^{16}O-^{16}O isotopologues. The Yang, et. al. result is consistent with the homonuclear propensity rule.

Results from Ottinger, Velasco, and Zare [76], document the remarkable strength of this propensity rule. In spectroscopic experiments performed on collisions of Ar with the $B\ ^1\Pi_u$ state of ^{6}Li-^{7}Li, the rate constants for $\Delta J = even$ collisions that preserve both +/- parity and e/f symmetry were determined to be much larger than those for $\Delta J = odd$ transitions that did not preserve +/- but did preserve e/f symmetry. Figure 3 depicts these transitions on an energy level diagram of a $^1\Pi_u$ state. This

discrepancy is especially pronounced at low values of ΔJ. For example, the e/f preserving, $\Delta J = 1$ rate constants are approximately an order of magnitude smaller than the $\Delta J = 2$ rate constants, despite the fact

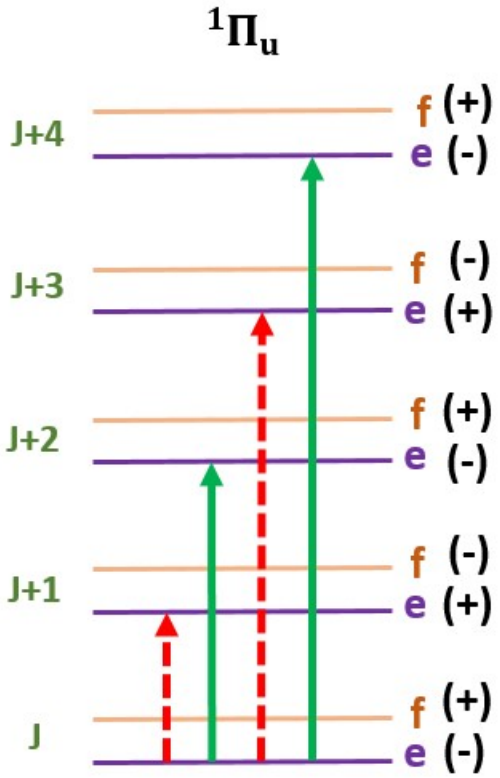

Figure 3-3: Energy level diagram for the $^1\Pi_u$ state considered by Ottinger, Velasco, and Zare. The arrows show e/f symmetry preserving collisional transfer. The $\Delta J = \text{odd}$ transitions are low propensity (red, dashed arrow) due to the +/- changing nature of the collision. Conversely, the $\Delta J = \text{even}$ transitions are high propensity (green, solid arrow) because +/- parity is conserved. This reflects the homonuclear propensity rule.

that the PG law would predict a substantially larger rate constant for $\Delta J = 1$, versus 2. Furthermore, when the average of the neighboring $\Delta J = odd$ rates are added to each $\Delta J = even$ rate, the resulting $\Delta J = even$ rates match the homonuclear ^{6}Li-^{6}Li collision rates (see: Figure 3-4) [65]. In other words, the total collision rate, summed over all values of ΔJ is the same for both heteronuclear and homonuclear S_2, consistent with the Yang, et. al. result [75].

McCurdy and Miller [77] have performed theoretical scattering calculations on asymmetric isotopologues of homonuclear molecules. Their calculations show that the near-symmetric selection rules are caused by a near-isotropic potential energy surface for the interaction between the molecule and its collision partner. We think of the intermolecular potential energy surface as entirely isotropic when the center of mass and the center of symmetry of the molecule are the same. In that case, an interference

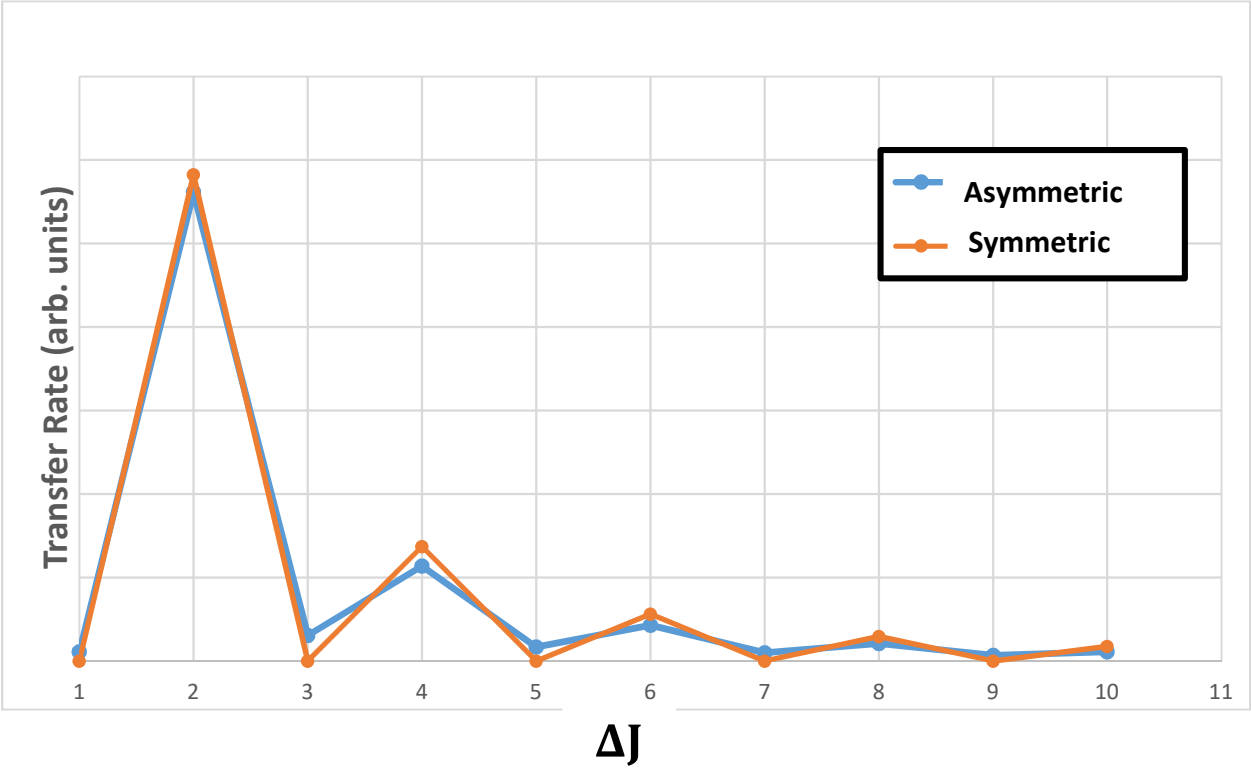

Figure 3-4: Hypothetical collisional transfer rate constants for e/f symmetry-conserving collisions. In this case, $\Delta J = \text{odd}$ collisions switch +/- total parity, while $\Delta J = \text{even}$ collisions conserve +/- parity. For the symmetric case (orange) only $\Delta J = \text{even}$ collisions are allowed, due to an interference effect in the scattering matrix (see text). For the asymmetric case (blue), the $\Delta J = \text{odd}$ transitions are allowed, but with low propensity. Note that the $\Delta J = \text{odd}$ transitions "borrow" their transition intensity from the $\Delta J = \text{even}$ transitions. That is, $\Delta J = \text{even}$ transitions are less probable in the heteronuclear case than in the homonuclear case, such that the total rotationally inelastic transition rate (summed over all $\Delta J's$) is equivalent in both cases.

effect in the scattering matrix completely destroys the cross section for the $+ \leftrightarrow -$ collisions. This is the case for symmetric molecules such as ^{32}S-^{32}S. For asymmetric homonuclear molecules, the difference in mass between the two isotopes moves the center of mass slightly away from the center of symmetry, meaning the interference effect destroys most, but not all, of the scattering matrix element.

My model, as a starting point, excludes +/- changing collisions. This is a limiting case, but one that closely reflects the empirical evidence presented in this section. To more explicitly express this starting point, I modify the expression in Equation 3.3 to give Equation 3.6.

$$k_{a\to b} = a|\frac{\Delta E}{B}|^{-\alpha}\delta_{p_a,p_b} \tag{3.6}$$

In Equation 3.6, p_a and p_b represent the total +/- parity of the initial and final states, and δ is the Kronecker delta symbol, which is 1 if $p_a = p_b$, and 0 otherwise. Section 8.3 addresses the possibility for +/- changing collisions in my model.

3.4. e/f Symmetry Changing Collisions

Unlike +/- parity, which nearly always has a strong propensity for conservation in collisions of asymmetric isotopologues of homonuclear molecules, rotationally inelastic collisions can *sometimes* change e/f symmetry. To determine the propensity rules for e/f changing collisions, we must consider the general forms of e and f symmetry Hund's case (a) basis states (Equations 3.7a and 3.7b, respectively).

$$|\, e >= {}^{1}/_{\sqrt{2}}(|\, J\ \Omega, v, \Lambda, S\ \Sigma > + |\, J\ (-\Omega), v, (-\Lambda), S\ (-\Sigma) >) \tag{3.7a}$$

$$|\, f >= {}^{1}/_{\sqrt{2}}(|\, J\ \Omega, v, \Lambda, S\ \Sigma > - |\, J\ (-\Omega), v, (-\Lambda), S\ (-\Sigma) >) \tag{3.7b}$$

Note here that the spin (S, Σ) and orbital (Λ) wave functions are different for e symmetry versus f symmetry states. Therefore, in general, collisions between e and f must also change the electronic properties of the wavefunction.

Gottscho [78] has considered e/f transfer in a variety of experiments performed on different $\Omega = 1$ systems. In alkali dimer experiments on ${}^1\Pi_u$ states, e/f changing $\Delta J = 1$ collisions have been readily observed. However, for a Hund's case (c) 1_u electronic state in Te_2, there is a strong propensity for *preserving* e/f symmetry. Gottscho reconciled these two observations by noting the differences in wavefunction between the ${}^1\Pi_u$ and 1_u states. For ${}^1\Pi_u$, we have Equation 3.8.

$$|^1\Pi_u\ e/f> = {}^1/_{\sqrt{2}}(|\Lambda=1>|\Sigma=0>|\Omega=1> \pm |\Lambda=-1>|\Sigma=0>|\Omega=-1> \qquad (3.8)$$

The Te_2 1_u electronic state correlates to part of a $^3\Sigma_u^-$ Hund's case (a) state. The wavefunction for 1_u is therefore given by Equation 3.9.

$$|1_u\ e/f> \approx {}^1/_{\sqrt{2}}(|\Lambda=0>|\Sigma=1>|\Omega=1> \pm |\Lambda=0>|\Sigma=-1>|\Omega=-1>) \qquad (3.9)$$

In a $^1\Pi_u$ electronic state, we see that e/f transfer does not involve a change in the electron spin wavefunction (because $\Sigma = 0$). In a 1_u state, however, e/f transfer **does** involve such a change. Gottscho's observations indicate a general principle: **In the short-duration (non-perturbing) limit, inelastic collisions can only move population between rotational states or between other, degenerate orbital (but not spin) electronic states.**

Putting these ideas into practice, we can now consider rotationally inelastic collisions in the B" $^3\Pi_u$ state. In the above two examples, we had either $\Lambda = 0$ (sigma state), or $\Sigma = 0$ (singlet state). Consequently, in Equations 8 and 9, the behavior of Λ was decoupled from that of Σ, and we expressed the wavefunctions in terms of separate spin and orbital electronic parts. In the $^3\Pi_u$ state, we can have both $|\Lambda| > 0$ and $|\Sigma| > 0$, so the spin and orbital wavefunctions are no longer separable, due to large energy difference between the spin-orbit Ω-components. As seen in Figure 3-1b, the states are energetically ordered by $\Omega = \Lambda + \Sigma$. An $\Omega = 0$ state, for example, has the following wavefunction: $|\Omega = 0\ (e/f) >= \frac{1}{\sqrt{2}} * |\Lambda = 1, \Sigma = -1> \pm |\Lambda = -1, \Sigma = 1>$, where the values of Λ and Σ are correlated. If collisions can only change Λ and not Σ, then changing $\Lambda = 1$ to -1 and vice versa leads to a change from $|\Omega = 0>$ to $|\Omega = 2>$. This violates Gottscho's general principle because the degeneracy of the different omega states has been removed by the diagonal matrix elements (AL_zS_z) of the spin-orbit Hamiltonian.

I apply the Gottscho principle to the B" state as follows: for rotationally inelastic collisions in the B" $^3\Pi_u$ state, e/f changing collisions are allowed in the $\Omega = 1$ spin-orbit component (because $\Sigma = 0$) and disallowed in the $\Omega = 0$ or $\Omega = 2$ spin-orbit components (because $|\Lambda| = |\Sigma| = 1$). These transfer rules

are summarized in Figure 3-5a, which shows the propensity rules for transfer in an $\Omega = 0/2$ spin-orbit component, and Figure 3-5b, which shows the same in a $\Omega = 1$ spin-orbit component. Because of its more perturbed nature in the case (a) basis, I will consider collisional transfer in the B state later on in this chapter.

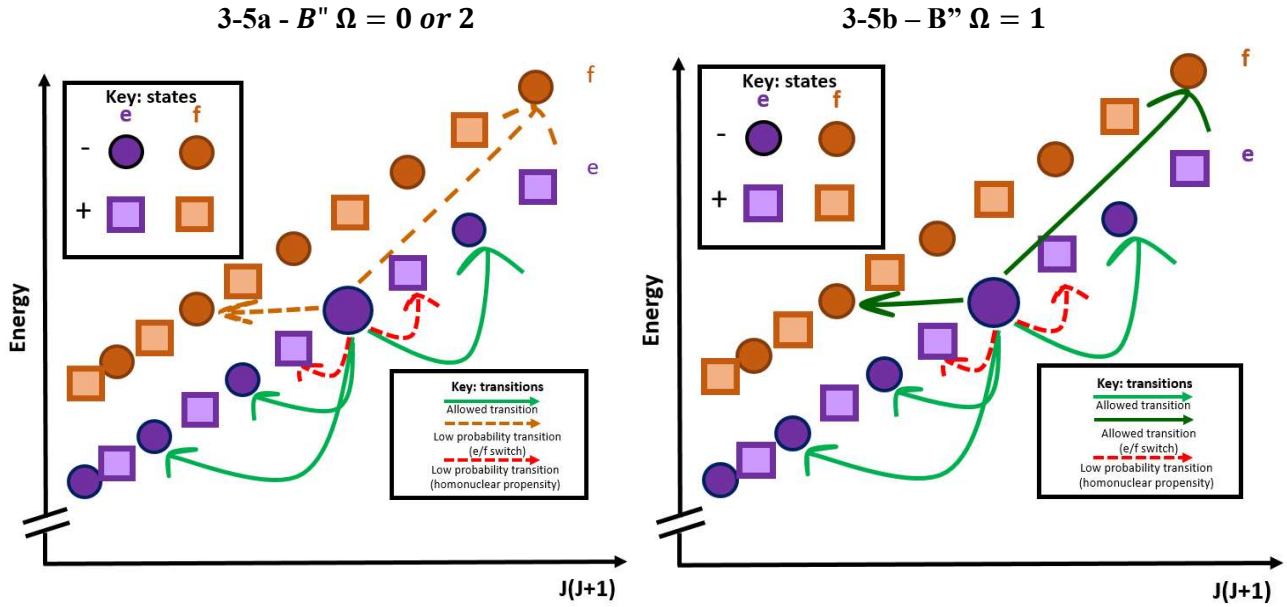

Figure 3-5: Gives examples of fully allowed (solid arrow) and low-propensity (dashed arrow) collisional transfer in an $\Omega = 0$ or 2 spin-orbit component (**5a – left**), and in a $\Omega = 1$ spin-orbit component (**5b – right**). The primary difference between the two is the allowed e/f parity switching collisions in the $\Omega = 1$ case.

Finally, in diatomic systems where e/f transfer is allowed, a strong propensity for J-increasing over J-decreasing collisions, or vice-versa, is sometimes observed [79]. This effect is due to differences in the orientation of the e and f symmetry orbital wavefunctions relative to the molecular plane of rotation. Specifically, Ottinger, Velasco, and Zare [76] have argued that collisions that change the orientation of the orbital wavefunction (and thus change e/f symmetry) have a particular trajectory relative to the rotational motion of the molecule. And this preference for a specific trajectory leads to a favoring of either $\Delta J > 0$ or $\Delta J < 0$ (Figure 3-6). Bergmann, Klar, and Schlecht [80] have performed theoretical calculations that confirm this effect. Their calculations show that the magnitude of this effect is highly sensitive to the shape of the intermolecular potential energy surface. As I have constructed my model to

be independent of any property that is specific to a particular electronic state, I do not include this effect in my collisional transfer model.

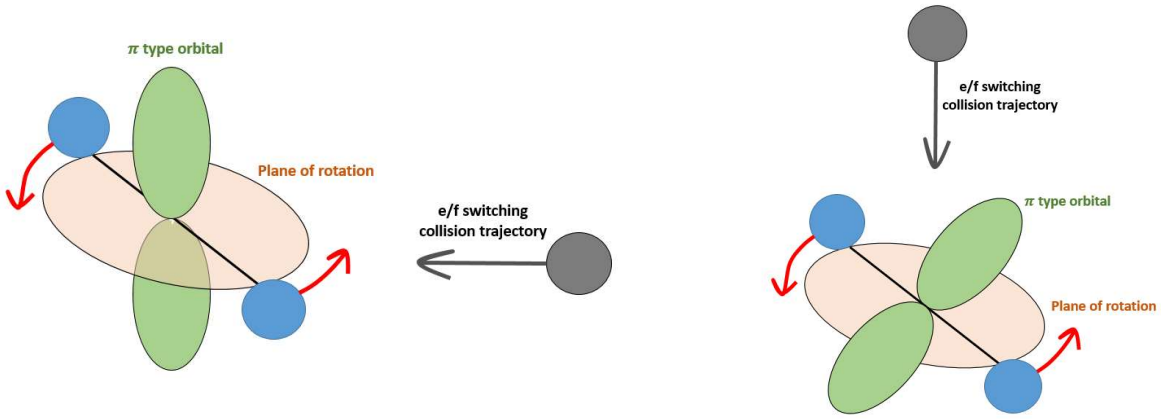

Figure 3-6: There are two, degenerate pi-type orbitals that have $|\Lambda| = 1$, one associated with e symmetry, the other with f. One of these pi orbitals exist in the plane of rotation, the other is perpendicular to it. The collisional trajectory required to torque the out-of-plane orbital (to convert it to the in-plane one) is in the plane of rotation and tends to decrease the rotational angular momentum. The collisional trajectory required to torque the in-plane orbital is out of the plane of the rotation and tends to increase the rotational angular momentum.

3.5. The Gelbart-Freed Model for Electronically Inelastic Collisions

The Gelbart-Freed (G-F) model for electronically inelastic collisions is unique in that it relies on the spectroscopic perturbations, described in Chapter 2, as the exclusive mechanism for collisional transfer between electronic states. In this section, I review the fundamentals of the G-F model, describe its similarity to the PG model for rotationally inelastic transfer, and discuss a few of its shortcomings.

To begin, consider Equation 3.10, which expresses the rate constant $k_{e_1 \to e_2}$ for transfer from electronic state e_1 to electronic state e_2 in terms of the total N_2/S_2* collision frequency, Z, and the probability, P, that a given collision transfers from e_1 to e_2

$$k_{e_1 \to e_2} = Z * P_{e_1 \to e_2}. \tag{3.10}$$

I now consider the eigenstates e_1 and e_2 to be linear combinations of two, pure (diabatic) electronic basis states, |C> and |D>. These eigenstates are given by Equations 3.11a-b, where the c and d coefficients can range from $|c|^2 = 0$ and $|d|^2 = 1$ (not perturbed) to $|c|^2 = |d|^2 = ½$ (50-50 mixture)

$$|e_1 >= c_1|C > + d_1|D > \quad (3.11a)$$

$$|e_2 >= c_2|C > + d_2|D >. \quad (3.11b)$$

I now introduce a scattering matrix, V, such that the matrix element $| < 1|V|2 > |^2$ is the probability that a collision induces a transition from state 1 to state 2. Plugging the eigenstates into Equation 3.10, I obtain equations 3.12a and 3.12b

$$k_{e_1 \to e_2} = Z * | < e_2|V|e_1 > |^2 \quad (3.12a)$$

$$k_{e_1 \to e_2} = Z * |c_1 c_2 < C|V|C > + d_1 d_2 < D|V|D > + c_1 d_2 < D|V|C > + c_2 d_1 < D|V|C > \ |^2. \quad (3.12b)$$

Here, I employ the fundamental assumption in the Gelbart-Freed model: V is diagonal in the |C>, |D> basis. **In other words, the probability that a collision directly transfers population from a pure C state to a pure D state is small compared to the probability of an electronically elastic collision**. If this is the case, we can ignore the cross terms, yielding Equation 3.13

$$k_{e_1 \to e_2} = Z * | c_1 c_2 < C|V|C > + d_1 d_2 < D|V|D > \ |^2. \quad (3.13)$$

Note that this assumption is very similar to one of the key assumptions in the PG model. Specifically, the PG model assumes that the collision is short in duration, and consequently does not affect the energy level structure of the S_2* molecule. Short, non-perturbing collisions are also unlikely to transfer population directly from one pure electronic state to another.

I now introduce P_C and P_D, the probabilities of **elastic** collisions in the C state and D state, respectively. In the absence of any other collisional transfer processes, it is reasonable to take $P_C = P_D = 1$. For $P_C = P_D = P$, I factor Equation 13, to give Equation 3.14

$$k_{e_1 \to e_2} = Z * |c_1 c_2 + d_1 d_2|^2 * P. \quad (3.14)$$

The factor $|c_1 c_2 + d_1 d_2|^2$ is equal to $|< 2|1 >|^2$, which is zero because C and D are orthogonal electronic eigenstates. Therefore, the G-F rate constant is always zero in cases where the elastic collision rates in state C and state D are equal.

For the pure C state and pure D state to have different elastic collision rates, they must have different inelastic collision rates (elastic rate + inelastic rate = total rate). Because the GF model excludes direct electronic transfer, this leaves either vibrationally or rotationally inelastic collisions as possibilities. To illustrate this principle, consider C and D as vibronic states rather than as just electronic states. Similar to Gelbart and Freed's analysis of singlet/triplet quenching in CH_2 (methylene), we will also assume that the vibronic state C is in its ground vibrational state ($v = 0$), and that vibronic state D is in in an excited vibrational state ($v \neq 0$). Furthermore, assume that the probability of a single collision causing vibrational relaxation in state D is Γ_D. In this context, Equation 3.9 becomes Equation 3.15

$$k_{e_1 \to e_2} = z * | c_1 c_2 \sqrt{P_C} + d_1 d_2 \sqrt{P_D - \Gamma_D} \,|^2. \quad (3.15)$$

For significant amounts of vibrational relaxation $|< 2|1 >|^2$ no longer factors out of the expression and $k_{e_1 \to e_2} \neq 0$. Figure 3-7 explains the intuitive basis for this model of electronic state transfer. Population in pure state C cannot move, and, therefore, all of its collisions are vibronically elastic, but state D is a "leaky bucket", with a significant amount of inelastic collisions. Therefore, population flows from state C

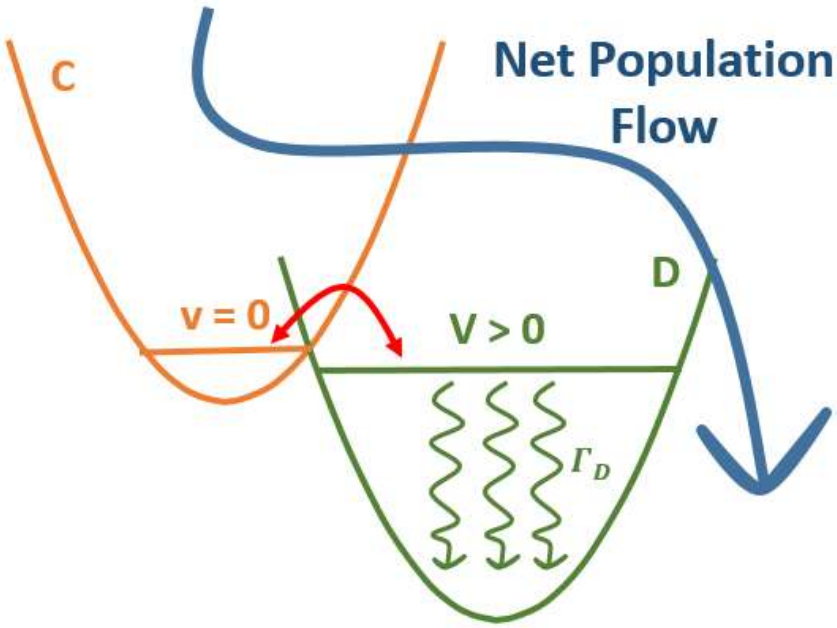

Figure 3-7: An example of vibronic state transfer in the Gelbart-Freed model. Here, the ground vibrational level of the C electronic state is perturbed by an excited vibrational state of the D electronic state. Population can exchange between the C and D states because of the difference in elastic collision rates between the two vibronic basis states. Specifically, the elastic collision rate for the D (v>0) vibronic state is reduced due to vibrational relaxation in the pure D state. This mechanism, wherein the perturbation acts as a "doorway" or "gateway" from the C state to the D state, is characteristic of Gelbart-Freed transfer and will be revisited at the end of this chapter.

to state D and out of the leak. In this sense, vibrationally inelastic transfer drives electronically inelastic transfer.[10] This "leaky bucket" concept will be critical to our analysis in Chapter 5.

[10] This is an oversimplification, but it is useful for intuition, as the real origin of the effect is quantum mechanical. For more insight, let us denote $P(1 \rightarrow 2)$ as the probability that a collision transfers from 1 to 2. Both of these eigenstates, 1 and 2, have partial C character and partial D character. Therefore I can define additional conditional probabilities, such as $P(C|1)$, the probability that a molecule would occupy state C, given the fact that it is in state 1. The term $P(2|C)$ is the probability that a molecule would occupy state 2, given the fact it occupies state C.. In this sense, the probability for a transfer from state 1 to state 2 could be written as $P(1 \rightarrow 2) = P(C|1) * P(2|C) + P(D|1) * P(2|D)$. as $P(1 \rightarrow 2) = P(C|1) * P(2|C) + P(D|1) * P(2|D)$. Plugging in the mixing coefficients we would obtain: $P(1 \rightarrow 2) = |c_1 c_2|^2 + |d_1 d_2|^2$This expression is almost correct, except we use probability amplitudes ($P^{A\prime}s$), instead of probabilities, i.e. $P(1 \rightarrow 2) = |P^A(C|1) * P^A(2|C) + P^A(D|1) * P^A(2|D)|^2$. Without rotational/vibrational relaxation, this expression reduces exactly to Equation 3.13 and is zero if 1 and 2 are eigenstates. However, if there is internal relaxation in state D then $P^A(D|1) = d_1\sqrt{1-\Gamma}$. Therefore, it is the discrepancy in the probability of occupying state C versus the probability of occupying to state D that induces the transfer. The use of probability amplitudes instead of probabilities will be addressed further in sections 3.8-3.10.

3.6. Shortcomings of the Gelbart-Freed Model

For the Gelbart-Freed model, transfer between two diabatic electronic states only occurs when the states perturb each other. As such, the collisional transfer follows the same set of selection rules that the spectroscopic perturbations do. For example, Gelbart-Freed collisional transfer preserves symmetry under inversion, i.e. only g ↔g and u ↔u electronic state transitions are allowed. Furthermore, in the B/B" system, the perturbation patterns dictate the collisional transfer propensity. Most prominently, $\Delta\Omega = 0$ transfer is relatively strong and $\Delta\Omega = 1$ transfer is relatively weak at low J.[11]

These perturbation-based selection and propensity rules, however, are not the entire story. Most notably, Alexander has modified the Gelbart- Freed model to include the effect of multipolar interactions, first applying this model to electronic state transfer in CaO. Specifically, he analyzed inelastic transfer rates from the long-lifetime $a^3\Pi$ state to the short-lifetime fluorescent $A^1\Sigma^+$ state, induced by collisions with N_2O. As in the B/B" system, the eigenstates of CaO are linear combinations of the a and A states, primarily due to spin-orbit interactions. Here, though, the permanent electric dipole moment of the ground state N_2O can induce a transition between two CaO eigenstates, which we label as 1 and 2. That is, the transfer rate constant is proportional to $|<2|\boldsymbol{\mu}|1>|^2$, where $\boldsymbol{\mu}$ is the electric dipole moment operator we first saw in Chapter 2, i.e. Equation 3.16

$$k_{1\to 2}\alpha|<1|\boldsymbol{\mu}|2>|^2. \tag{3.16}$$

As with our discussion of the Gelbart-Freed model, we begin with two electronic states that are linear combinations of the two diabatic electronic basis states (Equations 3.17a-b)

$$\left|1,J"\right> = A_{1,J"}\left|A,{}^1\Sigma^+,J"\right> + a_{1,J"}|a,{}^3\Pi,J"> \tag{3.17a}$$

$$\left|2,J'\right> = A_{2,J'}\left|A,{}^1\Sigma^+,J'\right> + a_{2,J'}|a,{}^3\Pi,J'>. \tag{3.17b}$$

[11] This is due to the strength of the spin-orbit interaction. At higher values of J, the L-uncoupling interaction, which has selection rules $\Delta\Omega = \pm 1$, becomes more significant, as it is proportional to $[J(J+1)]^{1/2}$.

Note here that the electronic states need not have the same total angular momentum quantum number (J" vs J').

Equation 3.18 shows that $k_{1\to2}$ is a function of the pure A electronic state permanent dipole moment ($\mu_A =< A|\boldsymbol{\mu}|A >$) , the pure a electronic state permanent dipole moment $\mu_a =< a|\boldsymbol{\mu}|a >$, and the transition dipole moment ($\mu_{Aa} =< A|\boldsymbol{\mu}|a >$)

$$k_{1\to2}\ \alpha\ a_{2,J"}A_{1,J"}\mu_A - a_{1,J"}A_{2,J'}\mu_a + \left[a_{2,J'}a_{1,J"} - A_{1,"}A_{2,J'}\right]\mu_{Aa}. \tag{3.18}$$

There are several differences between the Gelbart-Freed perturbation model and the Alexander perturbation/dipole transfer model. These include interference effects, due to the relative signs of the μ_A and the μ_a terms, and a stronger dependence on the J quantum number. Most prominently, every μ term in Equation 18, connects states of opposite parity, in contrast to the +/- parity preservation inherent to the G-F model. The Alexander extension of the G-G model has been applied to a variety of other systems where two electronic states perturb each other, including with MgO with N_2O [81], CN with Ar [82], and N_2O with He, Ar, and N_2 [83].

However, transitions have also been observed in systems where the *two electronic states do not perturb each* other. For example, auroral N_2 emissions in the Earth's atmosphere are best explained when incorporating collisional transfer between the B ($^3\Pi_g$) state and the B' ($^3\Sigma_u^-$), the W state ($^3\Delta_u$), and the A ($^3\Sigma_u^+$) state, induced by collisions with other N_2 molecules [84]. In these cases, the pure Gelbart-Freed model predicts a rate constant of zero ($g \leftrightarrow u$), but a multipolar interaction can induce collisions between electronic states of different symmetry. In the case of auroral N_2, collisions between one excited N_2 molecule and another excited N_2 molecule (which are governed by an electric dipole transition moment) can induce this transfer. The ability of collisions to transfer population between electronic states of opposite symmetry (g/u or +/-) will be relevant to our discussion in the final chapter, though I do not consider these effects directly in this work.

3.7. The Synthesis of The SPG Model and the Gelbart-Freed Model

To begin to combine the PG and Gelbart-Freed models, I note that, as in Equation 3.12a, the rate constant for any collisional transfer process from eigenstate 1 to eigenstate 2 can be expressed in terms of the total collision rate, Z, and the probability that a single collision transfers from 1 to 2 (Equation 3.19)

$$k_{1,J_1\rightarrow 2,J_2} = Z * |<2,J_2|V|1,J_1>|^2. \tag{3.19}$$

As in the previous analysis, the fundamental assumption of the Gelbart-Freed model is that the collisions are short in duration and do not appreciably perturb the electronic states. Consequently, V is diagonal in electronic state. As a simple illustration of this point, consider eigenstate 1 and eigenstate 2 to be linear combinations of two diabatic electronic states, |C> and |D>, as in Equations 3.11a-b. The expression for V is given by Equation 3.20a, with Equation 3.20b reminding us that the matrix is expressed in the |C>, |D> basis

$$V = \begin{bmatrix} P_C^{\frac{1}{2}} & 0 \\ 0 & P_D^{\frac{1}{2}} \end{bmatrix} \tag{3.20a}$$

$$basis\ vector = \begin{bmatrix} C \\ D \end{bmatrix}. \tag{3.20b}$$

Again, P_C and P_D are the elastic collision probabilities in the pure C and D basis states respectively. While short-duration collisions do not induce electronic transfer, **they can induce rotational transfer**, as we discussed in the section on the PG model (Recall that the power gap law dependence was derived in the limit where the duration of the collision, τ, is zero). Therefore, we must consider an expanded basis set, incorporating the rotational sub-states of the C and D vibronic states. In this context, V is given in Equation 3.21a, for a basis set given by Equation 3.21b

$$V = \begin{bmatrix} 0 & P^{1/2} & P^{1/2} & \cdots & 0 & 0 & 0 \\ P^{1/2} & 0 & P^{1/2} & \cdots & 0 & 0 & 0 \\ P^{1/2} & P^{1/2} & 0 & \cdots & 0 & 0 & 0 \\ \vdots & \vdots & \vdots & \ddots & \vdots & \vdots & \vdots \\ 0 & 0 & 0 & \cdots & 0 & P^{1/2} & P^{1/2} \\ 0 & 0 & 0 & \cdots & P^{1/2} & 0 & P^{1/2} \\ 0 & 0 & 0 & \cdots & P^{1/2} & P^{1/2} & 0 \end{bmatrix} \quad (3.21a)$$

$$basis\ set = \begin{bmatrix} C\,J_x \\ C\,J_y \\ C\,J_z \\ \vdots \\ D\,J_x \\ D\,J_y \\ D\,J_z \end{bmatrix}. \quad (3.21b)$$

The $P^{1/2}$'s represent the probability amplitudes for collisional transfer from one rotational state to another, ***within*** either the C state or the D state. Note here that:

1. The matrix $\boldsymbol{V}$ is still block diagonal in C and D, consistent with the fundamental assumption of the Gelbart-Freed model.
2. The complete expression for the $P^{1/2}$'s, should include a phase factor, because the probability is defined as $|<2,J_2|V|1,J_1>|^2$. However, I ignore the phase factors in this calculation. For a full explanation as to why the phase factors are ignored, see Appendix 1.
3. For the B/B" system, the matrix is also, generally, diagonal in +/- parity and e/f symmetry, with the exception for e/f symmetry in the B" $\Omega = 1$ state as noted in Figure 5.
4. The diagonal matrix elements are zero, i.e. I assume that all collisions are rotationally inelastic. I will explore the rationale for, and consequences of, this assumption later on in this chapter, as well as in Chapter 4.

I now must determine the probability amplitudes for the rotational transfer process. I begin by restating the PG model (Equation 3.22)

$$k_{J_1 \to J_2} = a|\frac{\Delta E}{B}|^{-\alpha}. \quad (3.22)$$

In Equation 3.22, J_1 is the rotational quantum number for the initial state, and J_2 likewise for the final state, with $J_1 \neq J_2$. Now, similar to Equation 3.19, I assume that $k_{J_1 \to J_2}$ is proportional to Z, the total collision rate. Therefore, I can write Equation 3.23

$$k_{J_1 \to J_2} = Z * a' | \frac{\Delta E}{B} |^{-\alpha}. \tag{3.23}$$

If Z is the total collision rate, then the remainder of the expression must be the probability that a given collision induces a transfer from J_1 to J_2, i.e. Equation 3.24:

$$P_{J_1 \to J_2} = a' | \frac{\Delta E}{B} |^{-\alpha}. \tag{3.24}$$

Where $a' = \frac{a}{z}$. This leads directly to Equation 3.25

$$P_{J_1 \to J_2}{}^{1/2} = a'' | \frac{\Delta E}{B} |^{-\alpha'}. \tag{3.25}$$

Where $a'' = \sqrt{a'}$ (again, I ignore phase), and $\alpha' = \alpha/2$. I now consider two eigenstates (1 and 2) that are linear combinations of an arbitrary number of vibronic basis states (Rather than just linear combinations of C and D). These basis states are given by Equation 3.26a-b

$$|1> = \sum_i c_{i,J1} |X_i, J_1> \tag{3.26a}$$

$$|2> = \sum_i c_{i,J2} |X_i, J_2>. \tag{3.26b}$$

Where the X_i 's are diabatic vibronic basis states, and the c_i's are their associated coefficients. As notated in Equation's 26, the c_i's refer to different rotational states in eigenstate 1 and 2. Finally, I can combine the expressions in Equation 3.26a and 3.26b with the expression in Equation 3.25 to give Equation 3.27

$$k_{1 \to 2} = z * | \sum_i c_{i,J1} c_{i,J2} a'' | \frac{E_i(J_2) - E_i(J_1)}{B_{X_i}} |^{-\alpha'} |^2. \tag{3.27}$$

Where $E_i(J_1)$ and $E_i(J_2)$ are the rotational state energies within vibronic basis state, X_i. The term B_{X_i} is the rotational constant for the vibronic state, X_i.

3.8. Collisional Transfer in the B state, an Illustrative Example

To illustrate how Equation 3.27 works in practice, I now consider rotationally/electronically inelastic collisions in the B electronic state (term symbol: $^3\Sigma_u^-$).

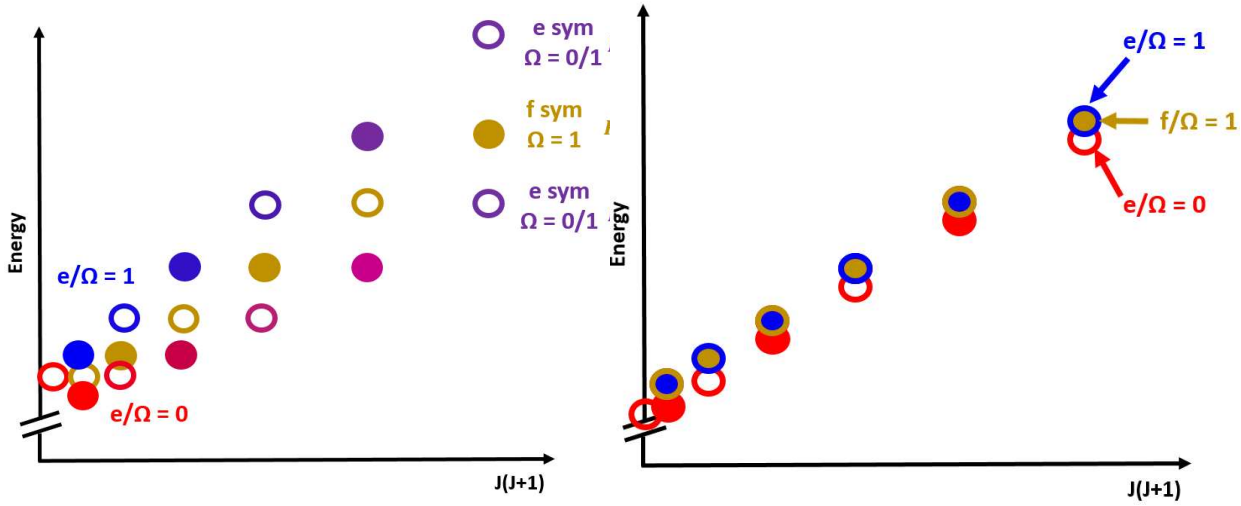

Figure 3-8: a (left): shows the rotational energy level structure and perturbed nature of the B state, which follows the Hund's case (b) coupling scheme. The central progression is a pure, f symmetry $\Omega = 1$ state (yellow). The other two e symmetry progressions begin as either $\Omega = 0$ (red) or $\Omega = 1$ (blue). As J increases, they are quickly mixed by the S-uncoupling part of the rotational Hamiltonian, which is proportional to $(J\,(J+1))^{1/2}$. This yields two e symmetry $\Omega = 0/1$ states (purple) at higher J. **Figure 3-8b (right):** shows the energy level structure, when S-uncoupling and other off-diagonal elements are ignored. The two e-symmetry states no longer mix together. The $\Omega = 0$ e state remains shifted somewhat due to the diagonal matrix elements of the rotational, spin-spin and spin-rotation Hamiltonians (see Chapter 2). The filled-in circles represent (-) parity states, while the hollow circles represent (+) parity states.

As shown in detail on Figure 3-8a, the B state, unlike the B" state, has important perturbations between some of its spin-orbit components. Most prominently, there is S-uncoupling between $\Omega = 0$ and $\Omega = 1$ e-symmetry states. Therefore, to treat the B state collisional transfer completely, I **must** use the synthesized G-F and PG model. Consider, as an example, the collisional transfer shown by Figure 3-9. The initial eigenstate (state 1 in Equation 27) is the $J = 3$ state of the lower e-symmetry $\Omega = 0/1$ component (the lower component is termed F_1 in spectroscopic notation). State 2 is the $J = 5$ state of the higher e symmetry $\Omega = 0/1$ component (termed F_3). The transition is $\Delta J = 2, e \leftrightarrow e, (-) \leftrightarrow (-)$, and would theoretically allowed by the rotational transfer selection rules discussed thus far in this chapter.

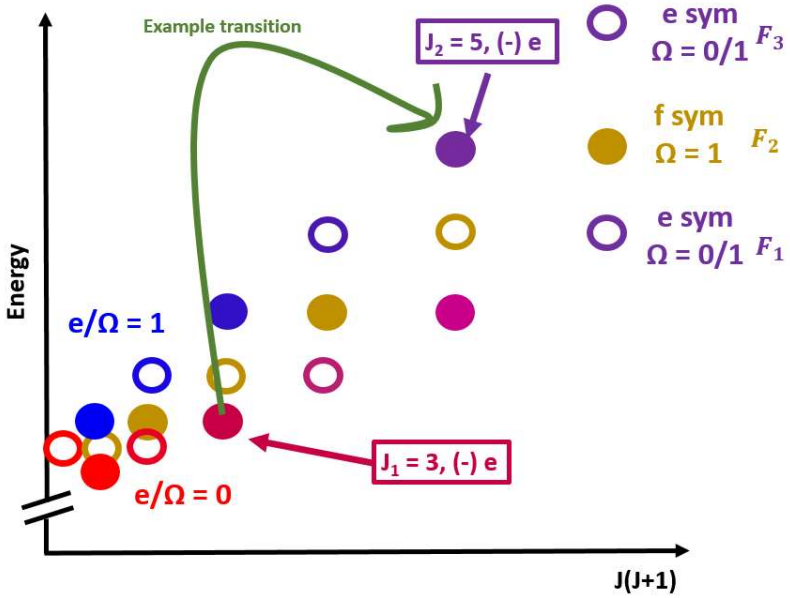

Figure 3-9: The example transition being considered in this section, which goes from an F_1, e-2symmetry, (-) parity, $J_1 = 3$ state, to an F_3, e symmetry, (-) parity, $J_2 = 5$ state. This transition is nominally allowed by the pure rotational transition propensity rules discussed in the preceding section. However, I must also consider the electronically inelastic nature of this collision.

I now return to Equation 3.27. There, the sum over i is over all unperturbed, basis electronic states. For eigenstate 1 and eigenstate 2, this is a sum over two states: $\Omega = 0\ e$ and $\Omega = 1\ e$. Therefore, I rewrite Equation 3.21 as Equation 3.28

$$k_{1\to 2} = z * \left| \sum_{i\,\epsilon\,\{\Omega=0\ e,\Omega=1\ e\}} c_{i,J1}c_{i,J2}a'' \left| \frac{E_i(J_2) - E_i(J_1)}{B_{X_i}} \right|^{-\alpha'} \right|^2 . \quad (3.28)$$

In Equation 3.28, I have color coded the two different components of the rate calculation. In the **orange** part of the calculation, I calculate the rotational transfer rate in either the pure, unperturbed $\Omega = 0\ e$ or the $\Omega = 1\ e$ states. This part of the calculation is illustrated in Figure 3-10.

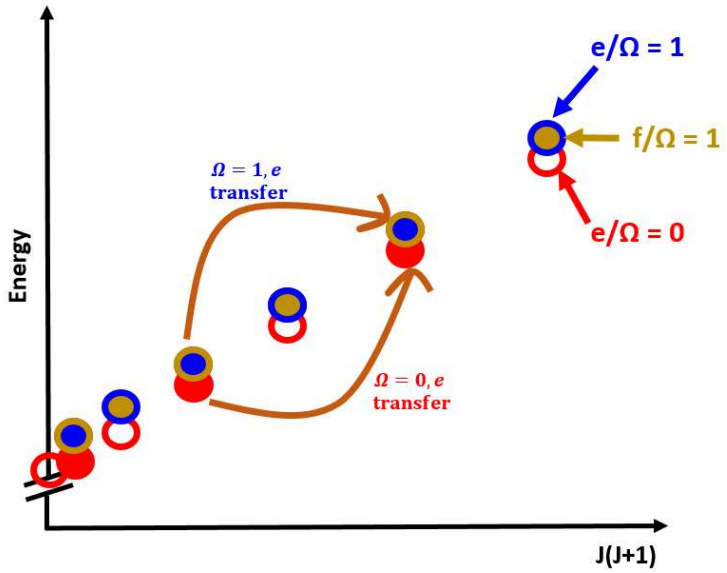

Figure 3-10: The collisional transfer processes used to calculate the orange part of Equation 28, i.e. rotationally inelastic transfer in the unperturbed $\Omega = 0$ e or $\Omega = 1$ e states. The rotational constant, B_X is the same for both terms in the sum. Likewise, the energy gap is also identical.

I note here that in both the $\boldsymbol{\Omega = 0\ e}$ and $\boldsymbol{\Omega = 1\ e}$ states, the rotational constant, B_{X_i}, is the same. Likewise, the energy gaps are identical, i.e. $\boldsymbol{E_{\Omega=0\ e}(J_2) - E_{\Omega=0\ e}(J_1) = E_{\Omega=1\ e}(J_2) - E_{\Omega=1\ e}(J_1)}$. Neither of these relationships is universally true, especially for B/B" mixed states, but for this example, we can write Equation 3.29. This equation states that the probability of a $J_1 = 3$ to $J_2 = 5$ transition is the same for both electronic basis states

$$P^{1/2}{}_{J_1\to J_2} = a'' \left| \frac{E_{\Omega=0\ e}(J_2 = 5) - E_{\Omega=0\ e}(J_1 = 3)}{B_{X_{\Omega=0\ e}}} \right|^{-\alpha'} = a'' \left| \frac{E_{\Omega=1\ e}(J_2 = 5) - E_{\Omega=0\ e}(J_1 = 3)}{B_{X_{\Omega=0\ e}}} \right|^{-\alpha'} . \quad (3.29)$$

Next, I consider the **purple** portion of Equation 3.28, i.e. the coefficients $c_{i,J1}$ and $c_{i,J2}$. These are the mixing coefficents for either member of the pair $i \epsilon \{\boldsymbol{\Omega = 0\ e},\ \boldsymbol{\Omega = 1\ e}\}$ basis states. We can estimate the c_i's as follows. We imagine a 2x2 Hamiltonian as in Equation 3.30, with basis set: $\{\boldsymbol{\Omega = 0\ e},\ \boldsymbol{\Omega = 1\ e}\}$

$$\begin{bmatrix} H_{diag} & H_{S-un} \\ H_{S-unc.} & H_{diag} \end{bmatrix} = \hat{H}. \tag{3.30}$$

In Equation 3.30, I have assumed, for simplicity, that the diagonal matrix elements are the same for both Ω states (this is not strictly true, due to effects such as spin-spin coupling, as shown in Figure 3-8b). The off-diagonal matrix elements come primarily from the spin-uncoupling part of the rotational Hamiltonian.

Equations 3.31a-b give the eigenvectors of the Equation 3.30 Hamiltonian

$$F_{1,e} = \frac{1}{\sqrt{2}}\begin{bmatrix} 1 \\ 1 \end{bmatrix} \tag{3.31a}$$

$$F_{3,e} = \frac{1}{\sqrt{2}}\begin{bmatrix} 1 \\ -1 \end{bmatrix}. \tag{3.31b}$$

where the first eigenvector (3.31a) belongs to the higher energy, F_1 manifold, while the second eigenvector (3.31b) belongs to the lower energy, F_3 manifold. If the amount of the S-uncoupling interaction was the same for the initial J = 3 F_3 eigenstate, and for the final J = 5 F_1 eigenstate was the same, we would have, in the language of Equation 3.28:

$$c_{\Omega=0,J=3} = {}^{1}/_{\sqrt{2}} \quad c_{\Omega=1,J=3} = {}^{1}/_{\sqrt{2}} \quad c_{\Omega=0,J=5} = {}^{1}/_{\sqrt{2}} \quad c_{\Omega=1,J=5} = {}^{-1}/_{\sqrt{2}}$$

If we include the condition given by Equation 3.29, then Equation 3.28 becomes Equation 3.32:

$$k_{1\to2} = z * |c_{\Omega=0,J=3}c_{\Omega=1,J=3} + c_{\Omega=0,J=3}c_{\Omega=1,J=3}|^2 P^{\frac{1}{2}}_{J_1\to J_2} = 0 \tag{3.32}$$

Note that the extent of the $\Omega = 0$, l-mixing perturbation does change from $J = 3$ to $J = 5$, so the rate is not strictly zero. However, this difference in sign between $c_{\Omega=1,J=3}$ and $c_{\Omega=1,J=5}$ does result in a new

propensity rule for B state rotational transfer, i.e.$F_1 \leftrightarrow F_3$ transfer is low probability in the B electronic state. This result matches empirical data on collisional transfer in the B state of S_2 from Gottscho [78] and Cauchey and Crosley [85]

ΔJ = 0 collisions.

Collisions that do not change rotational quantum number, J, (i.e. rotationally elastic collisions) are not included in my model. These types of collisions, which shift the frequency of spectroscopic transitions, are generally not observed in linear molecules, such as S_2 [86]. Furthermore, such collisions are incompatible with the Gelbart-Freed/PG model as currently constructed. For example, $|\Delta E|^{-\alpha}$ converges to infinity because the initial and final basis energy states are identical. Additionally, if the probability of rotationally elastic collisions is similar in the B versus the B" state, then $|< 2|1 > |^2$ factors out of the rate constant expression and the rate is zero, as in Equation 3.14. The assumption that all collisions are rotationally inelastic will be discussed further in Chapter 4.

3.9. Summary of Collisional Transfer Propensities in the B state of S_2.

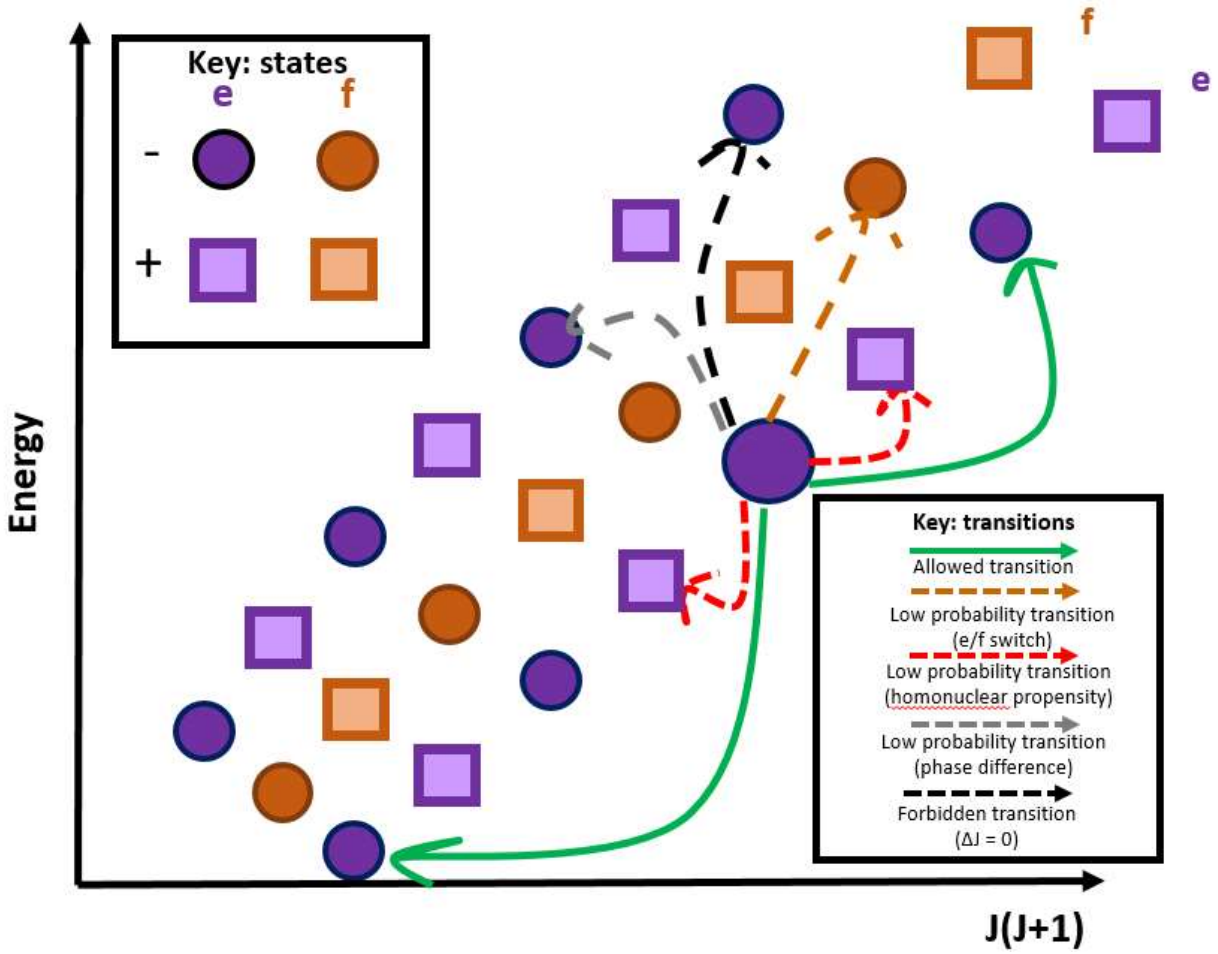

Figure 3-11: The selection and propensity rules for collisional transfer in the B electronic state of S_2. These are identical to the selection rules in the B" state ($\Omega = 0/2$), with the addition of the low propensity $F_1 \nleftrightarrow F_3$ transitions, and the forbidden $\Delta J = 0$ transitions.

Figure 3-11 summarizes the collisional transfer rules and propensities in the B state of S_2. The usual rotational propensity rules $+\leftrightarrow +/-\leftrightarrow -$ and $e \leftrightarrow e/f \leftrightarrow f$ still apply. But here I add $F_1 \nleftrightarrow F_3$ and $\Delta J \neq 0$.

3.10. The Big Picture: Collisional Transfer in the B/B" system.

The propensity rule against $.F_1 \leftrightarrow F_3$ transfer in the B state can be understood in terms of the general principle from our discussion of Gottscho's rule for e/f symmetry transfer [78]. That is: **In the short-duration (non-perturbing) limit, inelastic collisions can only move population between rotational states or other, degenerate orbital (but not spin) electronic states.** In the B" case, the degeneracy of the different Ω states is removed by a diagonal spin-orbit matrix element, and the transfer

rate between omega states is small because there are only small L-uncoupling interactions perturbations between them. In the B state case, by contrast, the degeneracy of the F_1 and F_3 components is removed by a large off diagonal, rotational Hamiltonian matrix element, and the transfer rate is small because of the sign difference in the probability amplitudes.[12]

I can now apply these principles to B/B" perturbations. The propensity for transfer from a primarily B vibronic state to a primarily B" vibronic state is small. The proof of this is very similar to the proof presented in Equations 3.30 to 3.32. We can instead have transfer from a *mixed* B/B" state to state that is primarily B or B" in character. This type of collisional transfer is called *doorway* or *gateway* mediated population transfer. It is illustrated in Figure 3-12. This doorway mechanism will be crucial to understanding the results presented in Chapter 5, and, especially, Chapter 6

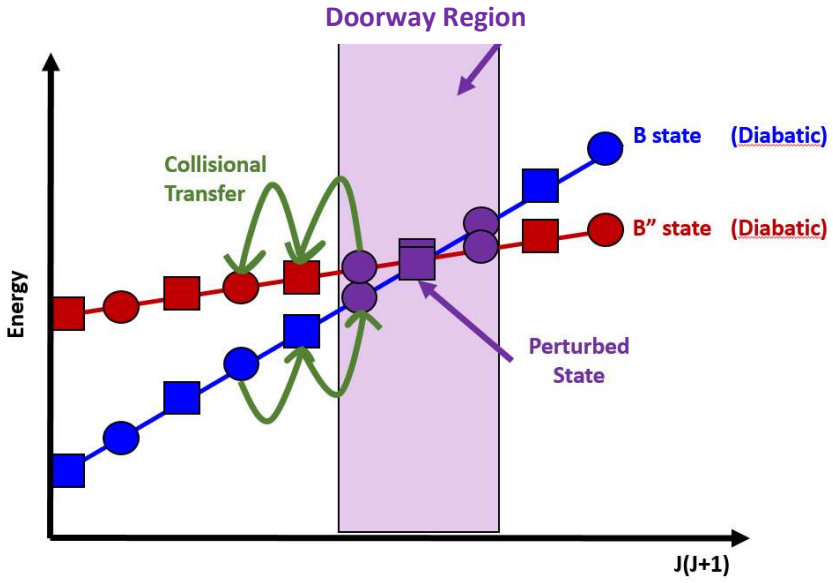

Figure 3-12: A summary of the doorway mediated population transfer mechanism. The B and B" states are simplified; they ignore fine structure and they do not show energy level shifts (i.e. are diabatic). When the two diabatic become near-degenerate, they state-mix and create a doorway (purple states). Rotationally inelastic collisions (green) can move population from a relatively pure B state to a relatively pure B" state via the doorway.

[12] Note that, had I used a case (b) basis set, the situation would be reversed. For example, the B" state spin-orbit interaction will now be off-diagonal, as opposed to on-diagonal and the rate will be small due to the phase dependence of the G-F rate constant.

Chapter 4 : Putting it All Together, A Master Equation Model for Population Transfer

Abstract: I now synthesize the eigenstate character of all bound levels of the B/B"-X system; the absorption, fluorescence, and predissociation processes; the electronically/rotationally inelastic transfer rates, and simple expressions for chemical transfer into the Archean rock record. Rates for all these processes are incorporated in a Master Equation kinetic model: a large system of coupled differential equations, where each equation represents a single rovibronic state in the system. To incorporate the collisional transfer rate constants from Chapter 3, small modifications must be made to account for my assumption that all collisions are rotationally inelastic, as well as to maintain detailed balance/thermal equilibrium with the surrounding atmosphere. The master equation model can be solved at steady state, which requires a "closed" system that ignores predissociation and chemical transfer. These process which "open" the system, require a time-dependent solution. This solution is generated using the matrix exponential method.

4.1. Overview:

In this chapter, I introduce a Master Equation kinetic model that incorporates all relevant, bound rovibrational states of the X, B, and B" states of S_2, and all radiative and collisional transfer processes between these states. For full details on these processes, see Chapters 2 and 3. More specifically, the Master Equation model incorporates:

(1) The complete eigenstate character of all 1208 X states and 16210 B/B" states involved in my model.

(2) Absorption and fluorescence to/from the B/B" states, described in Chapter 2.

(3) The synthesized Gelbart-Freed/PG collisional transfer model, described in chapter 3.

(4) Predissociation via spin-orbit perturbations by the repulsive 1_u state described in Chapter 2. The repulsive state fully predissociates for vibrational states with $v_B > 9$ and $v_{B"} > 21$. In this model, I only include states with $v_B <= 9$ or $v_{B"} <= 21$. However, there are a number of higher rotational levels of $v_B = 8, 9$ and $v_{B"} = 19, 20, 21$ that are above the predissociation limit at ~35,999 cm^{-1}. The predissociation of these states to S + S **is included** the model.

(5) Chemical reactions that irreversibly move excited state S_2 into the reduced rock record via the S_2 -> S_8 -> FeS_2 polymerization mechanism described in Chapter 1.

The Master Equation model uses the above information as inputs and can be solved in multiple ways, to output the following information:

(1) The population of every X, B, and B" rovibrational state under the "steady state approximation" (where the system is at equilibrium and all the transfer rates converge to zero). Note that this approximation is only valid in a closed system, i.e. when there are no processes that chemically change the system. This excludes predissociation to S + S and polymerization to S_3, S_4, etc.

(2) The population of every X, B, and B" rovibrational state as a function of time. I use this, more general, solution to incorporate the predissociation and polymerization chemistry described above.

(3) I also adjust a variety of parameters, including the relative strength of the B/B" perturbations, the predissociation lifetime, the magnitude of the isotope shift, etc. These changes do not reflect the physical reality of the B/B"-X system. However, observation of both the steady-state and time-dependent behavior as a function of these parameters provides general insight the mechanisms of electronic state transfer, and how those mechanisms could affect mass independent fractionation in other systems. This will be explored further in Chapters 6, 7, and 8.

4.2. The Master Equation Model: An Introduction

A master equation model is a system of coupled, first -order differential equations, as given by Equation 4.1

$$\frac{d\vec{P}}{dt} = \boldsymbol{A}\vec{P}(t). \tag{4.1}$$

Here, $\vec{P}(t)$ is a vector that lists the population of each B, B", and X rovibrational quantum state as a function of time. The matrix $\boldsymbol{A}$ is a special form of matrix called a Markov matrix. The Markovian nature of $\boldsymbol{A}$ is notable for two reasons. First, the future time evolution of a Markov system depends only on its current state and not any preceding state. Second, the solutions to the Markovian equations of motion

given by Equation 4.1 are exponential functions. I will invoke both of these properties later on in this chapter. For now, we should think of $\boldsymbol{A}$ as a network of connections (transfer rates) between the individual states of $\vec{P}$. The master equation is a very common formalism for detailed modeling of chemical kinetics. For example, it has been used to analyze combustion processes [87], protein and peptide folding [88, 89], and quantum mechanical energy transfer [90]. I now detail the construction of a master equation model that completely describes processes (1)-(5) in the preceding section.

4.3. Modeling Absorption and Fluorescence in the B/B" system

The first order rate expressions for absorption and fluorescence in a simple two level system are given by Equations 4.2a and 4.2b

$$\frac{d[x]_i}{dt} = A_{b_i \to x_i}[b]_i - B_{x_i \to b_i}\rho(\nu, T_{sun})[x]_i \tag{4.2a}$$

$$\frac{d[b]_i}{dt} = -A_{b_i \to x_i}[b]_i + B_{x_i \to b_i}\rho(\nu, T_{sun})[x]_i. \tag{4.2b}$$

Here, $[x]_i$ and $[b]_i$ are the populations of the ground state and upper states, respectively. The $A_{b_i \to x_i}$'s and $B_{x_i \to b_i}$'s are called the Einstein A and B coefficients, respectively. The term $\rho(\nu, T_{sun})$ is the radiation density of the sun in SI units of W·s/m^2, where ν is the $[x]_i$ <->$[b]_i$ transition frequency and $T_{sun}$is the surface temperature of the sun.

The ρ term can be reasonably estimated as a blackbody with temperature, T_{sun}. However, I instead use empirical data from Rottman, Woods, and McClintock, who reported solar irradiance measurements taken using the Solar Radiation and Climate Experiment (SORCE) spacecraft [91]. This data somewhat overestimates the radiation density, as the sun's luminosity has gradually increased during the history of the solar system [92]. The Archean solar flux, in particular, is thought to be 20-30% lower than its present value. The temperature of the planet, however, was about as warm as it is now, and much higher than this low solar flux would suggest [92, 93]. This apparent contradiction is referred to as the

"faint, young sun paradox" [94]. A number of mechanisms including OCS radiative forcing [95] and reduced cloud cover [96] have been proposed to help resolve this paradox.

The coefficients $A_{b_i \to x_i}$ and $B_{x_i \to b_i}\rho(\nu, T_{sun})$ constitute first order rate constants with dimension: [time]$^{-1}$. Equation 4.3a relates the absorption cross section, σ_{xb}, calculated in Chapter 2, to the Einstein A coefficient, and Equation 4.3b does the same for the Einstein B coefficient

$$A_{b_i \to x_i} = \frac{8\pi\nu^2(2J" + 1)}{c^2(2J' + 1)}\sigma_{xb} \tag{4.3a}$$

$$B_{b_i \to x_i} = \frac{c}{\nu h}\sigma_{xb}. \tag{4.3b}$$

where ν is the transition frequency, c is the speed of light, h is Planck's constant, and J" and J' are the total angular momentum quantum numbers of the b and x states, respectively.

These coefficients are included as terms in the matrix $\boldsymbol{A}$ from Equation 4.1. The selection rules from Chapter 2 determine the ground and excited rovibrational states of $\vec{P}$ that they connect.

4.4. Modeling B/B" Collisional Transfer

The first-order rate constants for collisional population transfer are also included in $\boldsymbol{A}$. They are determined using an expression derived in Chapter 3. This expression is rewritten here as Equation 4.4, where states 1 and 2 are different B/B" eigenstates.

$$k_{1\to 2} = Z * |\sum_i c_{i,J1}c_{i,J2}a''|\frac{E_{X,i}(J_2) - E_{X,i}(J_1)}{B_{X_i}}|^{-\alpha'}|^2 \tag{4.4}$$

Recall that Z is the total hard-sphere collision rate, which is a function of temperature and pressure, and the sum is over all possible vibronic states, i. The $c_{i,J1}$ and $c_{i,J2}$ are the coefficients for the initial and final J state ***within*** the pure vibronic state, i .The parameter a'' is a proportionality constant, $E_{X,i}(J_2) - E_{X,i}(J_1)$

is the energy gap between the initial and final diabatic state, B_{X_i} is the rotational constant for state X_i, and $\alpha' = 0.6$ (see section 3.7).

While this sum over i is theoretically over all Hund's case (a) vibronic states in the B/B" system, in this calculation, I limit the sum to the five most probable basis states within eigenstate 1. Furthermore, while collisional transfer can theoretically occur between any two states that share at least some case (a) basis state character, here again I limit transfer to the 5 final states with the largest transfer rates. Finally, I limit the maximum change in rotational quantum number to $|\Delta J| \leq 10$. All these limitations are in service of computational efficiency.

As discussed in chapter 3, I assume that every collision is rotationally inelastic. That is, for each eigenstate, i, we must have the condition given by Equation 4.5

$$\sum_j k_{i\to j} = Z. \tag{4.5}$$

In other words, the total transfer rate out of eigenstate i must be equal to the total collision rate, Z. In the rate expression given by Equation 4.5, I define the proportionality constant for each eigenstate as: $(a_i'')^2 * Z = A_i$. To determine A_i, I must first determine the total hard-sphere collision rate, using the standard expression given by Equation 4.6

$$z = \rho_{N_2} \pi d_{N_2S_2}^2 < v_{N_2S_2} >, \tag{4.6}$$

where: ρ_{N_2} is the number density of molecules; $d_{N_2S_2}$ is the average collision diameter of the N_2 and S_2; and $< v_{N_2S_2} >$ is the mean speed of the nitrogen molecules. In this calculation, ρ_{N_2} is given by the ideal gas law, and $< v_{N_2S_2} >$ is calculated using the Maxwell-Boltzmann probability distribution. The typical expressions for ρ and $< v >$ are given by Equations 4.7a and 4.7b, respectively

$$\rho_{N_2} = \frac{P}{k_B T} \tag{4.7a}$$

$$< v_{N_2S_2} > = (\frac{8k_BP}{\pi\,\mu_{N_2S_2}})^{\frac{1}{2}}. \quad (4.7b)$$

Where P is the pressure and T is the temperature of the atmosphere, k_B is Boltzmann's constant, and $\mu_{N_2S_2}$ is the N_2/S_2 reduced mass.

From here, I use Z to determine the $A_i's$ **for each eigenstate, *i*,** as shown in Equation 4.8[13]

$$A_i = \frac{Z}{\sum_j k_{i\to j}}. \quad (4.8)$$

With this, Equation 4.3 becomes Equation 4.9

$$k_{1\to 2} = A_i|\sum_i c_{i,J1}c_{i,J2}|\frac{E_{X,i}(J_2) - E_{X,i}(J_1)}{B_{X_i}}|^{-\alpha'}|^2\,. \quad (4.9)$$

I must now include the constraints on the +/- parity and e/f symmetry changing collisions discussed in Chapter 3. Let p_1 and p_2 be the total (+/-) parity of state 1 and state 2, respectively. Likewise, let r_1 and r_2 be the e/f symmetry of the initial and final states. Let e be the electronic state character (B or B") of the basis electronic state, i. Finally, let Ω_i be the spin character of the ith B" state. These conditions lead to Equation 4.10.

$$k_{1\to 2} = z * A_i|\sum_i c_{i,J1}c_{i,J2}|\frac{E_{X,i}(J_2) - E_{X,i}(J_1)}{B_{X_i}}|^{-\alpha'}\delta_{p_1p_2}[1-(1-\delta_{r_1r_2})(1-\delta_{e,B"}\delta_{\Omega_i,1})]|^2 \quad (4.10)$$

In Equation 4.10, the $\delta_{i,j}$'s are Kronecker delta functions, which are equal to 1 if $i = j$, and 0 otherwise. The conditional $\delta_{i,j}$ structure in the right part of Equation 4.9 reproduces the same rotational transfer selection/propensity rules as in Chapter 3, Figure 3-4. In Equation 4.9, note that Equation 4.10 gives $k_{1\to 2} = k_{2\to 1.}$

[13] The sum in Equation 7 ($\sum_j k_{i\to j}$) is the same as summing over the ith column in the matrix **A**, excluding the diagonal matrix element, $A_{i,i}$.

4.5. The Principle of Detailed Balance and the Boltzmann Weighting of Rate Constants

The principle of detailed balance states that, at equilibrium, the total probability of a transition *out* of a quantum state must be equal to the total probability of a transition *into* a quantum state. While the $k_{1\to2} = k_{2\to1}$ condition seems to satisfy this criterion, I must account for the differing velocities of the N_2 collision partners. In other words, I average the rate constant, as a function of velocity, over the velocity distribution of the N_2 molecules (Equation 4.11)

$$k(T) = \int_0^\infty k(v)f(v)dV. \tag{4.11}$$

Here, $f(v)$ is the Maxwell-Boltzmann probability distribution for the relative velocities which is given in Equation 4.12

$$f(v) = 4\pi(\frac{\mu}{2\pi k_B T})^{\frac{3}{2}}v^2 e^{-mv^2/2k_B T}. \tag{4.12}$$

In equation 4.12, T is the temperature of the atmosphere k_B is Boltzmann's constant, v is the relative velocity of the N_2/S_2 molecules, and μ is the reduced mass, i.e. $\mu = \frac{\mu_{N_2}\mu_{S_2}}{\mu_{N_2}+\mu_{S_2}}$. From Equations 4.11 and 4.12, it can be shown that the $k_{1\to2}$ and $k_{2\to1}$ are related as follows (Equation 4.13).

$$\frac{k_{2\to1}}{k_{1\to2}} = \frac{(2J_1+1)}{(2J_2+1)}e^{\frac{\Delta E}{k_B T}}. \tag{4.13}$$

Where J_1 and J_2 are the initial and final total angular momentum quantum numbers, and ΔE is the energy gap between the initial and final states. Intuitively, we can understand Equation 4.13 as a condition such that, in the long time limit, the inelastic transfer process will produce a Boltzmann distribution of rotational states. Note that the $(2J+1)$ M-degeneracy factor, which I had previously ignored when deriving the PG model in Chapter 3, returns here.

To ensure that the relationship in Equation 13 is satisfied for all pairs of collisional transfer rate constants, I apply the following weight to each rate constant (Equation 4.14) [65]

$$k_{1\to 2,w} = k_{1\to 2}(2J_2 + 1)e^{{E_1 - E_>}/{k_B T}}. \quad (4.14)$$

Where, $E_>$ is the larger of E_1 and E_2, and $k_{1\to 2}$ is the standard collisional transfer rate constant, calculated using Equation 4.3.

Finally, I incorporate the weighted $k_{1\to 2,w}'s$ into the Master Equation model as follows in Equations 4.15a-b:

$$\frac{d[1]}{dt} = k_{2\to 1,w}[2] - k_{1\to 2,w}[1] \quad (4.15a)$$

$$\frac{d[2]}{dt} = k_{2\to 1,w}[1] - k_{2\to 1,w}[2]. \quad (4.15b)$$

4.6. Open Systems: Chemical Reactions and Predissociation

The system described thus far is ***closed***, in the sense that the system of differential equations is capable of satisfying Equation 4.16, without the trivial solution $\vec{P} = \vec{0}$:

$$\frac{d}{dt}\vec{P} = 0. \quad (4.16)$$

In other words, the B/B" and X states can evolve to a point where the system is at equilibrium and there is not net flow of population into or out of any individual state. However, Equation 4.16 is sometimes impossible to satisfy. I will refer to systems that cannot satisfy Equation 4.16 as "open", meaning that there is a net flow of population either into or out of the B/B"-X system. In this work, I will be especially interested in flow of population *out* of the system due to two processes: chemical reactions and predissociation.

In chapter 1, I discussed the process by which S_2 leaves the atmosphere. Specifically, S_2 polymerizes to S_4 and S_8, which precipitates out of the atmosphere as elemental sulfur aerosol particles. It

is then stored in the rock record as reduced species, such as pyrite (FeS_2). In this sense, the atmosphere is an open system, and we can model this (ultimately) irreversible chemical process by adding an additional rate constant to each B/B" state $[b]_i$ differential equation, as in Equation 4.17.

$$\frac{d}{dt}[b]_i = -A_i[b]_i + \sum_g B_{g\to i}\,\rho(\nu,T)\,[g] - \sum_j k_{i\to j}[b]_i + \sum_j k_{j\to i}[b]_j - \boldsymbol{k_{chem}[b]_i}. \qquad (4.17)$$

Where, in the bolded term, k_{chem} is the **net** rate of the chemical reaction that removes S_2 from the atmosphere, by transforming it to S_3, S_4, and eventually FeS_2. Because I am concerned about the net rate of transfer, I do not include a back reaction term, such as $+\boldsymbol{k_{chem,back}[S_3]}$.

It is important to note: I initially assume that the rate of chemical reactions in the excited state is much, much larger than the reaction rate in the ground state. That is, I only include chemical reactions with the B/B" states. I will revisit the validity and consequences of this assumption later on in this work.

Likewise, I can also include the effects of predissociation from S_2 to $S(^3P)$ + S (^3P) via a spin-orbit interaction with a 1_u state, as discussed in Chapter 2. Because my model focuses on the non-predissociating vibrational states, I only include predissociation for rotational states of $v_B < 9$ and $v_{B"} < 21$ that exceed the predissociation limit of $35{,}999\ cm^{-1}$. The longest lifetime of the $v_B < 9/v_{B"} < 21$ predissociating states τ_p is about 10 ns. Unless otherwise stated, I will use this lifetime as an estimate for τ_p in my model. This was observed by Green and Western [46] for $\Omega = 0$ states of $v_B = 10$. Because the B/1_u state interaction is primarily spin-orbit in nature (i.e. $\Delta\Omega = 0$), the v = 10, $\Omega = 0$ manifold has the weakest predissociation to the $\Omega = 1$ repulsive state.

The parameter τ_p is adjustable in my model. I include it in the B/B" differential equations for as follows in the bolded portion of Equation 4.18.

$$\frac{d}{dt}[b]_i = -A_i[b]_i + \sum_g B_{g\to i}\,\rho(\nu,T)\,[g] - \sum_j k_{i\to j,w}[b]_i + \sum_j k_{j\to i,w}[b]_j - k_{chem}[b]_i - \boldsymbol{(\frac{1}{\tau_p})[b]_i}. \qquad (4.18)$$

As with the chemistry portion of the equation, I do not include a back reaction (i.e. $S + S \rightarrow S_2$) in this version of my model.

4.7. Visualizing the Master Equation Model

Figures 4-1a-f visualize and summarize the transfer processes in the B/B"-X system, which are encoded in the matrix **A.** The matrix A is expressed in the following basis set (Equation 4.19)

$$basis\ set = \begin{bmatrix} \boldsymbol{B_1\ J_1} \\ \boldsymbol{B_1\ J_2} \\ \vdots \\ \boldsymbol{B_2\ J_1} \\ \boldsymbol{B_2\ J_2} \\ \vdots \\ \boldsymbol{B_n\ J_1} \\ \boldsymbol{B_n\ J_2} \\ \vdots \\ \boldsymbol{X_1\ J_1} \\ \boldsymbol{X_1\ J_2} \\ \vdots \\ \boldsymbol{X_2\ J_1} \\ \boldsymbol{X_2\ J_2} \\ \vdots \\ \boldsymbol{X_N\ J_1} \\ \boldsymbol{X_N\ J_2} \\ \vdots \end{bmatrix}. \tag{4.19}$$

Where the $B_i's$ are B/B" vibronic states, and the $X_i's$ are X vibronic states.

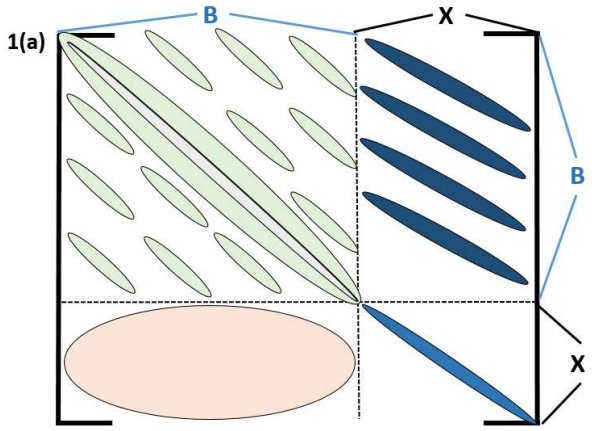
1(a)
B
X
B
X

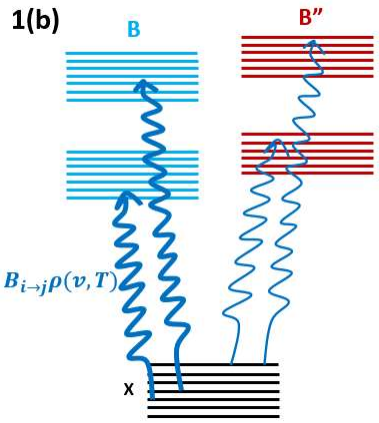
1(b)
B
B"
$B_{i\to j}\rho(v,T)$
X

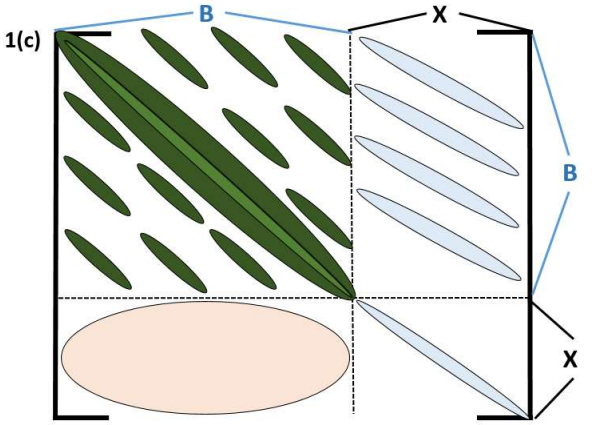
1(c)
B
X
B
X

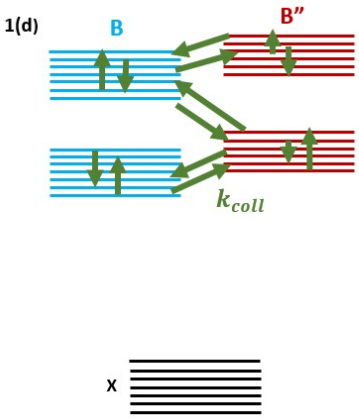
1(d)
B
B"
k_{coll}
X

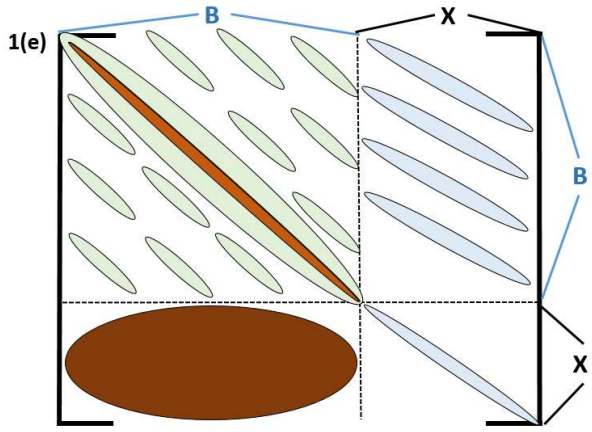
1(e)
B
X
B
X

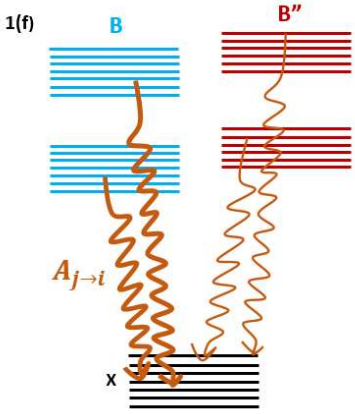
1(f)
B
B"
$A_{j\to i}$
X

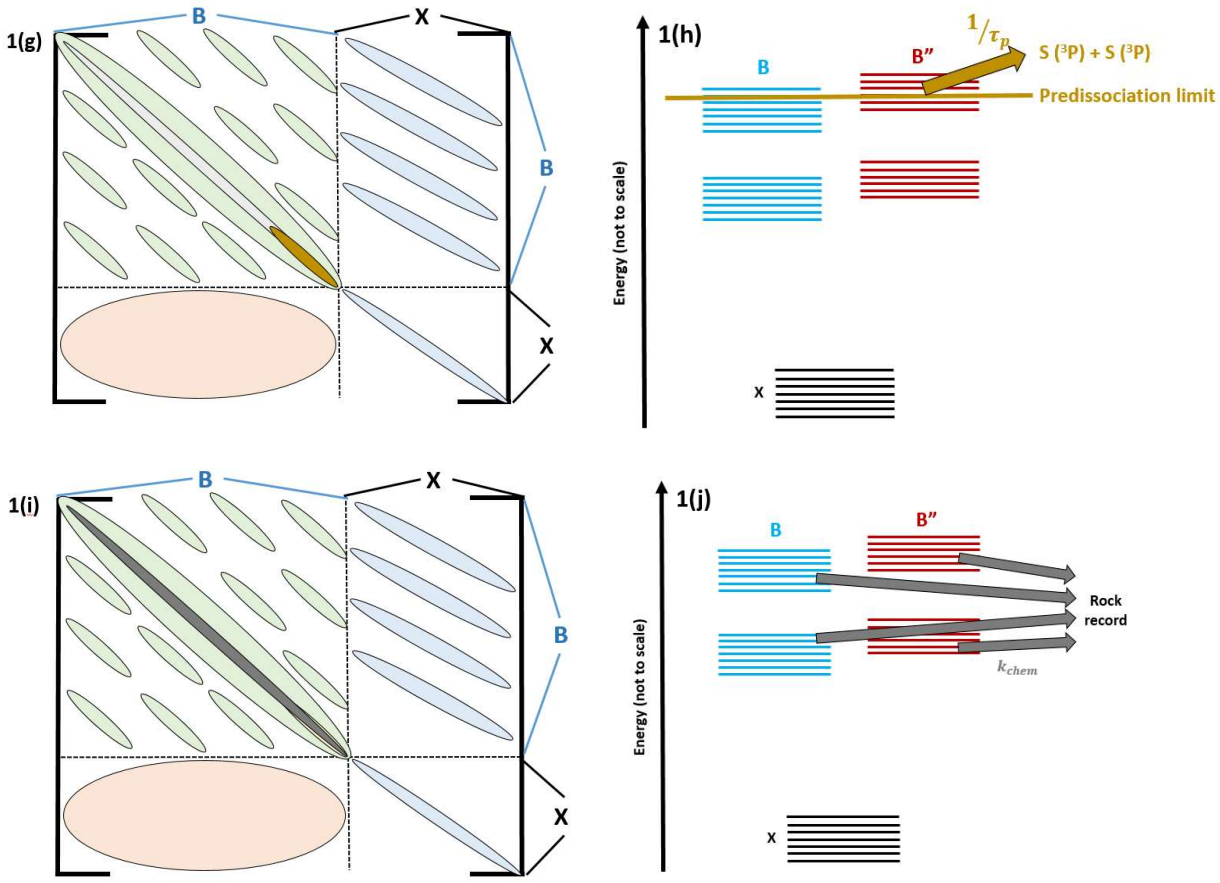

Figure 4-1: Summarizes the connections between the various states in the B/B" system. The left-side figures are cartoons that visualize the nonzero matrix elements for each of the transfer processes represented in the simplified (and not-to-scale) energy level diagrams on the right. Note that, for the matrix A, the column represents the initial state and the row represents the final state. These connections are: absorption (**1a** and **1b**), B/B" collisional transfer (**1c** and **1d**), fluorescence (**1e** and **1f**), predissociation (**1g** and **1h**), and excited state chemistry (**1i** and **1j**). The closed system processes (a-f) have two sets of non-zero matrix elements one for leaving the initial state (diagonal) and one for entering the final state (off-diagonal). The open system processes (g-j) only have terms for leaving the B/B" state (diagonal).

One note about the fluorescence process, visualized in Figures 4-1e-f: In general, the final distribution of vibrational states for fluorescence from the B/B" state to the X state is determined by the B/B"-X Franck-Condon factors. However, my model only includes $v_x = 0 - 1$. To bridge this gap, I simply assume that the initial Franck-Condon distribution is thermalized on a timescale that is short relative to the "lifetime" of the X state. (The "lifetime" is the characteristic time spent in the ground state in-between excitations to the B/B" state). To do this, I allow fluorescence to every J state in $v_x = 0 - 1$, and apply a corresponding Boltzmann weight to each of the Einstein A coefficients.

4.8. Solving the Master Equation Model: Closed Systems

If I do not include chemical transfer to the rock record and predissociation, then the system is closed and I solve the Master Equation model at steady state (see: Equation 4.15). To illustrate this process, consider a system with a set of upper state differential equations given by Equation 4.20:

$$\frac{d}{dt}[b]_i = 0 = -A_i[b]_i + \sum_g B_{x\to i}\,\rho(\nu,T)\,[x]_i - \sum_j k_{i\to j,w}[b]_i + \sum_j k_{j\to i,w}[b]_j\,. \tag{4.20}$$

In Equation 4.20, the Einstein A and B coefficients and the weighted collisional transfer rate constants are defined as before; $[x]_i$ is the ground state population; and the differential equation is set to zero to satisfy the steady state approximation. I assume the $[x]_i's$ to be constant, and, consequently, I do not write their differential equations. This leads directly to Equation 4.21

$$\sum_g B_{g\to i}\,\rho(\nu,T)\,[x]_g = -A_i[b]_i + -\sum_j k_{i\to j,w}[b]_i + \sum_j k_{j\to i,w}[b]_j\,. \tag{4.21}$$

Where the $[x]_g$'s are given by the Boltzmann distribution (Equation 4.22):

$$[x]_g = \exp\left(-\frac{E_{[x]_g}}{k_b T}\right)\Big/ Q\,. \tag{4.22}$$

Where $E_{[x]_g}$is the eigenstate energy of ground state $[x]_g$, and Q is the canonical partition function. Abstracting Equation 4.21 to matrix notation, let $\vec{x}$ be the vector containing the $\sum_g B_{g\to i}\,\rho(\nu,T)\,[x]_g$ terms from the left side of Equation 21, for each upper state. The vector containing the relative populations of the $[b]_i$ states is $\vec{P}$ and it is given by Equation 4.23

$$\vec{P} = \boldsymbol{A}^{-1}\vec{x}. \tag{4.23}$$

Where $\boldsymbol{A}^{-1}$ is the inverse of the matrix $\boldsymbol{A}$. This inversion procedure is performed in Matlab version 2017a.[14]

4.9. Solving the Master Equation Model: Open Systems

If predissociation or irreversible chemical reactions are included, then the system is *open* and the steady state approximation no longer applies. Instead, I must solve for $\vec{P}$ as a function of time, i.e. $\vec{P}(t)$. The general solution to the Master Equation model (Equation 4.1) is given by Equation 4.24

$$\vec{P}(t) = e^{\boldsymbol{A}t}\vec{P}(0). \tag{4.24}$$

The term $e^{\boldsymbol{A}t}$is called the *Matrix Exponential.* It is defined using the Maclaurin series expansion of the function e^x (Equation 25)[15]

$$e^{\boldsymbol{A}t} = 1 + \boldsymbol{A}t + \frac{1}{2}\boldsymbol{A}^2t^2 + \frac{1}{6}\boldsymbol{A}^3t^3 + \frac{1}{24}\boldsymbol{A}^4t^4 + \cdots \tag{4.25}$$

The Matrix Exponential is computationally inexpensive to calculate because the $n\ x\ n$ matrix $\boldsymbol{A}$ can be diagonalized as shown in equation 4.26

$$\boldsymbol{A} = \boldsymbol{S}\boldsymbol{\Lambda}\boldsymbol{S}^{-1}. \tag{4.26}$$

Where $\boldsymbol{S}^{-1}$and $\boldsymbol{S}$ transform into and out of the eigenstate basis of **A,** respectively. The matrix $\boldsymbol{\Lambda}$ is diagonal with the eigenvalues $\lambda_1, \lambda_2, \ldots \lambda_n$as the diagonal matrix elements (Equation 4.27)

[14] It is not strictly necessary to assume that the $[x]_g$'s are constant. In this case, the matrix A is generally **not** invertible, but $\vec{P}$ can still be solved for by determining the nullspace of **A**. However, this procedure is both computationally expensive, and unnecessary, as the population of the $[x]_g$'s are much larger than those of the $[x]_i$'s, so I can assume the $[x]_g$'s to be constant.

[15] I have used both aforementioned properties of Markov matrices here. The solution to the differential equations are exponentials and I can completely determine the future behavior of the system given starting state $\vec{P}(0)$.

$$\boldsymbol{\Lambda} = \begin{bmatrix} \lambda_1 & 0 & \cdots & 0 \\ 0 & \lambda_2 & \cdots & 0 \\ \vdots & \vdots & \ddots & 0 \\ 0 & 0 & 0 & \lambda_n \end{bmatrix}. \tag{4.27}$$

Plugging into Equation 4.25, I obtain Equation 4.28.

$$e^{\boldsymbol{At}} = 1 + \boldsymbol{S\Lambda S^{-1}}t + \frac{1}{2}\boldsymbol{S\Lambda S^{-1}S\Lambda S^{-1}}t^2 + \frac{1}{6}\boldsymbol{S\Lambda S^{-1}S\Lambda S^{-1}S\Lambda S^{-1}}t^3 + \frac{1}{24}\boldsymbol{S\Lambda S^{-1}S\Lambda S^{-1}S\Lambda S^{-1}S\Lambda S^{-1}}t^4 + \cdots \tag{4.28}$$

Because $\boldsymbol{SS^{-1}} = \mathbf{I}$, where **I** is the identity matrix, I can write the simpler expression that is shown in Equation 4.29

$$e^{\boldsymbol{At}} = 1 + \boldsymbol{S}\left(\boldsymbol{\Lambda}t + \frac{1}{2}\boldsymbol{\Lambda^2}t^2 + \frac{1}{6}\boldsymbol{\Lambda^3}t^3 + \frac{1}{24}\boldsymbol{\Lambda^4}t^4 + \cdots\right)\boldsymbol{S^{-1}}. \tag{4.29}$$

And $\boldsymbol{\Lambda^i}$ is simply given by Equation 4.30

$$\boldsymbol{\Lambda^i} = \begin{bmatrix} {\lambda_1}^i & 0 & \cdots & 0 \\ 0 & {\lambda_2}^i & \cdots & 0 \\ \vdots & \vdots & \ddots & 0 \\ 0 & 0 & 0 & {\lambda_n}^i \end{bmatrix}. \tag{4.30}$$

Therefore, the matrix exponential reduces to a simple diagonalization procedure, which is also performed in Matlab 2018a.

The solution to Equation 23, $\vec{P}(t)$, is the population of each state in the B/B" system as a function of time. It provides a wealth of information that I will begin to analyze in Chapter 5.

Chapter 5 : Fundamentals – Fractionation in the Real B/B”-X System

Abstract:

The output of the master equation model, solved at steady state without predissociation or chemical reactions, closely approximates mass-dependent fractionation. However, each interaction between B and B” vibronic states generally behaves in a random manner. The one exception is a series of B” states with f rotationless symmetry, odd vibrational quantum numbers, and spin-orbit component, Ω, equal to zero. These states have weak state-mixing, compared to most of the B/B” system, because there is not a corresponding B, **f**, $\Omega = 0$ state, so the large spin-orbit, $\Delta\Omega = 0$ interactions cannot occur. This creates a “safe-zone” mechanism. “Safe-zones” are regions with very large B” state lifetimes that only occur in weakly state-mixed systems. The size of the safe-zone is determined by mass-dependent vibrational level shifts, with heavier isotopologues having smaller safe-zones. This trend reverses for a predissociating system, because lighter isotopes cross the predissociation threshold at lower rotational quantum numbers than do heavier ones. The most important conclusions drawn: Weak state-mixings are more likely to generate mass-independent fractionation than are strong state-mixings. (2) Collisional transfer in the B/B” state is unlikely to be the origin of Archean S-MIF (3) The mass-dependent nature of the fractionation from strongly predissociating states, makes such systems unlikely as origins for the S-MIF in the Archean rock record. (4) Spectroscopic parameters such as Franck-Condon factors, rotational constants, etc. are important for creating the systematic patterns that generate the mass-dependent fractionation.

5.1. The Steady State Model: General Results

Figure 5-1 shows the output of a very simple run of the B/B” kinetic model that I detailed in Chapter 4. In this run, predissociation does not exist and the quantity measured on the dependent axis is the fraction of the total population occupying any excited state (f_{ex})[16], for each of the four S-32

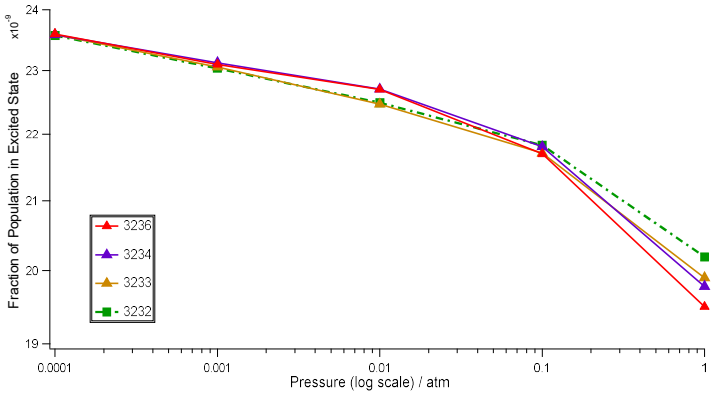

Figure 5-1: For each isotopologue, the steady-state fraction of the total population in the excited B/B” state is plotted as a function of pressure (logarithmic scale). 3232 has half of the rotational states, as described in Chapter 2, and is therefore differentiated from the other isotopologues using a dashed line. The temperature is 300 K.

[16] This fraction is on the order of 10^{-8}. Most of the population remains in the ground state.

containing isotopologues (3232, 3233, 3234, and 3236), *at steady state*. The temperature is 300 K. The independent axis is the pressure of the atmosphere on a logarithmic scale. Clearly, as the pressure increases, the overall excited state fraction decreases. Note also that, at higher pressures, the isotopologues begin to sort themselves by mass, with the lightest molecule (3232) having the largest fraction in the excited state and the heaviest (3236) having the smallest fraction. This striation is especially pronounced for the 1 atm data point.

As we noted in Chapter 1, the term "Sulfur Mass-Dependent Fractionation" (S-MDF) describes the isotope effect originating from a very specific isotope exchange phenominon. However, the mass sorting seen at the higher pressures in Figure 1 closely approximates S-MDF. This is seen more clearly in Figure 5-2, which plots $f_{ex}(at\ 1\ atm)$ of each isotopologue as a function of the reduced mass, and, to emphasize this point, it also includes a least squares fit of that data. Here, the large correlation coefficient for the least squares fit ($R^2 = 0.96$) indicates an isotope effect that closely approximates a mass-dependent relationship ($R^2 = 1$). This observation leads to two questions:

(1) Why does the the collisional transfer between the B and B" states generate mass-dependent behavior, even though this kinetic collisional transfer mechanism is completely unrelated to the thermodynamic relationship used to define the S-MDF relationship?
(2) Overall, why does the excited state population decrease with increasing pressure?

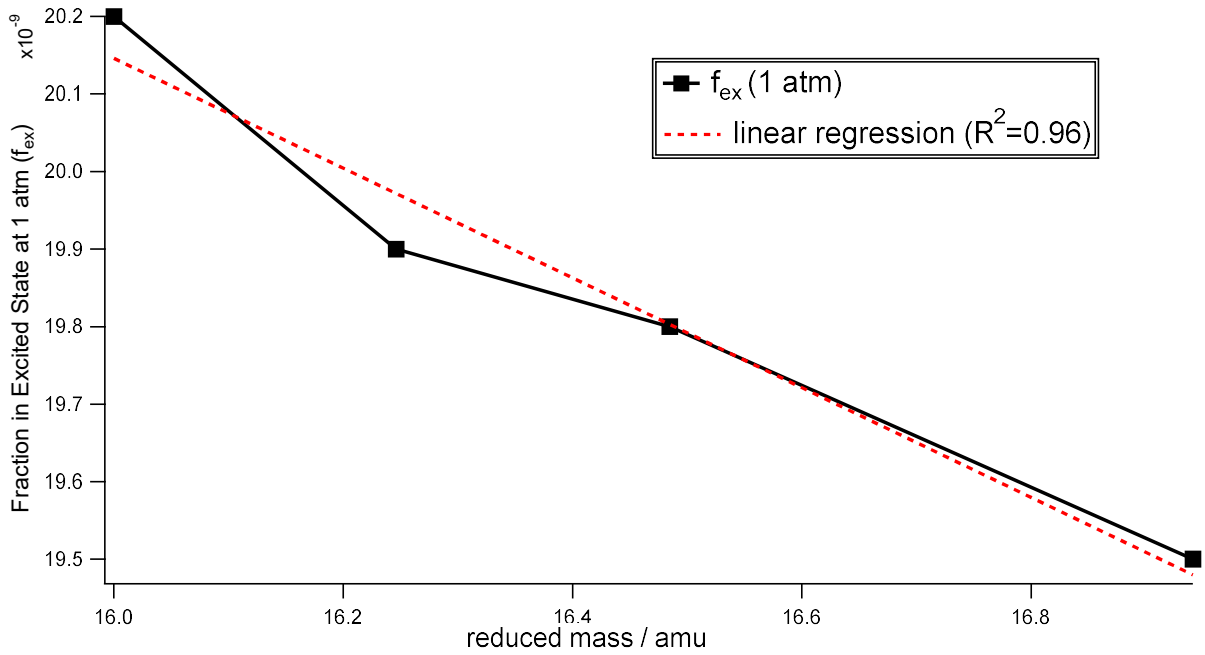

Figure 5-2: The black line shows f_{ex} at 1 atm for the data shown in Figure 4-1 (independent axis), as a function of reduced mass (dependent axis). The dashed red line shows a linear least squares fit of this data. The correlation coefficient ($R^2 = 0.96$) shows that the pattern approximates a purely S-MDF relationship, which would have an $R^2 = 1$.

5.2. A Vibrational State Analysis of Steady State Fractionation

To address question (1), I must break down the behavior of the B/B" system by e/f symmetry, electronic state, and vibrational level. For each vibrational state, I summed the steady state population over all of its constituent rotational states, as in Equation 5.1, where S is the sum, the subscripts v, e, p indicate that the sum is for a specific vibrational (v), electronic (e), and e/f symmetry (p), x_i is the steady state population of a given rovibronic state, and the sum is over all rotational levels.

$$S_{v,e,p} = \sum_{i \in J=J_{min}-100} x_i \tag{5.1}$$

Figure 5-3 is a bar chart that plots, at 1 atm, the difference in $S_{v,e,p}$ between 3236 (smallest f_{ex}) and 3232 (largest), such that a positive value indicates that the rovibronic state has more population in 3236, and a negative value indicates more population in 3232. The quantity plotted on the dependent axis of Figure 5-3 is made more explicit in equation 5.1

$$S_{v,e,p}(3236) - S_{v,e,p}(3232). \tag{5.2}$$

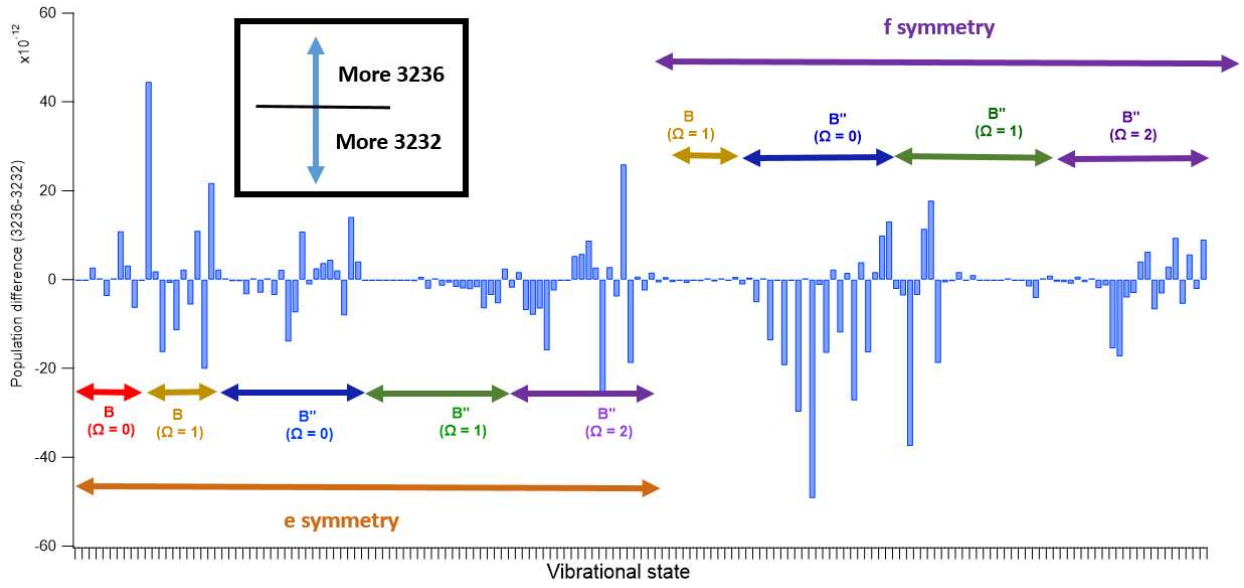

Figure 5-3: A bar chart depicting the difference in vibrational state population between the 3232 and 3236 states. Positive values indicate more population in 3236 for a given vibrational state, while negative values indicate more population in 3232. The vibrational states are sorted first by e/f symmetry, then electronic state, then spin-orbit component. While there is clearly a wide spectrum of behavior, it is not random. In particular, the f-symmetry B", $\Omega = 0$ vibrational states, show systematic bias toward 3236, and therefore suggest a possible origin of the pseudo mass-dependent fractionation effect seen in Figure 5-2.

In contrast with systems we will study later on, the isotope effect here varies substantially depending on the vibrational state, and while the behavior is complex, it is not entirely random. In particular, the bias towards 3232 in the f-symmetry B", $\Omega = 0$ vibrational states stands out as the primary origin of the pseudo mass-dependent effect we saw in Figure 5-2. Figure 5-4 displays this portion in more detail.

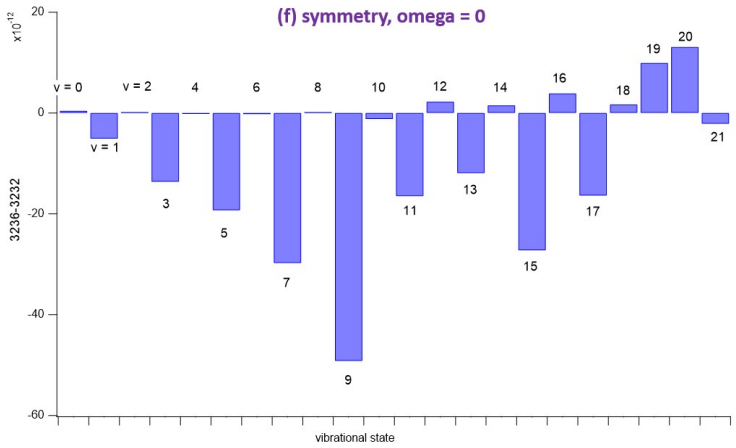

Figure 5-4: The B", f-symmetry, $\Omega = 0$ component of Figure 5-3. The numbers above or below each bar represent the vibrational quantum numbers. Note both the widespread, systematic bias towards 3232 and the even/odd alternation in the isotope effect.

In particular, note the even/odd alternation in the isotope effect over a broad swath of vibrational levels, from $v = 0$ to $v = 18$. The even levels, overall, favor neither 3232 nor 3236, while the odd levels significantly favor 3232. To understand the origin of this behavior, we will consider the interaction of these B" vibrational levels with nearby B vibrational levels. Figure 5-5 shows the reduced term value plots of two representative 3236 vibrational states: $v_{B"} = 7$ and $v_{B"} = 8$, as well as their neighboring B and B" states. For simplicity and clarity, I do not show the energy level shifts caused by perturbations between the B state and the B" state.

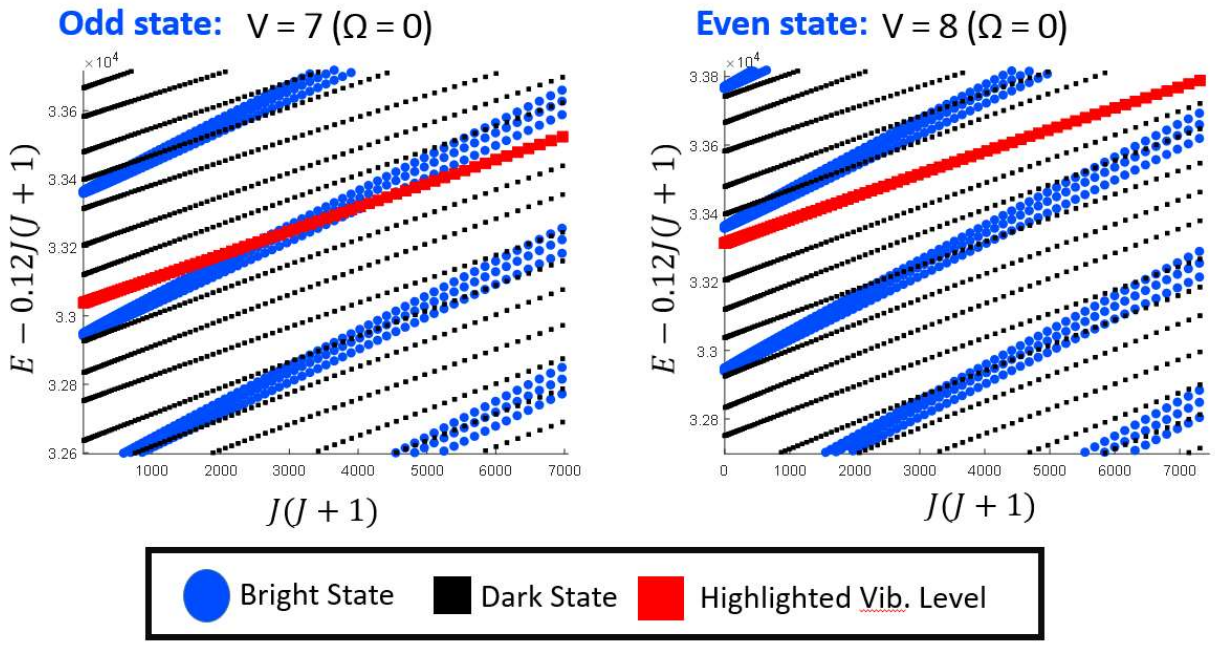

Figure 5-5: The B", f-symmetry, $\Omega = 0$ component of Figure 5-3. The numbers above or below each bar represent the vibrational quantum numbers. Note both the widespread, systematic bias towards 3232 and the even/odd alternation in the isotope effect.

The difference between the two is quite significant: the B" $v_{B"} = 7$ state crosses the B ($v_B = 3$) state at approximately $J = 20$, whereas the B" $v_{B'} = 8$ state does not cross the B state until very high levels of J.

5.3. v = 7 e/f Symmetry Comparison: The Effect of State-Mixing on Fractionation in B" Ω = 0, v = 7

5.3.1 The e-Symmetry Fractionation Behavior

We now must explore the *mechanism*, i.e. why does this low-J crossing cause a substantial isotope effect? At this point in the analysis, it is worthwhile to explore the differences in behavior between the e symmetry and f symmetry components of the B" $\Omega = 0$ states. The e symmetry B" $\Omega = 0$ $S_{v,e,p}(3236) - S_{v,e,p}(3232)$ plot is shown in Figure 5-6. Note that the scale of this plot is the same as in Figure 5-4.

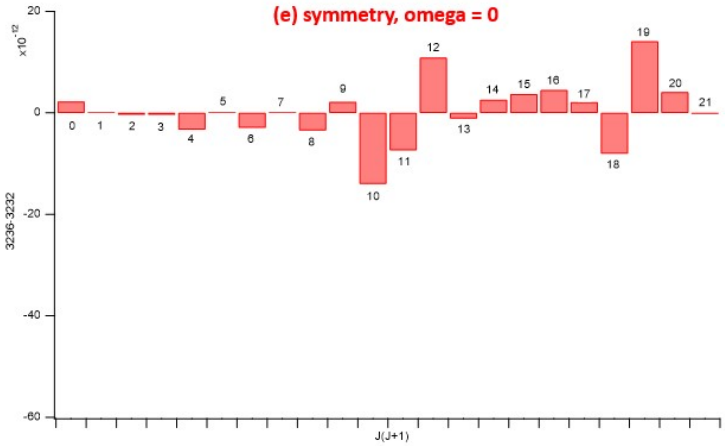

Figure 5-6: The B", **e-symmetry**, $\Omega = 0$ component of Figure 5-3. The numbers, again, represent the vibrational states. This graph is shown on the same scale as is Figure 5-4 (f-symmetry states), revealing a greatly diminished isotope effect. Furthermore, the systematic patterns are less pronounced here than for the f-symmetry states.

The e-symmetry vibrational states exhibit an isotope effect that is greatly reduced in magnitude, compared to their corresponding f-parity vibrational levels. Additionally, the pronounced even/odd alternation observed over the vast majority of f-symmetry levels, is not present.

5.3.2. State-Mixing of the e and f Symmetry Components of $\Omega = 0, v = 7$.

The large difference in behavior between the e symmetry and f symmetry components of the B" $\Omega = 0$ state is due to state-mixing with the B state. Figures 5-7a-b depict the structure of the B/B" perturbations. As we noted in Chapter 3, the B state has term symbol $^3\Sigma_u^-$, and consequently, each vibrational state has three rotational progressions (named: F_1, F_2, and F_3). Two of the progressions (F_1 and F_3) have e symmetry and mixed $\Omega = 0$ and $\Omega = 1$ character[17], while the third (F_2) is f symmetry and $\Omega = 1$. There is, however, no f symmetry, $\Omega = 0$ component of the B state. This is very important because the major $\Delta\Omega = 0$ B/B" perturbation matrix elements originate from a different portion of the effective Hamiltonian than do the $\Delta\Omega = 1$ B/B" perturbations. The former are termed "homogeneous perturbations"

[17]The $\Omega = 0$ and $\Omega = 1$ spin-orbit character is mixed by the S-uncoupling portion of the rotational Hamiltonian.

and the latter, “heterogeneous.” The homogeneous matrix elements, which originate from both the spin-orbit and rotational Hamiltonian, are given by Equation 5.3.

$$< B, \Omega{=}0| \hat{H}_{SO} + \hat{H}_{ROT} |B'', \Omega{=}0> = <B, 0| \left(\frac{1}{2}A + B\right)(\hat{L}_+\hat{S}_- + \hat{L}_-\hat{S}_+) |B'', 0>, \quad (5.3)$$

where A and B are the spin-orbit and rotational constants, respectively (see Chapter 3 for more details). And $\hat{L}_+, \hat{S}_-$, etc. are raising and lowering operators associated with orbital and spin angular momentum, respectively. The heterogeneous matrix originate solely from the rotational Hamiltonian; they are given by Equation 5.4.

$$< B, \Omega{=}1| \hat{H}_{ROT} |B'', \Omega{=}0> = <B, 1| - B(\hat{J}_+\hat{L}_- + \hat{J}_-\hat{L}_+) |B'', 0> \quad (5.4)$$

For the interaction between the v = 7, B” state and the v = 4, B state, the homogeneous matrix element is 21.37 cm^{-1}, whereas the heterogeneous matrix element (which has an explicit J dependence) is only 0.084 cm^{-1} at $J = 20$. This is a difference of over 2 orders of magnitude.

Figures 5-7a and 5-7b depict the level structure of an $\Omega = 0$, B” state interacting with a B state. The size of the perturbations is reflected in the size of the rectangles connecting the B and B” states.

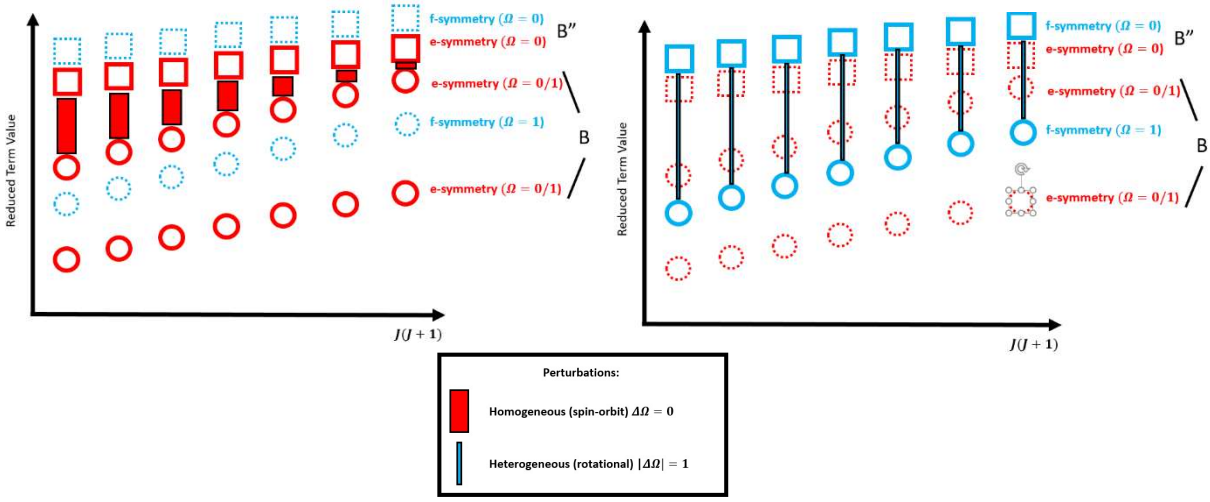

Figure 5-7a (left): highlights the interactions between the e symmetry B and B” states. The perturbations are large (red rectangles) due to a homogeneous, spin-orbit interaction. In **Figure 5-7b (right):** we see the perturbations between the f symmetry B and B” states. They are small (blue rectangles) due to a heterogeneous, rotational interaction.

Figure 5-8 shows the effect of the homogeneous interaction on the mixed B/B" character of the e symmetry B" $v = 7$ state (the rotational progression) with the crossing at $J = 20$. Both 3232 and 3236 are shown relative to their corresponding B state F_3 component (the branch with the highest energy). Also shown (in pink) is the equilibrium Boltzmann rotational state distribution at 300 K.

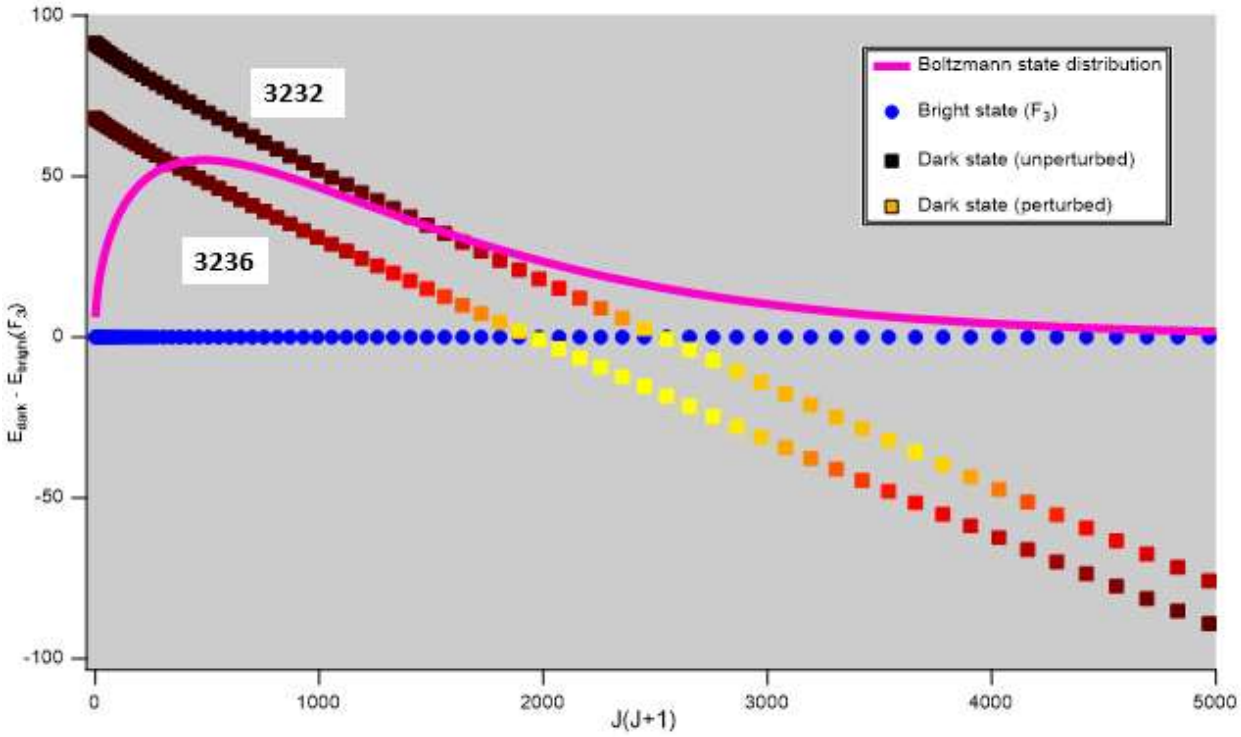

Figure 5-8: shows the effect of the homogeneous interaction on the mixed B/B" character of the e symmetry B" $\Omega = 0$ v = 7 state. Two isotopologues (3236 and 3232) are depicted, their energies calculated relative to the F_3 component of their respective B v = 4 state (blue dots). To facilitate the visual comparison, I have added in the 3232 states that do not actually exist, due to nuclear permutation symmetry considerations (see chapter 2). The black squares show relatively unperturbed states (B" character greater than 90%), the red, orange, and yellow squares represent increasingly perturbed states (up to ~50%). Due to vibrational level shifts caused by an increased mass, 3236 crosses its B v= 4 state at lower J than does 3232. This level shift hints at a possible origin for the pseudo mass-dependent isotope effect observed in Figure 5-2. The pink line shows the B" Boltzmann equilibrium rotational state distribution. It is clear that, in the 3232 case, the population statistically samples more "dark" B"-character rotational states, than it does the 3236 case.

5.3.3. Why a Difference in Excited State Lifetime Does Not Cause Fractionation in the e Symmetry States

The plot shows, for 3232, the B" population samples rotational states with more B" "dark" state character than does 3236. The average fluorescence lifetime of a 3232 state, therefore, ought to be larger than that for 3236. Figure 5-9 shows that, indeed, this is what I observe.

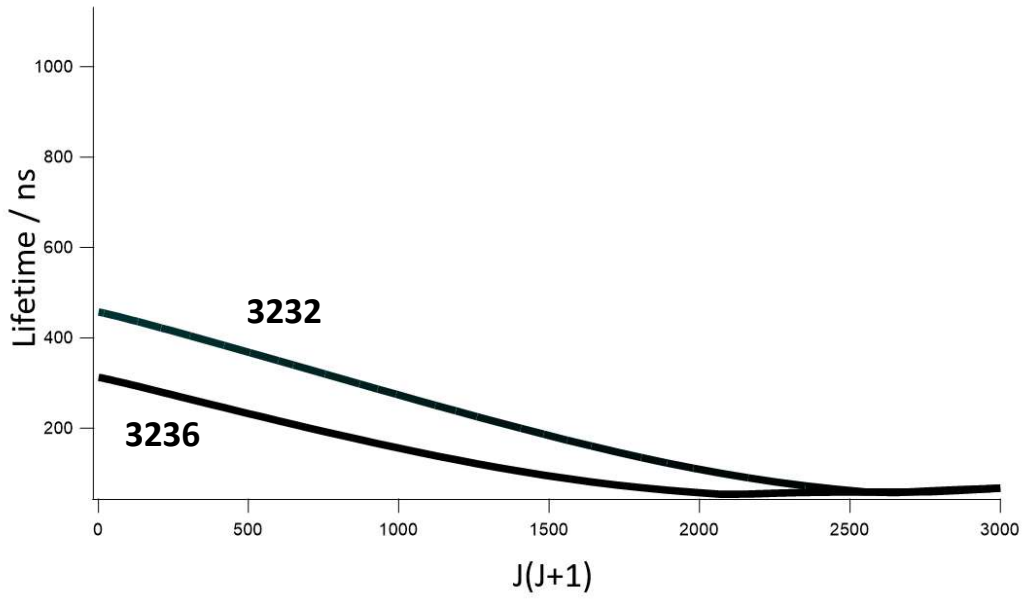

Figure 5-9: The lifetimes of the 3232 isotopologue (e symmetry, B", $\Omega = 0$, v = 7 vibronic state), compared to the lifetime for the same vibronic state of the 3236 isotopologue, as a function of J(J+1). The lifetimes decline as the states mix increasingly with the F_3 component of the e symmetry, B, F_3, v = 3 state. Due to vibrational level shifts, the lifetime at J = 1 for is approximately 50% larger for 3232 compared to 3236. However, observe that the lifetimes are both relatively low compared to the natural lifetime of the B" state (~4200 ns).

However, as I have previously noted, the e-symmetry states do not generate an isotope effect. I must therefore account for the fact that a ~50% difference in average lifetime does not translate into an appreciable effect. To do so, I consider a simple system, consisting of a single excited electronic state (e) and multiple ground electronic states ($g, v = 0,1,2$ ...). Rotational levels are ignored here, as they do not change the overall analysis but do complicate the mathematics. This system is depicted in Figure 5-10, where k_{abs} and k_{fl} are the absorption and the *total* fluorescence rate constants, respectively. The rate constant, k_{fl}, is the sum of the fluorescence rates to individual vibrational levels ($k_{v=0} + k_{v=1} + \cdots$). This hypothetical system reflects the nature of the B/B"-X system. Due to Boltzmann statistics,

absorption almost exclusively (96%) occurs out of the v = 0 state of the X electronic state, but the molecule then fluoresces to multiple vibrational levels, determined by the distribution of Franck-Condon factors. I now consider population flow between the excited state [e] and the ground vibrational states, referred to collectively as [g].

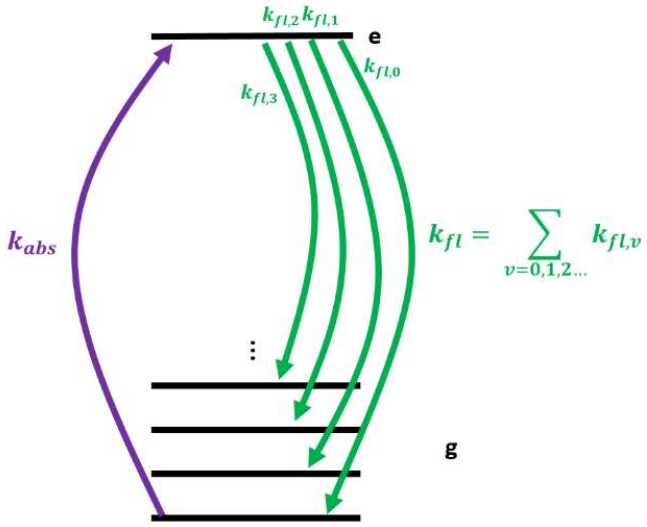

Figure 5-10: A hypothetical system consisting of one excited vibronic state, and multiple vibrational levels (v = 0,1,2 ...) of the ground state. Due to Boltzmann statistics, the absorption only occurs out of the ground vibrational state. However, the fluorescence occurs to multiple states.

The two-level system of differential equations is given by Equations 5.5a and 5.5b

$$\frac{d[e]}{dt} = k_{abs}[g] - k_{fl}[e] \tag{5.5a}$$

$$\frac{d[g]}{dt} = -k_{abs}[g] + k_{fl}[e]. \tag{5.5b}$$

These equations can be trivially solved to obtain $[e](t)$ and $[g](t)$. The solutions are given as Equation 5.6, for initial condition $[g](0) = p_g$ and $[e](0) = 0$ (i.e. all population is initially in the ground state).

$$\begin{bmatrix} g(t) \\ e(t) \end{bmatrix} = p_g \begin{bmatrix} \frac{k_{fl}}{k_{abs}+k_{fl}} \\ \frac{k_{abs}}{k_{abs}+k_{fl}} \end{bmatrix} + p_g \begin{bmatrix} \frac{k_{abs}}{k_{abs}+k_{fl}} \\ -\frac{k_{abs}}{k_{abs}+k_{fl}} \end{bmatrix} e^{-(k_{abs}+k_{fl})t} \tag{5.6}$$

Because the system is closed (see: Chapter 4), it has a steady state ($t \rightarrow \infty$) solution. I concern myself here with the steady state solution for the excited state $[e]$. Due to the relatively weak radiation density of the sun, I have $k_{abs} \ll k_{fl}$, and, therefore, Equation 5.7

$$[e](steady\ state) \approx p_g \frac{k_{abs}}{k_{fl}}. \tag{5.7}$$

As noted in Chapter 4, $k_{abs} = B_{g,v=0\rightarrow e}\rho(\nu, T)$, and $k_{fl} = \sum_v \mathrm{A}_{e\rightarrow g,v}$, where A and B are, again, the Einstein A and B coefficients. I can rewrite Equation 5.7 as follows (Equation 5.8)

$$[e](ss) \approx \frac{B_{g,v=0\rightarrow e}\rho(\nu, T)}{\sum_v \mathrm{A}_{e\rightarrow g,v}}. \tag{5.8}$$

Upon substitution of the expressions for the Einstein coefficients, I obtain Equation 5.9 (again, ignoring rotational states)

$$[e](ss) \approx \frac{\rho(\nu, T)\frac{2\pi^2}{3\epsilon_0 h^2}|R_e|^2 q_{e-g,v=0}}{\frac{16\pi^3|R_e|^2}{3\epsilon_0 hc^3}\sum_v {\upsilon_{e-g,v}}^3 q_{e-g,v}}. \tag{5.9}$$

This reduces to Equation 5.10

$$[e](ss) \approx \frac{c^3}{8\pi^3 h}\frac{\rho(\nu, T)q_{e-g,v=0}}{\sum_v {\upsilon_{e-g,v}}^3 q_{e-g,v}}. \tag{5.10}$$

First, note that, due to the ~31000 cm^{-1} difference in energy between the X and B/B" states, the quantities ${\upsilon_{e-g,v}}^3$ and $\rho(\nu, T)$ do not change significantly with the small, isotopologue-dependent vibrational level shifts. Most importantly, however, note that the $|R_e|^2$ terms cancel in Equation 5.10. For the B state, I calculate $|R_e|^2 = 1.89$ Debye. For the B" state, I calculate $|R_e|^2 = 0.0243$ Debye. In other words, the two-orders-of-magnitude difference in absorption rate and in fluorescence lifetime between primarily dark states and primarily bright states is due to the electronic component of the transition dipole moment. The cancelation of the $|R_e|^2$ terms indicates that the lifetime of the excited state is irrelevant to

excited state population at steady state. The faster the absorption rate, the faster the fluorescence rate.[18] The 50% difference in lifetime between 3232 and 3236 observed in B", $\Omega = 0, v = 7$ does not, therefore, translate to a large isotope effect.

5.3.4. Aside: The Rate of Convergence to Steady State

Equation 5.6 has another noteworthy feature: the rate at which $[e]$ and $[g]$ reach steady state. This rate is determined by the $e^{-(k_{abs}+k_{fl})t}$ term, where the characteristic time at which the system reaches equilibrium is the *sum* of the absorption and fluoresce rates. Although the rate of absorption driven by UV radiation from the sun is very slow (largest absorption rate to any B/B" rovibrational state $\approx 5 * 10^{-4}\ s^{-1}$), the fluorescence rate is quite fast ($3.1 * 10^{7}\ s^{-1}$ for the B state, $2.4 * 10^{5}\ s^{-1}$ for the B" state). Therefore, the steady state, equilibrium solution is reached in tens to thousands of nanoseconds. For the ground electronic state, at 300K and 1atm, the rate for the $S_2(X) + S + M \rightarrow S_3 + M$ reaction is approximately $6 * 10^{-15}\ s^{-1}$. Though the rate for the $S_2(B/B") + S + M \rightarrow S_3 + M$ is unknown, I will assume, for the remainder of this thesis, that the rate of the reaction is slow, compared to the rate of fluorescence, and, therefore, steady state is achieved between the X and $B/B"$ states. For this assumption

[18] This is somewhat of an oversimplification. In reality, the electronic transition dipole moment of an eigenstate of the B/B" system is a linear combination of the B and B" state electronic transition dipole moment. However, the general point holds: the higher the rate of absorption, the higher the rate of fluorescence.

to be invalid, the excited state reaction rate must be greater than 19 orders of magnitude larger than the ground state reaction rate.

5.3.5. State-Mixing in the f symmetry state

We return now to my comparison of the $B'', \Omega = 0, v = 7$, e and f symmetry states, having established the absence of an e symmetry isotope effect. I now continue and compare the structure of the f symmetry manifold to the previous discussion of e symmetry. Figure 5-11 shows the interaction between the f-symmetry states and the B state. As in Figure 5-8, the energy levels for both 3232 and 3236 are shown relative to the F_3 component of the $v = 3$, B state. While the overall structure is similar to the e symmetry states, the perturbations matrix elements are much weaker, due to the heterogeneous, l-

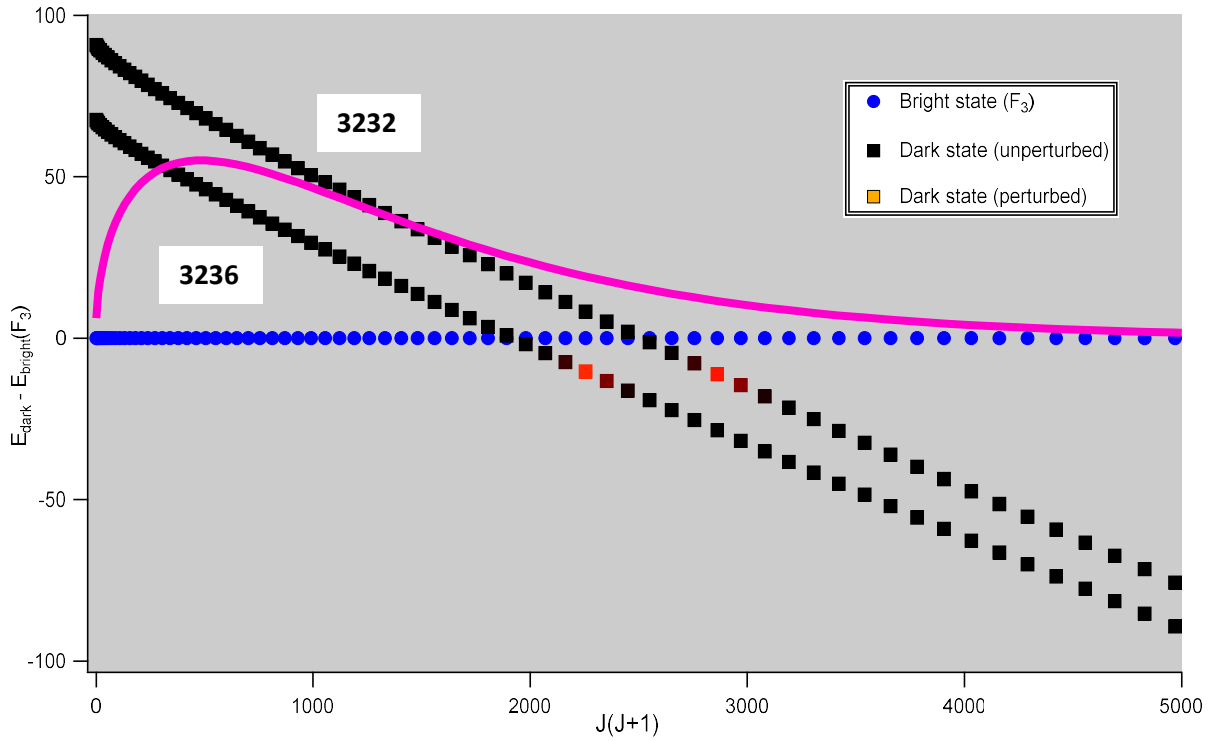

Figure 5-11: shows the effect of heterogeneous perturbations on the interaction between the f symmetry $B'', \Omega = 0, v = 7$ state and the $B, v = 3$ state. As in Figure 5-8, the energies of the 3232 and 3236 states are shown relative to the F_3component of the $B, v = 3$ state, and the pink line shows the B" Boltzmann distribution. The state-mixing (shown on the same color scale as Figure 5-8) is much weaker than for the e symmetry components. The f symmetry ensemble samples rotational states with far greater B" character than does the e symmetry ensemble.

uncoupling interaction that originate from the rotational Hamiltonian. Consequently, the Boltzmann distribution (shown in pink) samples states with a far higher degree of dark state character.

It is now important to note that excited state lifetime is a very non-linear function of the mixing fraction between the B and B" state. I can represent an eigenstate ($|\Psi>$) of the B/B" Hamiltonian as a linear combination of the B state ($|\psi_B>$) and the B" state ($|\psi_{B"}>$) follows in Equation 5.11

$$|\Psi> = \alpha|\psi_B> + \beta|\psi_{B"}>. \tag{5.11}$$

where $\alpha = \sqrt{1-\beta}$ and represents the fraction of B state character, and β represents the B" state fraction.

The characteristic lifetime of an electronic state (τ) is simply the inverse of the Einstein A coefficient (Equation 5.12)

$$\tau = \frac{1}{A}\,. \tag{5.12}$$

If I account for mixed B/B" character, as well as the natural lifetimes of the B and B" states, I obtain Equation 5.13

$$\tau = \frac{1}{(1-\beta)\left(\frac{1}{32\,ns}\right) + \beta\left(\frac{1}{4200\,ns}\right)}. \tag{5.13}$$

This equation is plotted, as a function of β, in Figure 5-12.

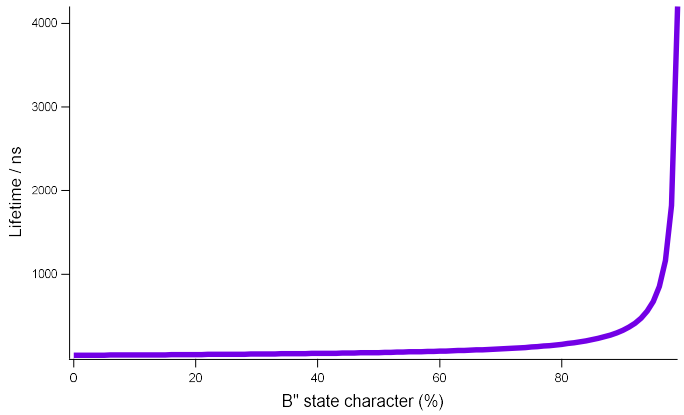

Figure 5-12: Excited state lifetime as a function of B" state character. The highly nonlinear behavior, as a function of state-mixing, is key to this analysis. As an example, the lifetime at 99% B" is 1824 ns, and 100% is 4200 ns, a nearly 250% increase.

5.3.6 The "Safe-Zone" Mechanism for Isotope Fractionation

This highly nonlinear behavior, where the lifetime does not increase substantially until very high values of β, is key to my analysis. Figure 5-13 shows a comparison of the B" character of the e symmetry state versus the B" character of the f symmetry state, for both 3232 and 3236, as a function of $J(J+1)$.

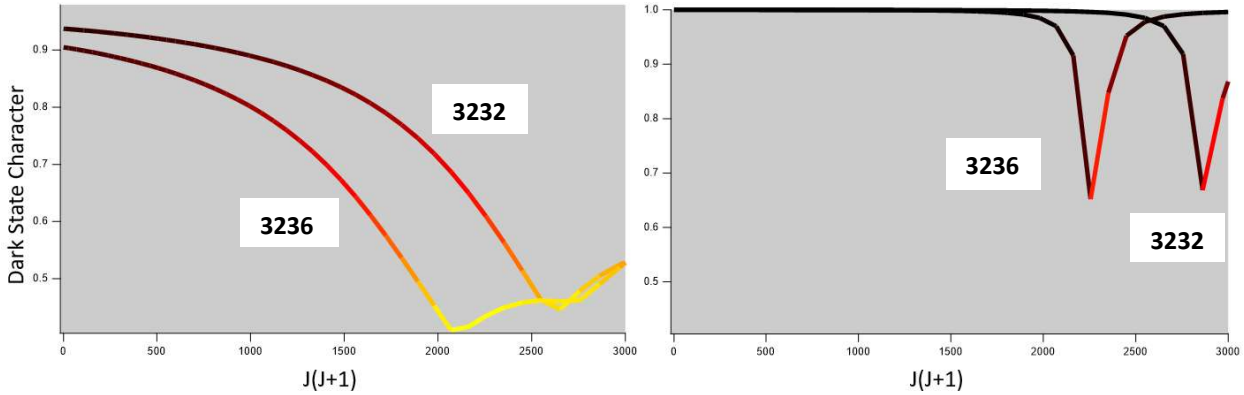

Figure 5-13: For 3232 and 3236, a comparison of the B" state character (state-mixing) of the v = 7, $\Omega = 0$ e symmetry states (left) and f symmetry states (right). Note, in particular, for f symmetry, the large regions of high B" character, followed by small, but highly perturbed regions. The color of the lines show the extent of the perturbations; they progress from black (low perturbation) to red to orange to yellow (high perturbation).

There is a large, important contrast between the two plots. The e symmetry states have a maximum dark state character of ~90%, and, therefore, have a very large region of high state-mixing. In other words, the e symmetry states never leave the "flat region" on the left of Figure 5-12. The f symmetry states have a large region with $\beta > 0.99$, followed by a shorter region with large state-mixing. These states *do* leave the flat region and sample the long-lifetime region of Figure 5-12. To make this more explicit, the lifetime of these states, as a function of J(J+1) is shown in Figure 5-14.

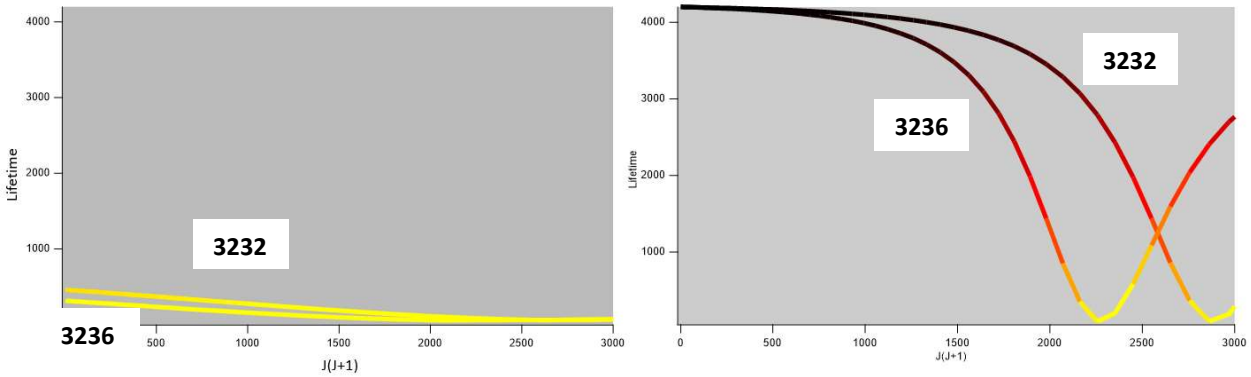

Figure 5-14: For 3232 and 3236, a comparison of the **excited state lifetime** of the v = 7, $\Omega = 0$ e symmetry states (left) and f symmetry states (right). The differences between the two symmetries are stark, as the e symmetry lifetimes do not exceed 400 ns, and, more importantly, do not change much as a function of J(J+1). Conversely, the lifetimes of the f symmetry states have a large region with lifetimes greater than 4000 ns, followed by a sharp decline in lifetime as the B" state crosses the B state.

This figure shows a large disparity between the behavior of the e symmetry and f symmetry states. For the e symmetry states, the lifetimes are consistently low (200-400 ns), and, crucially, **do not change much as a function of $J(J+1)$**. For the f symmetry states, the lifetimes are very high (>4000 ns) at low J and decline very sharply around J = 20-30. I note, again, that the f symmetry states show a strong isotope effect with ($f_{ex}(3232) > f_{ex}(3236)$), this suggests a "safe-zone" mechanism for isotopic fractionation. A cartoon illustrating this fractionation mechanism is shown in Figure 5-15.

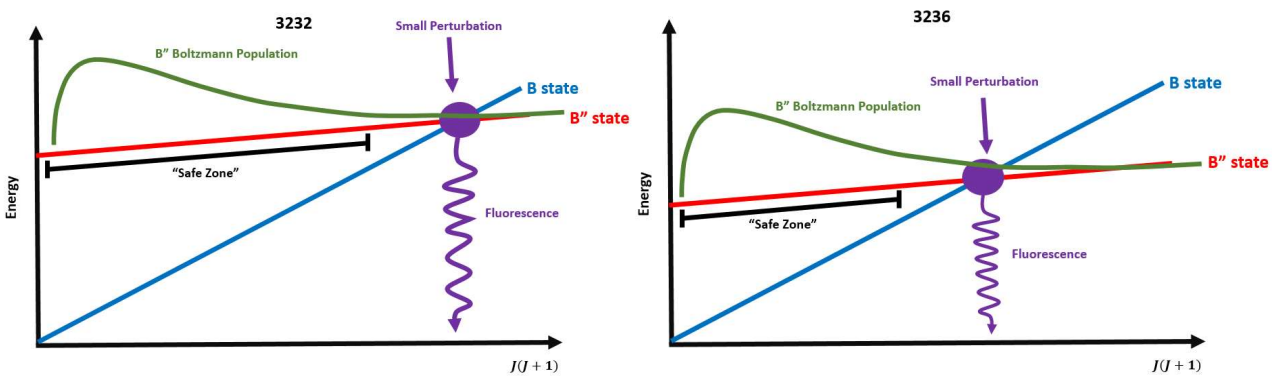

Figure 5-15: The proposed "safe zone" mechanism for isotopic fractionation in the B", $\Omega = 0$, v = 7, f symmetry states. The weak, heterogeneous perturbations create a "safe zone" of long lifetime states. Because the B" state crosses the B state earlier in 3236, than 3236, the population has a lower propensity for being collisionally transferred outside of the safe zone.

In words, the mechanism operates as follows. First, I observe that, despite its "dark" character, the B" state has a similar population to the "bright" B state, because the $|R_e|^2$ terms cancel in the steady state expression (recall Equation 10 from Section 5.3.3.). This population is collisionally scattered around the B" rotational levels in a Boltzmann probability distribution (green curve). This population primarily samples the "safe zone", states with very high lifetimes ($\tau > 4000\, ns$), but population will occasionally undergo a random walk into the small perturbed region, where the probability of "leaking" down to the ground state is much higher. Because, in 3236, the B" state crosses the B state at a smaller value of J than it does in 3232, its "safe zone" is smaller, i.e. the perturbed rotational states are sampled with a higher propensity. This mechanism mirrors the "leaky bucket" mechanism I used in Section 3.5 to describe the Gelbart-Freed model for electronically inelastic transitions.

5.4. Broader Conclusions for the entire B/B" System

While I have only discussed a single B/B" crossing, there are a number of broader conclusions to draw:

5.4.1 Rotationally inelastic collisions can drive perturbation-based isotope effects

In the mechanism described in Figure 5-15, the crucial point is not that the average excited state lifetime is lower for 3236 than for 3232, as that is compensated by a greater degree of excitation from the

ground state (Equation 5.10). Instead, it is that population can be moved, via rotationally inelastic collisions, from a "safe-zone" state to a "leaky" state. This "flow" from high lifetime to low lifetime states generates the isotope effect. This concept of diffusion to a leak will be vital to my discussion of statistical isotope effects in Chapter 6.

5.4.2 Weak perturbations generate larger isotope effects than do strong perturbations

This is seen most clearly in Figure 5-14. For the strongly-perturbed e symmetry states, there is very little change in the lifetime ("leakiness") as a function of J. Therefore, the "safe-zone" mechanism is much less effective for e symmetry states than for the weakly state-mixed f symmetry states. The difference in behavior is due to the highly nonlinear relationship between B/B" mixing fraction and lifetime seen in Figure 12. In my discussion of Figure 5-2, I noted that the $B", \Omega = 0$, f symmetry states were responsible for creating the systematic isotope effect in the B/B" system. Returning to Figure 5-2, note especially that the $\Omega = 1$ e and f symmetry states do not generate isotope effects. This is because the B $^3\Sigma_u^-$ $\Omega = 1$ states have both e and f symmetry components, and, therefore, both the e and f B" states are strongly perturbed by the homogeneous spin-orbit interactions (see Equation 5.3, Section 5.3.2.).

5.4.3. The isotope effect shows systematic patterns over multiple energy levels because the energy levels have systematic patterns.

This heading may seem almost tautological, but it is important for the broader conclusions at the end of this chapter. I observed in Figures 5-3 and 5-4 that the fractionation pattern favors lighter isotopologues over a wide range of odd v B" vibrational levels. It is clear from my analysis that the "safe-zone" mechanism for isotopic fractionation favors lighter isotopologues over heavier isotopologues because the B" state crosses the B state from above. This type of crossing occurs because the B" state has a softer potential well. It therefore has a larger equilibrium bond distance, and this makes the B" state

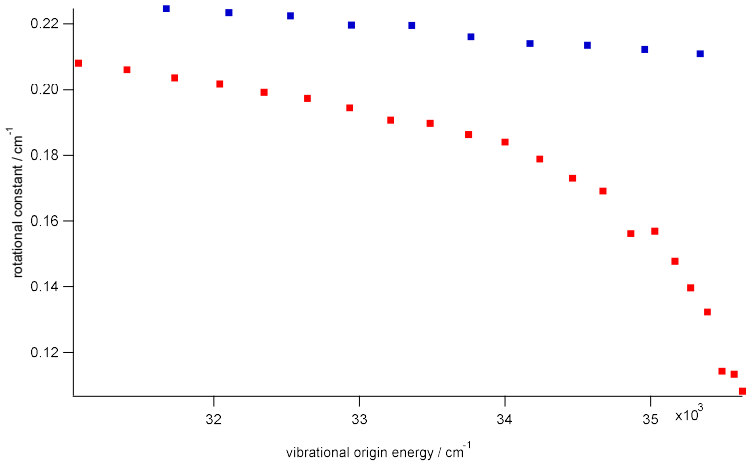

Figure 5-16: The rotational constants for the B vibrational levels (blue) and the B" vibrational levels (red), as a function of vibrational origin energy. Due to the larger equilibrium bond distance, the rotational constants are always smaller in the case of B". This creates a systemic isotope effect favoring 3232.

rotational constants consistently smaller than the B state rotational constants (Figure 5-16). Were this trend reversed, if the B state had the softer well and the B" states crossed the B state from below, the isotope effect would favor more population in heavier isotopes, at steady state.

Additionally, I observed, in Figures 5-3 and 5-4, an even/odd alternation in vibrational quantum number, wherein odd vibrational states exhibited a large isotope effect and even vibrational states exhibited none. The reason for this alternation is seen in Figure 5-17, which shows the vibrational energy level spacing ($E(v_{i+1}) - E(v_i)$) as a function of vibrational energy level, $E(v_i)$. For the $B"$ vibrational states with the strongest isotope effect (roughly $v = 5 - 15$), the average energy level spacing is 229 cm^{-1}. For the B states with similar $E(v_i)$ (roughly $v = 2 - 8$) the average energy level spacing is 402 cm^{-1}.

This nearly 2:1 ratio creates the even/odd alternation in isotope effect. For the odd states (like B" v = 7 in Figure 5-5), the vibrational origin for the B" state origin starts just above the vibrational origin of its corresponding B state. Due its smaller rotational constant, the B" state then crosses the B state at relatively low J. Conversely, for the even states (like B" v = 8 in Figure 5-5), the B" state starts just below the corresponding B state, and doesn't cross the B state until around J = 80 (a region with negligible Boltzmann population, compared to J = 20). This is also shown clearly in Figure 5-5.

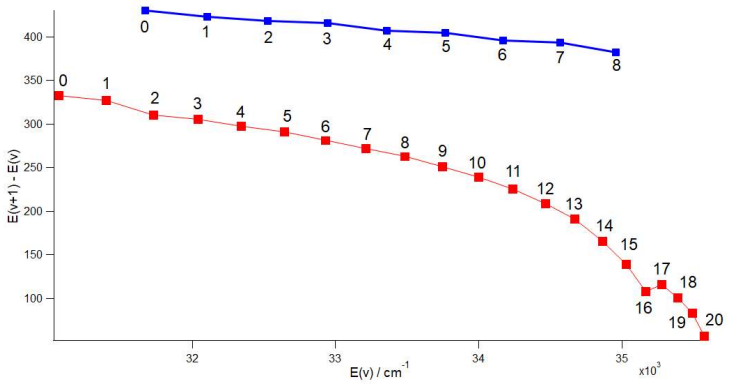

Figure 5-17: The vibrational energy level spacing (roughly ω_e), as a function of $E(v_i)$. In particular, note that the B" vibrational states with $v = 5 - 15$ (the region with the most pronounced isotope effect) have an average energy level spacing of 229 cm^{-1}. The B vibrational states with similar energies $(v = 2 - 8)$ have an average energy level spacing of 402 cm^{-1}.

5.4.4. Franck Condon factors determine the steady state behavior of the B/B" system

One lingering question from my analysis thus far: in Figure 5-4, why does the isotope effect seem larger, generally, for the vibrational levels in the center of the distribution$(i.e. v = 5 - 17)$, than they do at low or high values of v? Figure 5-18 juxtaposes a plot of isotope effects as a function of f-symmetry vibrational level with a plot of $v_X = 0 \rightarrow v_{B"} = x$ Franck Condon factors.

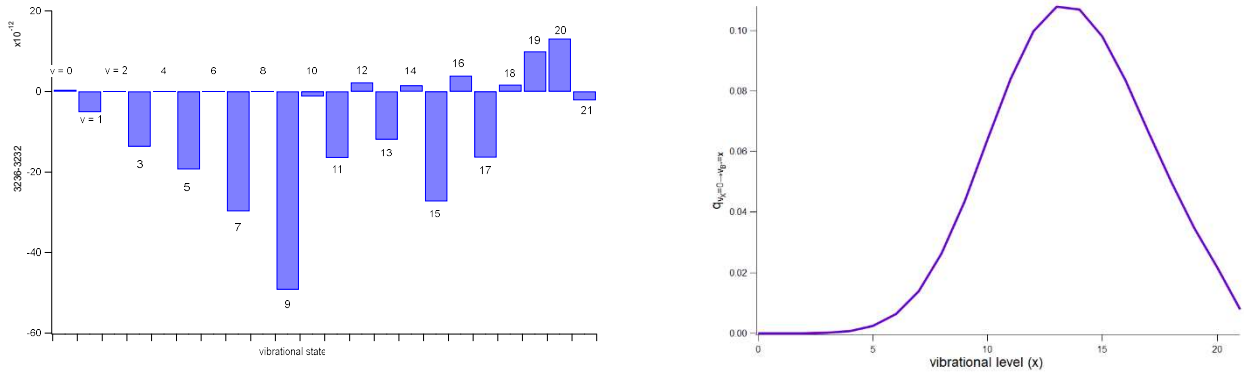

Figure 5-18: A comparison of the $v_x = 0 \rightarrow v_{B"} = x$ Franck-Condon factors (right) and the f symmetry isotope effect, as a function of vibrational (right). The left figure is identical to Figure 4.

Here, it can be seen that the B" Franck Condon factors (right) follow a very similar pattern to the odd-v isotope effect. Larger FC factors are toward the middle of the distribution, smaller ones at high v and at low v; this closely mirrors the magnitudes of the isotope effects (left), as a function of vibrational level. In effect, we can think of the B/B" system as a series of bright state/dark state crossings that are statistically weighted by the B" Franck Condon factors.

The cause of this correlation can be seen in Equation 5-10. While the electronic state character does not affect the steady state population of a given excited state (because darker states have both lower absorption and correspondingly lower fluorescence rates), the population is statistically weighted by the $v_x = 0 \rightarrow v_{B/B"} = x$ Franck-Condon factor. This is because absorption occurs primarily out of $v_X = 0$, while fluorescence occurs to a variety of X state vibrational levels (see Figure 12, section 5.3.3). Therefore, odd vibrational levels within the v = 5-15 states, which, coincidently, have the low J B/B" state crossings required to drive the overall behavior of the B/B"-X system.

The effect of the Franck Condon weights will be discussed further in chapter 8. For now, I will use them to answer one more question raised at the beginning of this chapter: why does the overall excited state population (f_{ex}) decrease as a function of pressure, as seen in Figure 1? Consider Figure 5-19, which shows the Franck Condon between $v_x = 0$ for the vibrational levels of the B and B" states, as a function of energy.

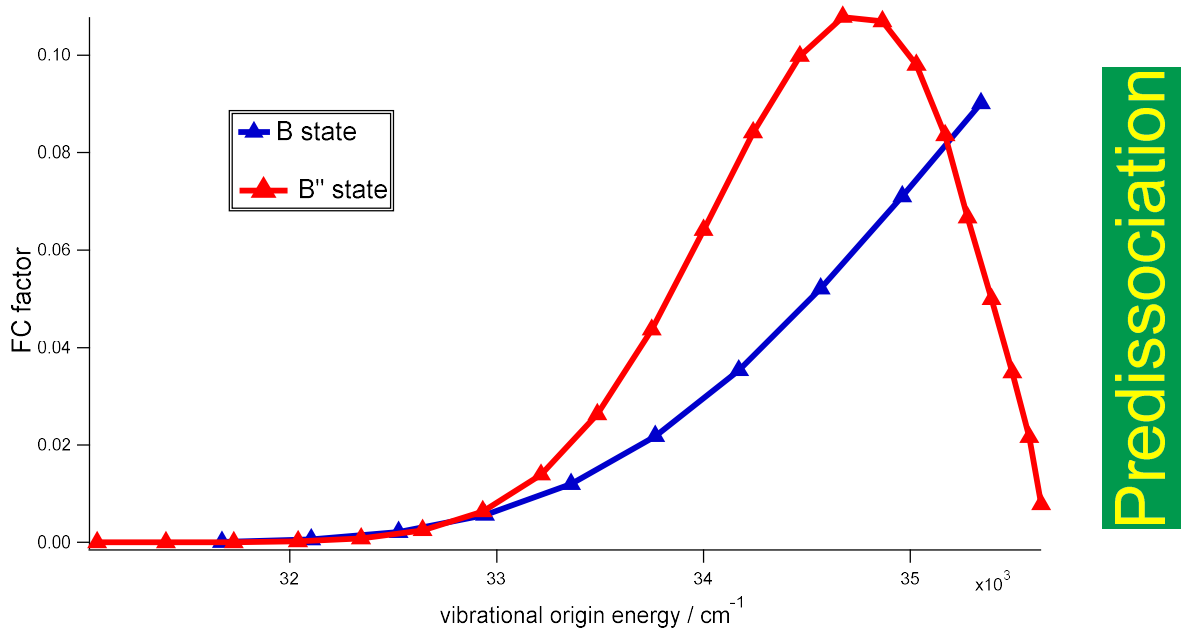

Figure 5-19: The Franck-Condon distributions, for absorption out of $v_x = 0$, as a function vibrational origin energy. Note that, for all B" vibrational levels from approximately $v_{B"} = 7$ to $v_{B"} = 16$, the B" Franck-Condon factor is substantially larger than the B Franck-Condon factor.

Figure 5-19 shows that, over the range of B" vibrational levels from $v_{B"} = 7$ to $v_{B"} = 16$, the B" Franck-Condon factors are larger than their B state counterparts. This discrepancy contributes to the overall behavior of the B/B" system. In my discussion of Figure 5-1, I observed that the excited state population declines as the pressure of the background gas (i.e. the pressure of the atmosphere) increases. Figure5- 20 is a cartoon showing how the steady state behavior of the system relates to these Franck-Condon factors.

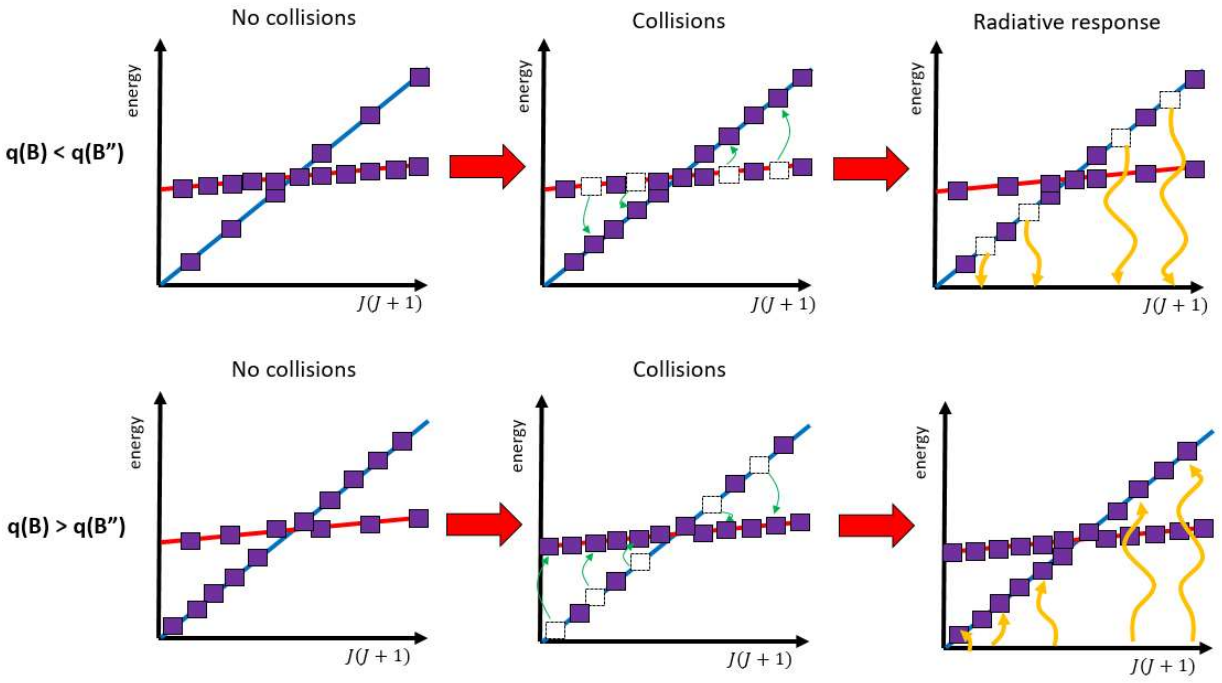

Figure 5-20: This cartoon illustrates the effect of the relative values of the B and B" state Franck-Condon factors for two vibrational levels involved in a curve crossing. The red line represents a B" state, the blue a B state. The purple squares represent an ensemble of population. The arrows represent a net flow of population. Collisional transfer is represented by green arrows, radiation is represented by yellow.

In Figure 5-20, the top three panels show the case where the B" FC factor is larger than the B FC factor. In the absence of collisions (top left), there is more population, at equilibrium, in the B" state, compared to the B state, due to its larger Franck Condon factor (Equation 5.10). The top central panel shows the effect of introducing collisions into the B/B" system. The overall rate constant for collisional transfer from B to B" is equal to that for transfer in the reverse direction. However, because there is greater population in B" compared to B, there is a *net* transfer from the B" state to the B state. This creates more total population in the B state than there was in the absence of collisions. Because the equilibrium between the B state and the X state is now perturbed, the B state fluoresces to reestablish this equilibrium (top right). Conversely, with q(B) > q(B") (bottom left) there is more population in the B state, compared to the B" state. When the collisions are introduced, there is a net flow of population from the B state into the B" state (bottom center), and the system reestablishes equilibrium via absorption of population from the X state to the B state (bottom right).

I have ignored one additional transfer process in this analysis. While I focused on the reestablishment of equilibrium between the X and the B state, equilibrium is also perturbed between the B" and X states, and the response of the system to reestablish this equilibrium counteracts the effects described in the previous paragraph. However, the reestablishment of equilibrium between the B" and X states occurs much more slowly than it does for the B and X states. This is due to the expression we derived in Equation 5.6, which shows that equilibrium in an B/B"-X two level system is established at a characteristic rate equal to the sum of the absorption and fluorescence rates. The absorption rate is much smaller than the fluorescence rate, so the equilibration rate is roughly equal to the fluorescence rate. Therefore, the much longer lifetime of the B" state implies a much slower establishment of equilibrium, compared to reestablishment of equilibrium in the B state. It is the latter process, then, that drives the overall behavior of the system.

In summary, I can explain the declining values of f_{ex} as a function of atmospheric pressure by noting the larger values of the B" FC factors relative to B FC factors, over a wide energy level range ($E \approx 33000\ cm^{-1} - 35000\ cm^{-1}$ of the B/B" system (see Figure 5-19).

5.5. Modeling the Fractionation Behavior of the S_2 B/B"-X System in the Atmosphere

5.5.1. Introduction to the Model

It is very important to note, at this point, that while my analysis of the B/B"-X system has yielded insight, it thus far does not reflect a complete picture of excited state S_2 in the Earth's atmosphere. To give a more complete picture, I introduce a few additional features:

(1) Predissociation: At this point, I open the B/B" system (see: Chapter 4). That is, I allow predissociation from rotational states with $v_B \leq 9$ and $v_{B"} \leq 21$, but energies above the $35{,}999\ cm^{-1}$ predissociation limit. Additionally, I allow predissociation via absorption to $v_B \geq 10$ and $v_{B"} \geq 22$ vibrational states.

(2) Chemistry: I also include a hypothetical chemical reaction that moves excited state S_2 (S_2*) toward the rock record. As an example, I have Equation 5.14[19]

$$S_2^* + S + M \rightarrow S_3 + M. \tag{5.14}$$

For ground state S_2, at atmospheric pressure, the reaction has a rate constant $\sim 10^{-1}\ \ s^{-1}$. I postulate that the reaction will happen much faster for excited state S_2^*. In this calculation, I use a rate constant $= \ 1 * 10^{-10}\ s^{-1}$, and assume that the rate is identical for any reaction B/B" rovibrational state. The value of the rate constant is arbitrary, but the behavior will be identical, as long as the rate of the chemical reaction is slow compared to the quantum mechanical processes (absorption/fluorescence and collisional transfer).

(3) Atmospheric profile for temperature and pressure: To make this calculation as reflective of the Earth's atmosphere as possible, I calculate the quantity of S_2 undergoing a chemical reaction as a function of height in the atmosphere. The pressure of the atmosphere decreases as the exponential function given in Equation 5.15 [97].

$$P(h) = (1\ atm)e^{-\frac{h}{7.4\ km}} \tag{5.15}$$

where h is the height in the atmosphere in km. and P(h) is the atmospheric pressure in atmospheres. Similarly, temperature is also a function of height in the atmosphere, though the relationship is somewhat more complex (Equation 5.16)

$$T(h) = \begin{cases} 288\ K - \left(9.76\frac{K}{km}\right)h & for\ h = 0 - 10\ km \\ 200\ K & for\ \ h = 10 - 30\ km\,. \end{cases} \tag{5.16}$$

[19] The reaction in Equation 5.14, is not the only possibility. The excited state S_2 adsorbs directly onto an elemental sulfur aerosol, as another example.

The first portion of Equation 5.16 represents the declining temperature in the troposphere due to convection. The second portion of equation represents the tropopause, an inversion layer between the troposphere and the stratosphere, where temperature is roughly constant [97].

(4) More isotopologues included in the calculation. While the S-32 isotopologues (32-32, 32-33, 32-34, 32-36) are the most relevant for calculating the $^{33}\Delta$ and $^{36}\Delta$ parameters, the S-34 isotopologues (34-33, 34-34, and 34-36) have a smaller, but significant impact (~5%).

5.5.2. The Time Dependent Behavior of This Open System

Because the system to be solved is now open, I must now solve the system of differential equations as a function of time, using the matrix exponential method described in Chapter 4. The time data is in Figure 5-21.

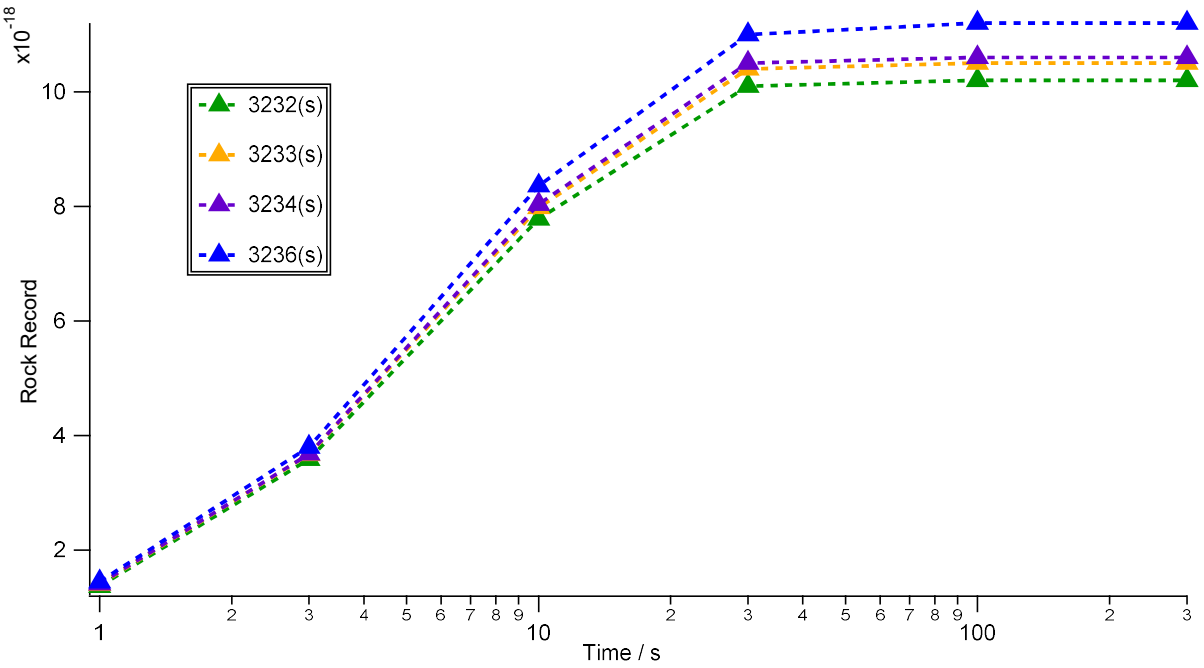

Figure 5-21: Amount of S_2 undergoing a chemical reaction, as a function of time (log scale). Note that all isotopologues are calculated assuming Bose-Einstein statistics for nuclear permutation symmetry, i.e. half of all energy levels are missing.(This speeds the calculation without losing the general principle discussed in the text).

This figure depicts a consistent pattern of behavior for all isotopologues. As time progresses, the amount of sulfur stored in the rock record increases. It increases at slightly different rates for each of the four isotopologues. In contrast to our earlier system, which excluded predissociation, in this system, the rocks are most enriched in S-36, followed by the lighter isotopes in order. This process continues for about 30 s, until all S_2 predissociates.[20]

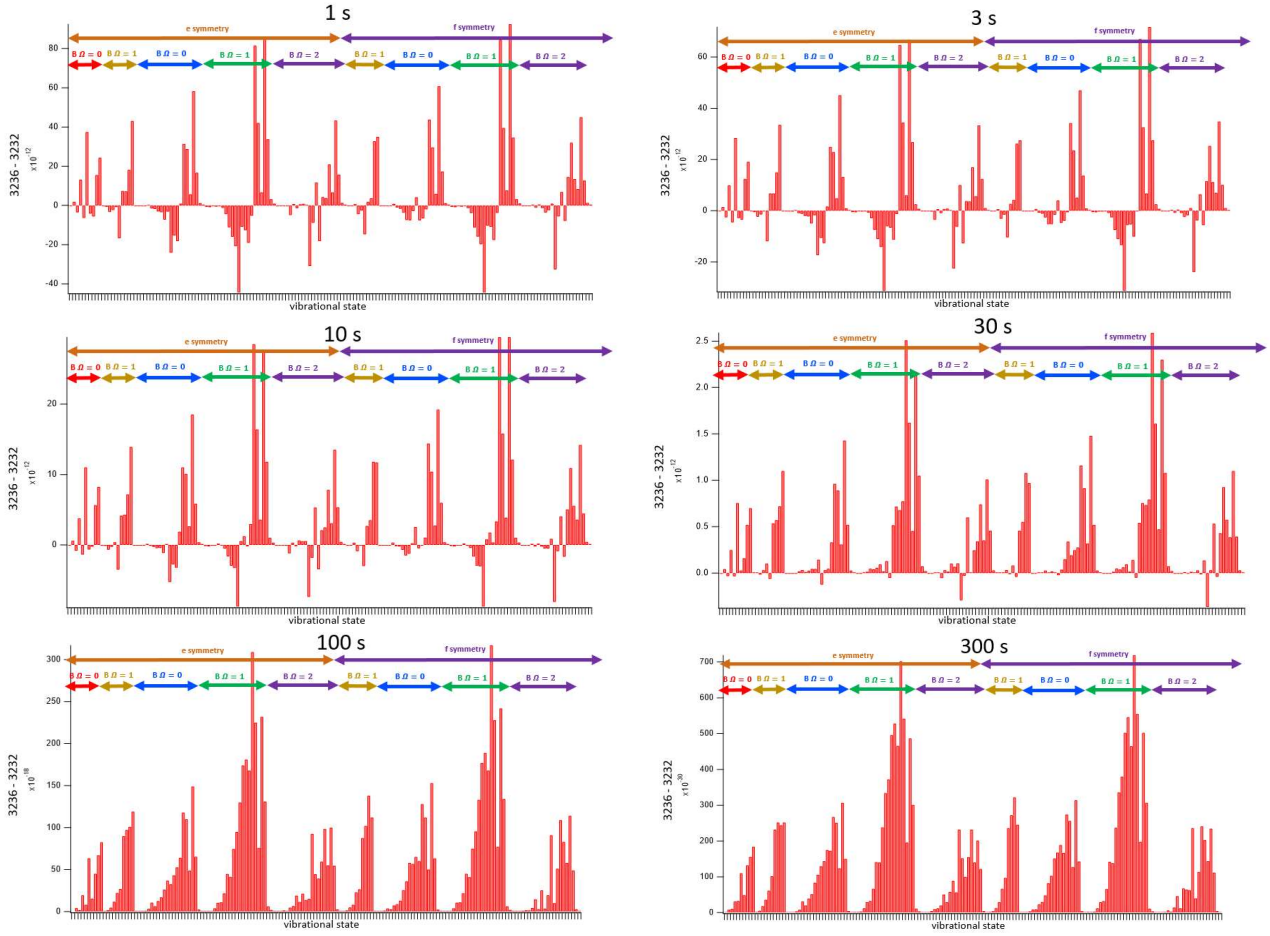

Figure 5-22: For our new predissociating, chemically reactive system, this figure shows the isotopic fractionation (reacted sulfur for 3236 minus 3232) for each vibrational state, similar to Figure 5-4. Each panel, from top left to bottom right, shows how the fractionation changes this time, from one second elapsed to 300 seconds elapsed. The colored arrows show the sorting of the vibrational states, by electronic state (B/B"), spin orbit state (Ω), and e/f symmetry. Within each category, the vibrational states are sorted from $v = 0$ to $v = 21$.

[20] In reality, some S_2 re-forms due to the reaction $S + S + M \rightarrow S_2$. However, this reaction occurs very slowly compared to this quantum mechanical dissociation process, so I ignore it in this analysis.

To understand the mechanism for this isotopic fractionation, consider Figure 5-22. This Figure is similar to Figure 5-4 – it shows isotopic fractionation (3236 – 3232) as a function of vibrational level. Each frame shows how this fractionation changes as a function of time.

5.5.3 Fractionation Behavior of the Predissociating System

At the earliest time, 1 second, Figure 5-22 shows a variety of fractionation patterns, some favoring 3236 (the positive values are generally at higher v's), and some favoring 3232 (the negative values are generally at lower v's). Most importantly, and unlike the non-predisscociating states in our previous discussion, this pattern manifests for *both* electronic states, for *both* e/f symmetries, and for *all* spin-orbit components. As time moves forward, this pattern gets more pronounced and encompasses more lower v vibrational states, until, eventually, every vibrational level is fractionated in favor of the higher mass 3236. I can interpret this pattern in the following way (Figure 5-23).

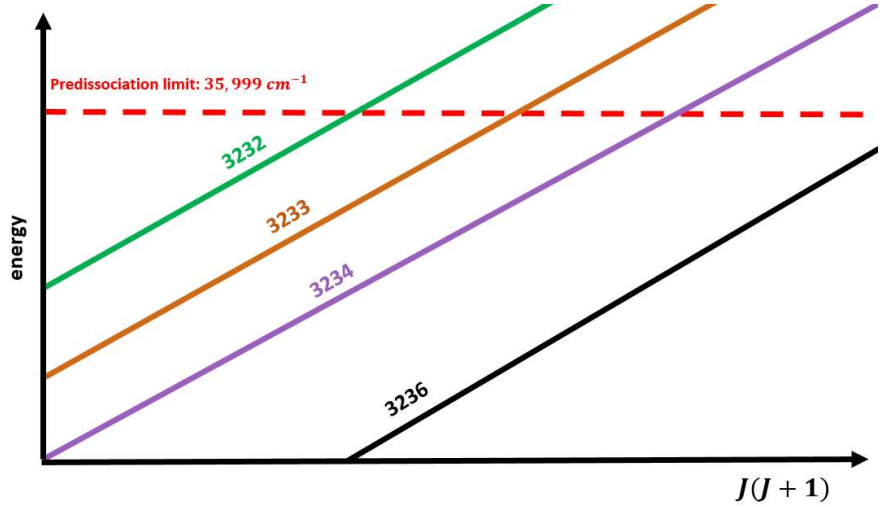

Figure 5-23: A cartoon that illustrates the fractionation mechanism for this predissociating system. The predissoication limit is set here as 35,599 cm^{-1} (red dashed line). Because predissociation is caused by a crossing between a bound state and a repulsive state, the predissociation limit does not change with isotopologue, as repulsive states do not possess vibrational levels. The bound rotational state progressions, represented here by colored, solid lines do change, as usual; they move lower in energy as reduced mass increases.

The predissociation limit, as seen in Figure 5-23, is not a function of reduced mass, because predissociation is caused by interactions between a bound state and a repulsive state. This repulsive state, by definition, does not have vibrational levels that can shift with reduced mass. The bound vibrational states, however, can shift. Thus, the lighter isotopologues cross the predissociation limit at lower rotational quantum number than do the heavier isotopologues. This is similar to the "safe zone" mechanism described for the previous model. In this case, however, a larger "safe-zone" protects the population from predissociation into S + S, rather than fluorescence to the ground state of S_2.

This mechanism explains the universality of the isotope effect over all symmetries, electronic states, and spin-orbit components, as all rovibrational levels above the $35{,}999\ cm^{-1}$ limit predissociate. It also explains the increasing preponderance of the isotope effect over time. As more of the molecule predissociates, there is less available to chemically react and to be stored in the rock record. The complete results of the atmospheric, predissociation model, as a function of pressure, are shown in Figure 5-24.

This plot shows a similar pattern to the simplified, steady-state model in Figure 1: the isotope effect is more pronounced at higher pressures than at lower pressures, because increasing the pressure increases the rate at which population is transferred into the predissociating states. But, most notably, the data is ordered by mass, with the lightest isotope at the bottom and heaviest at the top. And while the mechanism, and mass ordering, is different, this plot seems to indicate another "pseudo mass-dependent" relationship. We can see this more clearly in Figure 5-25, which shows the quantity reacted at 1 atm versus the reduced mass of each of the seven isotopologues. While the correlation is positive instead of negative, the linear regression again reveals a nearly linear relationship ($R^2 = 96\%$), indicating pseudo

mass-dependent behavior. **Predissociation, therefore, is not likely to be the origin of the S-MIF signature in the rock record.**

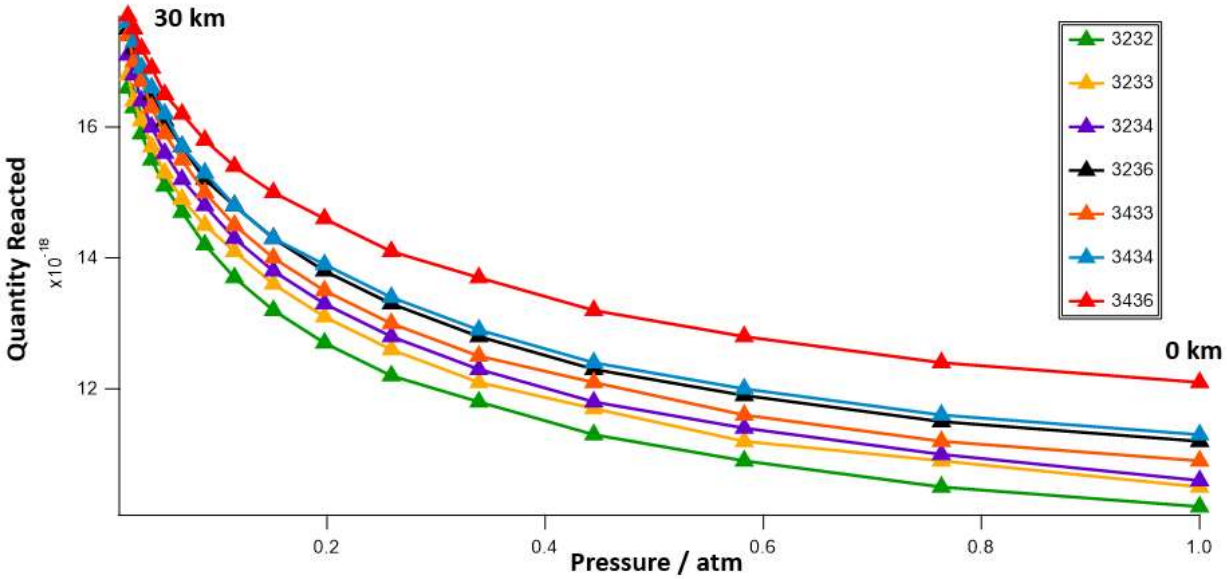

Figure 5-24: The results of the atmospheric, predissociation model described in this section. All 32 and 34 isotopes are shown. Each data pointrepresents a height in the atmosphere. The leftmost state was calculated at 30 km, each subsequent data point calculated 2 km lower, reaching 0 km at the rightmost point.

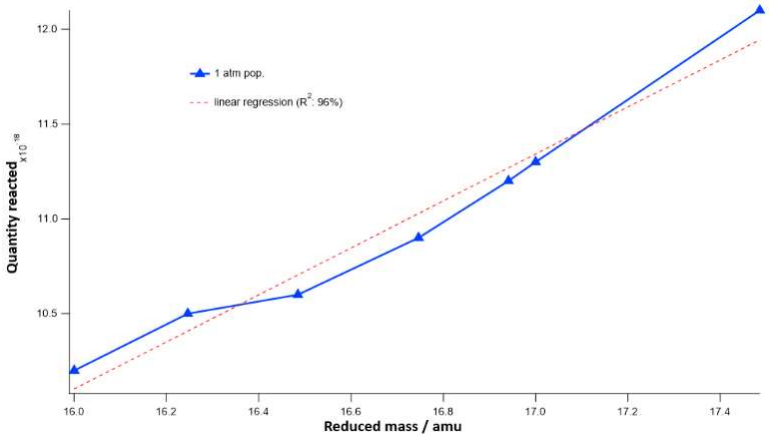

Figure 5-25: For our predissociating model, this plot shows the quantity reacted at 1 atm (dependent axis) as a function of reduced mass for all 7 isotopologues . The dashed red line shows a linear regression. The R^2 value is 96%, indicating a mostly, but not exclusively mass dependent relationship.

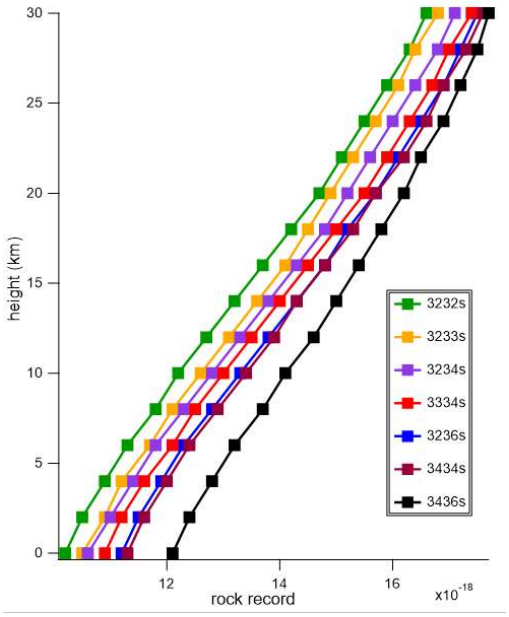

Figure 5-26: Quantity reacted for each isotopologue, as a function of height in the atmosphere.

5.5.4. Fractionation Behavior of S_2 in the Atmosphere

To see this more clearly, consider Figure 5-26, which directly shows the quantity reacted for each isotopologue, as a function of height in the atmosphere. This plot shows that, due to varying pressure (and, to a far lesser extent, temperature), the magnitude of the isotope effect can change significantly with the height in the atmosphere at which it was generated. In particular, the larger isotope effects are generated closer to the ground, due to the larger number of inelastic collisions available.

I now use the data to project what the S-MIF fractionation would look like if this predissociation mechanism was the sole source of the isotope effect in the atmosphere. This projection is shown in Figure 5-27.

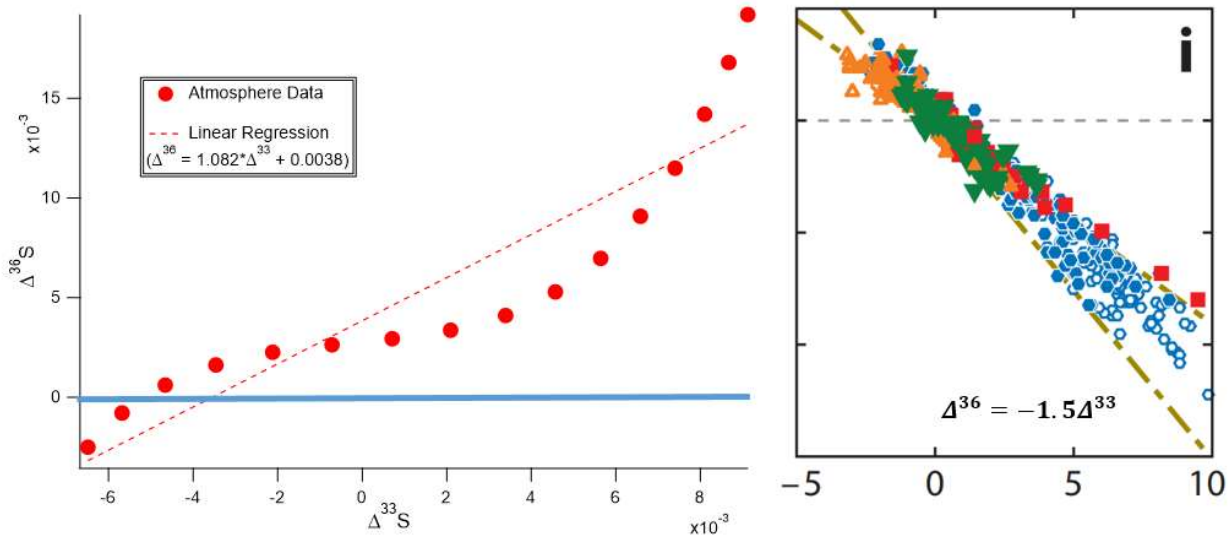

Figure 5-27: Δ^{36} S vs Δ^{33} S shown for the data in Figure 5-26. The red circles represent rocks formed from sulfur that reacted at different heights in the atmosphere. The dashed line represents a linear regression performed on this simulated data ($\Delta^{36} = 1.08\Delta^{33}$). The other figure (right), is from Ono, et. al. (2017) *[26]*, which represents the actual rock samples that constitute the Archean Reference Array. The different colors in the Ono figure represent rock samples gathered at different locations. For this real data, the linear regression is $\Delta^{36} \approx -1.5\Delta^{33}$.

Figure 5-27 shows that the isotope effect generated by the predissociation mechanism does not match the Archean Record Array. The magnitude of the isotope effect is too small compared to the rock record, and the correlation is positive as opposed to negative.

5.6 Conclusions thus far and next steps

In a limited sense, this chapter has failed in its goal of providing a plausible explanation for the Archean Reference Array. Neither collisional transfer mechanism that included the predissociation, nor the one that ignored it could reproduce the pattern shown in the rock record. Because both relied on mechanisms where curve crossings would shift with reduced mass, they both generated pseudo mass dependent isotope effects. However, I have reached a number of conclusions, which will guide my analysis in the next three chapters.

(1a) Small perturbations generate larger isotope effects than do large perturbations. We saw this most clearly in our analysis of B" $\Omega = 0$ e symmetry and f symmetry states, where the f

symmetry states had perturbation matrix elements ~1% of those for e symmetry states. This leads to a corollary:

(1b) Western's deperturbation of the B/B" system, while extremely extensive, is incomplete for my purposes. If perturbations on the order of only 0.01 cm^{-1}drive isotope effects, then it may be the case that *even weaker* perturbations may generate *even larger* isotope effects. Western's model was, fundamentally, an energy level fit model. In such a model, B/B" perturbations are included only if they substantially improve the calculated energy levels, relative to the empirically observed ones. Therefore, the smaller perturbations are least likely to be included, even though they may be the most significant for the purposes of this work.

(2) In the real B/B" system, described in this chapter, the missing states for homonuclear S_2 (i.e. 32-32 and 34-34), do not seem to influence the overall isotopic fractionation trends. This is congruent with my proposed mechanisms in the predissociating and non-predissociating case, as both involve curve crossings that shift in a mass-dependent manner. I note here that the B/B" perturbations span over many rotational levels. Returning to Figure 5-14, even for the weakly perturbed f-symmetry states, there still remains a region of approximately ~6 rotational states, where the lifetime of these states is less than 1000 ns. Therefore, even if half of the rotational levels are missing, there is still a significant region of rotational state space where the B" state "leaks" to the ground state, thereby retaining the expected pseudo-mass dependent fractionation mechanism. This is another argument in favor of weaker perturbations. If the "leaky" regions could be reduced to spanning a single rotational state, mass-*independent* mechanisms may come into play. This idea will be the focus of Chapter 6.

(3) As described in Chapter 1, the experiments that analyze isotopic fractionation for gas-phase SO_2 involve absorption of broadband UV radiation, followed by isotopic analysis of the resulting elemental sulfur that precipitates out of the gas phase. This process, as I discussed, cannot provide insight into the mechanism by which the isotopic fractionation occurs. For example, it has been

assumed that the $\widetilde{C}$ state generates a mass-*independent* pattern when absorbing radiation from ~220-190 nm due to predissociation. **The results presented in this chapter call that interpretation into question**. I would expect that, if the $\widetilde{C}$ state fractionation mechanism was dominated by predissociation, we would observe a largely mass-*dependent* effect. There may be some other, potentially very weak, interaction responsible.

These three observations lead to a single conclusion: understanding weak perturbations is essential to understanding isotopic fractionation. This perhaps reduces the prospects of using experiments (which are far better at observing large perturbations) to determine the fractionation mechanism. However, I will proceed, in Chapter 6, by artificially reducing both the homogeneous and heterogeneous perturbations in the B/B" system. While this artificial system will no longer reflect the empirical studies of Green and Western, it is now doubtful that the perturbations contained in their model can completely describe the fractionation behavior of the B-X system. There may be other, weakly perturbing electronic states that are important to this discussion. The objective of chapter 6, therefore, will be to obtain deeper insight into the collisional transfer fractionation mechanism using these weaker perturbations.

Chapter 6 : Statistical Isotope Effects in Weakly Perturbed Systems

Abstract: At the end of Chapter 5, I hypothesized that weak state-mixings have a larger potential to generate significant fractionation patterns than do strong state-mixings. Therefore, I examine a "weak perturbation" model in which the perturbation matrix elements are set to 1% of Green and Western's original values. I propose that, if the state-mixing J-regions are small enough, the fractionation may have a statistical component, i.e. the doorways can be treated as occurring randomly. Here, I derive a simple statistical doorway model that predicts the following: homonuclear S_2 (missing rotational states) and heteronuclear S_2 (all rotational states) would have the same ensemble, limiting behavior if there were an infinite number of B/B" vibronic level crossings. However, because the asymmetric isotopologues have twice the number of rotational states, they require fewer inelastic collisions to converge to this limiting behavior, and they, therefore, converge at lower pressures. The "weak perturbation" model ***does*** generate S-MIF. Through comparison with a control model, I show that the additional states partially homogenize the behavior of the three asymmetric isotopologues, as predicted. This makes the isotope effect more similar to the Archean Reference Array, though significant discrepancies remain. Additionally, there is significant evidence of non-statistical effects in the "weak perturbation" model. These effects are analyzed in Chapter 7.

6.1 Introduction: Why Consider a Weak Perturbation Model?

In this chapter, and continuing into chapter 7, I will consider a model in which the perturbation matrix elements that connect the B and B" states are artificially set to 1% of the values given by Green and Western. This artificial model ***does not*** **reflect the physical reality of the B/B"-X system**. However, it is extremely useful to consider because the physical models (both predissociating and non-predissociating) produce isotope effects that approximate sulfur mass *dependent* fractionation (S-MDF), while the Archean Reference Array displays mass *independent* fractionation (S-MIF). In this introduction, I briefly consider how the patterns of B/B" interactions are fundamentally different in this new model (which I will term the "weak perturbation model"), compared to those considered in the previous chapter (i.e. the "strong perturbation models"). Additionally, I consider how this difference might create S-MIF patterns in the weakly perturbed system.

Fundamentally, the B/B" state mixing that is created by an off-diagonal matrix element can be estimated using second-order, non-degenerate, time-independent perturbation theory. For the strong perturbation model, this second order expression is given by Equation 6.1:

$$m_{B/B"}(strong) = \frac{|\widehat{H}_{B/B"}|^2}{\Delta E}. \quad (6.1)$$

where $m_{B/B"}$ is the state-mixing fraction, ΔE is the difference in energy between the *diabatic* (i.e. unperturbed) B and B" states, and $\widehat{H}_{B/B"}$ is the off diagonal matrix element, the perturbation that connects the two states, as tabulated by Green and Western. For the weak perturbation model, I use Equation 6.2

$$m_{B/B"}(weak) = \frac{|0.01\widehat{H}_{B/B"}|^2}{\Delta E}. \quad (6.2)$$

I now graph, in Figure 6-1, the $m_{B/B"}$, as a function of ΔE, for both the strong perturbation case and the weak perturbation case.

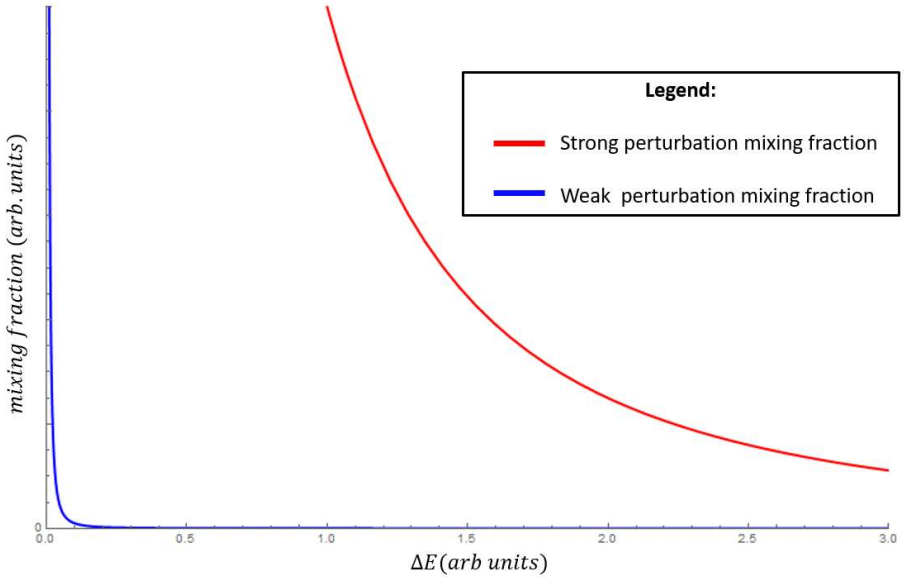

Figure 6-1: The B/B" state-mixing fractions, predicted by second-order non-degenerate perturbation theory (Equations 1 and 2), as a function of ΔE for both the strong perturbation model (Chapter 5), and the weak perturbation model considered in this chapter.

Figure 6-1 makes clear that the energy gap required to induce significant B/B" mixing is much smaller in the weak perturbation model, compared to the strong perturbation model. This simple idea has large ramifications for the behavior of the weak perturbation model relative to the model considered in Chapter 5. This difference in relative behavior is depicted in a cartoon (Figure 6-2).

As Figure 6-2 shows, there is a fundamental difference in behavior between the strong perturbation and the weak perturbation models. In the strong perturbation case, many rotational levels are significantly state-mixed, and an isotope-dependent, vibrational level shift simply changes which rotational levels are perturbed, in a mass-dependent way. In Figure 6-2, as the crossing shifts downward, rotational states with smaller-rotational quantum numbers are perturbed correspondingly. This type of

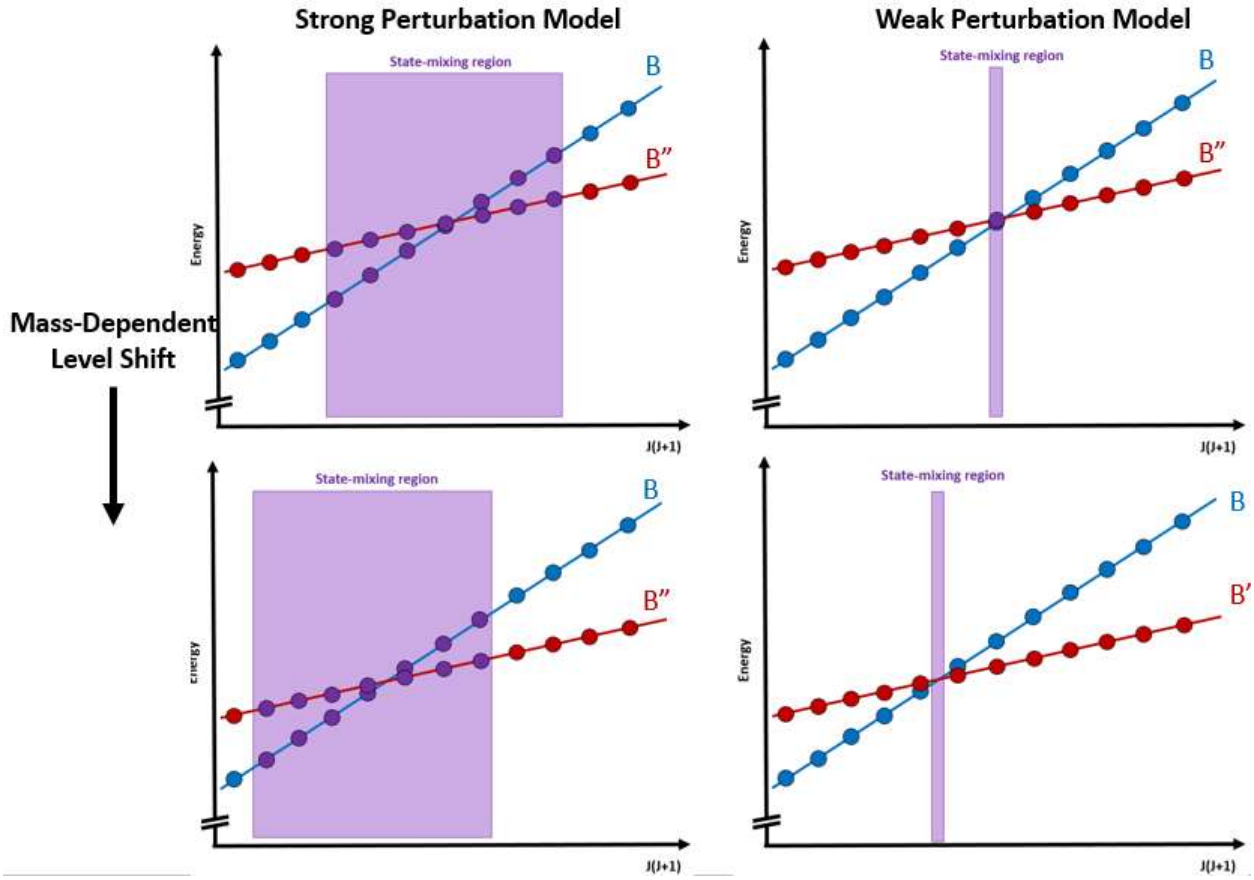

Figure 6-2: gives a justification for study of the weak perturbation model, even though it does not match the physical reality of the B/B" system. Each panel shows a hypothetical B/B" vibronic level crossing, where each circle represents a rotational quantum state. The left column illustrates a strong perturbation model, while the right column illustrates a weak perturbation model, where the purple rectangles represent a region where the B and B" states can be considered significantly state-mixed. The bottom two panels show the effect of the vibrational level shifts (i.e. a change in isotopologue) on this crossing. In the strong-perturbation case, the behavior is systematic. In the top panel, many rotational levels are perturbed. As the level crossing shifts to lower J's, the state-mixing region shifts correspondingly and lower-J states are perturbed. In the weak perturbation case, a vibrational level shift may cause a perturbed region to go unsampled the small doorway region. The difference of this "quantum sampling" behavior, compared to the level-shift behavior discussed in the pervious chapter, will be the focus of this Chapter's analysis.

systematic interaction was discussed at length in the previous chapter. However, the weak perturbation model may behave very differently. If the state-mixing region is small enough, the rotational quantum states may "sample" the perturbed region for one isotopologue but not another. In such a case, I hypothesize, the patterns of perturbations may behave in a *statistical* fashion.

The potential for statistical behavior is relevant to my discussion of S-MIF. Specifically, and as discussed in Chapter 1, the S-MIF pattern in the Archean reference array can be approximated using the following relation: $[36]/[36]_n \approx [34]/[34]_n \approx [33]/[33]_n > [32]/[32]_n$. In other words, the rock sample is enriched in the three rare isotopes, compared to S-32. This is significant because the three rare isotopes come primarily from asymmetric isotopologues, i.e. 32-36, 32-34, and 32-33, while the most abundant isotope, S-32, comes primarily from 32-32, a symmetric isotopologue.

As discussed in Chapter 2, the three asymmetric isotopolgues have a fundamental statistical difference from the symmetric isotopologues: they have twice as many rotational quantum states than 32-32. This Chapter, then, explores whether a statistical explanation for S-MIF in the rock record is plausible. It is important to note at the outset: the behavior of the weak perturbation is *not truly statistical*. It is, ultimately, determined by systematic mathematical patterns (i.e. Equations 1-2, and the level shift patterns discussed in Chapter 2, Section 2.3). The non-statistical aspects of the weak-perturbation model are important, and will be analyzed in Chapter 7.

This chapter will demonstrate that, although the limiting, ensemble behavior of the asymmetric and the symmetric isotopologues is the same, the number of inelastic collisions required to reach that limit is different, and that this difference can generate S-MIF.

6.2 The importance of total parity in symmetric vs. asymmetric comparisons.

The characterization of asymmetric S_2 isotopologues as simply having twice as many rotational states than symmetric S_2, while technically true, ignores one important complication. As discussed in Chapter 2, the symmetric isotopologue, 32-32, has only rotational states with (-) total parity. By contrast, asymmetric isotopologues have two manifolds of rotational states, one with (-) parity and one with (+)

parity. Crucially, collisions *cannot* switch between states with two different parities (see section: 3.3). This is illustrated in Figure 6-3.

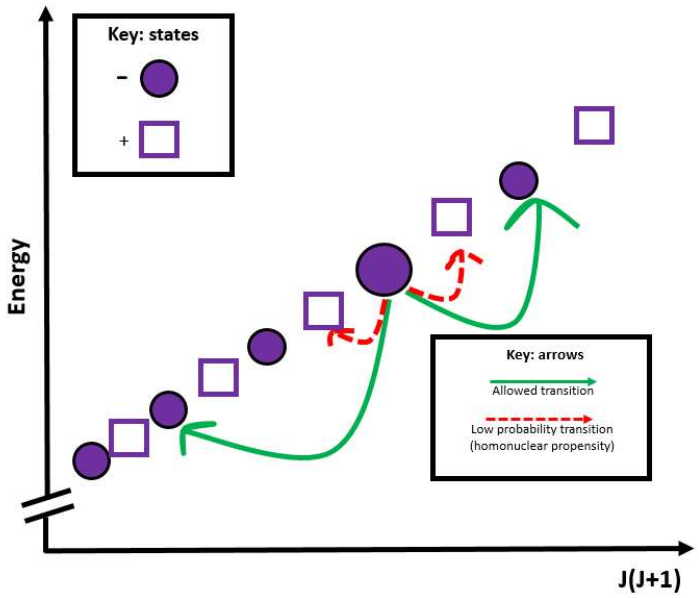

Figure 6-3: A cartoon depicting a single e/f symmetry component of a Hund's case (a), B" state. The (+) parity states and the (-) parity states alternate with J. In this model, collisions cause cannot transfer from (-) to (+) and vice versa.

This figure shows that, for a given rotational state progression, the total parity alternates back and forth with rotational quantum number, J. Therefore, I have two different, independent rotational state manifolds that occupy similar, but not entirely identical perturbation environments. Each of these manifolds contains approximately half of the total excited state population.

My hypothesized mechanism for fractionation utilizes *doorway-mediated* collisional transfer between the short-lifetime B state and the long-lifetime B" state. In this mechanism, the highly mixed states (the purple states in Figure 6-2) act as "doorways" between the B and B" diabatic electronic states. In other words, population in a B doorway state has a significant chance to be collisionally transferred into a B" state and vice versa. In the weak perturbation model, it may be possible that some isotopologues "sample" a doorway, while others do not. Isotopologues that sample the perturbed, doorway regions may collisionally transfer more population into long lifetime B" states. These isotopologues would have a

longer average excited state lifetime, and may more readily undergo excited state chemistry, thereby resulting in preservation of this isotopologue enrichment in the rock record.

6.3 Modeling a doorway-mediated mechanism:

To analyze the ability of a statistical doorway mechanism to generate S-MIF, I create two simple models, one for the symmetric case and one for the asymmetric case. For the symmetric model, an excited state molecule is created at time $t = 0$. This excited electronic state exists in a particular rotational state s_i, within a manifold of rotational states $s_1, s_2 \ldots$ When the molecule is created at $t = 0$, a random integer integer, n, between 1 and 1000 is also selected. This represents the distance, in number of rotational states, that this excited state must walk to reach a doorway state. Once the doorway state is reached, the molecule is "stored" in the other electronic state, from which it does not leave.[21] Finally, I introduce an excited state lifetime τ_{ex}. This introduces a "time limit". If a molecule does not reach a doorway state before it fluoresces, it is not stored in the long lifetime state.

I can model the competition between rotational wandering and fluorescence using a system of differential equations. I will let $k_{fl} = {}^{1}/_{\tau_{ex}}$ be the first-order rate constant for fluorescence out of the excited state. I will also postulate a total collision rate, Z. Here, a single collision has 50% probability of transferring population from $s_i \; to \; s_{i-1}$ and 50% probability of transferring population from $s_i \; to \; s_{i+1}$. For this hypothetical random walk, the number of collisions required to transfer population a distance of n states is n^2. The rate of transfer from the initial state to a doorway state that is n states distance is thus ${}^{Z}/_{n^2}$. Letting [ex] be the population of this entire excited state manifold and [D] be the population that

[21] This model can work two different ways. It could represent transfer from a bright state to a large manifold of dark states, from which it never escapes. Alternatively, it could represent transfer from a dark state to a bright state where the excited population is lost to fluorescence. For this specific B/B" system, it seems to be the latter case, though that is not definitive. Evidence in favor of this hypothesis is presented in sections 5.2, 7.5.3, and 8.3.

reaches the doorway state and is "stored" becomes a long lifetime state, I express the coupled differential equations in Equations 6.3a and 6.3b

$$\frac{d[D]}{dt} = {}^{Z}/_{n^2}\,[ex] \tag{6.3a}$$

$$\frac{d[ex]}{dt} = -{}^{Z}/_{n^2}\,[ex] - k_{fl}[ex]. \tag{6.3a}$$

The time dependent solutions for this system are given by Equation 6.4

$$\begin{bmatrix} D(t) \\ ex(t) \end{bmatrix} = \begin{bmatrix} \dfrac{{}^{Z}/_{n^2}}{k_{fl} + {}^{Z}/_{n^2}} \\ 0 \end{bmatrix} + \begin{bmatrix} \dfrac{-{}^{Z}/_{n^2}}{k_{fl} + {}^{Z}/_{n^2}} \\ 1 \end{bmatrix} e^{-\frac{(kn^2 + Z)}{Z}t}. \tag{6.4}$$

As $t \rightarrow \infty$, the solution for $[D](t, n)$ converges to Equation 6.5 (assuming an initial excited state population of 1). This equation is also parametrized by n, the number of states the molecule must move to reach the doorway:

$$[D](t \rightarrow \infty, n) = \frac{{}^{Z}/_{n^2}}{k_{fl} + {}^{Z}/_{n^2}}. \tag{6.5}$$

I now plot Equation 6.5 as function of n, using the values from my model, where Z is $4.9 * 10^9\ collisions/s$ (see section 4.4.) and k_{fl} is the B state fluorescence rate = $1/(32\ ns)$. Note that the

choice of the B state lifetime is arbitrary. I could have assumed the B" state was the initial state and the analysis would proceed identically. This plot is Figure 6-4.

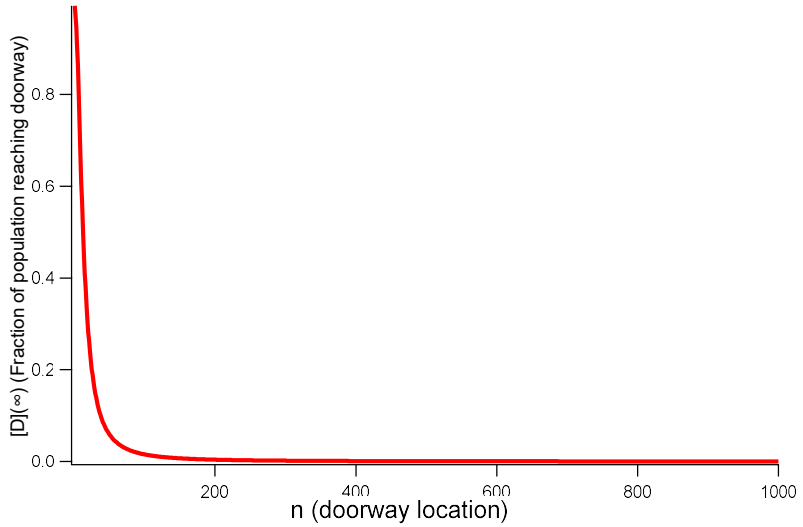

Figure 6-4: For the simple doorway model, the fraction of population reaching a doorway state, as a function of n, the (randomly chosen) number of states between the initial excited state and a doorway state. Because the number of collisions required scales as n^2, only initial excited states that spawn near a doorway state can reach the long lifetime state.

Due to the n^{-2} dependence of the initial state to doorway transfer rate, the function shown in Equation 6.5 and Figure 6-4 is very nonlinear. Only initial states that are within approximately n = 40 rotational levels, have a significant probability (>10%) to be collisionally removed from the bright B state to the long-lifetime B" state. The nonlinearity of this function will be critical to our discussion of the pressure dependence later on in this chapter.

If this process is repeated for different, randomly chosen values of n, (representing excitations to different regions of the rotational state manifold), I would compute a statistical sample average of the fraction of the population moved to the doorway, $\overline{D}_{sym}$, as shown in Equation 6.6

$$\overline{D}_{sym} = \frac{1}{N}\sum_{i=1}^{N} D(t = \infty, n_i)\,. \tag{6.6}$$

The sum is over all N samples, and, for each sample, the number of steps to the doorway is randomly chosen. If I repeat this process a sufficient number of times, I obtain the *ensemble average*, $< D >$, as in Equation 6.7

$$< D >_{sym} = \lim_{N\to\infty} \frac{1}{N} \sum_{i=1}^{N} D(t = \infty,\, n_i)\,. \tag{6.7}$$

Here, $< D >$ is the ensemble average number of initial excitations that reach the doorway (at steady state), given a randomly chosen doorway location, n.

In statistical mechanics, the ensemble average is given by an alternate expression, Equation 6.8

$$< D >_{sym} = \sum_{n=1}^{1000} p_n D(t = \infty, n)\,, \tag{6.8}$$

where p_n is the probability of a particular doorway location being chosen. In this case, the doorway location, n, has an equal chance of being any number between 1 and 1000. Therefore, p_n = 1/1000 for all values of n. (This probability distribution is called a *microcanonical ensemble*.) $D(t = \infty, n)$ is simply the expression given by Equation 6.5. Now, Equation 6.8 becomes Equation 6.9

$$< D >_{sym} = \frac{1}{1000} \sum_{n=1}^{1000} \frac{{}^{Z}/_{n^2}}{k_{fl} + {}^{Z}/_{n^2}}. \tag{6.9}$$

Intuitively, the ensemble average is valid when D is calculated every possible microstate of the system (every possible value of n_i) according to the probability of occupying that particular microstate.

The concept of an ensemble average is essential for comparing the symmetric isotopologue model to an asymmetric isotopologue model. The asymmetric isotopologue model has two, entirely separate manifolds that, in this model, do not connect with each other. The probability of excitation to each of these manifolds is 0.5. Thus, the ensemble average $< D >_{asym}$ is defined as in Equation 6.10

$$< D >_{asym} = 0.5 < D >_{+} + 0.5 < D >_{-}. \quad (6.10)$$

The terms $< D >_{+}$ and $< D >_{-}$ are the ensemble averages of the (+) parity and (-) parity manifolds, respectively. Because, in this chapter, I am interested only in statistical effects, I assume that the (+) and

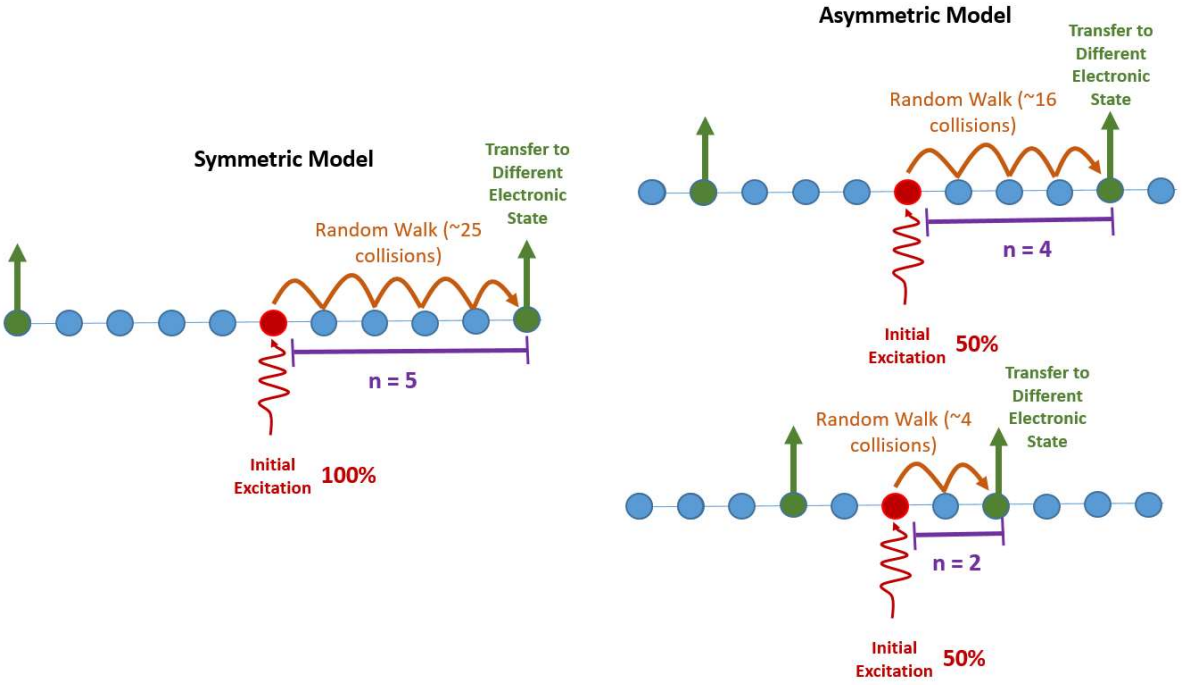

Figure 6-5: A summary of the symmetric and asymmetric models considered thus far. In the symmetric model, there is a single manifold of states. A molecule is excited into an initial state, and a number n is randomly chosen. This number represents the number of states between the initial excited state and a doorway state leading to a long lifetime B" state. The average number of collisions required for a random walk from the initial state to a state n away is n^2. The asymmetric model is statistically identical to the symmetric model with the following two changes: (1) two different manifolds, with two separate n's selected and (2) the molecule has a 50% probability of excitation into either manifold. The values of n = 5, n =4, and n = 2 were chosen arbitrarily. There are two doorways (green arrows) in each manifold because the model is agnostic as to the direction (positive or negative) of the doorway.

(-) manifolds follow the same rules as a symmetric manifold.[22] That is, $< D >_{+} = < D >_{-} = < D >_{sym}$. This, trivially gives $< D >_{asym} = < D >_{sym}$. It is crucial to note here: this result would be universal for any chosen probability distribution for D, not only the steady state model used here.

[22] In other words, there is no reason, *a priori*, to assume the (-) parity manifold is more or less likely to sample doorway states, relative to the (+) parity manifold. In order to predict the behavior of these two manifolds, we would require knowledge of the vibrational origins, rotational constants, etc. These are non-statistical aspects that we will consider in the next chapter.

Intuitively, although the asymmetric case has twice the number of chances to find a nearby doorway, each nearby doorway only counts half us much, because there is a 50% chance of excitation from the ground state into the other manifold. These factors of 2 and 0.5 cancel. Figure 6-5 summarizes the symmetric and asymmetric models thus far.

Again, the parameters $< D >_{asym}$ and $< D >_{sym}$ represent the fraction of excited molecules, at steady state, that reach a doorway state, averaged over all possible doorway locations. The result, $< D >_{asym} = < D >_{sym}$, does not preclude the possibility of a statistical isotope effect, however. In particular, it is not necessarily the case that $\overline{D}_{sym} = \overline{D}_{asym}$ for a particular sample size, N. The next section will demonstrate that ***the rate of convergence of $\overline{D}_{sym}$ and $\overline{D}_{asym}$ to the ensemble average $< D >_{asym} = < D >_{sym}$ is not the same.*** This difference in convergence rate generates the statistical isotope effect we are looking for.

6.4 The Doorway Model Results

Figure 6-6 compares representative results from a single model run of the symmetric model to a single run of the asymmetric model. For the Nth step, in a symmetric run, a random doorway location, n_N, is chosen, and a running statistical average is calculated using this n_N, as well as n_{N-1}, $n_{N-2}\ldots n_1$. This is Equation 6.11

$$\overline{D}_{sym}(N) = \frac{1}{N}\sum_{i=1}^{N} \frac{Z/n_i^2}{k_{fl} + Z/n_i^2}. \tag{6.11}$$

For each step, N, in an asymmetric run, *two* random doorway locations, m_N and n_N are chosen, and the running statistical average is calculated, as in Equation 6.12, where the factor of 0.5 represents the 50-50 chance of absorbing to either the (+) parity or the (-) parity manifold

$$\overline{D}_{asym}(N) = \frac{0.5}{N}\sum_{i=1}^{N} \frac{Z/n_i^2}{k_{fl} + Z/n_i^2} + \frac{0.5}{N}\sum_{i=1}^{N} \frac{Z/m_i^2}{k_{fl} + Z/m_i^2}. \tag{6.12}$$

In Figure 6-6, $\overline{D}_{asym}$ and $\overline{D}_{sym}$ are displayed on the dependent axis, while N, the number of samples is the independent axis. Figure 6-6 represents the average behavior of a single S_2 molecule over a repeated series of N excitations to random locations in the rotational state manifold.

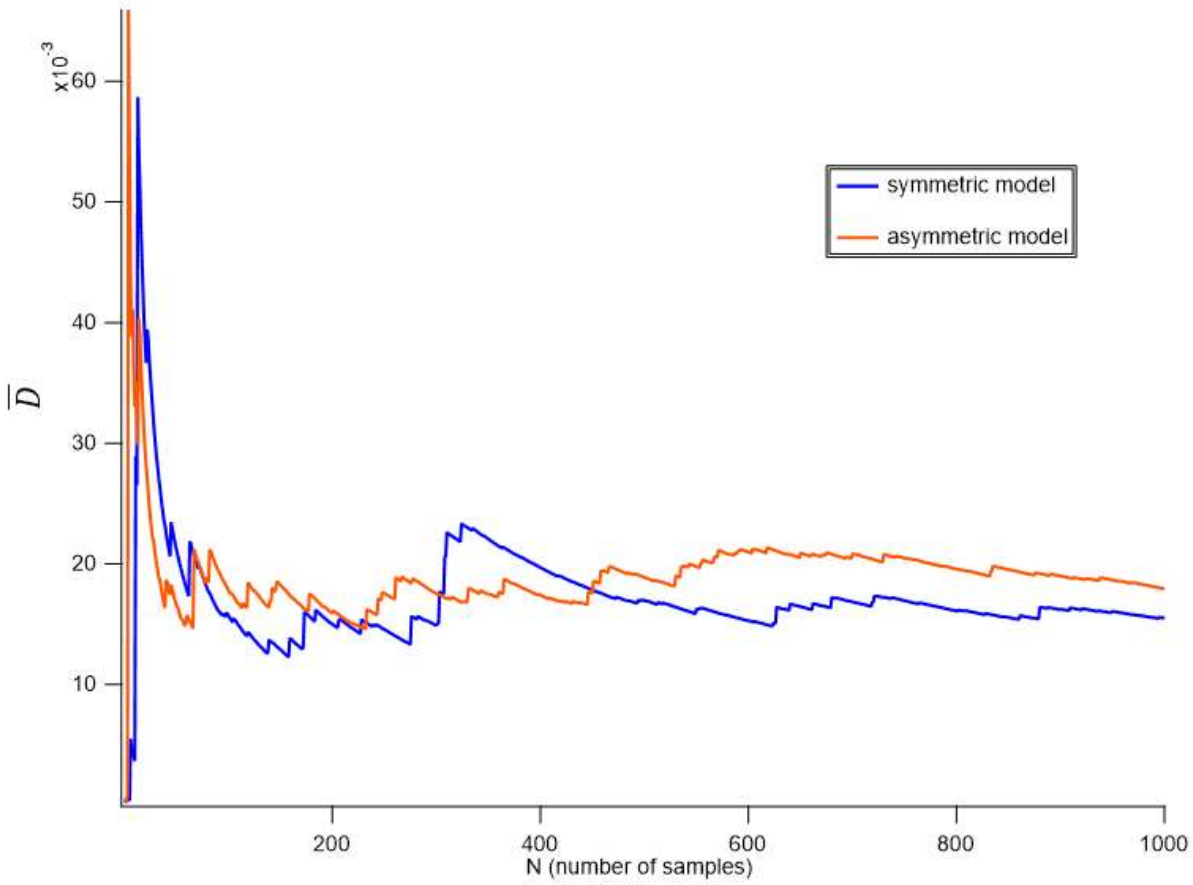

Figure 6-6: Representative examples of a single run of the symmetric and asymmetric models. The independent axis is the number of excitations, N. The dependent axis, $\overline{D}(N)$, is a running statistical average of the number of excitations that reach the doorway, given a randomly chosen doorway location.

Figure 6-6 shows $\overline{D}_{asym}$ and $\overline{D}_{sym}$, the fraction of excitations that reach the doorway (at steady state), averaged over different randomly chosen doorway locations. Both of these averages fluctuate a significantly for small sample sizes, but as the N approaches 1000, they both begin to converge to approximately the same value, the ensemble average $< D >$. Repeated runs of this model give $< D > \approx 0.01906$. It is also clear from these two particular model runs that the asymmetric model appears to converge to the ensemble average faster (i.e. at smaller N's) than does the symmetric model. Figure 6-7

demonstrates that this observation is not unique to the two particular model runs shown in Figure 6-6. It displays $|\overline{D}_{asym} - < D >|$ and $|\overline{D}_{sym} - < D >|$ averaged over 1000 model runs. Physically, if a single run represents a single S_2 molecule undergoing N repeated excitations. Averaging over a series of model runs represents the behavior of an *ensemble* of many S_2 molecules undergoing N repeated excitations.

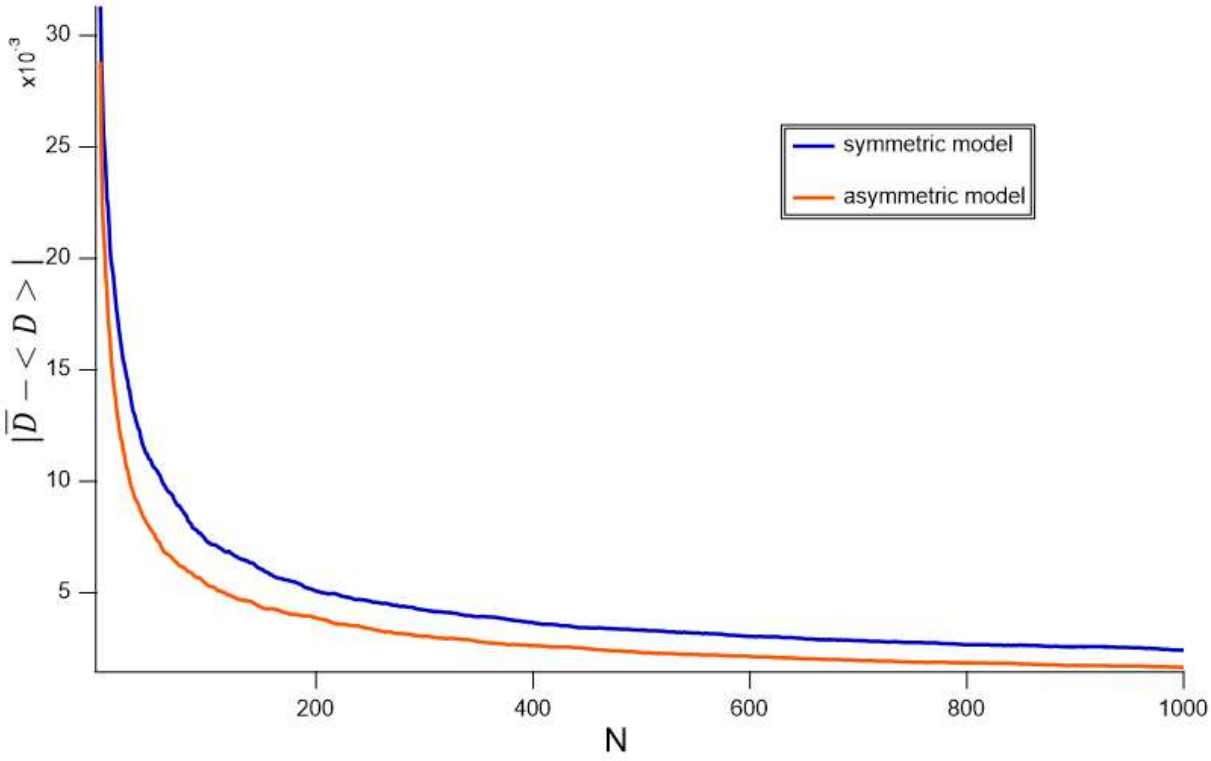

Figure 6-7: The values of $|\overline{D}_{asym} - < D >|$ and $|\overline{D}_{sym} - < D >|$, averaged over 1000 model runs, as a function of sample size, N. This plot shows the rate at which the statistical averages, $\overline{D}$ converge to the ensemble average $< D >$. The asymmetric model clearly converges faster (at lower N) than does the symmetric model.

The asymmetric model converges faster than does the symmetric model. In the following sections, I explain this phenomenon in two different ways: the first intuitive, the second more formal.

6.5 Mathematical Intuition: Two Games of Chance

Imagine two different games of chance. In the first game, I am allowed to select between one of five different treasure chests. Four of these five chests contain nothing. The fifth contains $1000. If D the

random variable that represents the amount of money I will have won after opening a single chest, then the expectation value, $< D >_{game\ 1}$ is given by Equation 6.13.

$$< D >_{game\ 1} = \frac{1}{5}(0 + 0 + 0 + 0 + \$1000) = \$200 \quad (6.13)$$

Now imagine a second game. In this game, there are *two* series of five chests, series A, and series B. The total prize money of $1000 is halved. $500 is placed randomly in one of the series A chests, and $500 is placed in one of the series B chests. In this game, I am allowed to choose 1 chest in each series. The expectation value, $< D >_{game\ 2}$, is the sum of expectation values for the money earned from series A and B, i.e. Equation 6.14.

$$< D >_{game\ 2} = < D >_A + < D >_B = \frac{1}{5}(0 + 0 + 0 + 0 + 500) + \frac{1}{5}(0 + 0 + 0 + 0 + 500) = \$200 \quad (6.14)$$

i.e. the expectation values are the same. These two games are depicted as Figure 6-8.

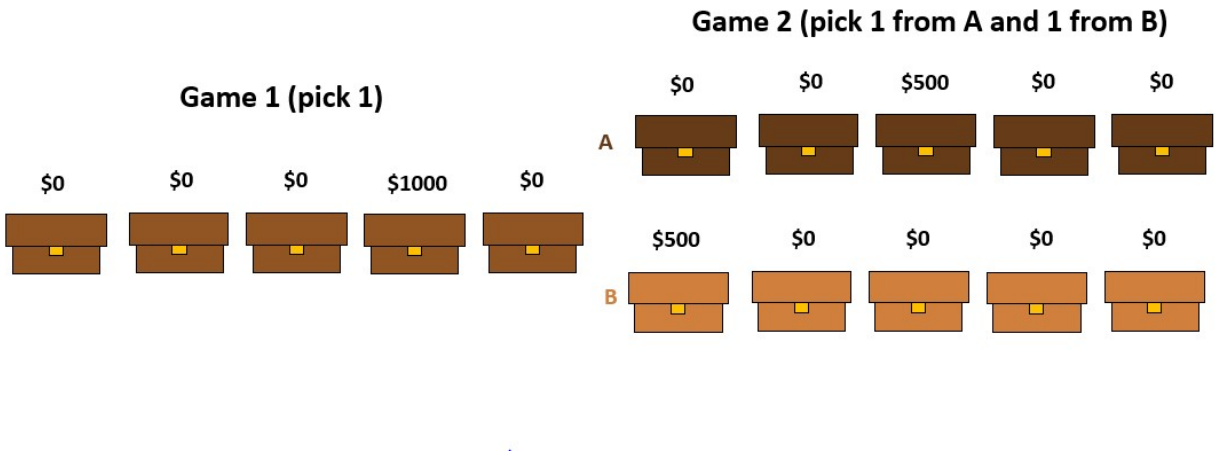

Figure 6-8: The two hypothetical games of chance being analyzed in this section. In the first game, $1000 is randomly placed in one chest of five. In the second, $500 is placed in one chest in one set of five (set A) and $500 is placed in another chest in a different set of 5 (set B). In the first game, I am allowed to pick one chest. In the second, I am allowed to select one chest from each set.

However, consider now the probability of winning *some* money (P(win)). For the first game, that probability is, trivially, 20%. For the second game, the probability of winning some money can be calculated as in Equation 6.15.

$$P(win) = 1 - P(don't\ win\ money, A) * P(don't\ win, B) = 1 - 0.8 * 0.8 = 0.36 = 36\% \quad (6.15)$$

My odds of winning some money nearly are nearly double in game 2, compared to game 1.

Put differently, if I was charged $10 to play either game 1 or game 2, and did not know, *a priori*, what the money values in the chests were, I would more quickly realize that in game 2 would I would win money than I would in game 1.

6.6 Mathematical Formalism: The Central Limit Theorem

The above games of chance give an intuitive illustration of the *Central Limit Theorem* from statistics. In the context of our doorway example, the theorem states the following:

If D_1, D_2,…, D_N are random samples of a random variable, D, where D has an ensemble average $< D >$, and statistical variance, σ^2, then the sample mean $\overline{D} = \sum_{i=1}^{N} D_i$ converges to a normal probability distribution with mean $< D >$, and standard deviation, $\frac{\sigma}{\sqrt{N}}$ as the sample size, $N \to \infty$.

Consider, now, my definitions of $\overline{D}_{sym}$ and $\overline{D}_{asym}$, the sample-averaged number of excitations that reach the doorway state in the asymmetric and symmetric models, respectively. These are restated as Equations 6.16a and 6.16b, respectively

$$\overline{D}_{sym}(N) = \frac{1}{N}\sum_{i=1}^{N} \frac{Z/_{n_i^2}}{k_{fl} + Z/_{n_i^2}}. \quad (6.16a)$$

$$\overline{D}_{asym}(N) = \frac{0.5}{N}\sum_{i=1}^{N} \frac{Z/_{n_i^2}}{k_{fl} + Z/_{n_i^2}} + \frac{0.5}{N}\sum_{i=1}^{N} \frac{Z/_{m_i^2}}{k_{fl} + Z/_{m_i^2}}. \quad (6.16b)$$

In particular, observe that $\overline{D}_{asym}$ and $\overline{D}_{sym}$ are related, as in Equation 6.17

$$\begin{aligned}\overline{D}_{asym}(N) &= \frac{1}{2} * \{\frac{1}{N}\sum_{i=1}^{N} \frac{Z/_{n_i^2}}{k_{fl} + Z/_{n_i^2}} + \frac{1}{N}\sum_{i=1}^{N} \frac{Z/_{m_i^2}}{k_{fl} + Z/_{m_i^2}}\} \\ &= \frac{1}{2N}\sum_{i=1}^{2N} \frac{Z/_{n_i^2}}{k_{fl} + Z/_{2n_i^2}} = \overline{D}_{sym}(2N). \end{aligned} \quad (6.17)$$

In words, $\overline{D}_{asym}$ is simply $\overline{D}_{sym}$ with double the sample size. The Central Limit Theorem, therefore, would predict that $\sigma_{\overline{D}_{asym}}/\sigma_{\overline{D}_{sym}}$ converges to $\sqrt{2}$ as the sample size, N increases. (Here, $\sigma_{\overline{D}_{asym}}$ is the standard deviation of the distribution of possible values for $\overline{D}_{asym}$). In Figure 6-9, I have used my model to calculate $\overline{D}_{asym}$ and $\overline{D}_{sym}$ 1000 times for each value of N between 1 and 1000. Figure 6-8 shows the ratio of $\frac{\sigma_{\overline{D}_{asym}}}{\sigma_{\overline{D}_{sym}}}$, as a function of N. **Because $\frac{\sigma_{\overline{D}_{asym}}}{\sigma_{\overline{D}_{sym}}}$ is strictly greater than 1, the asymmetric model converges to the mean faster (i.e. at smaller sample sizes) than does the symmetric model.**

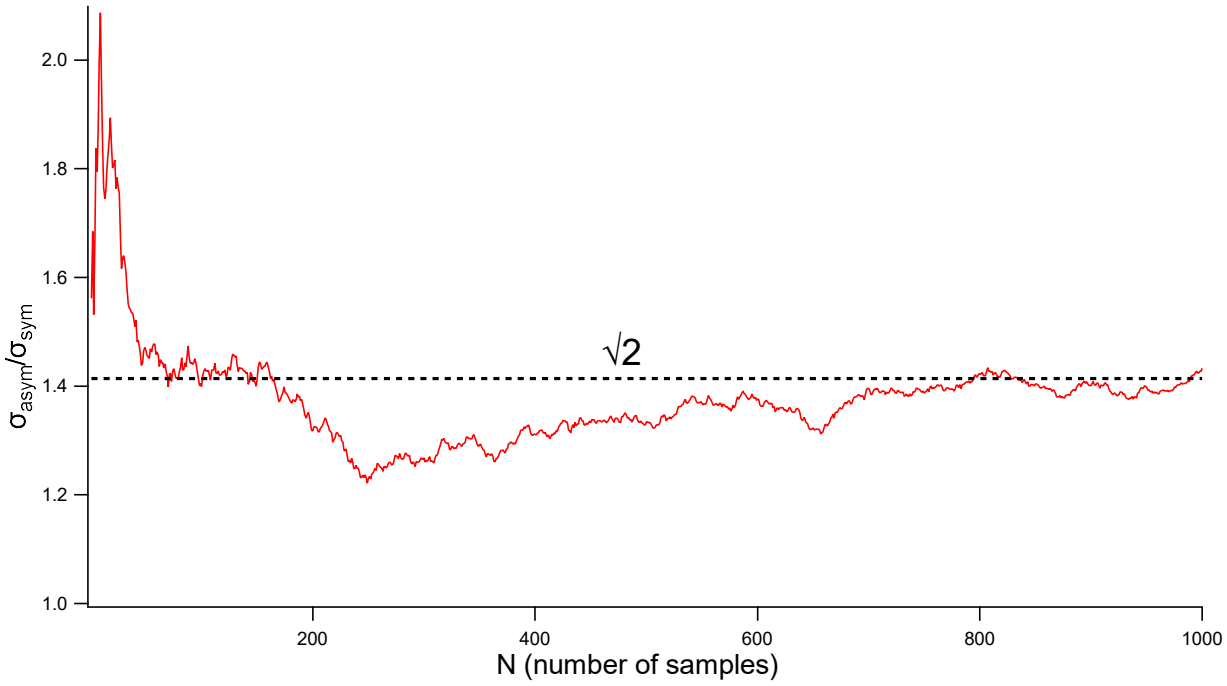

Figure 6-9: An illustration of the Central Limit Theorem for the $\overline{D}_{asym}$ and $\overline{D}_{sym}$ parameters considered in this chapter. For each data point, $\sigma_{\overline{D}_{asym}}$ is the standard deviation of 1000 different calculations of $\overline{D}_{asym}$ each using sample size, N, and likewise for σ_{sym}. As the sample size increases, the ratio $\sigma_{asym}/\sigma_{sym}$ approaches $\sqrt{2}$ (dashed black line), as predicted by the Central Limit Theorem.

Thus far, I have discussed a simple model for doorway mediated transfer from a relatively bright B state to a relatively dark B" state. At steady state, this model determines the fraction of initially excited

state molecules that reach a doorway state, given a collisional random walk at rate Z, and a fluorescence rate k_{fl}. I have labeled this fraction as the random variable, D. I imagine a *single* S_2 undergoing a series of N excitations, in which the distance between the initial excited state and the doorway state is chosen randomly for each excitation. The number of molecules that reach the doorway state, averaged over all N excitations is $\overline{D}$. As N increases, every possible distance between the initial excitation and the doorway state is sampled, and $\overline{D}$ approaches the ensemble average, $< D >$. For the symmetric model and the asymmetric model, $< D >_{asym} = < D >_{sym}$. However, $\overline{D}_{asym}(N)$ is, effectively, equal to a $\overline{D}_{sym}$ with double the samples (2N). Therefore, per the Central Limit Theorem, the asymmetric sample converges to the ensemble average at smaller sample size, N. It is this difference in convergence rate that, I hypothesize, generates the S-MIF signature in the rock record.

6.7 Convergence rate, as a function of pressure

Before considering the weak perturbation model's isotope effect as a function of atmospheric pressure. I must consider the effect that pressure has on the rate at which $\overline{D}$ converges to $< D >$ (rate, in this context, means the number (N) of samples required for convergence). Recall that, for a randomly chosen distance between initial excitation and doorway, n, the probability distribution for D is as follows in Equation 6.18

$$D(n_i) = \frac{Z/_{n_i{}^2}}{k_{fl} + Z/_{n_i{}^2}}. \tag{6.18}$$

For 1 atmosphere and $300\ K$, the collision rate is approximately $Z = 4.9 * 10^9\ s^{-1}$ (see section 4.4.). Figure 6-10 shows the $D(n_i)$ at several different atmospheric pressures.

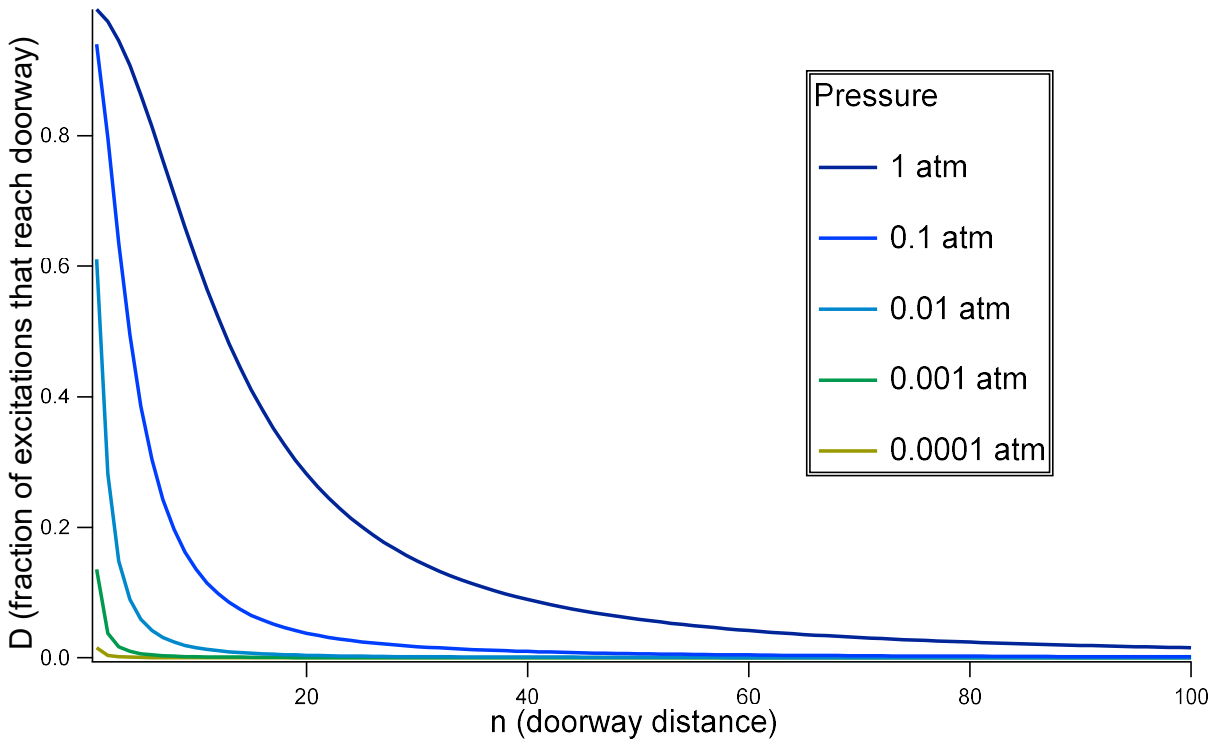

Figure 6-10: The probability distribution for D (the fraction of excitations in which the excited state molecule reaches the doorway), as a function of n (the number of states between the initial excited state and the doorway), calculated at a variety of pressures at 300 K. These different pressures correspond to different

Figure 6-10 shows that, as the pressure (i.e. the number of collisions) decreases, there are two important consequences. First, the distance, n, necessary for successful collisional transfer between the initial state and the doorway state becomes much smaller. This makes intuitive sense: if the number of collisions is decreased, the molecule explores smaller fraction of the total state space available to it. Second, as the number of collisions continues to decrease, the maximum fraction of molecules reaching the doorway correspondingly decreases. Intuitively, if $k_{fl} > Z$, most molecules fluoresce before encountering a collision.

Consequently, I postulate the following: the state space sampled by an excited state molecule increases correspondingly as the pressure increases. Increasing the pressure, therefore, will decrease the number of repeated excitations, N, required to converge $\overline{D}$ to $< D >$.

6.8 Introduction to the Weak Perturbation Model:

With this background, I now formally introduce the weak perturbation model. It is identical to the strong perturbation model with the following three changes:

(1) **Weak Perturbations:** All perturbations (the alpha and beta parameters from Chapter 2) are set to 1% of the values reported by Green and Western. This applies to both heterogeneous ($\Delta\Omega = 0$) and homogeneous ($\Delta\Omega = 1$) perturbations.

(2) **No predissociation for high rotational states of bound vibrational states:** As I showed in Chapter 5, the predissociation mechanism creates a pseudo-mass-dependent isotope effect, which will make the weak perturbation analysis significantly more complicated. For this reason, I ignore the predissociation for $v_B \leq 9$, and $v_{B''} \leq 21$. A subtle point: the predissociation for the $v_B > 9$ and $v_{B''} > 21$ levels is retained. Because all of these states are predissocating for all isotopologues, this does not introduce an isotope effect. However, it does simulate either a "real" situation where atmospheric S_2 is only in the atmosphere for a limited time because it is exposed to solar radiation and, eventually, photodissociates. Alternatively, this model can simulate a "laboratory" situation, where a finite amount of sulfur is exposed to broadband UV radiation, with some S_2 dissociating. Regardless, it gives me a finite time at which our "experiment" is over, i.e. eventually all sulfur that has not undergone excited state chemistry dissociates to $S + S$. I must also note that I am only considering the possibility for isotope effects from reactions of excited state S_2 to form S_3 and S_4, and, eventually, S_8. Any fractionation caused by the creation of atomic sulfur is ignored.[23]

(3) **A uniform Franck-Condon distribution:** To give every B~B" vibrational state crossing an equal weighting, I set the Franck-Condon factors for the transition from X, v = 0 to each of the 10

[23] My analysis of the predissociating model from chapter 5 suggests that this is a plausible assumption, as it largely creates Mass *Dependent* Fractionation.

bound B state vibrational levels equal to 0.1 (i.e. $^1/_{10}$). Similarly, I set the Franck-Condon factors for each of the 22 bound B" states equal to 0.046 (i.e. $^1/_{22}$). This also simplifies my analysis, as the isotope effects will be related to the characteristics of the B/B" vibrational state crossings, and not weighted by the Franck-Condon distribution, making for easy comparisons. The Franck Condon distribution, as discussed in Chapter 5, affects the relative contribution of each vibrational level crossing. However, in this chapter we are interested in a statistical effect that affects all crossings.

6.9 The Results of the Weak Perturbation Model

Figure 6-11 shows the results of two different weak perturbation models. The first model is a control: all four isotopologues, 3232, 3233, 3234, and 3236, are calculated using symmetric nuclear permutation symmetry rules, i.e. all four isotopologues have half of their rotational levels missing. The second model calculates the three asymmetric isotopolgues using the asymmetric nuclear permutation symmetry rules, i.e. both a (+) and (-) parity manifold of states.

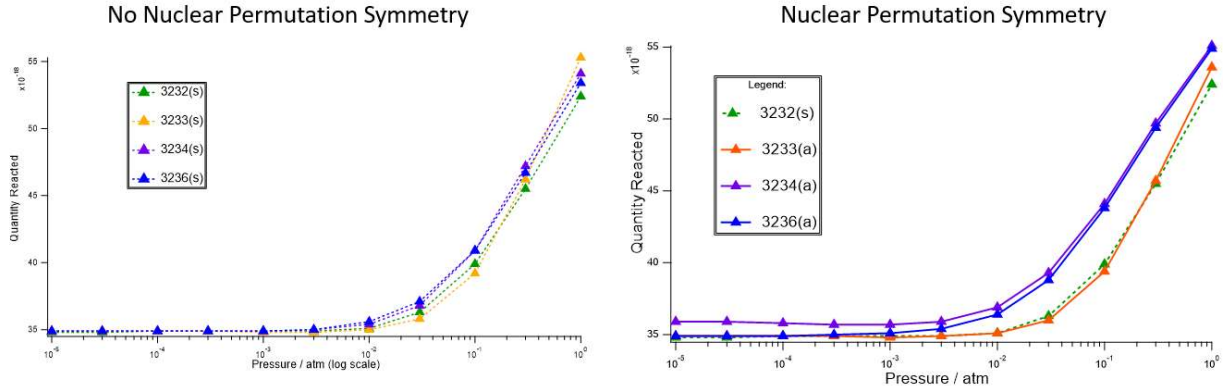

Figure 6-11: A comparison of two different weak perturbation models. The independent axis is the pressure of the atmosphere (logarithmic scale). The dependent axis is the fraction of the S_2 molecules that have undergone excited state chemistry. The left plot is calculated with all four of the isotopologues following symmetric nuclear permutation symmetry rules, i.e. half rotational states missing (dashed lines) It serves as a control for comparison to the right plot, which shows the three asymmetric isotopologues (3233, 3234, 3236) calculated with their standard (asymmetric) permutation symmetry rules.

The control plot (left) indicates the following relationship at 1 atm: $[33]/[33]_n > [34]/[34]_n > [36]/[36]_n > [32]/[32]_n$ (where the ratio $[33]/[33]_n$is the ratio of the amount of the S-33 entered into the rock record, relative to the natural abundance). The plot using the asymmetric symmetry rules (right), shows a different relationship at 1 atm: $[34]/[34]_n \approx [36]/[36]_n > [33]/[33]_n > [32]/[32]_n$. This relationship is much closer to the Archean Reference Array: $([34]/[34]_n \approx [36]/[36]_n \approx [33]/[33]_n > [32]/[32]_n$.

Especially noteworthy: the three asymmetric isotopologues, begin behaving disparately, but then begin to converge as the pressure increases. This behavior, I hypothesize, occurs because the asymmetric isotopologues more completely sample all possible doorway states as the pressure increases. In the mathematical language of my simple model, $\overline{D}_{3233}(p)$, $\overline{D}_{3234}(p)$, and $\overline{D}_{3236}(p)$ begin to converge, as a function of pressure, to a limiting, ensemble behavior, $< D > (p)$. This convergence happens at lower pressures for the three asymmetric isotopologues than it does for the symmetric isotopologue, 3232, **because the asymmetric isotopologues can sample two different rotational state manifolds, as opposed to one.**

If this sampling hypothesis is correct, I should observe that the 3232 isotopologue converges to the other three, as the pressure continues to increase. Figure 6-12, therefore, shows the asymmetric isotopologue at pressures up to $10\ atm$.

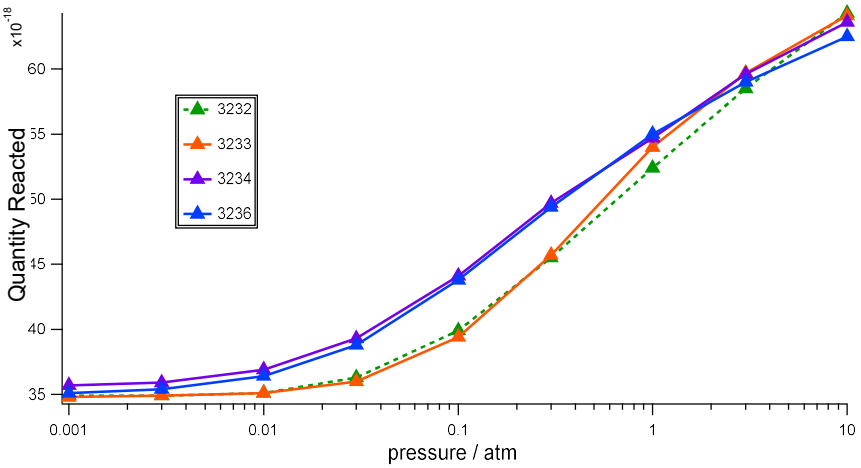

Figure 6-12: The asymmetric weak perturbation model from Figure 6-11 (right), beginning at 0.001 atm and continuing to 10 atm. This plot shows the convergence of 3232 to the other three as the pressure increases above 1 atm.

This is, indeed, what I observe.

6.10 Fractionation from the Weak Perturbation Model

Using this model, I now calculate the fractionation patterns that would be formed if only excited state S_2 reacts to form the S_8 aerosols that precipitate and become a part of the rock record. Figure 6-13 plots the three lower case delta parameters, δ^{33}, δ^{34}, δ^{36} as a function of pressure (300 K).

Recall that, for a rare isotope, x, the lowercase delta parameter, δ^x is given by Equation 6.19.

$$\delta^x = \frac{[x]_s / [32]_s}{[x]_n / [32]_n} - 1, \tag{6.19}$$

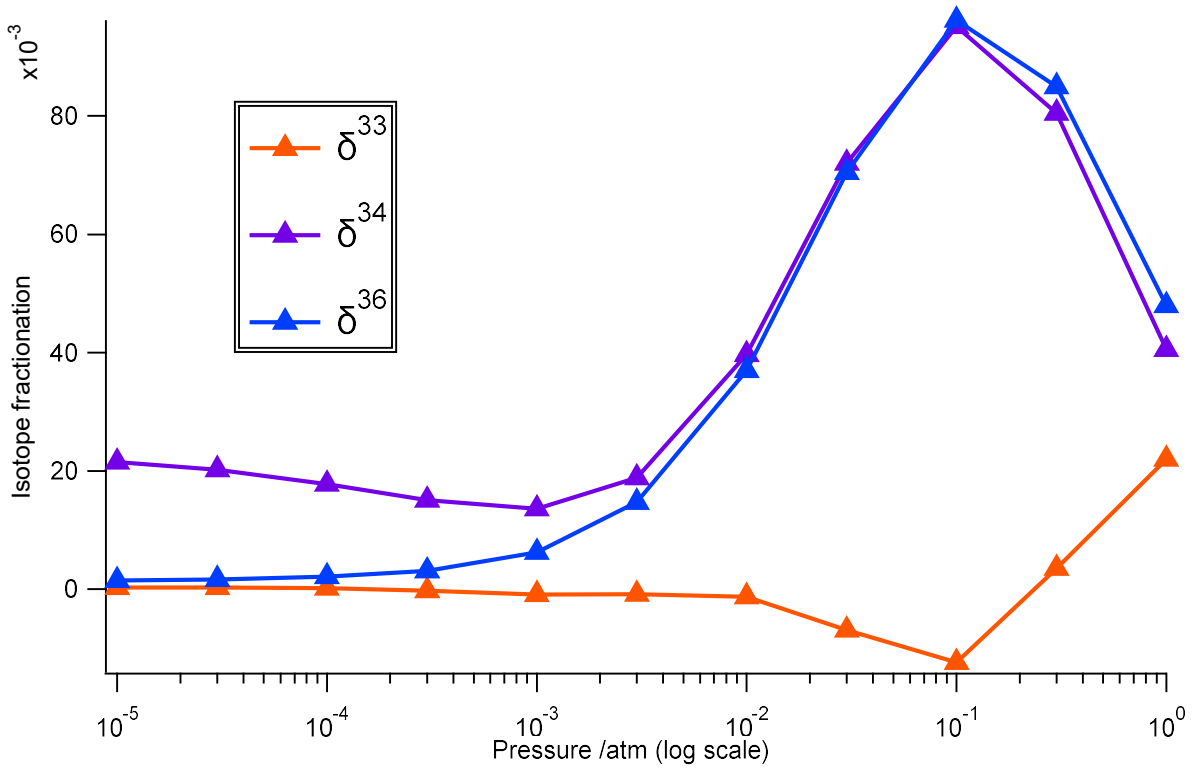

Figure 6-13: The three lowercase delta isotopic fractionation parameters, as a function of pressure, for the asymmetric model shown in Figure 6-11(right).

where $[x]_s/[32]_s$ is the ratio of the rare isotope to 32 in the rock sample under consideration, while $[x]_n/[32]_n$ is the natural abundance ratio of the rare isotope to 32. The δ^x parameter is positive if the sample is enriched in the rare isotope, negative if depleted. The convergence of the δ^x parameters to a positive number with increasing pressure reflects the convergence of the three asymmetric isotopologues, relative to 3232 as seen in Figure 6-10.

Recall from Chapter 1 that the capital delta $\Delta^{33}$and Δ^{36} parameters are functions of the δ^x parameters as in Equations 6.18a and 6.18b

$$\Delta^{33} = \delta^{33} - 0.515\delta^{34} \qquad (6.18a)$$

$$\Delta^{36} = \delta^{36} - 1.9\delta^{34}\,. \qquad (6.18b)$$

If we have $\delta^{33} \approx \delta^{34} \approx \delta^{36} > 0$, as we do at 1 atm of pressure. Then we have $\Delta^{33} > 0$, and $\Delta^{36} < 0$ and, consequently, $\Delta^{36}/\Delta^{33} < 0$. These three trends match the Archean Reference Array in the rock record.

Figure 6-13 shows the effect this asymmetric convergence has on the Δ^{36}/Δ^{33} ratio. It is positive for most pressures, but, as the three δ^{x} values converge, the Δ^{36}/Δ^{33} value becomes negative. The magnitude of this negative value does not match the rock record: We'd expect either $\frac{\Delta^{36}}{\Delta^{33}} = -1.5$, or $\frac{\Delta^{36}}{\Delta^{33}} = -0.9$, and we actually have only $\frac{\Delta^{36}}{\Delta^{33}} = -0.04$. However, the sharp trend toward $\Delta^{33} > 0$, $\Delta^{36} < 0$, and $\Delta^{36}/\Delta^{33} < 0$ is extremely clear.

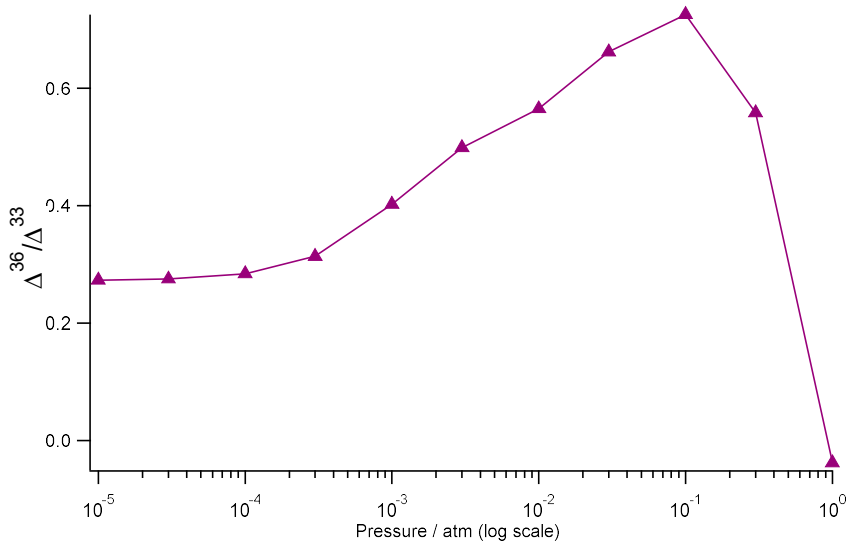

Figure 6-14: The $\frac{\Delta^{36}}{\Delta^{33}}$ ratio for the data from Figure 6-12. The increase that occurs between 10^{-4} and 10^{-3} atm is due to the convergence of δ^{34} and δ^{36}. The sharp decline is due to the near convergence of δ^{33} with δ^{34} and δ^{36} at approximately 10^{-1} atm.

This convergence behavior, where the three asymmetric isotopologues converge to a limiting behavior because they sample two rotational state manifolds, compared to the one manifold sampled by the symmetric isotopologue, is observed in the behavior of the weak perturbation model. However, this description is also somewhat incomplete. For example, the 3234 and 3236 isotopologues converge at approximately 0.01 atm, while 3233 doesn't converge until 0.1-1 atm. Second, the convergence isn't perfect; each of the four isotopolgues still exhibits some idiosyncratic behavior, even at high pressures. This is indicative of non-statistical effects. The origins of these effects will be explored in Chapter 7.

Chapter 7 : Non-statistical Effects in the Weakly Perturbed B/B" system

Abstract: In Chapter 6 I developed a statistical doorway model to explain sulfur mass-independent fractionation in a "weak perturbation model" where the B/B" perturbation matrix elements were set to 1% of their original values. This statistical model explained some of the fractionation behavior, but there was significant evidence of non-statistical behavior. To explore the mechanisms for non-statistical behavior, I consider in this chapter a "control model", where all isotopologues have symmetric nuclear permutation symmetry restrictions, to eliminate the statistical factors from my analysis. The weakly-perturbed control model behaves quite differently to the strongly-perturbed system in Chapter 5. Specifically, the system behaves more globally, with all vibrational levels fractionated toward the same isotopologue, instead of more localized behavior. Here, I analyze three specific vibrational levels to highlight three important non-statistical fractionation mechanisms. (1) Electronically inelastic transfer between a B and B" states that do not cross and are state-mixed less than 0.01%. (2) Non-statistical doorway sampling, i.e. doorway sampling that is not entirely random, but contains some dependence on vibrational level shifts. (3) Non-local effects where the local effect of one doorway is effectively "canceled out" by a larger, but more energetically remote doorway. Points (1) and (3) help explain the global behavior of this model, compared to its strongly-perturbed counterpart. Point (2) is important to the discussion in section 8.3. All three points show that there are a large range of level crossings potentially capable of generating fractionation relevant to the rock record.

7.1. Introduction

Chapter 6 had two objectives. First, it developed a statistical doorway model for Sulfur Mass-Dependent fractionation. In this model, I postulated a limiting behavior, $< D > (p)$, i.e. the ensemble averaged fraction of excited S_2 molecules that reach the doorway to a long-lived B" state, $< D >$, as a function of pressure, p. I then argued that the asymmetric S_2 isotopologues, such as 32-33, 32-34, 32-36 converged to this limiting behavior with fewer repeated excitations (i.e. smaller sample sizes) than did the symmetric S_2 isotopologues. Second, I applied the statistical doorway model to a B/B" model where the perturbation matrix elements were set to 1% of their known values in Green and Western's deperturbation model. These results are reproduced here as Figure 7-1.

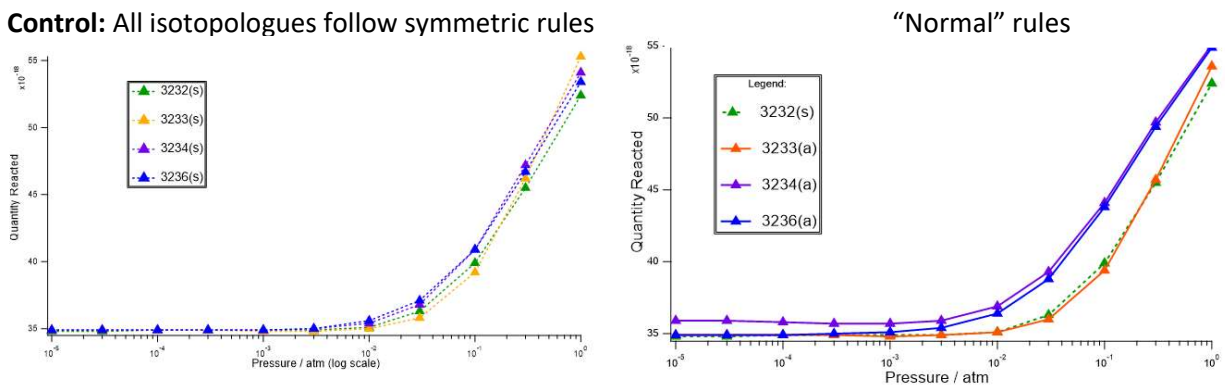

Figure 7-1: Reproduced from Chapter 6, this figure shows the results of the weak perturbation model for two different sets of rules. The left is a control, where all isotopologues follow symmetric nuclear permutation symmetry rules. On the right, all isotopologues follow "normal" nuclear permutation symmetry rules. The independent axis is the pressure of the atmosphere on a logarithmic scale. The dependent axis is the quantity of each isotopologue that has entered the rock record, assuming an excited state reaction rate that is slow relative to the radiative and collisional transfer processes (i.e. steady state). The right plot shows evidence of the statistical doorway isotope effect discussed in Chapter 6. The left plot shows evidence of non-statistical Mass Independent Fractionation.

The right plot, where the isotopologues follow their "normal" nuclear permutation symmetry rules, was the focus of the discussion in Chapter 6. The asymmetric case (3233, 3234, 3236) shows clear evidence of faster convergence to a limiting behavior compared to the symmetric 3232 case. However, this statistical mechanism does not explain every aspect of the model. For example, the 3233 isotopologue does not converge to the limiting behavior as fast as the other two isotopologues do. The left plot, where all isotopologues have one half of their rotational levels missing, shows that 3233 also lags behind the other isotopologues as the pressure increases, before catching up.

This indicates important "non-statistical" behavior. In the statistical doorway model, we assumed that the locations of the doorway are completely random. This is, of course, not entirely the case, so such behavior is to be expected. In this chapter, therefore, I consider the origins of the isotope fractionation in the control model, where all isotopologues follow the symmetric rules. Specifically, I use examples of three different B/B" interactions in the control model to show three different effects not considered in the statistical doorway model: 1) Electronically inelastic collisions between states that do not cross. 2) Mass-dependent (non-random) doorway sampling. 3) Non-local effects where the local effect of one doorway is

effectively "canceled out" by a larger, but more energetically remote doorway. There are many reasons why an analysis of the control model is valuable. First, removing nuclear permutation symmetry from the model allows me to isolate the nonstatistical effects. This allows me to better understand these effects in the "normal",non-control model. Second, while the S-MIF signature in the rock record can be *primarily* explained by differences in statistical behavior between asymmetric and symmetric isotopologues, it is not a *perfect* explanation. Specifically, for a rock sample enriched the same amount in the three rare isotopes, 33, 34, and 36, the $\frac{\Delta^{36}}{\Delta^{33}}$ ratio would be -1.8. The actual rock record, however, has $\frac{\Delta^{36}}{\Delta^{33}} = -1.5$, and/or $\frac{\Delta^{36}}{\Delta^{33}} = -0.9$. Therefore, there must be non-statistical effects that influence the Archean Reference Array.

7.2. Initial Analysis of the "Control" Model

In the remainder of this chapter, I will consider the control model, in which all isotopologues follow symmetric nuclear permutation symmetry rules, at 1 atmosphere of pressure and 300 K. First, I establish that the control model generates a significant S-MIF signature. This is Figure 7-2.

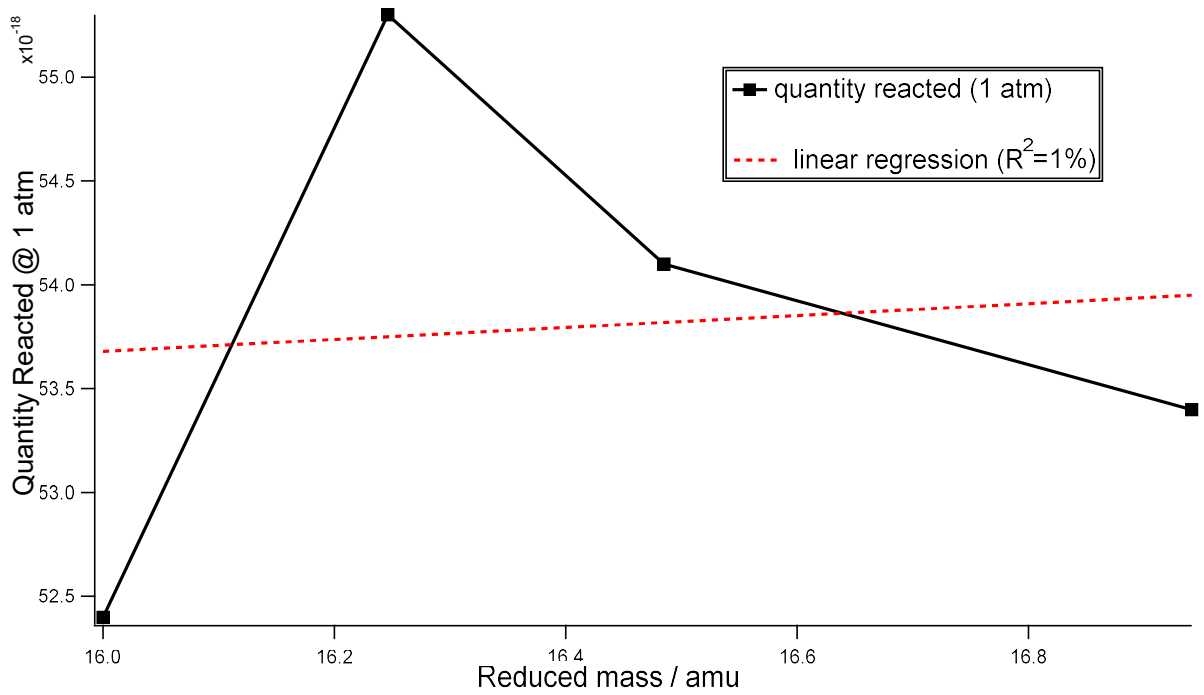

Figure 7-2: The control model data (black) at 1 atm, as a function of reduced mass, plotted alongside a linear regression (red dashed line). The relationship is very far from the mass-dependent limit, as evidenced by the correlation coefficient, $R^2 = 1\%$.

The linear regression in Figure 7-2 has a correlation coefficient of 1%, which is extremely small relative to the two pseudo mass dependent models discussed in Chapter 5. As a comparison, for the strong-perturbation, non-predissociating model, the correlation coefficient was 96%. For the large-perturbation, predissociating model, the correlation coefficient was also 96%. Qualitatively, the 1 atm data that display the largest enrichment is that for 3233, while the smallest is for 3232. Also, as in Chapter 5, I compare these two isotopologues by analyzing, for 3233 vs. 3232, which of the B/B" near degenerate pairsvibrational levels have more population at steady state. Figure 7-3 shows the results of the comparison between 3233 and 3232.

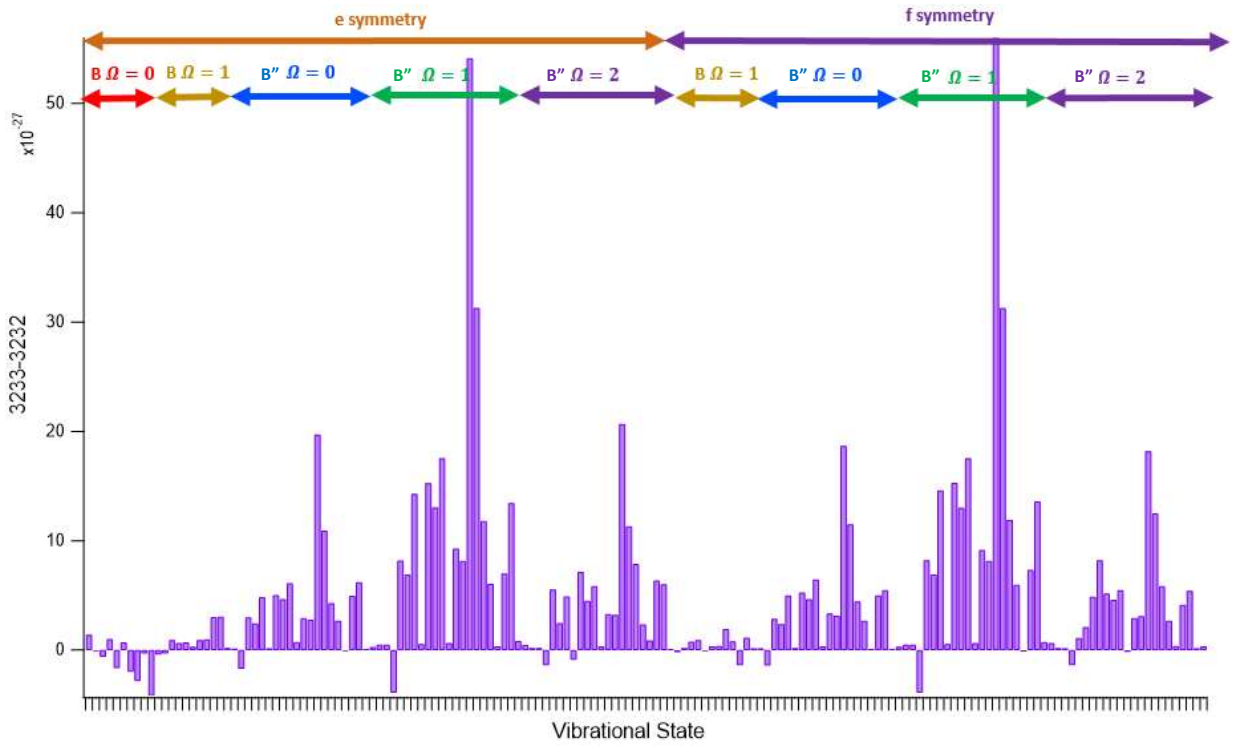

Figure 7-3: A comparison of the isotope effects for the 3233 versus 3232 for the control model (1% perturbations and both isotopologues following symmetric nuclear permutation symmetry rules). Each bar represents the difference between the steady state vibrational population for 3233 and same vibrational population for 3232. Positive bars indicate more population for 3233, and negative bars represent more population for 3232. The arrows indicate the organization of the vibrational states, which are sorted by e/f-symmetry, then by electronic state (B or B"), then by spin-orbit component (Ω). Within each component, the vibrational states are rank-ordered from low vibrational quantum numbers (left) to high (right).

The most striking feature: the fractionation mechanism here appears to operate more much more globally than in the strong perturbation model shown in Figure 5-4 of Chapter 5. In other words, the strong perturbation model has some vibrational states that favor one isotopologue and some vibrational states that favor another. In this plot, nearly all the vibrational states, to varying degrees, favor the same isotopologue: 3233 over 3232 (in other words, an ensemble of 3233 vibronic states holds more excited state population). Furthermore, the strongest isotope effect appears to be for the $B"\ \Omega = 1$ vibrational states, while the $B"\ \Omega = 0$ vibrational states had the strongest isotope effect in the strong perturbation model. Third, it is noteworthy that the same vibrational states show the strongest isotope effect for all three spin-orbit components, *and for both* e/f-symmetries. Recall that, in the strong perturbation model, each spin-orbit component behaved differently, and there were large differences in behavior between e-

symmetry and f-symmetry. The main purpose of this chapter remains to highlight three different examples of perturbation behavior that violate the assumptions of the statistical model presented in Chapter 6. However, the three mechanisms also provide a synthesized explanation for the more global, uniform fractionation behavior shown in Figure 7-3. I will return to this broader discussion in Section 7.6, at the end of this chapter.

The three B" vibrational states that will be highlighted in this chapter are shown in Figure 7-4. This figure is a zoomed-in version of Figure 7-3, focusing on the B", $\Omega = 1$ states. The $\Omega = 1$ spin orbit component is chosen because it displays the strongest favoritism toward 3233.

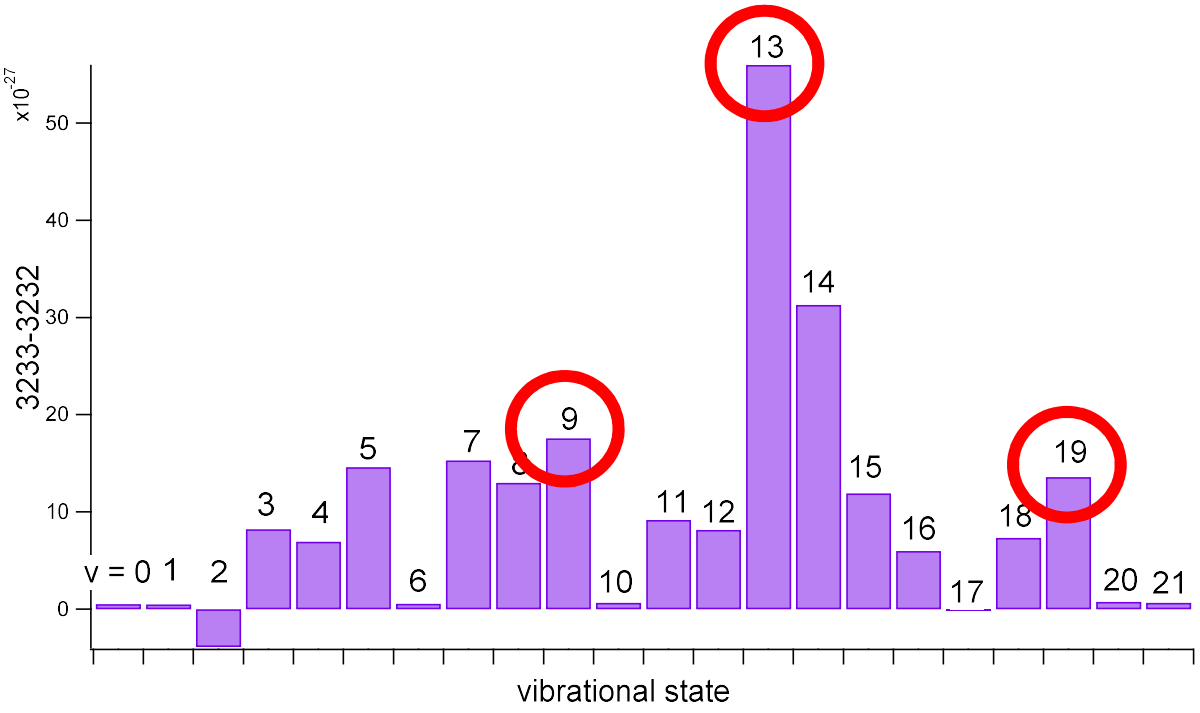

Figure 7-4: An enlarged version of Figure 4, showing the B" f symmetry, $\Omega = 1$ states. The numbers display the vibrational quantum number of each level. The red, circled states will be the focus of the following analysis. Each represents a different, non-statistical fractionation mechanism.

The red, circled vibrational states, $v = 9, v = 13, v = 19$, will be the focus of my analysis in this chapter. Note, in particular, that each of these three vibrational levels have, locally, the largest

fractionation. I begin with $v = 9$, which demonstrates the importance of electronically inelastic transfer, even in very weakly state-mixed systems.

7. 3. Electronically inelastic transfer in a weakly state-mixed system: B", $\Omega = 1$, $v = 9$:

7.3.1 Introduction to the B", $^3\Pi_u$ $\Omega = 1$, $v = 9$ state:

The first example in our analysis of the B" $\Omega = 1$ states is $\boldsymbol{v = 9}$, which will exhibit a non-statistical, electronically inelastic transfer mechanism. As in Chapter 5, I begin my analysis of this B/B" interaction with a reduced term value plot, Figure 7-5.

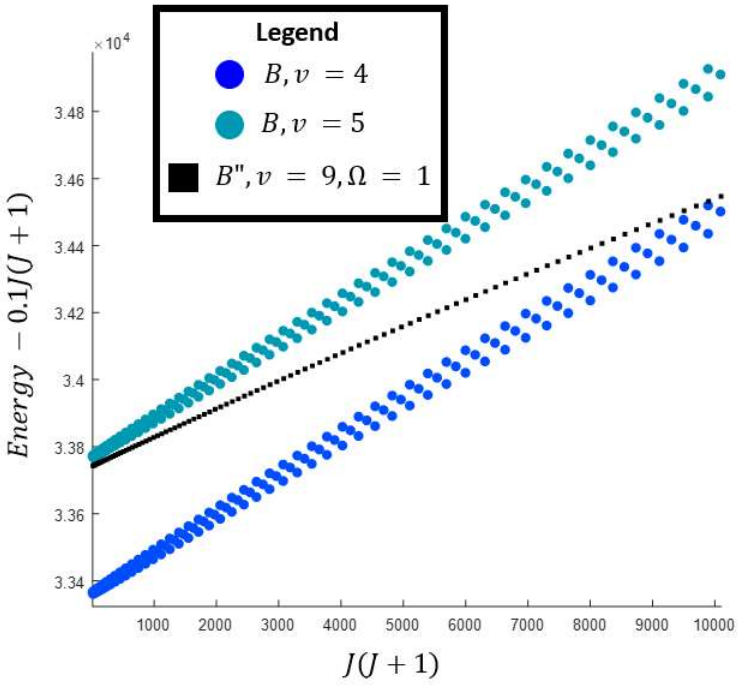

Figure 7-5: The reduced term value plot showing the interaction between the B" v = 9 state and the neighboring B v = 4 and v = 5 states. Note, in particular, that the B" state does not cross either of the B states, from J = 0, all the way up to J = 100.

This plot shows the rotational levels of B" $v = 9$, which are flanked by two B vibrational states: $v = 4$ is below and $v = 5$ is above. Recall that this energy level structure resembles the even v states in the strong perturbation model from Chapter 5. In particular, the B" state never crosses a B state at any thermally relevant value of J. In the strong perturbation system, the even-v states produced essentially zero isotope effect. However, in this weakly state-mixed system, there *is* a strong isotope effect. To

further emphasize the weak state-mixing, consider Figure 7-6, which shows the B" mixing fraction, as a function of $J(J+1)$ for both the e-symmetry (left) and f-symmetry (right) states.

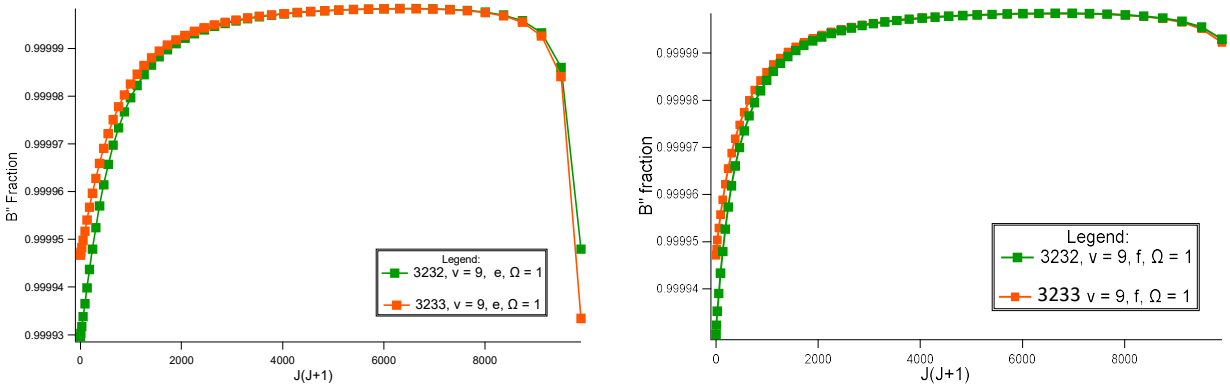

Figure 7-6: Fractional B" character, for the B", $\Omega = 1$ state, as a function of J(J + 1), for both 3232 and 3233 in the control model. The e-symmetry states are on the left, the f-symmetry states are on the right. For these plots, note, in particular, the scale of the dependent axis. Neither the e-symmetry, nor f-symmetry include states with greater than 0.01% B (bright) state character.

Although radiative lifetime is a strongly non-linear function of mixing fraction, this state-mixing is so weak that the B" lifetimes, in all cases, are very close to the unperturbed lifetime of the B" state ($4200\ ns$). This is shown more clearly in Figure 7-7, which displays the lifetime as function of $J(J+1)$.

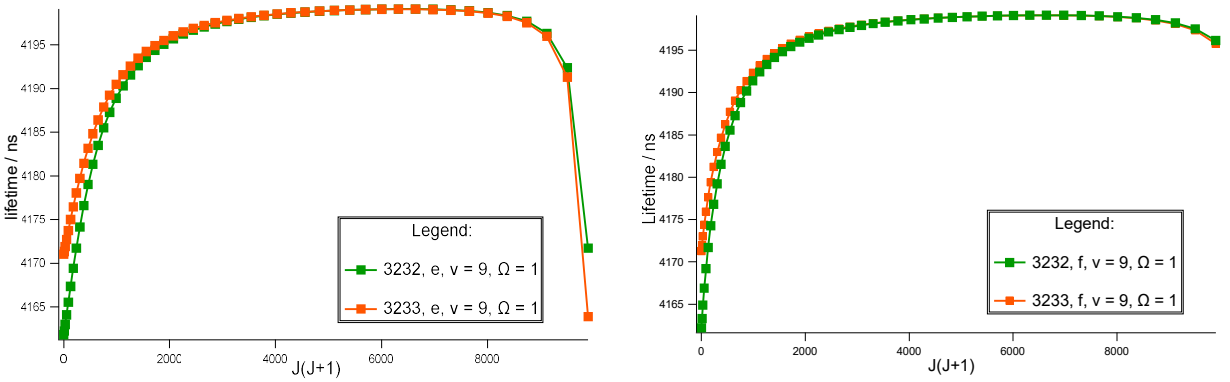

Figure 7-7: The excited state lifetime as a function of J(J + 1), for both 3232 and 3233, as well as e-symmetry (left) and f-symmetry (right). Note, again, the dependent axis. None of the lifetimes are below 4160 ns.

These two plots show extremely "dark" states, for which not a single rotational state has a lifetime shorter than 4100 ns. For the 3232 istopologue's rotational state manifold, the shortest lifetime is 4161 ns. For the 3233, the lifetimes are even longer, with a shortest lifetime of 4167. Therefore, at maximum, there is a difference of 0.1% between the lifetimes of the two isotopologues. This makes it far more difficult to invoke the "safe-zone" mechanism from Chapter 5. As a reminder, the differences in lifetime for the vibrational states in that chapter span a range larger than 30%. For this particular B/B" interaction, I hypothesize that another mechanism is responsible for the large fractionation: electronically inelastic transfer.

7.3.2 The Electronically Inelastic Transfer Mechanism

In Appendix B, I derive a simple expression for the rate of collisions that transfer between B and B" states,$R_{B\leftrightarrow B"}$, for weakly state-mixed systems like the one considered here. This expression is Equation 7.1[24]

$$R_{B\leftrightarrow B"} = mZ. \tag{7.1}$$

Here, the quantity m is the B/B" state-mixing fraction, and the quantity Z is, as before, the total rate of collisions. To reiterate, this expression is only valid for electronically inelastic transfer in weakly perturbed systems (see Appendix B for more details). With Equation 7.1 it is easy to illustrate why the electronically inelastic mechanism is more pertinent to this system than the "safe zone" mechanism. If I take the mixing fractions of the most perturbed states, I obtain the following expression (Equation 7.2)

$$\frac{R_{B\leftrightarrow B"}(3232)}{R_{B\leftrightarrow B"}(3233)} = \frac{7.1 * 10^{-5}}{5.3 * 10^{-5}} = 1.34. \tag{7.2}$$

[24] You may have noticed that I seem to be ignoring an important result from Sections 3.7 and 3.8: in a two level system, the relative phases for the mixing coefficients would cause the predicted transfer rate between the B and B" states to be approximately zero. However, in practice, this is not a two level system. Therefore, the principle from 3.7 and 3.8 becomes more a propensity rule and not a selection rule. For more information, please see References [78, 85].

That is, the rate of electronically inelastic transfer (i.e. the rate of leaking out of the long-lifetime B" state to the short-lifetime B state) is 34% larger for the 3232 isotopologue, compared to the 3233 isotopologue. This percent difference is comparable to the differences in fluorescence lifetime for the systems discussed in Chapter 5. This indicates that electronically inelastic transfer is a plausible mechanism for significant fractionation in weakly state-mixed systems. For more evidence of electronically inelastic transfer, I consider the following questions: (1) If electronically inelastic transfer can cause fractionation in a system with less than 0.01% state-mixing, what is the lower limit for the extent of state-mixing that can cause significant electronic state transfer? (2) Is there evidence of this lower limit in the Control Model analyzed in this Chapter?

7.3.3. The Lower Limit for Electronically Inelastic Transfer

The more definitive answer to this question is contained in Appendix B. Here, I simply present the results. The condition for electronically inelastic collisions to create a significant isotope effect is given as Equation 7.3:

$$mZ\tau > 1, \tag{7.3}$$

where τ, here, is the lifetime of the B" state. As discussed in Appendix B, this condition is equivalent to the following expression (Equation 7.4):

$$\frac{electronically\ inelastic\ transfer\ rate\ from\ B"\ to\ B}{B"\ fluorescence\ rate} > 1. \tag{7.4}$$

In words, when the $mz\tau > 1$ criterion is satisfied, there is more than one electronically inelastic collision within the characteristic lifetime of the *B"* state.

To answer the second question, I consider whether this $mz\tau > 1$ criterion applies to all 22, B" $\Omega = 1$, bound vibrational states. To do so, I plot the isotope effect (total population of 3233 minus total

population of 3232), as a function of the minimum B" state mixing fraction[25] for each $\Omega = 1$ B" vibrational state. This is Figure 7-8.

There are several notable features here. First, there is, in general, no strong correlation between the extent of B/B" state-mixing and isotope effect. Second, even in this weak perturbation model, where the matrix elements are 1% of their actual standard values, there are still several vibrational levels where the state-mixing is on the order of 50-90%. This is more evidence for the statistical doorway mechanism described in Chapter 6 (i.e. there are some vibrational levels that coincidentally sample regions where the diabatic B" energy levels are nearly degenerate with those of the B state). I explore two of these more state-mixed systems in sections 7.4 and 7.5. Last, and most important for the current discussion, there is a set of vibrational states that does not exhibit fractionation.

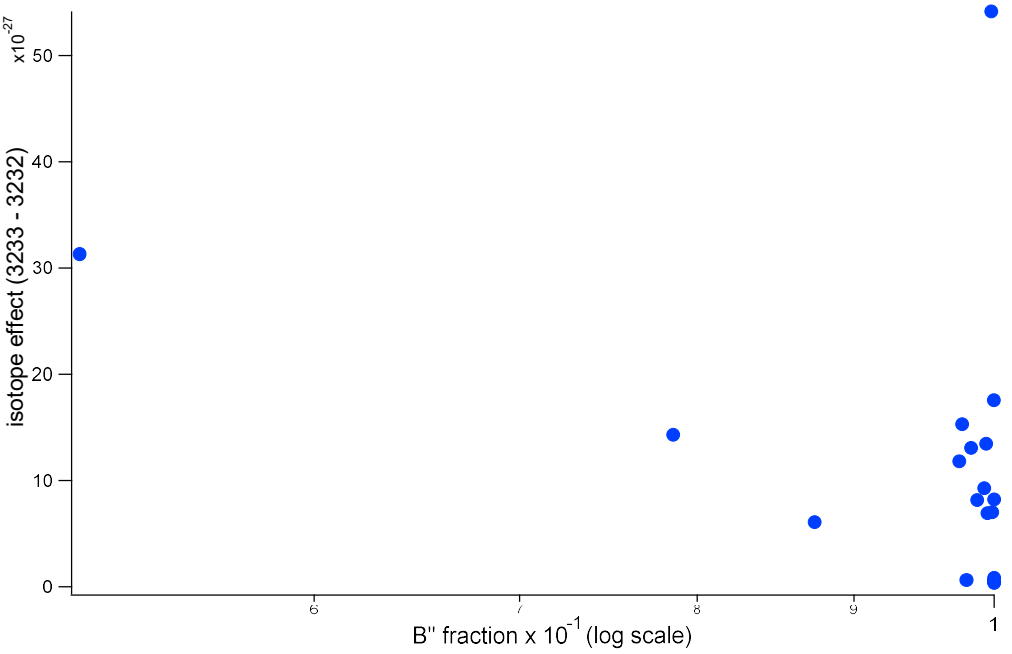

Figure 7-8: Isotope effect, as a function of minimum B" state-mixing fraction for each B" $\Omega = 1$ vibrational state. Here, isotope effect is defined, for a given vibrational state, as the total population in 3233 subtracted from the total population in 3232.

[25] In other words, the dependent axis of Figure 7-8 is the B" state mixing fraction of the rotational state that is the has maximum state-mixing

To see these non-fractionating states more clearly, consider Figure 7.9, which has the same dependent axis as Figure 7-8, but zooms in on these very weakly perturbed states.

.

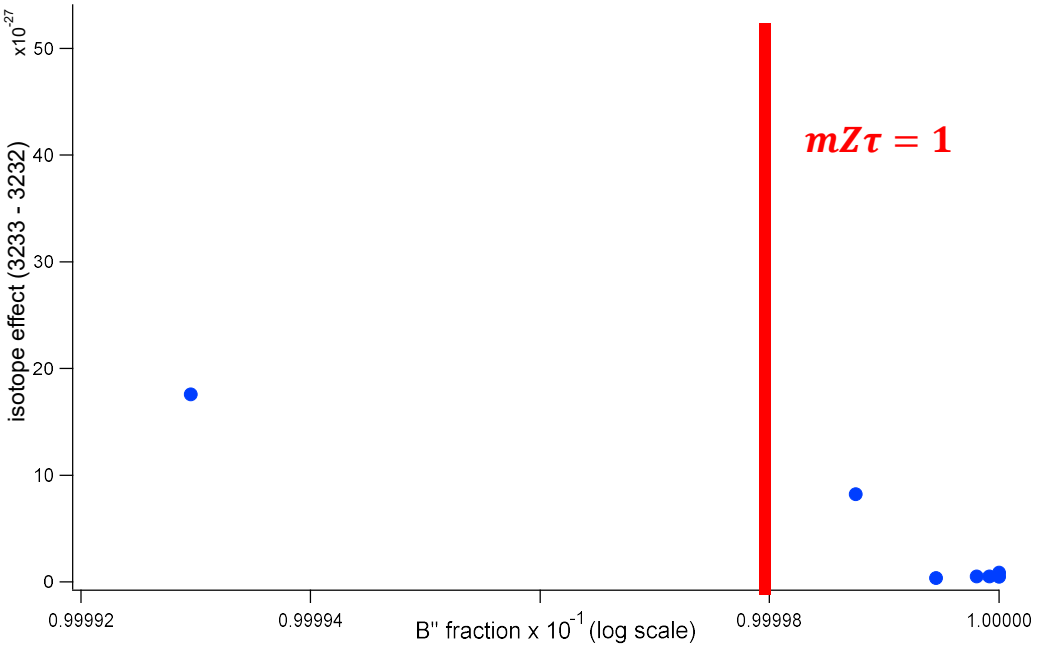

Figure 7-9: A zoomed-in version of Figure 7-8, focusing on the region around the $mz\tau = 1$ limit, which is drawn as a red line. The dependent (isotope effect) axis is on the same scale as Figure 7-8.

In Figure 7-9, the red line is based on 1 atm of pressure, 300 K, and a lifetime of 4200 ns, and divides the graph into two sections. On the left side ($m < 0.99998$), the state-mixing is large enough, such that there is at least one electronically inelastic collision within the lifetime of the B" state. On the right side of the line ($m > 0.99998$), there is not at least one such collision. In the former case, there is significant fractionation, but in the latter case, the fractionation declines as the state-mixing fraction, m, continues toward unity. This is evidence that the $mz\tau > 1$ criterion applies across all weakly state-mixed systems.

7.3.4. Conclusion

This result is significant for two reasons. First, it could partially explain the delayed response of the 3233 isotopologue relative to the other two, asymmetric isotopologues (3234 and 3236), discussed in sections 6.10 and 7.1. As a reminder, the term "delayed response" describes a behavior where the 3234 and 3236 isotopologues become enriched in the rock record, at lower atmospheric pressures; however,

higher atmospheric pressures are required before 3233 also becomes enriched. From Equation 7.1, I can estimate the average number of inelastic collisions within the lifetime of the B" state. For 3232 I calculate 1.46 collisions within that lifetime. For 3233, I calculate 1.06 collisions. If the pressure decreases by a factor of ten, there are, trivially, only 0.146 and 0.106 collisions, respectively. In other words, the full effect of these electronically inelastic collisions is only realized at these higher pressures.

Second, I must touch on the lifetime, τ, dependence of the $mz\tau$ relation. If I was to consider transfer out of a much darker electronic state with a lifetime of 1 ms, the perturbations could be as small as 1e-10 and still undergo electronically inelastic collisions within the lifetime of the longer-lived lifetime. This greatly expands the range of potential electronic state interactions that can be considered for future studies, as sources for collisional mass-independent fractionation.

7.4 Non-statistical doorway sampling in the B" $v = 13, \Omega = 1$ state:

I now consider a B" vibrational state that has much stronger perturbations: the $v = 13, \Omega = 1$ state. We should expect, based on the discussions in Chapters 5 and 6, that the fractionation in this system is driven by rotationally inelastic collisions. In Chapter 6, we considered a model where a state-mixing doorway is sampled randomly. The B" vibrational state considered here is an example of *non*-statistical doorway sampling.

To begin, Figure 7-10 shows, for 3232, the reduced term value plot for the interaction between the B" $v = 13$, $\Omega = 1$ state and the B, $v = 7$ state.

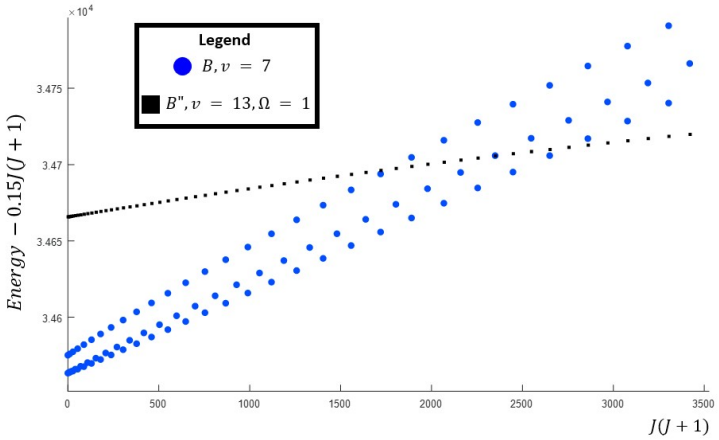

Figure 7-10: For 3232, a reduced term value plot, displays the interaction between the B, v = 7 state (blue circles) and the B", v = 13, Ω = 1 state (black squares).

This is a fairly typical B/B" interaction. The B" state approaches the B state from above because the B"-state rotational constant is smaller and the two manifolds overlap in energy around J = 40. What makes this interaction unique, in the context of the Control Model, is seen in Figure 7-11. This Figure displays the lifetimes of *all four isotopologues* (3232, 3233, 3234, and 3236), as a function of $J(J+1)$.

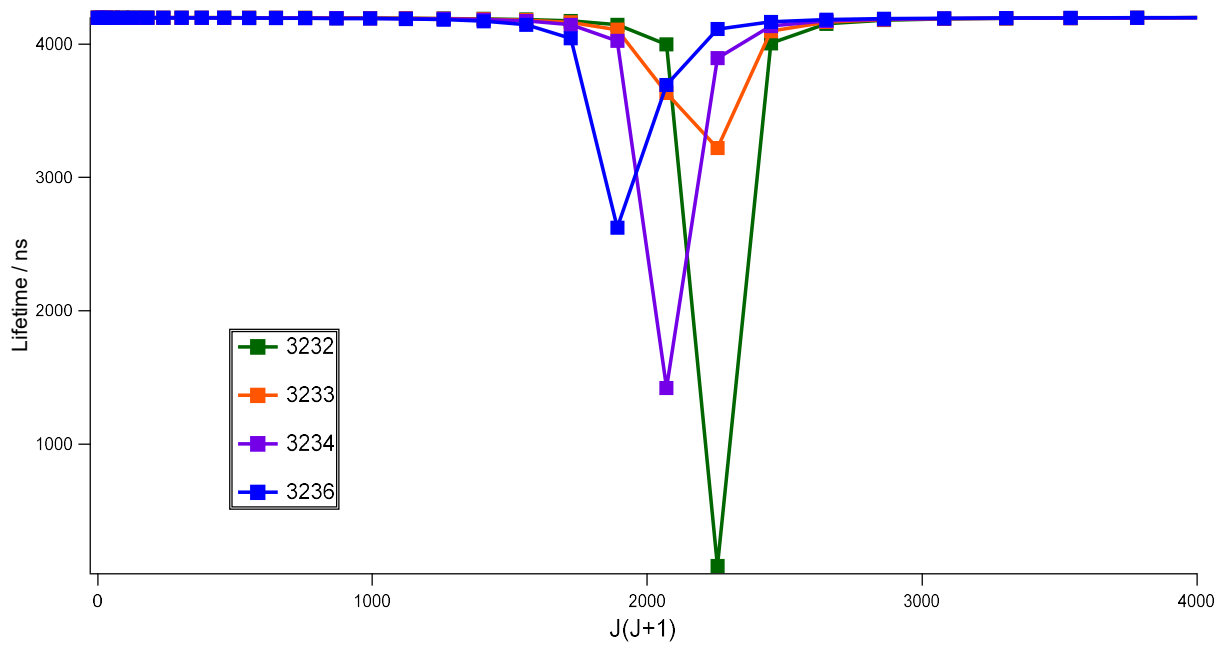

Figure 7-11: The radiative lifetimes of the v = 13, Ω = 1, f-states for all four isotopologues, as a function of J(J + 1).

Figure 7-11 shows the doorway mechanism "in action".[26] In particular, note that the isotopologue that best samples this perturbation the best is 3232 and the isotopologue that samples it least is 3233. This explains the large fractionation observed in Figure 7-4, which showed much more population in this vibrational state for 3233, relative to 3232 (i.e. the 3233 state is less "leaky"). Moreover, the doorway region, where the B and B" states are more strongly state-mixed, is approximately only a single rotational level "wide". That is, the doorway is large enough to be significantly sampled by at least one rotational state, but not much wider than that. Because of this, the sampling is not truly random. The 3232 samples best, while 3233 samples the worst because the mass-dependent level shifts moves those specific J = 47 diabatic rotational states away from the J-value of near degeneracy. Recall that these level shifts cause the B and B" states to cross at lower rotational quantum numbers (Chapter 5). As the level-shift becomes still larger for 3234, the J = 46 diabatic states become more degenerate and sample the doorway region. Figure 7-12 is a cartoon that illustrates this fractionation mechanism in more detail. This pattern of tuning into and out of degeneracy is not pseudo mass dependent, as it was for the larger doorway regions seen in Chapter 5, but it also is not truly random. I could hypothesize, therefore, that this B/B" interaction may represent an intermediate case. As the perturbations become even smaller than those considered in this Control Model, I hypothesize that they may become more "random", and better approximated by the statistical doorway model from Chapter 6. I will examine this hypothesis a bit further in Chapter 8.

[26] Note, however, that this is technically the opposite of the mechanism discussed in Chapter 6. Population moves from the B" state to the B state, rather than from the B state to the B" state.

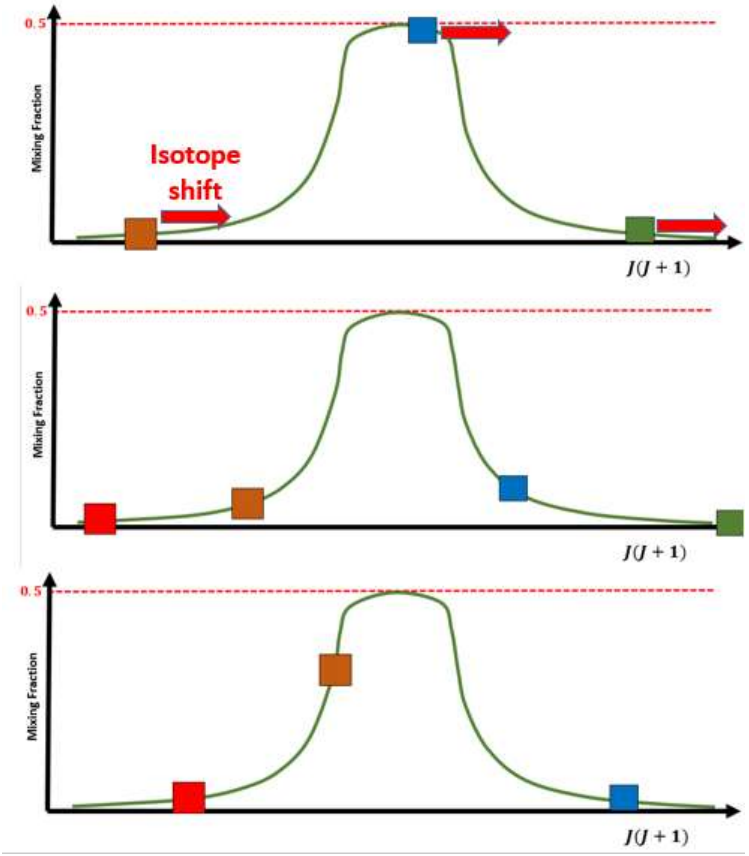

Figure 7-12: A cartoon that illustrates the mechanism responsible for mass-independent fractionation. The independent axis is J(J + 1) and the dependent axis is the B/B" mixing fraction. For a curve crossing between a B and B" state, the mixing fractions roughly follow an inverse square law with energy. However, if the perturbation matrix element is small enough, this continuous function (green) is not completely sampled by the rotational quantum states (colored squares). For one isotopologue (top) the blue rotational state is strongly mixed, but for another isotopologue (middle) the level crossing shifts such that no states are strongly mixed. For an isotopologue where the curve crossing is shifted yet further, a different rotational state becomes mixed (bottom).

7.5. Non-Local Effects in B", $\Omega = 1$, $v = 19$:

7.5.1. Introduction

In every B/B" system considered thus far, the fractionation can be explained by careful consideration of one single interaction. By "single interaction", I mean the B" vibronic state, and the B vibronic state it crosses (or, in the case of section 7.3, the B vibronic state it most closely approaches at thermally relevant values of J). The fractionation typically can be explained by the magnitude and J-location of the local state-mixing, as well as a fundamental understanding of the collisional transfer

model. For the final example interaction discussed in this chapter, I consider the B", $\Omega = 1, v = 19$ state, which cannot be explained by a single, local interaction. This example will force us to consider the larger B/B" system. It is worthwhile to do so, because the fractionation behavior is collective, as opposed to local. That is, nearly all the B" states are fractionated in favor of 32-33, relative to 32-32 (see Figure 7.4).

7.5.2 Fundamentals of the System

Figure 7-13 is the usual reduced term value plot, which shows the interaction between the B", $\Omega = 1, v = 19$ state (red), and the B, $v = 9$ state that it crosses at around $J = 40$ (blue). However, I highlight here that the B state rotational manifold also interacts with the B" $\Omega = 0, v = 19$ state (black)

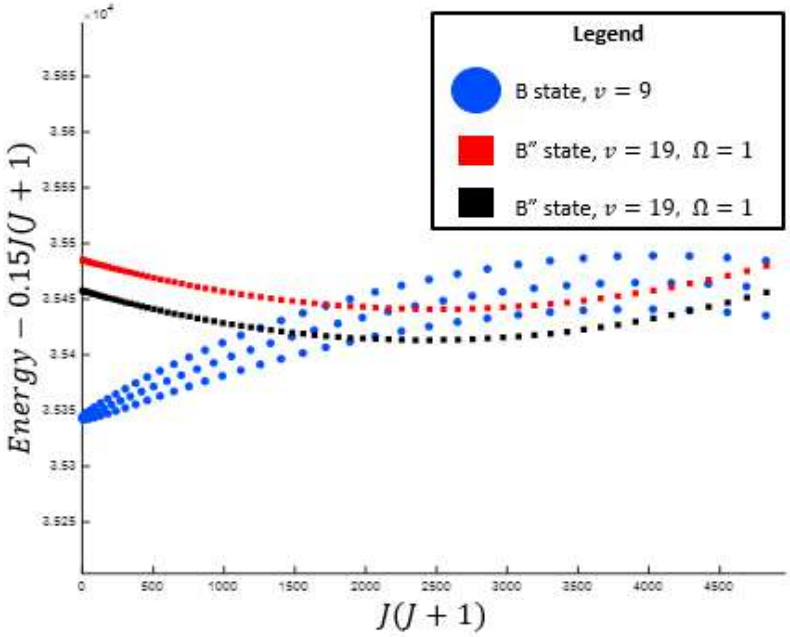

Figure 7-13: A reduced term value plot that describes the level crossing in detail between the B, $v = 9$ (blue circles); the B", $\Omega = 1, v = 19$ (red squares); and the B", $\Omega = 0, v = 19$ (black squares). Note that, in the real system, energy levels above 35,999 cm^{-1}, predissociate. This figure documents the consequently unusual nature of the crossing. The B" states effectively cross the B state twice. This graph is for the 3232 isotopologue.

One other feature to highlight: the two spin-orbit components of $v = 19$ cross the B state in an unusual pattern. For example, the $\Omega = 1$ spin-orbit component crosses both the F_3 and F_2 states in two separate J-locations. This odd interaction occurs because the states predissociate above $35{,}999\ cm^{-1}$. Therefore, Green and Western were only able to fit the rovibronic states below the predissociation limit. This makes it necessary to treat the states above the predissociaton limit by extrapolation, i.e. the energy level structure of the B/B" interaction here is not based completely on available spectroscopic data. However, despite the need for this extrapolation, investigation of this interaction will still yield general insight that will carry forward to our discussion of the B/B" system as a whole.

To continue with the analysis, I plot the B" $v = 19, \Omega = 1$ rotational state lifetimes as a function of $J(J+1)$, for both the 3232 and 3233 isotopologues. I also do this for both f symmetry and e symmetry. This is Figure 7-14.

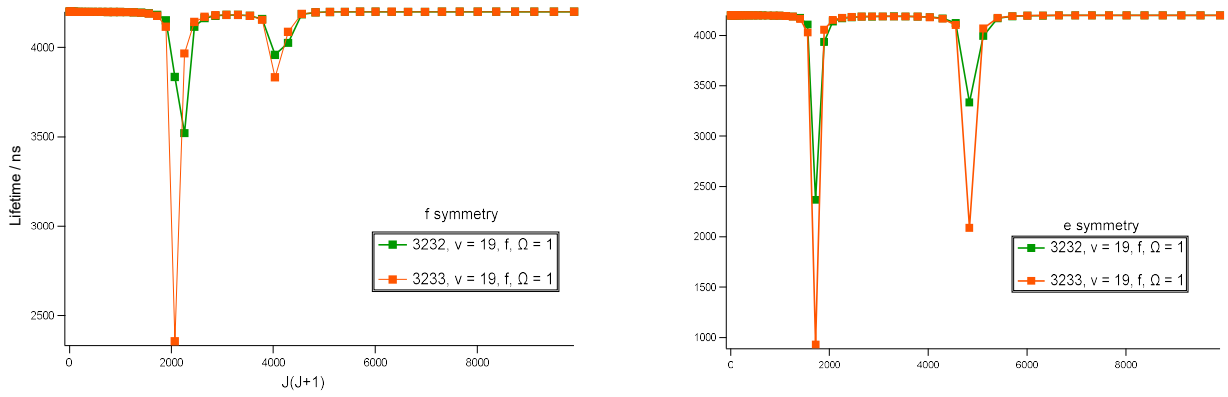

Figure 7-14: The lifetime of the 3232 and 3233 isotopologues, as a function of $J(J+1)$ for the f symmetry $v = 19, \Omega = 1$ states (left), and the e symmetry states (right).

For both e and f symmetries, it is the 3233 isotopologue that samples the more strongly perturbed regions than the 3232. This observation is not consistent with my previous analysis, in both Chapter 5 and in sections 7.3 and 7.4. In general, we would expect the isotopologue that is the "leakiest", i.e. the one with the shortest average lifetime, would contain the least population. However, it is the leaker isotopologue, 3233, that is more populated.

7.5.3 Finding a Fractionation Mechanism

It would be possible, here, to make a similar argument to that in Chapter 6. I could take the perspective of the B, v = 9 state, and argue that because 3233 isotopologue is more state-mixed, it acts as a better doorway, and the B state is better able to move population into the long-lifetime. There are several potential problems with this interpretation:

(1) In Chapter 6, the principal factor in the discussion was the rate of convergence to an equilibrium behavior. That is, the rate at which $\overline{D}$ converges to the equilibrium behavior, $< D > (p)$, was different because asymmetric isotopologues had twice the number of states, compared to the symmetric ones. However, in this control model, all isotopologues are treated as having the same number of states.

(2) The B" states have a greater impact on the isotope fractionation than do the B states. This, of course, is evident from Figure 7.3. But it also follows from the analysis given in sections 5.3.3. and 5.3.4. To summarize, steady state between a ground state and an excited state is established at a characteristic rate $k_{fl} + k_{abs} \approx k_{fl}$. Here, k_{fl} is the fluorescence rate and k_{abs} is the absorption rate. The sum approximately equals the fluorescence rate because $k_{fl} \gg k_{abs}$. This makes the B" state much more important in determining the differences in lifetime, electronic state transfer, etc. A molecule occupying a primarily B" state has more time to fully explore its rotational state manifold than a molecule occupying a primarily B state. This means that a localized doorway (region with large state mixing) has a much larger impact for a molecule occupying a level of the B" state than one occupying a level of the B state.[27]

[27] The reader may recall that a similar argument was made in Chapter 6. The more collisions a molecule experiences, the more likely it is to find a doorway. In this case, a molecule that occupies a B" state has more time to find a doorway than one occupying a B state.

(3) Following a similar line of reasoning, the $v = 19, \Omega = 1$ state crosses a B" state at a relatively high value of J (around J = 40). To see this more clearly, consider Figure 7-15. This figure shows, for the e-symmetry state, the location of the perturbed regions, juxtaposed with on the Boltzmann population distribution for $v = 19$.

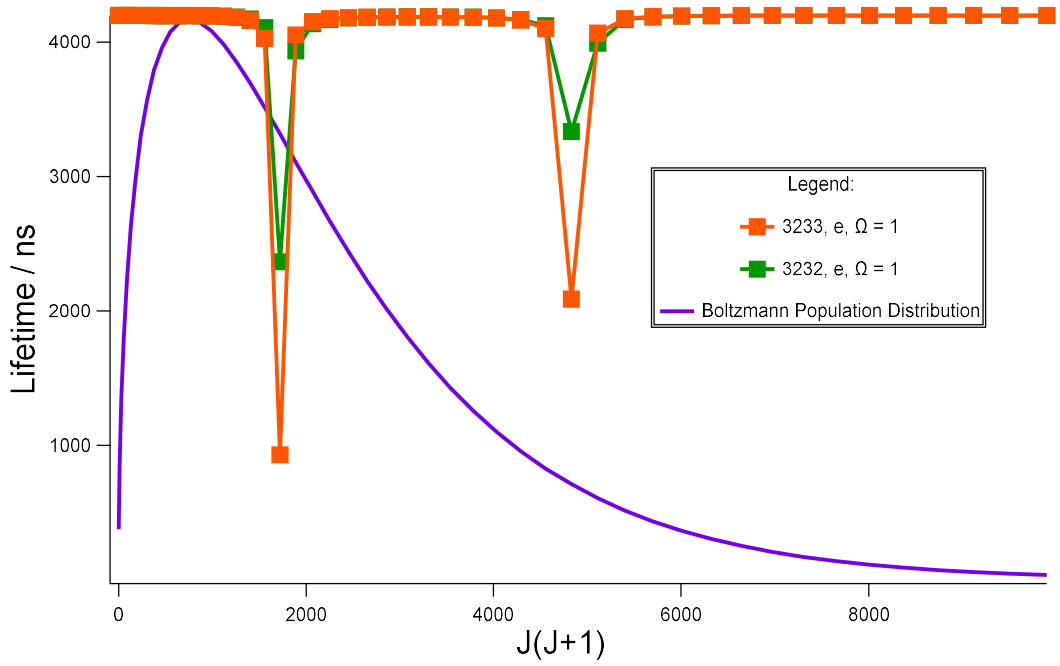

Figure 7-15: A lifetime versus J(J+1) plot for the e-symmetry, v = 19, $\Omega = 1$ states (for 3232 and 3233) This time, it is displayed with the Boltzmann population distribution, shown in purple.

This plot shows that, while the perturbation around J = 40 is significantly sampled, it is still located around 20 rotational states above the maximum of the Boltzmann distribution.

These observation lead me to propose an alternative mechanism by which the $v = 19, \Omega = 1$ may store more population for the 3233 isotopologue than the 3232 isotopologue. This mechanism involves the B" $\Omega = 0$ state. To begin, consider Figure 7-16, which is identical to Figure 7-15, except it displays the $\Omega = 0$ state, instead of $\Omega = 1$.

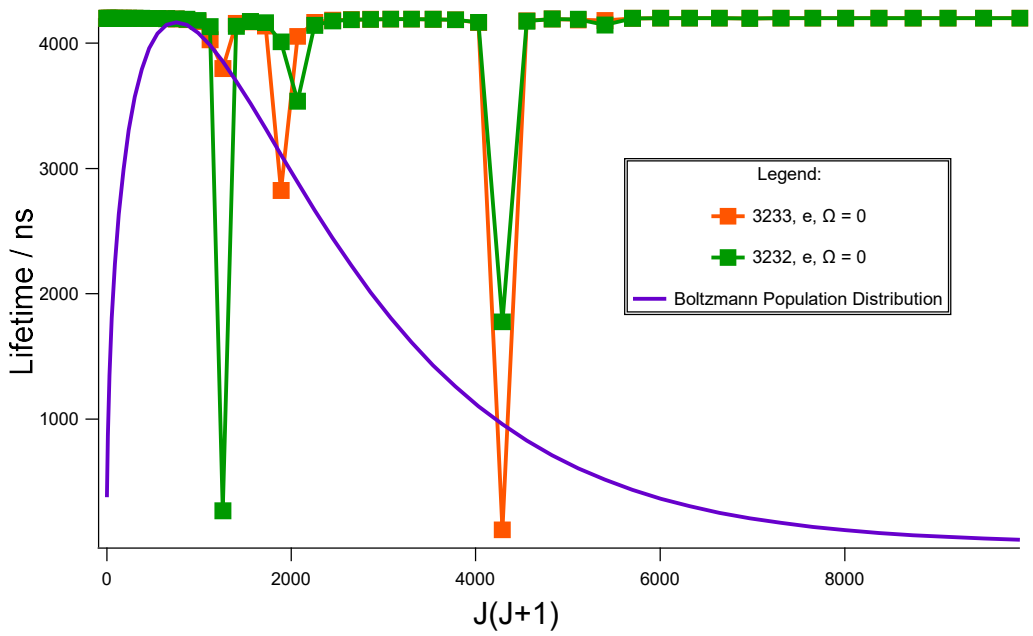

Figure 7-16: The J(J+1) vs lifetime plots (e symmetry) for the **omega = 0 states**.

In this plot, note that there is a very large difference (~1400%) in lifetime between isotopologues at the perturbation closest to the maximum of the Boltzmann distribution. Note also that this 3233-favoring perturbation lies closer to the maximum of the distribution than the 3232-favoring perturbation for the omega = 0 states.

Finally, I must consider the mechanism by which the strongly fractionated $\Omega = 0$ states can influence the $\Omega = 1$ states. Here, I propose electronically inelastic collisions, introduced in section 7.3. The B" $\Omega = 1$ and $\Omega = 0$ states are mixed by the rotational part of the effective Hamiltonian (see section 2.5). For these $v = 19$ states, at J = 35, the mixing fraction, m, is 0.035. If I use the $mZ\tau$ relation (section 7.3.3. and Appendix B) and assume a lifetime of 4200 ns, I calculate that there are approximately 700 collisions that exchange population between the $\Omega = 0$ and $\Omega = 1$ states within the B" state lifetime.

This proposed $\Omega = 1$ fractionation mechanism is illustrated in Figure 7-17. Population is excited into the $\Omega = 1$ manifold, and is transferred back and forth to the $\Omega = 0$ spin-orbit component several hundred times over the course of the B" state lifetime. Over the course of these exchanges, and in combination with random walks in the respective rotational state manifolds, the molecule is exposed to

two different perturbations. The first perturbation, in $\Omega = 1$, affects both the 3233 and 3232 isotopologues, but favors 3232 because it has a 2x larger excited state lifetime than its 3233 counterpart. For the second perturbation, in $\Omega = 0$, the difference in lifetimes is far greater (14x), and favors 3233. Intuitively, we can think of the population "flowing" in the direction of the largest leak, as in Figure 3-7 from Section 3.5.

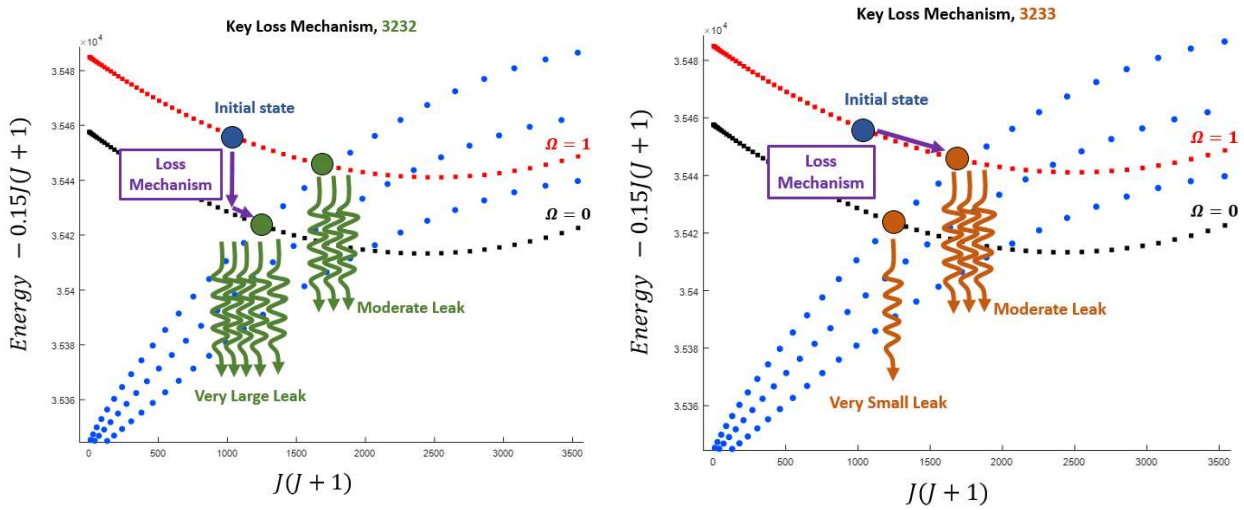

Figure 7-17: A cartoon that depicts the most important loss mechanisms for population that originates around the maximum of the Boltzmann distribution in the $\Omega = 1$, $v = 19$ state (blue circle). For 3232 (left plot), there is a very large "leak" in the $\Omega = 0$ manifold. Therefore, the most important loss process, for the purposes of explaining the fractionation, is electronically inelastic transfer to the $\Omega = 0$ manifold, followed by rotational transfer to the leak. This transfer process is depicted by purple arrows. This loss process is important for the proposed fractionation mechanism because it does not occur in the 3233 isotopologue (right plot). For the 3233 isotopologue, the most accessible leak is the one in the $\Omega = 1$ manifold. While this $\Omega = 1$ leak is larger for the 3233 isotopologue than for the 3232 isotopologue, the magnitude of the discrepancy is not nearly so large as for the $\Omega = 0$ case. I hypothesize that this $\Omega = 0$ leak is responsible for the fractionation in the $\Omega = 1$ state.

Of course, the population is not literally flowing; it is undergoing a random walk. However, if we consider the trajectory of a single molecule that occupies the B" manifold, the most likely final state is the shortest-lifetime state. Likewise, the rotational states adjacent to the perturbation are likely candidates for the second-to-last state occupied, and so on. If I was to average over a large number of random trajectories, the most likely trajectory would manifest a tendency to "flow" in the direction of the leak.

7.6 Applying These Three Examples to the Broader B/B" system

I return now to the questions posed in Section 7.2. (1) Why do the three Ω components of the Control Model behave have similar fractionation patterns? (2) Why do the e/f symmetry components also have similar fractionation patterns?

The first question is the easiest to answer: long-distance, electronically inelastic collisions. As demonstrated in section 7.5, the rotational perturbations that slightly state-mix the B" spin-orbit components generally satisfy the $mZ\tau$ criterion. Note, in particular, Figure 7-17, where the "jump" from the $\Omega = 1$ state to the $\Omega = 0$ state has a ΔE larger than 20 cm^{-1}. These long-range interactions, where population is rapidly transferred back and forth among all three spin orbit components likely homogenizes their fractionation patterns.

The second question requires a more complex explanation. Recall from Section 3.4 that e/f-symmetry changing collisions are generally forbidden in a $^3\Pi$ state because they involve a change in spin-eigenfunctions ($\Sigma = -1 \leftrightarrow +1$,). There is one exception, however, and that is the $\Omega = 1$ component, which has $\Sigma = 0$. Therefore, e/f-changing collisions are allowed in this particular spin-orbit component. Evidence of this "special" property of the $\Omega = 1$ levels can be seen in Figure 7-4. While all three B" spin-orbit components have the same pattern (i.e. they all hold more population for the 3233 isotopologue than for the 3232 isotopologue), the $\Omega = 1$ component has the largest magnitudes. Now, recall Section 7.5. In that section, I explored the concept of non-local behavior, where a localized perturbation was, in effect, overridden by a larger perturbation in a neighboring spin-orbit component. (Or to use different terminology, the excited state population tends to "flow" toward the largest leak.) Viewed in this context, the e/f breaking collisions expand the total state space available to the $\Omega = 1$ states. In other words, if there is an especially strong perturbation, the e/f breaking collisions increase the number of states that can easily access it. Put still differently, the e-f breaking collisions allow population to "flow" more easily. If we combine the conclusions from sections 7.3. and 7.5, we arrive at a plausible explanation for the "global behavior" observed in Figure 7-4: The $\Omega = 1$ component acts as a "bridge" between the e-symmetry and f-symmetry states, and the effects of this bridge extend into the other two

spin-orbit components because population can exchange between them via an electronically inelastic mechanism.

The most important aspect of these results is that the weak state-mixings are able to generate significant fractionation, even in the absense of the statistical effects, due to the extremely large number of collisions at 300 K and 1 atm of pressure (on the order of 10^9 collisions per second). As seen in the previous sections, the Control Model is perhaps best thought of as a large network of states, a large space for an excited S_2 molecule to "explore". The space is so large because weakly interacting states that are 10's of wavenumbers apart in the diabatic picture can still exchange population because there are a large number of collisions within the B" state lifetime. This is the essence of the $mZ\tau > 1$ criterion.

Recall from section 7.3 that, assuming a 4200 ns lifetime for the B" state, the minimum value of $m = 0.002$ %. If I were to consider an excited state with a lifetime of 4.2 ms, the minimum value of m drops to 0.000002%. This does not guarantee that state-mixings this small will generate interesting or significant isotope effects. For example, if off-diagonal matrix elements become too small, accidental degeneracies between the diabatic curves may become too rare. However, the results from Chapter 6 and Chapter 7 show that weakly perturbing systems may be key to understanding isotope effects in excited states of S_2, as well as in other molecules. I will address this question, in a preliminary manner, in Chapter 8.

Chapter 8 : Can Statistical Isotope Effects be the Origin of S-MIF in the Archean Reference Array? Next Steps and Concluding Remarks

8.1 Introduction:

In the preceding three chapters, I have drawn a number of conclusions regarding excited state collisional transfer as a mechanism for sulfur mass-independent fractionation (S-MIF). In chapter 5, I concluded that, for the B/B"-X system neither a mechanism that involved predissociation, nor one that involved only bound states, was a likely source of S-MIF in the rock record. Instead, the observed fractionation approximated a mass-dependent pattern. And, in particular, the weakly state-mixed vibrational levels of the long-lifetime B" state were responsible for generating the largest amount of this pseudo-mass-dependent fractionation.

This analysis led to a hypothesis that small perturbation matrix elements and/or weak state-mixings may be more effective than the B/B"-X at generating S-MIF. I demonstrated this in Chapters 6 and 7 by artificially changing the perturbation matrix elements to be 1% of their empirically determined values. These isotope effects were observed to have both statistical (Chapter 6) and non-statistical (Chapter 7) elements. In particular, I observed in Chapter 7 that electronically inelastic collisions can generate fractionation at very small state-mixings (approximately 0.002%).[28]

The primary scope of this work has been to characterize mechanisms by which collisional transfer can induce isotope fractionation. In this final chapter, I begin to expand the scope and consider the following question: what are the ideal conditions for generation of the statistical S-MIF signature described in Chapter 6? This question is of particular interest because that pattern best approximates the Archean Reference Array. The answer is likely a complicated function of a variety of parameters: the vibrational levels of the two electronic states, their rotational constants, their relative lifetimes, the size of the off-diagonal matrix elements that connect them, etc.

[28] This is the $mz\tau$ criterion, described in section 7.3.

In section 8.2, therefore, I consider a single parameter: the size of the perturbation matrix elements and begin to determine whether there is an optimal value to produce a prominent statistical isotope effect. In section 8.3, I consider the robustness of the predicted fractionation with changing temperatures and other adjustable parameters. In section 8.4, I consider the effect of a total +/- parity changing collisions on the fractionation of the three asymmetric isotopologues.

The analyses in this chapter will be shorter and somewhat more speculative, compared to the more extensive discussions in the preceding chapters. Their purpose is to take an initial few steps down several suggested routes for further study. In sections 8.5 and 8.6, I conclude this thesis and attempt to place these results in a wider context.

8.2. Statistical Isotope Effects and Perturbation Matrix Element Size

In this section, I use a model very similar to that considered in Chapter 6. That is, I use the B/B" system described and fitted by Green and Western, with a few modificiations: uniform Franck Condon factors and no predissociation for high rotational states of vibrational states bound at $J = 0$. For the complete details, see section 6.8. Here, however, I vary the size of the perturbation matrix elements on a logarithmic scale from 0% percent to 10% of those reported by Green and Western.

Figure 8-1 shows the usual pressure versus quantity-reacted plots, for the lowest three matrix element sizes, 0%, 0.001%, and 0.01%. The first, 0% perturbation plot serves as a control; there is no change in the quantity reacted into the rock record, as a function of pressure. This is in agreement with our understanding of the collisional transfer mechanism, as no doorways between the B and B" states exist for this 0 % control model. The next two plots show very weakly perturbed systems. In the middle plot, 0.001%, there is no apparent change in fractionation with pressure. This, of course, implies a lower limit, i.e. perturbations can be too small to generate any significant isotope effect. We begin to observe a small amount of fractionation with the third and final plot, though it only appears at pressures around 1 atm. This could be interpreted in terms of the doorway mechanism. As the size of the matrix elements

increase, the ability of an excited B state molecule to find a doorway to a B" state correspondingly increases.

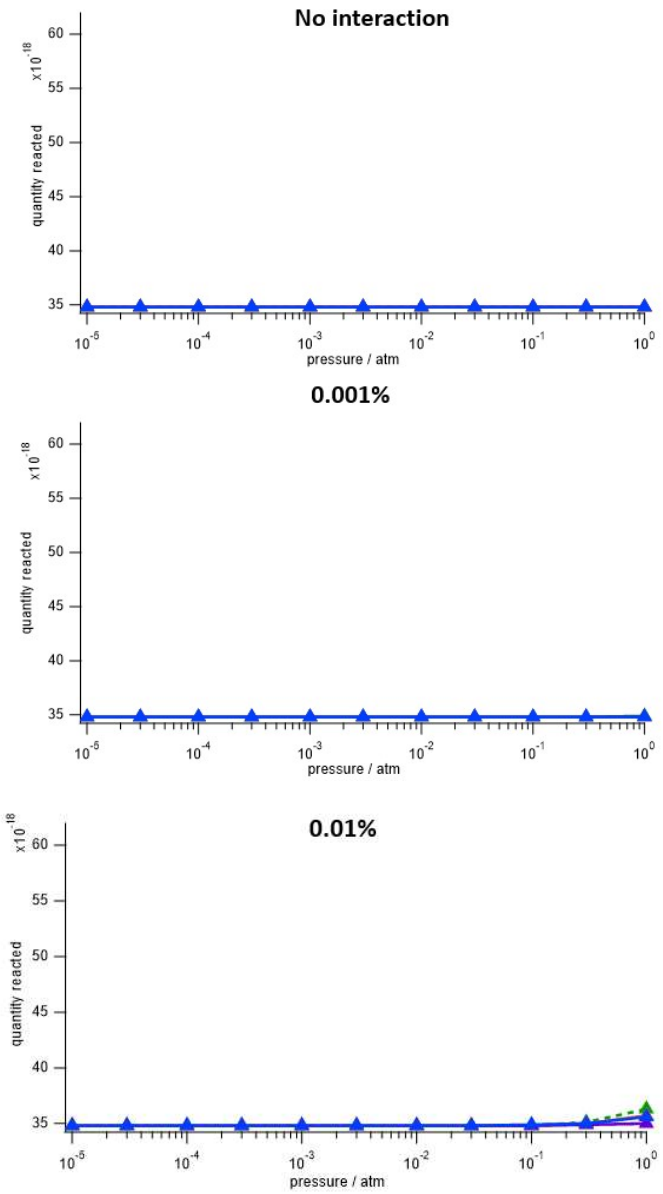

Figure 8-1: Quantity of each isotope entering the rock record, as a function of pressure, for the smallest perturbation matrix elements (0%, top; 0.001% middle, and 0.01% bottom of the values reported iby Green and Western). In these plots, the blue solid line represents 3236; the purple solid line, 3234; the orange solid line, 3233, and the green dashed line, 3232.

Next, Figure 8-2 shows similar plots, but with larger perturbation matrix elements $(0.1\%, 0.3\%, 0.75\%, 10\%)$.

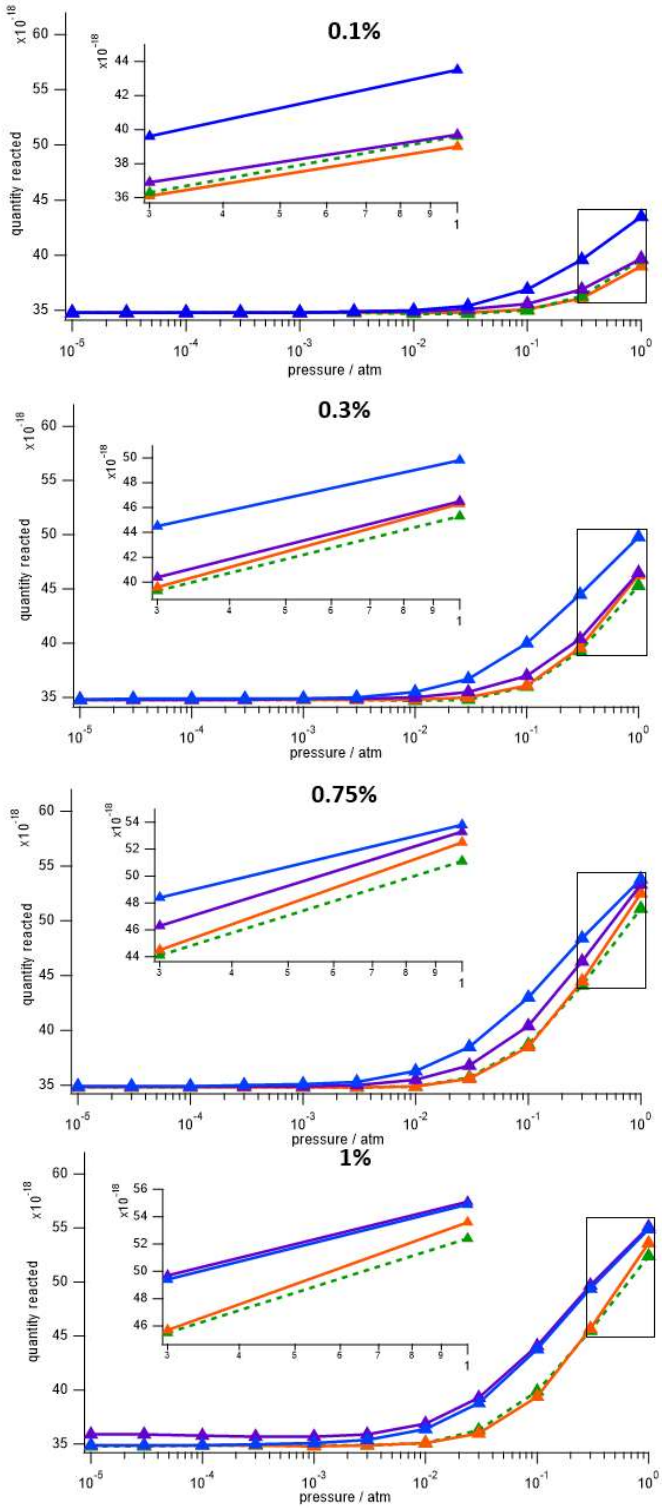

Figure 8-2: Quantity of each isotopologue entering the rock record, as a function of pressure, for the moderately-sized perturbation matrix elements. The percentages indicate the size of the perturbation matrix elements, relative to the values reported in Green and Western. The insets highlight the 0.3 and 1 atm data points. In these plots, the blue solid line represents 3236; the purple solid line, 3234; the orange solid line, 3233, and the green dashed line, 3232.

In these plots, we should first note that the fractionation begins at lower pressure as the state-mixing increases, as is expected. Second, the top two plots (0.1% and 0.3%), show an isotope effect that strongly favors 3236. This is even more clearly visible in the insets. As the matrix elements increase in size, the other two asymmetric isotopologues (3233 and 3234) converge in behavior to 3236, while 3232 becomes the least reactive. This is especially true for the 0.75% case, and the 1 % case (which we, of course, explored in Chapters 6 and 7).

Figure 8-3 shows the three cases with the largest state-mixings, 3%, 7.5%, and 10%.

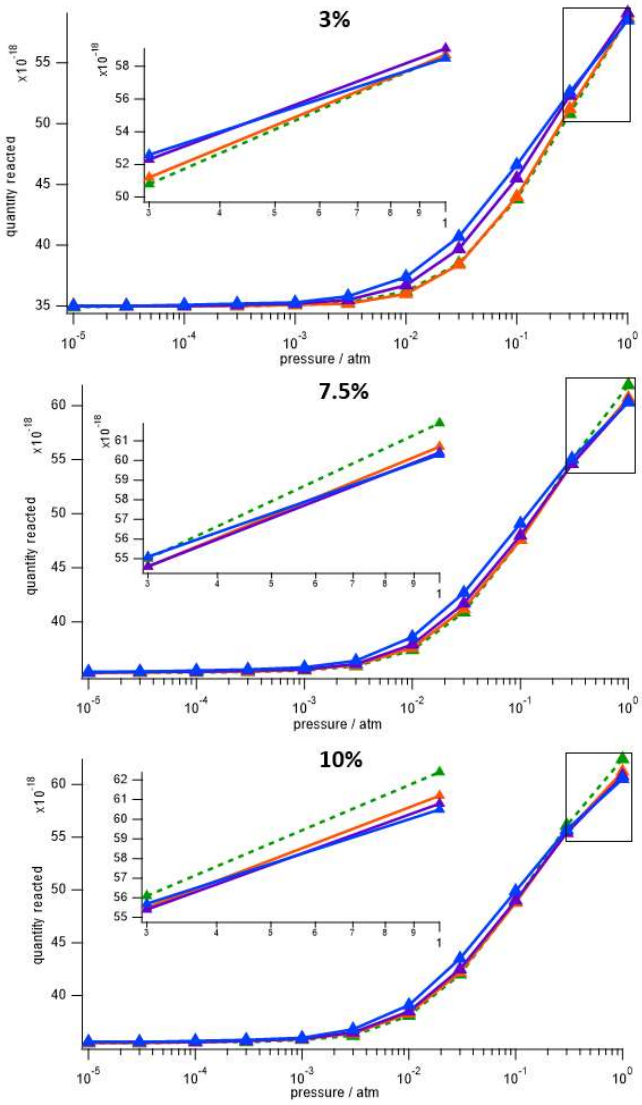

Figure 8-3: Quantity of each isotopologue entering the rock record, as a function of pressure, for the largest perturbation matrix elements, 3%, 7.5%, and 10% of those determined by Green and Western.

For these plots, the 3232 isotopologue switches from the least reactive to the most (see the 0.3 and 1 atm insets).

A speculative interpretation of these patterns is as follows: for the 0.1% and 0.3% plots, shown in Figure 8-2, sulfur mass-independent fractionation is observed. However, this is not the more statistical pattern (where the three asymmetric isotopologues are enriched relative to 3232) observed in the rock record. Instead, 3236 is enriched relative to all other isotopologues. Doorways may exist for 3236 that do not exist for the other three isotopologues.[29] This would occur because the accidental degeneracies are too rare, due to the small matrix elements (recall Figure 6-1 from section 6.1). Therefore, even with the large number of collisions at one atmosphere of pressure, the behavior of the three asymmetric isotopologues does not converge.[30]

For the 0.75% and 0.1% plots, statistical convergence behavior is observed. In fact, the convergence behavior is even more pronounced for the 0.75% plot than it is for the 1% plot that was analyzed in Chapters 6 and 7.

For the final three plots, 3%, 7.5%, and 10%, the isotopolouges begin to separate according to their reduced masses. Note, in particular, the 10% inset, where we have the 3232 > 3233 > 3234 > 3236 pattern that we first observed in the non-predissociating model from Chapter 5. That is, when the perturbations become large enough, the doorway is always sampled. Therefore, the energy level structure

[29] Alternatively, this could indicate that doorways exist for three of the four other isotopologues that do not exist for 3236.

[30] Recall from Chapter 6, that D is a random variable that represents the fraction of excited state molecules that reach a doorway. This variable is sampled by the various state-crossings in the B/B" system. In the case of the 0.1% and 0.3%, where the perturbation matrix elements are very small, the variance of D is very large. That is, it is unlikely that a single crossing will result in a coincidental degeneracy. Therefore, even with a large number, N, of state crossings, the sample average, $\overline{D}$ still has a large standard deviation. Per the Central Limit Theorem, because σ for D is so large, $\sigma/\sqrt{N}$ for $\overline{D}$ remains large.

of the B/B" system becomes more important, and the fractionation behavior reflects the systemic, pseudo-mass-dependent behavior that is described in detail in sections 5.3 and 5.4.

These observations, taken together, may indicate a type of "Goldilocks" behavior. If the state-mixings are too large the behavior becomes, pseudo-mass-dependent. If the state-mixings are too small, the odds of sampling a doorway are too small, and we observe more erratic fractionation behavior, if any at all. This behavior, while technically mass-independent, does not show the statistical convergence required to explain the Archean Reference Array. The 0.75% and 1% plots shows a possible regime where the perturbations are "just right", i.e. neither too large nor too small.

As a summary of this behavior, consider Figure 8-4, which uses the 1 atm data for all of the plots shown in Figures 8-1 through 8-3. This plot shows the **difference** between the symmetric 3232 isotopologue and an **average** of the three asymmetric isotopologues, as a function of the perturbation matrix element size.

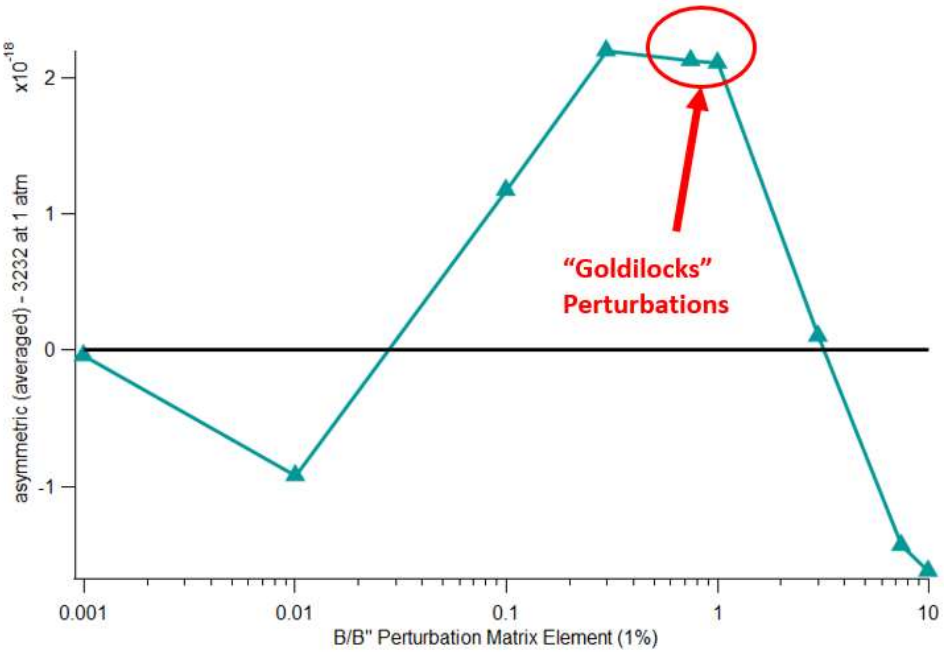

Figure 8-4: For the 1 atm data points from the previous three figures (8-1, 8-2, and 8-3), the difference between the average of the three asymmetric isotopologues and the symmetric 3232. The two "Goldilocks" perturbations, those that produce the convergent behavior described in Chapter 6, are circled in red.

This plot does not provide a complete picture of the behavior. For example, the 0.3% data point favors the asymmetric isotopologues strongly but does not display the convergent behavior that the 0.75 and 1% data points do. However, the behavior shown by this graph matches the interpretation presented in this chapter. The three data points with the smallest perturbations show erratic behavior, while the three data points with the largest show the system shifting toward the pseudo-mass-dependent behavior, which favors the lightest isotopologue, 3232.

Finally, I plot Δ^{33} and Δ^{36}, as a function of perturbation matrix element size. This is Figure 8-5. The two "Goldilocks" states are the only two that display $\Delta^{33} > 0$ and $\Delta^{36} < 0$, as in the Archean Reference Array.

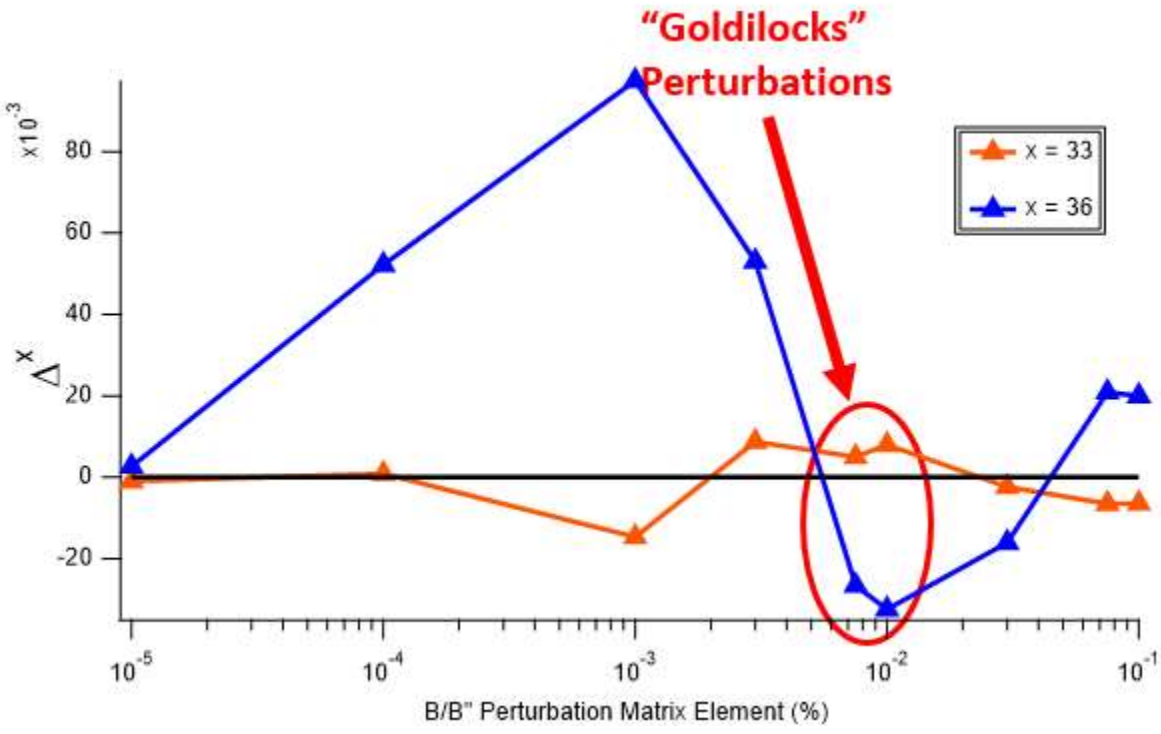

Figure 8-5: Δ^{33} and Δ^{36}, as a function of perturbation matrix element size.

8.3 The Robustness of the S-MIF isotope effect.

In this thesis, I have not yet explored the effects of two adjustable parameters on the S-MIF signature produced by the master equation model. The first of these two parameters was introduced in Chapter 3. Recall the Power Gap (PG) Law from Chapter 3, reproduced here as Equation 8.1.

$$k_{J_1 \rightarrow J_2} = a\left|\frac{\Delta E}{B}\right|^{-\alpha} \tag{8.1}$$

In this equation, a is a proportionality constant. I can solve for a easily, if I assume that all collisions are rotationally inelastic (see: Equations 4.8 and 4.9). The parameter ΔE is the difference in energy between the initial and final rotational states (see: Chapter 2), and B is the rotational constant. This leaves α, which we have, until this point, assumed to be equal to 1.2. Recall from Chapter 3 that fif an internuclear potential, V(r), is given by Equation 8.2

$$\mathrm{V(r)} = r^{-n}, \tag{8.2}$$

where r is the internuclear distance between the S_2 molecule and its inert collision partner. The parameter γ is related to the parameter n as follows (Equation 8.3) [65] .

$$\alpha = \frac{n}{n-1} \tag{8.3}$$

Therefore, the choice of $\gamma = 1.2$ corresponds to $n = 6$, i.e. a van der Waals interaction.

The power gap law has been fit to a wide variety of experimental data. In these studies, the fitted values of α have varied from approximately 1.0 to 1.4. This is the first adjustable parameter that will be analyzed in this section.

The second is the temperature, T. Recall from Chapter 4 that the rotationally inelastic collisions are weighted by a Boltzmann factor that is, itself, a function of temperature. I reproduce this expression here as Equation 8.4

$$\frac{k_{2\to1}}{k_{1\to2}} = \frac{(2J_1+1)}{(2J_2+1)} e^{\frac{\Delta E}{k_B T}}, \tag{8.4}$$

where $k_{1\to2}$ is the rate constant for a transfer from eigenstate 1 to eigenstate 2, and vice versa for $k_{2\to1}$. J_1 and J_2 are the rotational quantum numbers for their respective eigenstate, ΔE is the difference in energy between the respective eigenstates, k_B is Boltzmann's constant, and T is the temperature. Recall that, by enforcing the constraint given in Equation 8.4, the rotational state distribution within a given vibronic state will converge toward a Boltzmann distribution as the number of collisions increases. Most factors in this expression are determined by the choice of states 1 and 2. The exception is the temperature, T. For most of this thesis, I have assumed the temperature to be constant at 300 K. The one exception was the temperature profile that was included in the isotope effect versus altitude described in section 5.5. In this section, the temperature is the second adjustable parameter. In simple terms, the temperature affects the "broadness" of the Boltzmann distribution, i.e. a higher-temperature system samples a wider range of rotational states, and also the *maximum* of that distribution, i.e. the higher the temperature the smaller the maximum of the probability distribution.

The goal for this section is to analyze the robustness of the fractionation produced by the S-MIF model. Or, in other words, I explore the extent to which uncertainty in the values of these adjustable parameters creates uncertainty in the predicted S-MIF. In this section I use the weak perturbation model, from Chapter 6, Section 6.8., because it produces larger S-MIF than the strong perturbation models from Chapter 5.

To begin, α will be varied from 1.0 to 1.6. Figure 8-6 shows the three δ^x parameters: δ^{33}, δ^{34}, δ^{36} as a function of α, for the weak perturbation model at 300 K and 1 atm. Likewise, Figure 8-7 shows the two Δ^x parameters, Δ^{33} and Δ^{36}. The dependent-axis scale is identical for both plots.

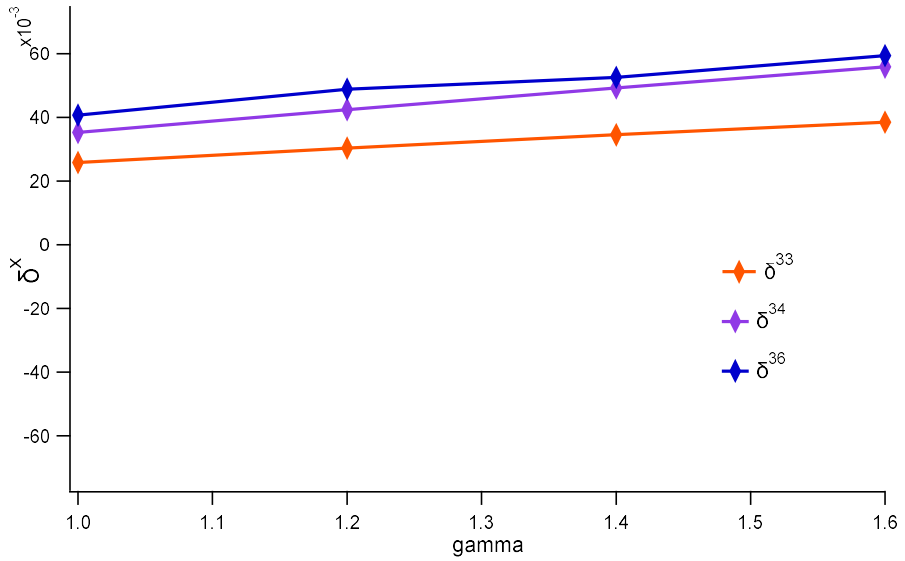

Figure 8-6: The δ^x parameters for the 33, 34, and 36 isotopes, as a function of the alpha,α, parameter from the power gap law shown in Equation 8.1.

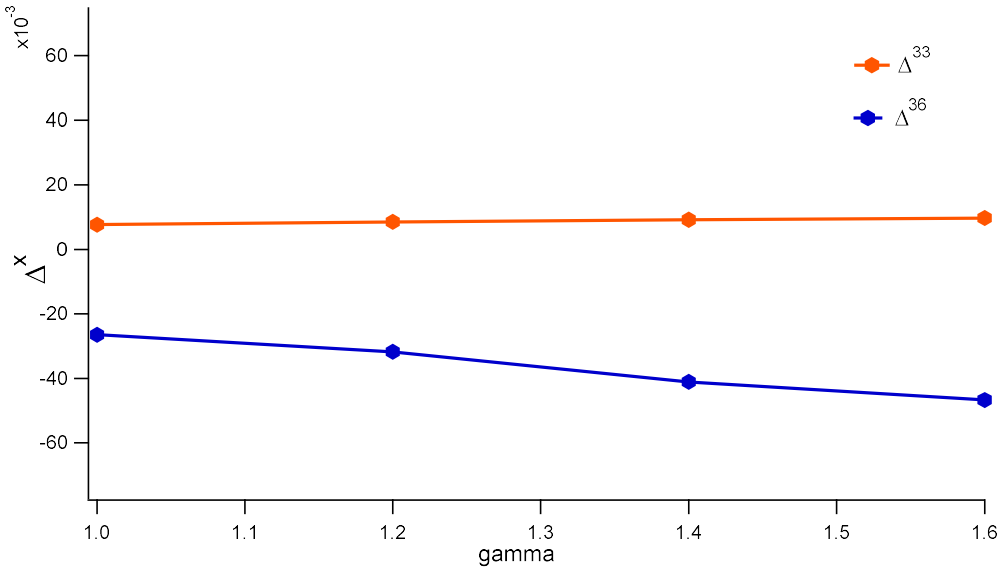

Figure 8-7: Δ^{33} and Δ^{36}parameters, calculated from the δ^x parameters shown in Figure 8-6, as a function of α.

These plots, taken together, show that variation of the α parameter does not have a large effect on the predicted fractionation. The Δ^{33} parameter does not change significantly. The δ^{36} parameter decreases relative to the δ^{34} and δ^{33} parameters for the values $\gamma = 1.4$ and 1.6. This corresponds to a 46% difference in the *magnitude* of the Δ^{36} parameter. However, the signs of both parameters remain the same.

Figures 8-8 and 8-9 display the effect of temperature on both the lower-case and capital delta parameters. Here, the temperature varies from 200 K to 350 K, with $\gamma = 1.2$. To facilitate comparison, the dependent axis scale remains the same as in the previous two figures.

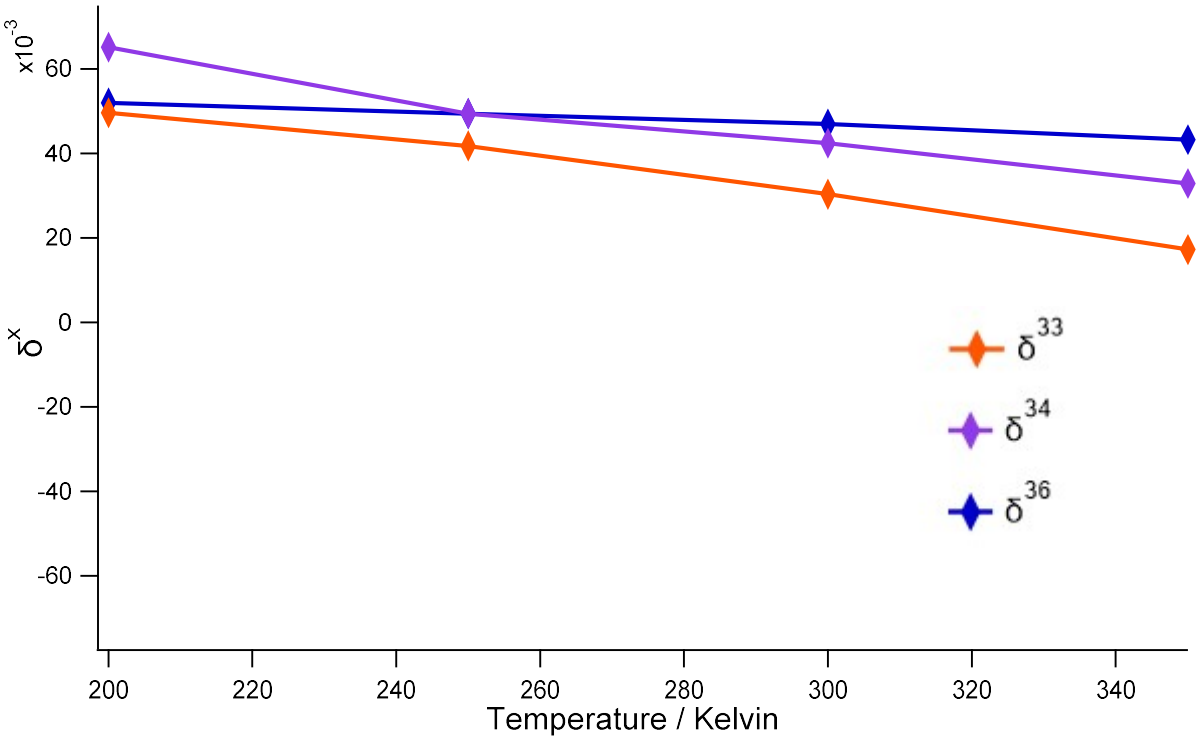

Figure 8-8: The three δ^xvalues, plotted as a function of temperature for the weak perturbation model.

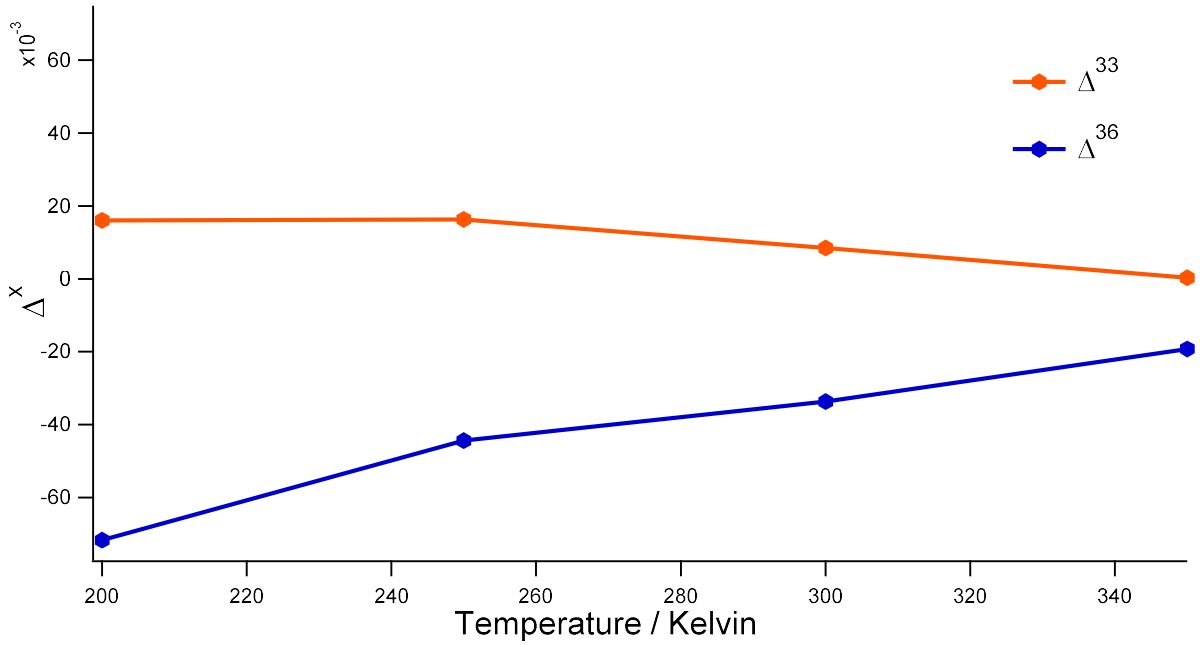

Figure 8-9: The Δ^{33} and Δ^{36}parameters, calculated from the δ^{x} parameters from Figure 3, as a function of temperature.

These figures show that temperature has a larger effect on the S-MIF signature than does α.The first plot, Figure 3 , shows that the δ^{34} parameter exchanges with the δ^{36} parameter as the temperature increases, $\delta^{34} > \delta^{36}$ to $\delta^{36} > \delta^{34}$. Consequently, the magnitude of the Δ^{36} parameter decreases by about a factor of 4.

Taken together, these four plots support two important conclusions.

(1) **The temperature has a more substantial effect on the predicted S-MIF than does the α parameter from the rotational power gap law.** This conclusion makes intuitive sense when considering Equation 8.1 in conjunction with Equation 8.4. Equation 8.1 tells us that, as α increases, smaller changes in energy are preferred over larger ones. This is the cause of small differences in fractionation patterns observed in the first two figures (1 and 2). However, varying α does not affect the Boltzmann constraint given by Equation 8.4. That is, at long times the rotational probability distribution will still converge to a Boltzmann distribution at

300 K. Recall from Section 7.3 that, at 1 atm, an S_2 molecule will undergo approximately 20,000 collisions within the lifetime of the B" state, which well exceeds the minimum required for such a convergence. Therefore, the molecule, despite different α values, will still display identical long-term behavior. The long-term behavior can only be changed by changing the temperature. Therefore, uncertainty in the temperature creates more uncertainty in the predicted S-MIF than does the exact form of the rotationally inelastic collision model.

(2) **The magnitude of the fractionation can change appreciably (especially with temperature) but the qualitative pattern remains the same.** In other words, when allowing α and T to vary over essentially all physically reasonable values, the signs of Δ^{33} and Δ^{36} do not change. This is especially true for α, but it remains true for T as well. This conclusion matches the analysis from the previous three chapters: it is the energy level patterns of the B and B" states, as well as the magnitudes and locations of their perturbations, that determines the qualitative fractionation pattern. A change in temperature will change the probability of sampling a given level crossing somewhat, but the overall structure of the rotational state space does not change.

Overall, of the two adjustable parameters considered here, temperature has a much stronger influence on the overall behavior. However, the qualitative behavior is much more strongly determined by spectroscopic patterns more than the specific choice of these two parameters.

8.4 The Inclusion of +/- parity Breaking Collisions

In every model considered thus far, I have excluded the possibility of *total parity changing collisions*, i.e. collisions that move population from a (+) parity state to a (-) parity state. In this section, I include the total parity conserving collisions as usual, but include $(+) \leftrightarrow (-)$ collisions as follows in Equation 8.5,

$$k_{J_1(+/-) \rightarrow J_2(-/+)} = 0.1 * a\left|\frac{\Delta E}{B}\right|^{-\gamma} \tag{8.5}$$

That is, the cross sections for parity changing collisions are set to be 10% as large as the power gap model would otherwise predict. This applies to only the asymmetric isotopologues, as the symmetric isotopologues have only a (-) parity manifold. 10% is also certainly an overestimate (see section 3.3.). However, such an overestimate is useful because it allows us to view the resulting isotope effects more clearly. Note that the sum of the inelastic rate constants into a given eigenstate are still normalized to the total collision rate, as in Section 4.4. That is, there are net zero additional collisions created by including Equation 8.5 into the Master Equation model. In this section, results are presented for both the "strong perturbation model" (section 5.1) and the "weak perturbation model" (section 6.8) at 300 K.

First, I show the results of the strong perturbation model, including the additional collisions given by Equation 8.5 (Figure 8-10).

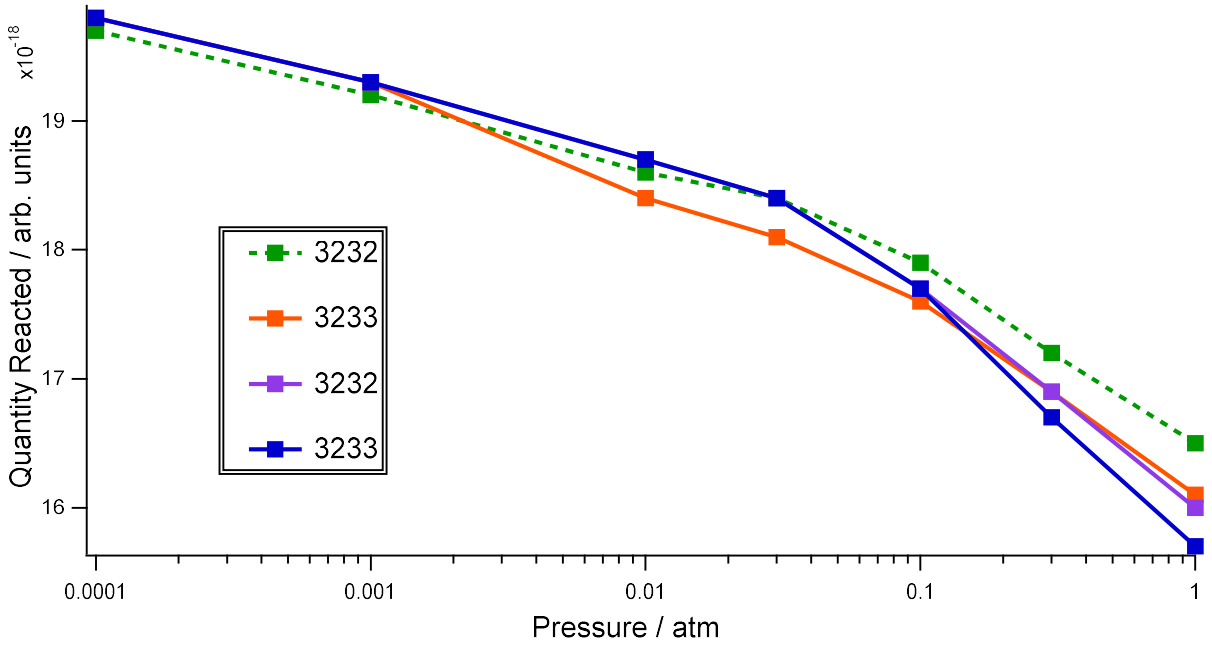

Figure 8-10: Results from the strong perturbation model with the 10% parity breaking collisions described in Equation 8.5. The independent axis is the pressure of the atmosphere at 300 K. The dependent axis is the quantity reacted.

Next, I show $\frac{\Delta^{36}}{\Delta^{33}}$, calculated for the data given in Figure 8-10. This is Figure 8-11.

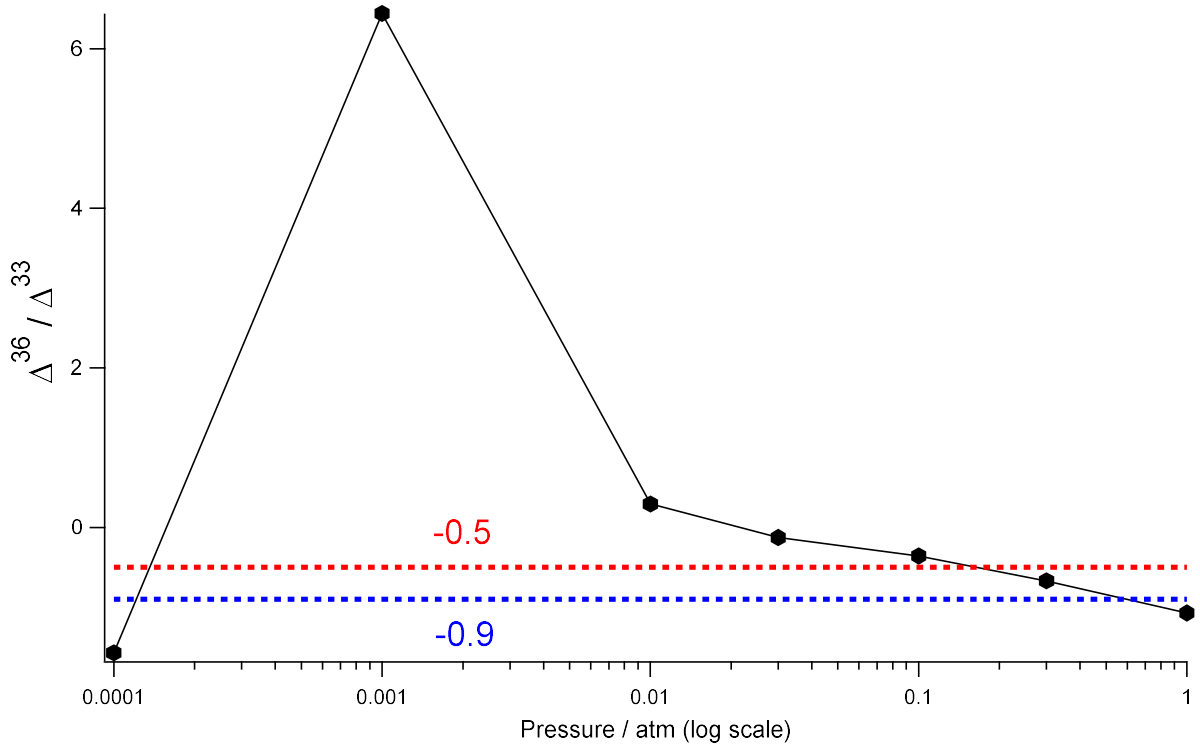

Figure 8-11: shows $\frac{\Delta^{36}}{\Delta^{33}}$, calculated for the data shown in Figure 8-10. The red line and the blue line show the two $\frac{\Delta^{36}}{\Delta^{33}}$ values observed in the rock record.

Figures 8-12 and 8-13 are identical to Figures 8-10 and 8-11, but are based on the weak perturbation model.

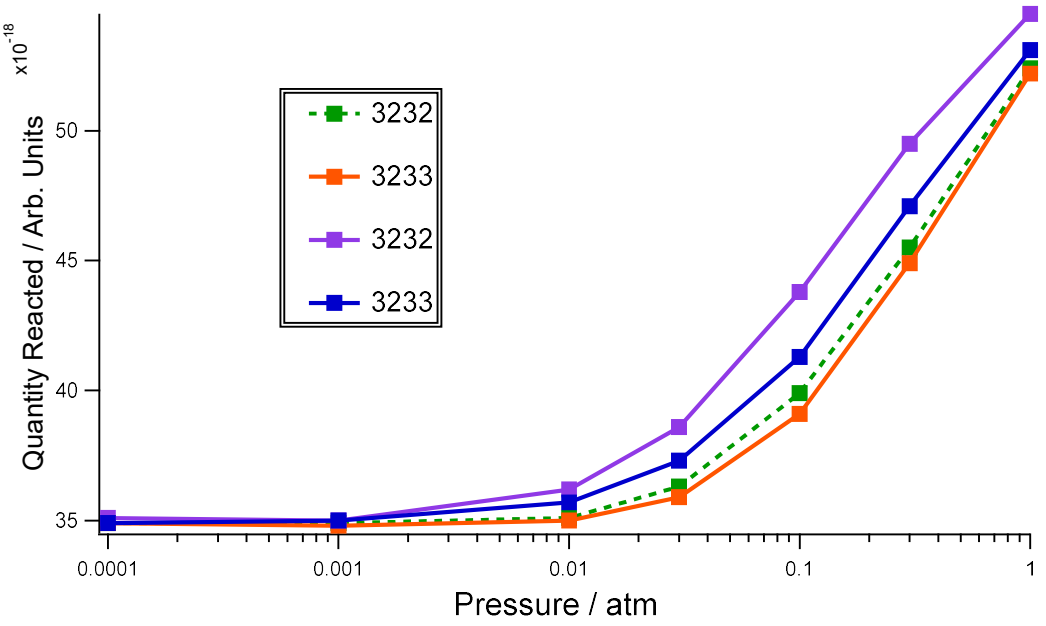

Figure 8-12: Results from the weak perturbation model when the 10% parity breaking collisions. The independent axis is the pressure of the atmosphere at 300 K. The dependent axis is the quantity reacted

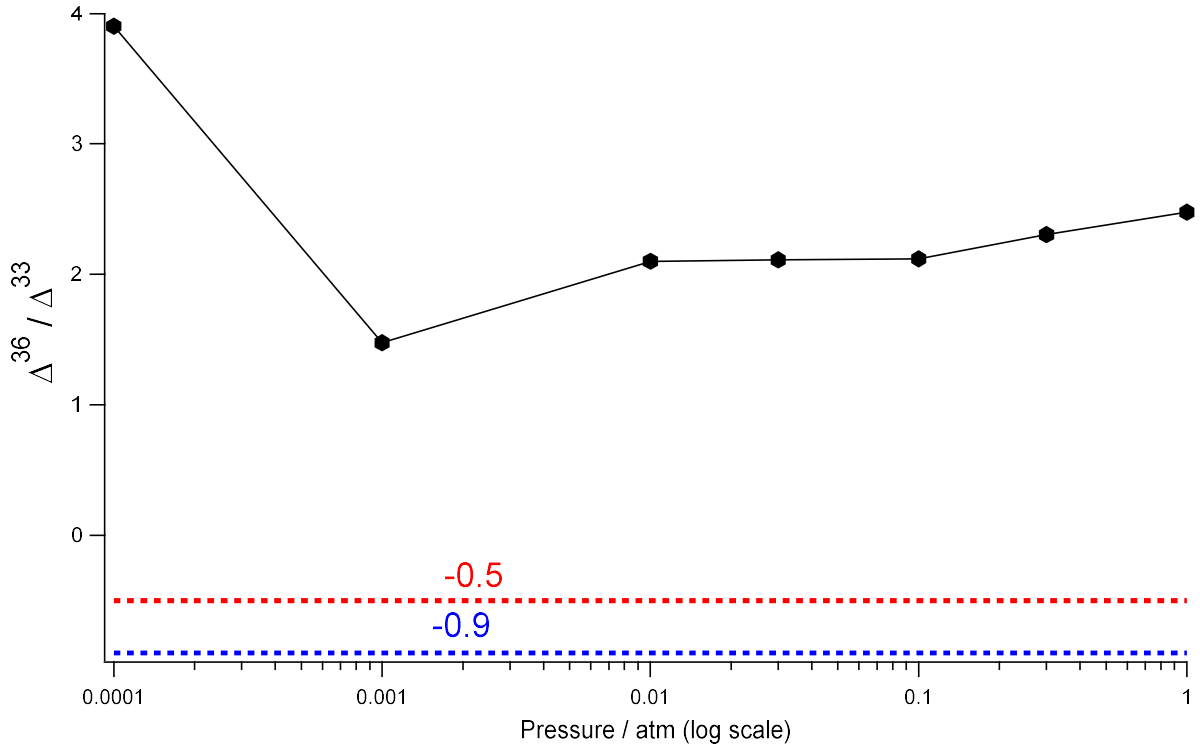

Figure 8-13: shows $\frac{\Delta^{36}}{\Delta^{33}}$, calculated for the data shown in Figure 8-12. The red line and the blue line show the two $\frac{\Delta^{36}}{\Delta^{33}}$ values observed in the rock record.

Note that, in general, the additional collisions cause the yields of the three asymmetric isotopologues to decrease relative to the symmetric 32-32. This occurs because the major fractionation mechanism, as seen in Chapters 5 and 7, is collisional transfer from the long-lived B" state to the short-lived ("leaky") B state. The additional (+)/(-) exchanging collisions increases the population "flow" rate (see the discussion in Section 7.4). That is, the molecules occupying a long-lived B" state have a higher probability of collisional transfer to the short-lived B state.

In a comparison of the strong perturbation model to the weak perturbation model, this same general effect has the opposite consequences. Recall from Chapter 5 that the strong perturbation model produces a largely mass-dependent effect. In Figures 5 and 6, however, we see that the $(+) \leftrightarrow (-)$, parity changing collisions destroy the mass-dependent relationship. The three asymmetric isotopolouges decrease relative to 32-32. At 0.1 to 1 atm, this generates a $\frac{\Delta^{36}}{\Delta^{33}}$ value very comparable to the values of -0.5 and -0.9 (red and blue lines in Figure 8-12, respectively) observed in the rock record. For the weak perturbation model, recall that the original model from Chapter 6 produced $\frac{\Delta^{36}}{\Delta^{33}} < 0$ at high pressures. This occurred because the three asymmetric isotopologues had larger excited state population than did the 32-32 isotopologue. In this case, however, the $(+) \leftrightarrow (-)$, parity changing collisions, which still decrease the reaction yield, create an S-MIF signature with $\frac{\Delta^{36}}{\Delta^{33}} > 0$, very different than the -0.5 and -0.9 values from the Archean Reference Array.

In summary, the additional, parity changing collisions may help differentiate the three asymmetric isotopologues from 32-32, but only in particular cases. The strong perturbation model generated the correct S-MIF pattern because the asymmetric isotopologues had smaller excited populations without the parity changing collisions. In other words allowing, parity changing collisions exaggerates an effect that is already present. For the weak perturbation model, the parity changing collisions *counteract* the original pattern.

8.5 Major Conclusions from This Work

In this section, I simply summarize six major results from this study

1) **The level structure of the two perturbing states plays a key role in determining fractionation behavior.** This principle was observed at a number of points throughout this work. For example, in section 5.3.4, I discussed B/B" level crossings where the B" state crossed the B state "from above", i.e. at low J, the B" states were higher in energy than the B states, and at high J, this pattern was reversed. This created an isotope effect that favored ligher isotopologues reacting over heavier ones. This mass-dependent pattern is reversed in a predissociating system, where the predissociation limit is approached from above. This applies in a wide variety of circumstances including the very weakly perturbed system analyzed in 7.3. This principle was perhaps most apparent in section 8.3, where a change in the temperature or the γ parameter affected the magnitude of the fractionation somewhat, but did not affect the qualitative behavior. The qualitative behavior is determined by the energy level and perturbation patterns.
2) **Weak state-mixings, in general, generate much larger fractionation than do strong state-mixings.** For example, in section 5.3, I compared the f-symmetry versus e-symmetry fractionation behavior. The f-symmetry states were more fractionated because they were subject to weaker state-mixing. Therefore, there was a greater discrepancy in excited state lifetime between the states near the level crossings and those farther away. In section 7.3, this concept was developed further. Here, we observed that collisional transfer can occur as long as the rate of electronically inelastic transfer is greater than the fluorescence rate. (This was the $mZ\tau > 1$ criterion). As long as this criterion is satisfied, there can be fractionation. **For the B", state, with a lifetime of 4200 ns, fractionation, the $mZ\tau$ criterion is satisfied for state-mixing as small as 0.002%.** This may greatly expand the range of electronic state interactions that should be analyzed for potential fractionation.

3) **The additional rotational states in 32-36, 32-34, and 32-33 relative to 32-32, can create statistical S-MIF, but only in certain circumstances.** In Chapter 6, I presented evidence that a statistical model, where asymmetric S_2 converges to a limiting behavior faster than does symmetric S_2, can explain a sizable amount of the fractionation behavior. This analysis, however, only applies for the weak perturbation model presented in Chapter 6 and not the strong-perturbation model presented in Chapter 5. This statistical behavior occurs for small doorway regions because there is a significant chance that the symmetric isotopologue will not sample the doorway. However, I also concluded that there was also evidence of non-statistical behavior, which was explored in Chapter 7. In section 8.2, I discussed the possibility for "Goldilocks perturbations". If perturbation matrix elements were too small, I argued, the probability of sampling a doorway was too small to be treated statistically. That is, the sample of B/B" vibronic level crossings was not large enough to observe statistical behavior. If the perturbation matrix elements are too large, the doorway is always sampled and the behavior is more systematic and mass-dependent, as in chapter 5. If the perturbations are "just right", however, statistical effects are observed. Finally, in section 8.4, we discussed the possibility of +/- parity changing collisions. A small percentage of these parity changing collisions may contribute to the statistical isotope effects, as well.

4) **Transfer from the long lifetime B" state to the short lifetime B state causes more fractionation than the reverse process.** This is simply because equilibrium between the excited state and the ground state is reestablished much more quickly in the B state than in the B" state (see section 5.3.4). This principle can be seen in both Chapter 5 (section 5.2), and Chapter 7 (section 7.2), where the B" states show fractionation behavior but the B states largely do not. Intuitively, the B state is the "leaky" state, and the fractionation behavior of the B" state is the

5) **Fewer restrictions on collisional transfer allows population to "flow" to find the largest "leak", which generates larger fractionation.** The most prominent example of this is seen in section 7.5, where major fractionation mechanism is electronically inelastic transfer from an $\Omega =$

1 spin orbit component to an $\Omega = 0$ spin orbit component with a very large "leak". Likewise, we observed in chapter 7 that the $\Omega = 1$ components of the B" state tend to have the large fractionations, because e/f symmetry changing collisions are allowed.

6) **The B/B"-X system is likely not the origin of S-MIF in the rock record, but we have identified a number of mechanisms that may help narrow the search.**

8.6. Proposing a New S-MIF Mechanism

Conclusion 6 from the previous section raises an important question: if the B/B"-X system in S_2 is not the origin of the S-MIF signature in the rock record, could another electronic state interaction be?

In this section, I propose one interaction as a candidate, justifying this choice using the conclusions from the previous section (8.5). It is worth emphasizing here, though, that this is only *a single possibility*. Figure 8-14 shows a Born-Oppenheimer potential energy curve plot of excited states of S_2 [43].

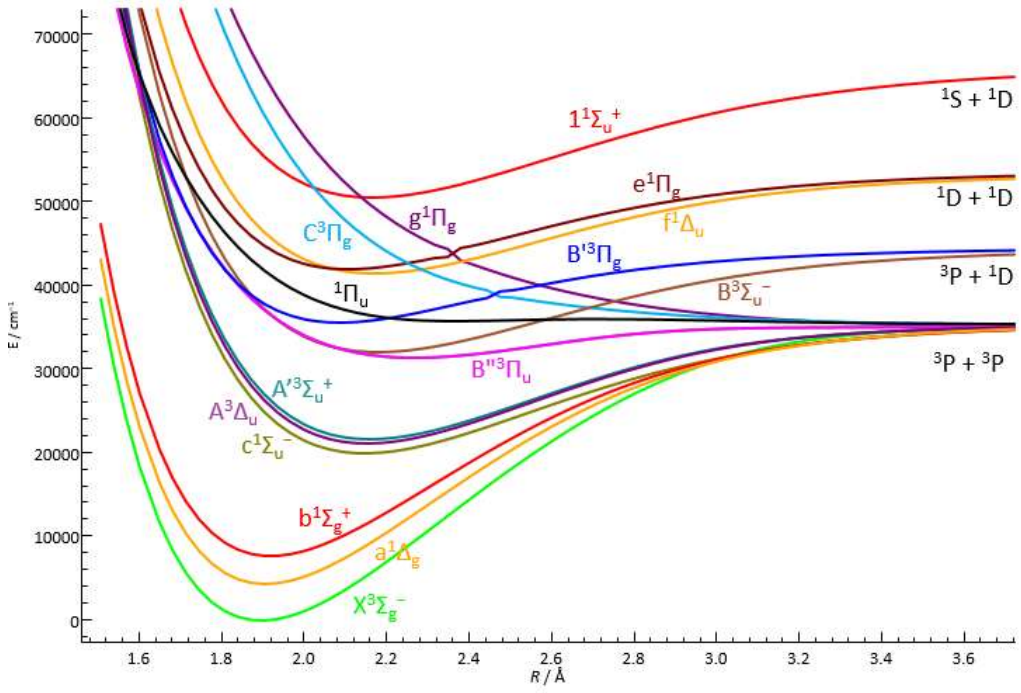

Figure 8-14: The Born-Oppenheimer potential energy curves of the various electronic states of S_2.

Any two pair of states that overlap in energy could be the origin of the S-MIF. And, indeed, conclusion 2 tells us that even very weakly interacting states may cause significant fractionation. Alternatively, it may be a combination of different interactions.

Here, however, I would like to propose one particular electronic state that we have not considered thus far: the $c\ ^1\Sigma_u^-$ state. Note in Figure 8-14 that it extensively overlaps with both the B state and the B" state. Moreover, its potential energy curve is quite different from that of the B or B" state. This would cause the vibrational overlap integral, the Franck Condon factor quite small (see: section 2.8). And, therefore, the perturbations between the c state and either the B or B" states would be correspondingly small. This would make collisional transfer between either the B or B" and the c state more likely to exhibit the statistical behavior discussed in Conclusion 3.

Conclusions 4 and 5 tell us that, in an ideal system (for matching the Archean Reference Array), the fractionation mechanism is a transfer from a short-lifetime state to a long-lifetime state that stores the population long enough for the molecule to react. In the B/B" system, the opposite was true. The primary fractionation mechanism, as seen in Chapters 5 and 7, was a transfer from the long-lived B" state to a short-lived B state. Therefore, the statistical effects discussed in Chapters 6 and 8 (section 8.4, in particular) would serve to deplete rare isotopes in the rock record, when they ought to be enriched. The $c\ ^1\Sigma_u^-$ state provides a method of storing excited state population. Note from Figure 8-14 that the upper vibrational states of $c\ ^1\Sigma_u^-$ overlap with the more strongly absorbing B/B" states, but the majority of the vibrational states would not. Therefore, vibrationally inelastic collisions could transfer population from more the state-mixed states to the unperturbed states. In this sense, the c state is the "leaky state", compared to the B/B" states. Therefore, the superior ability of asymmetric isotopologues to "flow" to the leak creates a *larger excited state population* for the three rare isotopes, potentially matching the rock record. Although vibrationally inelastic collisions have a collisional cross section approximately three orders of magnitude less than rotationally inelastic collisions, there will still be many vibrationally inelastic collisions within the lifetime of the B and B" states (see the discussion in section 8.3).

Appendix A: The Relative Phases of the Probability Amplitudes for Rotationally Inelastic Collisions

A.1. Introduction

This discussion is a supplement to Chapter 3, where I derived matrix elements of the scattering matrix, $\boldsymbol{V}$. Recall that, for any two quantum states of the B/B" system, 1 and 2, the probability of collisional transfer from 1 to 2 ($P_{1\to2}$) is given by Equation A.1,

$$P_{1\to2} = |<1|\boldsymbol{V}|2>|^2. \qquad (A.1)$$

Therefore, the matrix elements of $\boldsymbol{V}$ are not probabilities, but probability amplitudes ($P^{1/2\prime}s$). We derived an expression for $P^{1/2}$, for rotationally inelastic collisions within a vibronic basis state, A (i.e. from $|A,J_1>$ to $|A,J_2>$). This expression is reproduced as Equation A.2, with the addition of an arbitrary phase, φ

$$P_{A,J_1\to J_2}{}^{\frac{1}{2}} = e^{i\varphi}a''|\frac{E(J_2)-E(J_1)}{B}|^{-\gamma'}. \qquad (A.2)$$

Where $\varphi \in \mathbb{R}$. Note, of course, that this expression for the probability amplitude still results in the usual PG expression, because $P_{A,J_1\to J_2} = |P_{A,J_1\to J_2}{}^{\frac{1}{2}}|^2$.

In Chapter 3, I ignored this arbitrary $e^{i\varphi}$ phase factor. In this Appendix, I justify this choice. This justification proceeds in three parts. The first part is a proof that the coefficients of the eigenvectors of the B/B" Hamiltonian can be chosen to be exclusively real. This proof requires basic knowledge of linear algebra theory. The second part uses part 1 to show that: all of the phase factors of $P_{C,J_1\to J_2}{}^{1/2}$ and $P_{D,J_1\to J_2}{}^{1/2}$ for any pair of vibronic states C and D must be either completely in-phase or 180° out-of-phase. The third part shows that the out-of-phase choice leads to obviously nonphysical collisional transfer rates, and the relative phase of any arbitrary $P_{C,J_1\to J_2}{}^{1/2}$ and $P_{DJ_1\to J_2}{}^{1/2}$ therefore can be ignored.

A.2. First Part: Proof that the B/B" Hamiltonian can have Exclusively Real Eigenvectors

As shown in Chapter 2, the B/B" Hamiltonian is both real and symmetric. A symmetric Hamiltonian satisfies the criterion that $\widehat{H} = \widehat{H}^T$, where T is the transpose operation, which switches the

row and column indices of every element in the matrix (i.e. $\widehat{H}_{i,j} = \widehat{H}^T{}_{j,i}$). The time-independent Schrodinger Equation requires that every eigenstate satisfy Equation A.3

$$\widehat{H}|\psi> = E|\psi>. \qquad (A.3)$$

Equation A.3 leads directly to Equation A.4

$$\left(\widehat{H} - E\hat{I}\right)|\psi> = 0. \qquad (A.4)$$

Where $\hat{I}$ is the identity matrix. I seek to prove the following: for any eigenvector $|\psi> = [c_1, c_2, c_3 \ldots]$ that satisfies Equations A3 and A4, I can choose[31] the c_1, c_2, c_3 ... such that all coefficients are real. Because $\widehat{H}$ and $\hat{I}$ are real, then it is sufficient to show that E is also real.[32]

Consider a wavefunction $|\psi>$ that satisfies Equations A.3-A.4. Now consider $<\psi H|H\psi>$. The proof that the E's are real proceeds as follows:

$$<\psi H|H\psi>$$

$$= \psi^T \widehat{H}^T \widehat{H}\psi$$

$$= \psi^T H^2 \psi$$

$$= \psi^T E^2 \psi$$

$$= E^2 \psi^T \psi$$

$$= E^2.$$

[31] Mathematically, if $|\psi>$ is an eigenvector, then $i|\psi>$ is also an eigenvector, with eigenvalue iE. Physically, however, energies cannot be imaginary, so I can ignore this possibility.

[32] If $\widehat{H}$, $\hat{I}$, and E are real then the columns of the matrix $\left(\widehat{H} - E\hat{I}\right)$ form a subspace of $\mathbb{R}^n$, where n is the number of rows/columns of this square matrix. The solutions to Equation A.4, must, therefore, also form a subspace of $\mathbb{R}^n$ (called the nullspace of $\widehat{H} - E\hat{I}$). Consequently, all coefficients of ψ can be chosen to be real.

Because $< \psi H | H\psi >$ must be real, and $E^2 = < \psi H | H\psi >$, E must therefore also be real.

A.3. Second Part: The Relative Phases of the $P^{\frac{1}{2}}$'s:

To begin, consider two eigenstates that are both linear combinations of two diabatic electronic states, C and D (Equations A.5a and A.5b)

$$|1\,J_1> = c_1|C, J_1> + d_1|D, J_1> \tag{A.5a}$$

$$|2\,J_2> = c_2|C, J_2> + d_2|D, J_2>. \tag{A.5b}$$

Note that, as derived in the previous part, the coefficients c_1, d_1, c_2, and d_2 are real.

The probability of transfer from state 1 to state 2 is given by Equation A.6

$$P_{1\to 2} = |< 2\,J_2|\,\boldsymbol{V}|1\,J_1>|^{\mathbf{2}}. \tag{A.6}$$

The Gelbart-Freed expansion of Equation A.6 is given by Equation A.7

$$P_{1\to 2} = |c_1 c_2 P_{C,J_1\to J_2}{}^{\frac{1}{2}} + d_1 d_2 P_{D,J_1\to J_2}{}^{\frac{1}{2}}|^{\mathbf{2}}. \tag{A.7}$$

I now factor out the phases from the $P^{\frac{1}{2}}$'s, yielding Equation A.8

$$P_{1\to 2} = |c_1 c_2 e^{i\phi_C} P^{+}{}_{C,J_1\to J_2}{}^{\frac{1}{2}} + d_1 d_2 e^{i\phi_D} P^{+}{}_{D,J_1\to J_2}{}^{\frac{1}{2}}|^{\mathbf{2}}. \tag{A.8}$$

Where I do not assume that $\phi_C = \phi_D$. The + notation in the $P^{+1/2}$'s indicates that the phase factor has been factored out (so the P^{+}'s are real). Expanding Equation A.8, we obtain Equation A.9

$$\begin{aligned} P_{1\to 2} = |c_1 c_2|^2 P_{C,J_1\to J_2} + |d_1 d_2|^2 P_{D,J_1\to J_2} + \boldsymbol{e^{-i\phi_C} e^{i\phi_D}} c_1 c_2 d_1 d_2 P^{+}{}_{C,J_1\to J_2}{}^{\frac{1}{2}} P^{+}{}_{D,J_1\to J_2}{}^{\frac{1}{2}} \\ + \boldsymbol{e^{i\phi_C} e^{-i\phi_D}} c_1 c_2 d_1 d_2 P^{+}{}_{C,J_1\to J_2}{}^{\frac{1}{2}} P^{+}{}_{D,J_1\to J_2}{}^{\frac{1}{2}}. \end{aligned} \tag{A.9}$$

The probability ($P_{1\to 2}$) must be positive and real. The only portions of Equation A.9, not guaranteed to be real are highlighted in red. These factors are both real if and only if the condition in Equation A.10 is satisfied:

$$|\phi_C - \phi_D| = n\pi. \qquad n \epsilon \mathbb{Z} \tag{A.10}$$

for any integer n. For even n, $e^{-i\phi_C}e^{i\phi_D} = e^{i\phi_C}e^{-i\phi_D} = 1$. For odd n, $e^{-i\phi_C}e^{i\phi_D} = e^{i\phi_C}e^{-i\phi_D} = -1$.

This proof can easily be extended to an arbitrary number of diabatic electronic basis states, E_i. In this case, we require that for every pair of ϕ_{E_i}, ϕ_{E_j}, we have $\left|\phi_{E_i} - \phi_{E_j}\right| = n\pi$, for some value of n.

A.4. Third Part: The choice of $e^{i\phi_C}e^{-i\phi_D} = -1$ leads to non-physical rate constants

In this section, as in the end of chapter 3, we consider collisional transfer in the B state of S_2. In the B state, which follows the Hund's case (b) coupling scheme, the $\Omega = 0\ (e)$ and $\Omega = 1\ (e)$ states are mixed by the S-uncoupling portion of the rotational Hamiltonian. Here, we consider a 4x4 Hamiltonian with basis states: $|\Omega = 0,\ J_1, e>, |\Omega = 1,\ J_1, e>, |\Omega = 0,\ J_2, e>, |\Omega = 1,\ J_2, e>$.

$$\widehat{H} = \begin{bmatrix} E_{\Omega=0}(J_1) & H_{s-unc} & 0 & 0 \\ H_{s-unc} & E_{\Omega=1}(J_1) & 0 & 0 \\ 0 & 0 & E_{\Omega=0}(J_2) & H_{s-unc} \\ 0 & 0 & H_{s-unc} & E_{\Omega=1}(J_2) \end{bmatrix} \tag{A.11}$$

In the case (b) coupling scheme we have $|H_{s-unc}| \gg |\mathrm{E}_{\Omega=0} - \mathrm{E}_{\Omega=1}|$. Therefore, we can simplify the mathematics by assuming $\mathrm{E}_{\Omega=0} \approx \mathrm{E}_{\Omega=1}$. The four eigenvectors and eigenvalues are given by Equations $A.12a - d$.

$$|F_1, J_1> = \frac{1}{\sqrt{2}}\begin{bmatrix} 1 \\ -1 \\ 0 \\ 0 \end{bmatrix} \qquad E_{F_1,J_1} = E(J_1) - H_{s-unc} \tag{A.12a}$$

$$|F_3, J_1> = \frac{1}{\sqrt{2}}\begin{bmatrix} 1 \\ 1 \\ 0 \\ 0 \end{bmatrix} \qquad E_{F_3,J_1} = E(J_1) + H_{s-unc} \tag{A.12b}$$

$$|F_1, J_2> = \frac{1}{\sqrt{2}}\begin{bmatrix} 0 \\ 0 \\ 1 \\ -1 \end{bmatrix} \qquad E_{F_1,J_1} = E(J_2) - H_{s-unc} \tag{A.12c}$$

$$|F_3, J_2> = \frac{1}{\sqrt{2}}\begin{bmatrix}0\\0\\1\\1\end{bmatrix} \qquad E_{F_1,J_1} = E(J_2) + H_{s-unc} \qquad (A.12d)$$

The F_1, as in Chapter 3, indicate as the state with the lower eigenenergy. The F_3, conversely, indicates the higher eigenenergy. Now let us consider the probability of $\Delta J = 2$ collisional transfer from $|F_1, J_1>$ to $|F_1, J_2>$. This time, however, we will allow for $P^{1/2}_{\Omega=0}$ and $P^{1/2}_{\Omega=1}$ to have different phases. The complete expression for the transfer probability is given by Equation A.13

$$P_{1\to2} = \frac{1}{4}[P_{\Omega=0,J_1\to J_1+2} + P_{\Omega=1,J_1\to J_1+2} + e^{-i\phi_0}e^{i\phi_1}P^{+}{}_{\Omega=0,J_1\to J_1+2}{}^{\frac{1}{2}}P^{+}{}_{\Omega=1,J_1\to J_1+2}{}^{\frac{1}{2}} + e^{i\phi_0}e^{-i\phi_1}P^{+}{}_{\Omega=0,J_1\to J_1+2}{}^{\frac{1}{2}}P^{+}{}_{\Omega=1,J_1\to J_1+2}{}^{\frac{1}{2}}]. \qquad (A.13)$$

If we make the reasonable assumption (see: Chapter 3) that $P_{\Omega=0,J_1\to J_1+2} \approx P_{\Omega=1,J_1\to J_1+2} \equiv P$, we obtain Equation A.14.

$$P_{1\to2} = \frac{1}{4}[2 + e^{-i\phi_0}e^{i\phi_1} + e^{i\phi_0}e^{-i\phi_1}]P \qquad (A.14)$$

If we choose $e^{-i\phi_0}e^{i\phi_1} = e^{i\phi_0}e^{-i\phi_1} = -1$. Then $P_{1\to2} = 0$. Conversely, if we consider the probability of $\Delta J = 2$ collisional transfer from $|F_1, J_1>$ to $|F_3, J_2>$, we obtain Equation A.15.

$$P_{1\to2} = \frac{1}{4}[2 - e^{-i\phi_0}e^{i\phi_1} - e^{i\phi_0}e^{-i\phi_1}]P \qquad (A.15)$$

Choosing $e^{-i\phi_0}e^{i\phi_1} = e^{i\phi_0}e^{-i\phi_1} = -1$ now gives $P_{1\to2} = P$.

Because we made several approximations in deriving these formulas, these are not strict selection rules. However, the choice of $e^{-i\phi_0}e^{i\phi_1} = e^{i\phi_0}e^{-i\phi_1} = -1$ clearly leads to a propensity rule against $F_1 \leftrightarrow F_1$ transfer and in favor of $F_1 \leftrightarrow F_3$ transfer. This directly contradicts empirically observed propensity rules in the B state of S_2. Also, intuitively, we would expect that (barring a symmetry-derived selection rule) collisional transfer rates should be larger for transfer between states with smaller energy

gaps between them. At $J = 20$ in the B state, the $F_1 \leftrightarrow F_1$ $\Delta J = 2$ transfer has $\Delta E \approx 10\ cm^{-1}$, whereas the $F_1 \leftrightarrow F_3$ $\Delta J = 2$ transfer has $\Delta E \approx 30\ cm^{-1}$. This proof can be extended to other examples, such as B/B" transfer (where the mixing between the two states is not necessarily 50-50). Therefore, I take $e^{i\phi_A} e^{-i\phi_B} = 1$.

Appendix B: Derivation of a Lower State-Mixing Limit for Isotopic Fractionation

B.1. Introduction

This Appendix is a supplement to Chapter 7. In that Chapter, I explore electronically inelastic collisions, which can cause fractionation in systems that are too weakly state-mixed for rotationally inelastic collisions. The example in Section 7.3 describes a system with a maximum state-mixing less than 0.01% that still exhibits significant fractionation. This naturally leads to a question: How weak is too weak to observe fractionation? In this Appendix, I derive a criterion for the minimum state-mixing required to observe electronically inelastic transfer from a bright state to a dark state, as a function of inelastic collision rate and dark state lifetime.

B.2. Preliminaries from the Gelbart-Freed Model

To begin, I postulate two different rovibronic states that are eigenvectors of my modified version of Green and Western's effective Hamiltonian. These eigenstates are Equations B.1a and B.1b:

$$|1, J_1> = \alpha_1|B, J_1> + \beta_1|B", J_1> \qquad (B.1a)$$

$$|2, J_2> = \alpha_2|B, J_2> + \beta_1|B", J_2> \qquad (B.1b)$$

As in Chapter 3, I introduce a scattering matrix, $\boldsymbol{V}$, which is used to calculate the probability of a collision transferring between two states. Specifically, the probability that a given collision induces transfer from state A to state B ($P_{A\to B}$) is Equation B.2

$$P_{A\to B} = Z|< B|\boldsymbol{V}|A>|^2 \qquad (B.2)$$

In this example, I want to evaluate Equation B.3:

$$P_{1\to 2} = Z|< 2, J_2|\boldsymbol{V}|1, J_1>|^2 \qquad (B.3)$$

This is because the rate constant for transfer between eigenstate 1 and eigenstate 2, $k_{1\to 2}$, is written in terms of $P_{1\to 2}$, as in Equation B.4

$$k_{1\to 2} = ZP_{1\to 2}. \qquad (B.4)$$

In Equation B.4, Z is the total collision rate.

I now plug Equation B.3 into Equation B.4 and expand to yield Equation B.5

$$k_{1\to 2} = Z|\alpha_1\alpha_2 < B,J_2|\boldsymbol{V}|B,J_2 > + \alpha_1\beta_2 < B",J_2|\boldsymbol{V}|B,J_2 > +\beta_1\alpha_2 < B,J_2|\boldsymbol{V}|B",J_2 > +\beta_1\beta_2 < B",J_2|\boldsymbol{V}|B",J_2 > |^2 . \qquad (B.5)$$

At this point, I use the crucial assumption from the Gelbart-Freed model: the cross terms $< B",J_2|\boldsymbol{V}|B,J_2 >$ and $< B,J_2|\boldsymbol{V}|B",J_2 >$ are negligible compared to $< B,J_2|\boldsymbol{V}|B,J_2 >$ and $< B,\mathrm{J_2}|\mathbf{V}|\mathrm{B},J_2 >$, i.e. collisions do not directly induce transitions from the $|B >$ basis state to the $|B" >$ basis state. This leaves Equation B.6

$$k_{1\to 2} = Z|\alpha_1\alpha_2 < B,J_2|\boldsymbol{V}|B,J_2 > + \beta_1\beta_2 < B",J_2|\boldsymbol{V}|B",J_2 > |^2. \qquad (B.6)$$

I can expand this further to give Equation B.7

$$k_{1\to 2} = Z\{|\alpha_1\alpha_2|^2| < B,J_2|\boldsymbol{V}|B,J_1 > |^2 + |\beta_1\beta_2|^2| < B",J_2|\boldsymbol{V}|B",J_1 > |^2 + 2\alpha_1\alpha_2\beta_1\beta_2 < B,\mathrm{J_2}|\mathbf{V}|\mathrm{B},J_1 >< B",J_2|\boldsymbol{V}|B",J_1 >\}. \qquad (B.7)$$

The terms $< B,\mathrm{J_2}|\mathbf{V}|\mathrm{B},J_2 >$ and $< B",J_2|\boldsymbol{V}|B",J_2 >$ can be determined from my modified version of Pritchard's model. A detailed derivation of these matrix elements is given in Chapter 3 and supplemented Appendix 1.

Similar to Gelbart and Freed's original model, I define $| < B,\mathrm{J_2}|\mathbf{V}|\mathrm{B},J_1 > |^2 = P_B$ and $| < B",\mathrm{J_2}|\mathbf{V}|\mathrm{B}",J_1 > |^2 = P_{B"}$, which represent the probability of an electronically elastic collision in the B and the $B"$ states, respectively. I can rewrite Equation B.7, now, as follows (Equation B.8)

$$k_{1\to 2} = Z\{|\alpha_1\alpha_2|^2P_B + |\beta_1\beta_2|^2P_{B"} + 2\alpha_1\alpha_2\beta_1\beta_2\sqrt{P_BP_{B"}}\} \qquad (B.8)$$

If we are considering purely rotational transfer, then $P_B \approx P_{B"}$ (see Chapter 3). However, I must also account for fluorescence from the B and B" states, which can introduce a significant disparity. I will model the fluorescence (i.e. leaks) out of the B and B" states by assuming that a certain number of

collisions are, in fact, inelastic. That is I write, $P_B = 1 - P_{B,fl}$, and $P_{B"} = 1 - P_{B",fl}$, where $P_{B,fl}$ and $P_{B",fl}$, are, formally, the probability that a molecule will have fluoresced in the time in between collisions. $P_{B,fl}$ and $P_{B",fl}$ are not trivial to calculate. For example, they depend on the collision rate, Z. As Z increases $P_{B,fl}$and $P_{B",fl}$ trend toward zero, as Z decreases, they tend toward one. However, there is also an intermediate case, were the collision rate Z is similar to the fluorescence rates. In this case, we have $P_{B,fl} \gg P_{B",fl}$ because the rate of fluorescence is greater from the B state to the B state.

B.3. Constraints on the Mixing Coefficients

Until this point, the derivation has been rigorous within the framework of the Gelbart-Freed model. However, in the interest of deriving a simple expression, I will only consider fluorescence from the B state. In this scenario, $P_{B"} = 1$. This is not a baseless assumption, as the fluorescence lifetime for the B state is two orders of magnitude smaller than that for the B" state. However, I must revisit this assumption at the end of this derivation. Equation B.8 becomes Equation B.9

$$k_{1\to 2} = Z\{|\alpha_1\alpha_2|^2(1 - P_{B,fl}) + |\beta_1\beta_2|^2 + 2\alpha_1\alpha_2\beta_1\beta_2\sqrt{1 - P_{B,fl}}\} \qquad (B.9)$$

I now consider the four coefficients $\alpha_1, \alpha_2, \beta_1, \beta_2$. To proceed further, I make the following assumptions relevant to the B" $\Omega = 1, v = 9$ state:

(1) State $|1, J_1>$, which is primarily B" in character, is state-mixed with $|1', J_1>$, which is primarily B in character.

(2) State $|2, J_2>$, which is primarily B in character, is state-mixed by $|2', J_2>$, which is primarily B" in character. The transition from 1 to 2, therefore, represents an electronically inelastic transition from B to B".

(3) Because J is a rigorously good quantum number, the effective Hamiltonian $\widehat{H}$ for the complete, four state system is block diagonal, with the two 2x2 blocks designated $\widehat{H}_1$ and $\widehat{H}_2$. The states

$|1, J_1>$ and $|1', J_1>$ are eigenstates of $\widehat{H}_1$, while $|2, J_2>$ and $|2', J_2>$ are eigenstates of $\widehat{H}_1$. I assume that $\widehat{H}_1 = \widehat{H}_2$.

These assumptions are valid for B and B" vibronic states that weakly state-mix and do not cross, where the off-diagonal, perturbing matrix element is not strongly a function of J. This describes the B" $\Omega = 1, v = 9$ state from Section 7.3.

I express $|1, J_1>$ and $|1', J_1>$ as linear combinations of $|B, J_1>$ and $|B", J_1>$, as follows (Equations B.10a and B.10b).

$$|1, J_1> = \alpha_1 |B, J_1> + \beta_1 |B", J_1> \quad (B.10a)$$

$$|1', J_1> = \alpha_1' |B, J_1> + \beta_1' |B", J_1> \quad (B.10b)$$

Due to the orthonormality of the two eigenstates of this 2x2 matrix, $\widehat{H}_1$, I have three constraints on the four coefficients α_1, α_1', β_1, β_1'. I list these constraints as Equations B.11a-c

$$\alpha_1^2 + \beta_1^2 = 1 \quad (B.11a)$$

$$\alpha_1'^2 + \beta_1'^2 = 1 \quad (B.11b)$$

$$\alpha_1 \alpha_1' + \beta_1 \beta_1' = 0 \quad (B.11c)$$

Using these constraints, I can algebraically list the other three coefficients in terms of α_1. These results are Equations B.12a-c

$$\beta_1 = f_{\beta_1} \sqrt{1 - \alpha_1^2} \quad (B.12a)$$

$$\alpha_1' = f_{\alpha_1'} \sqrt{1 - \alpha_1^2} \quad (B.12b)$$

$$\beta_1' = f_{\beta_1'} \alpha_1 \quad (B.12c)$$

Here, the $f_{\beta_1}, f_{\alpha_1}, f_{\alpha_1}$, represent a +/- phase (i.e. real) factor.[33] It is possible to derive relationships between these factors. However, these relationships are not relevant to this derivation.

Finally, I use the postulate that the state 1 is primarily B" in character, and the postulate that state 1' is primarily B in character. Therefore, I define $E_{B"}$ as the eigenvalue of $\hat{H}_1$ associated with $|1, J_1> = \alpha_1|B, J_1> + f_{\beta_1}\sqrt{1-\alpha_1{}^2}\,|B", J_1>$, and I define E_B as the eigenvalue of $\hat{H}_1$ associated with $|1', J_1> = f_{\alpha_1'}\sqrt{1-\beta_1{}^2}|B, J_1> + f_{\beta_1'}\alpha_1|B", J_1>$.

Similarly, I can express $|2, J_2>$ and $|2', J_2>$ as linear combinations of $|B, J_2>$ and $|B", J_2>$ (Equations B.13a and B.13b)

$$|2, J_2> = \alpha_2|B, J_2> + \beta_2|B", J_2> \qquad (B.13a)$$

$$|2', J_1> = \alpha_2'|B, J_2> + \beta_2'|B", J_2>. \qquad (B.13b)$$

I now use the postulate that the $|2, J_2>$ is primarily B" in character. Because $\hat{H}_1 = \hat{H}_2$, I must have the condition given by Equation B.14

$$|2, J_2> = f_1 f_{\alpha_1'}\sqrt{1-\beta_1{}^2}|B, J_1> + f_1 f_{\beta_1'}\alpha_1|B", J_1>. \qquad (B.14)$$

That is, the J_2 eigenstate with primarily B state character ($|2, J_2>$) is equal to the J_1 eigenstate with primarily B state character ($|1', J_1>$)to within an arbitrary +/- phase factor, f_1. This is true because they must have the same eigenvalue, E_B. This gives the expression for in Equation B.15

$$|2, J_2> = f_1\,|1',, J_1> = f_1\, f_{\alpha_1'}\sqrt{1-\beta_1{}^2}|B, J_1> + f_1\, f_{\beta_1'}\alpha_1|B", J_1>. \qquad (B.15)$$

This then gives the following two relations (Equations B.16a and B.16b)

[33] Because the Hamiltonian is real and symmetric, the phase factors can be chosen to be all real.

$$\alpha_2 = f_1 f_{\alpha_1}{}'\sqrt{1-{\alpha_1}^2} \qquad (B.16a)$$

$$\beta_2 = f_1 f_{\beta_1}{}'\alpha_1. \qquad (B.16b)$$

Again, I could derive relationships between the phase factors but they are not necessary.

B.4. Final Steps

I now proceed by substitution of the expressions in 12a, 16a, and 16b into the expression for $k_{1\to2}$. This is Equation B.17

$$k_{1\to2} = Z\{|f_1 f_{\alpha_1}{}'\alpha_1\sqrt{1-{\alpha_1}^2}|^2\left(1-P_{B,fl}\right) + \left|f_1 f_{\beta_1} f_{\beta_1}{}'\alpha_1\sqrt{1-{\alpha_1}^2}\right|^2 + f_{\alpha_1}{}' f_{\beta_1} f_{\beta_1}{}'{\alpha_1}^2(1-{\alpha_1}^2)\sqrt{1-P_{B,fl}}\,\}. \qquad (B.17)$$

It can be rigorously shown that $f_{\alpha_1}{}' f_{\beta_1} f_{\beta_1}{}' = -1$.[34] Equation 17 then factors into Equation B.18

$$k_{1\to2} = Z\{{\alpha_1}^2(1-{\alpha_1}^2)\}(1+\left(1-P_{B,fl}\right)-\sqrt{1-P_{B,fl}}). \qquad (B.18)$$

In this derivation I am concerned with the perturbation at which the rate electronically inelastic transfer from the B state to the B" state stops being competitive with the B" fluorescence rate. This threshold is approximated by Equation B.19

$$\frac{electronically\ inelastic\ transfer\ rate\ from\ B"\ to\ B}{B"\ fluorescence\ rate} = 1. \qquad (B.19)$$

Recall that the term $P_{B,fl}$ is the probability that a *pure B* state will have fluoresced in between collisions. At the threshold in Equation B.19, because the B fluorescence is very fast relative to B" fluorescence it is reasonable to assume that $P_{B,fl} = 1$. This simplifies Equation B.19 to Equation B.20

[34] There are two ways to show this. The first is to track the signs while solving Equations B.11a-c. The second is a proof by contradiction. If the sign of $f_{\alpha_1}{}' f_{\beta_1} f_{\beta_1}{}'$ is positive, then the rates of electronically inelastic transfer are far greater than those for the electronically elastic case, which cannot be the case.

$$k_{1\to 2} = Z\{{\alpha_1}^2(1-{\alpha_1}^2)\}. \qquad (B.20)$$

I have expressed α_2, β_1, β_2 in terms of α_1. Therefore I make the substitution $m = {\alpha_1}^2$, where m is the state-mixing between the weakly perturbing 1 and 2 states. This is Equation B.21

$$k_{1\to 2} = Z\{m - m^2\} \approx Zm. \qquad (B.21)$$

The reduction to Zm is valid when m is small. Noting that the rate constant for B" fluorescence $k_{fl,B"} = {}^{1}/_{\tau_{B"}}$. The criterion in Equation B.19 becomes Equation B.22.

$$\boldsymbol{mz\tau_{B"} = 1} \qquad (B.22)$$

Bibliography

[1] M. F. Miller, I. A. Franchi, M. H. Thiemens, T. L. Jackson, G. Kurat, A. Brack and C. T. Pillinger, "Mass-independent fractionation of oxygen isotopes during thermal decomposition of carbonates," *Proc. Nat. Acad. Sci.,* vol. 99, pp. 10988-10993, 2002.

[2] W. G. Mook, J. C. Bommerson and W. H. Staverman, "Carbon isotope fractionation between dissolved bicarbonate and gaseous carbon dioxide," *Earth and Planet. Sci. Lett,* vol. 22, pp. 196-176, 1974.

[3] L. S. Sherman, J. D. Blum, K. P. Johnson, G. J. Keeler, J. A. Barres and T. A. Douglas, "Mass-independent fractionation of mercury isotopes in Arctic snow driven by sunlight," *Nat. Geosci.,* vol. 3, pp. 173-177, 2010.

[4] T. Röckmann, C. A. M. Brenninkmeijer, G. Saueressig, P. Saueressig, J. N. Crowley, H. Fischer and P. J. Crutzen, "Mass-independent oxygen isotope fractionation in atmospheric CO as a result of the reaction CO + OH," *Science,* vol. 281, pp. 544-546, 1998.

[5] P. S. Hill, E. A. Schauble and E. D. Young, "Effects of changing solution chemistry on Fe3+/Fe2+ isotope fractionation in aqueous Fe-Cl solutions.," *Geochim. Cosmochim. Acta.,* vol. 74, no. 23, pp. 6669-6689, 2010.

[6] B. A. Bergquist and J. D. Blum, "Mass-dependent and -independent fractionation of Hg isotopes by photoreduction in aquatic systems," *Science,* vol. 318, no. 5849, pp. 417-420, 2007.

[7] R. Park and S. Epstein, "Carbon isotope fractionation during photosynthesis," *Geochim. Cosmochim. Acta,* vol. 21, pp. 110-126, 1960.

[8] G. D. Farquhar, J. R. Ehleringer and K. T. Hubick, "Carbon isotope discrimination and photosynthesis," *Annu. Rev. Plant Physiol. Plant Mol. Bio,* vol. 40, pp. 503-37, 1989.

[9] N. Dauphas and E. A. Schauble, "Mass fractionation laws, mass-independent effects, and isotopic anomales," *Annu. Rev. Earth Planet. Sci.,* vol. 44, pp. 709-783, 2016.

[10] R. Gonfiantini, W. Stitcher and K. Roznanski, "Standards and intercomparison materials distributed by the International Atomic Energy Agency for stable isotope measurements," International Atomic Energy Agency (IAEA), Report Number IAEA-TECDOC-825, 1995.

[11] T. Ding, S. Valkiers, H. Kipphardt, P. De Bièvre, P. D. Taylor, R. Gonfiantini and R. Krouse, "Calibrated sulfur isotope abundance ratios of three IAEA sulfur isotope reference materials and V-CDT with a reassessment of the atomic weight of sulfur," *Geochim. Cosmochim. Acta,* vol. 65, no. 15, pp. 2433-2437, 2001.

[12] W. M. Haynes, Ed., CRC Handbook of Chemistry and Physics, 95th Edition, CRC Press, 2014.

[13] S. D. Domagal-Goldman, B. Porier and B. Wing, "Summary Report from Workshop on 'Mass-Independent Fractionation of Sulfur Isotopes, Carriers, and Sources'," NASA Astrobiology Institute,

2013. [Online]. Available: https://nai.nasa.gov/media/medialibrary/2013/08/S-MIF_WorkshopSummary.pdf. [Accessed 30 July 2019].

[14] B. H. Muskatel, F. Remacle, M. H. Thiemens and R. D. Levine, "On the strong and selective isotope effect in the UV excitation of N2 with implications toward the nebula and Martian atmosphere," *Proc. Natl. Acad. Sci. U.S.A.,* vol. 108, no. 15, pp. 6020-6025, 2011.

[15] A. A. Pavlov and J. F. Kasting, "Mass-independent fractionation of sulfur isotopes in archean sediments: strong evidence for an anoxic Archean atmosphere," *Astrobiology,* vol. 2, no. 1, pp. 27-41, 2004.

[16] G. Luo, S. Ono, N. J. Beukes, D. T. Wang, S. Xie and R. E. Summons, "Rapid oxygenation of Earth's atmosphere 2.33 billion years ago," *Science,* vol. 2, no. 5, 2016.

[17] R. E. Kopp, J. L. Kirschvink, I. A. Hillburn and C. Z. Nash, "The Paleoproterozoic snowball Earth: A climate disaster triggered by the evolution of oxygenic photosynthesis".

[18] A. Bekker and A. J. Kaufman, "Oxidative forcing of global climate change: A biogeochemical record across the oldest Paleoproterozoic ice age in North America," *Earth Planet. Sci. Lett.,* vol. 258, no. 3-4, pp. 486-499, 2007.

[19] A. H. Knoll, "The early evolution of eukaryotes: a geological perspective," *Science,* vol. 256, no. 5057, pp. 622-627, 1992.

[20] C. T. Edwards, M. R. Saltzman, D. L. Royer and D. A. Fike, "Oxygenation as a driver of the Great Ordovician Biodiversification Event," *Nat. Geosci.,* vol. 10, pp. 925-929, 2017.

[21] E. A. Sperling, C. A. Frieder, A. V. Raman, P. R. Girguis, L. A. Levin and A. H. Knoll, "Oxygen, ecology, and the Cambrian radiation of animals," *Proc. Natl. Acad. Sci. U.S.A.,* vol. 110, no. 3, pp. 13446-13451, 2013.

[22] J. Farquhar, H. Bao and M. Thiemens, "Atmospheric Influence of Earth's Earliest Sulfur Cycle," *Science,* vol. 289, no. 5480, pp. 756-758, 2000.

[23] J. Farquhar and B. A. Wing, "Multiple sulfur isotopes and the evolution of the atmosphere," *Earth Planet Sci. Lett.,* vol. 213, no. 1-2, pp. 1-13, 2003.

[24] J. R. Lyons, "Atmospherically-derived mass-independent sulfur isotope signatures, and incorporation into sediments," *Chem. Geol.,* vol. 267, no. 3-4, pp. 164-174, 2009.

[25] J. F. Kasting, "The Rise of Atmospheric Oxygen," *Science,* vol. 293, no. 5531, pp. 819-820, 2001.

[26] S. Ono, "Photochemistry of Sulfur Dioxide and the Origin of Mass-Independent Isotope Fractionation in Earth's Atmosphere," *Annu. Rev. Earth Planet. Sci.,* vol. 45, pp. 301-329, 2017.

[27] S. Ono, N. J. Beukes and D. Rumble, "Origin of two distinct multiple-sulfur isotope compositions of pyrite in the 2.5 Ga Klein Naute Formation, Griqualand West Basin, South Africa," *Precambrian Research,* vol. 169, no. 1-4, pp. 48-57, 2009.

[28] J. Farquhar, M. Peters, D. T. Johnston, H. Strauss, A. Masterson, U. Wiechert and A. J. Kaufman, "Isotopic evidence for Mesoarchean anoxia and changing atmospheric sulfur chemistry," *Nature,* vol. 449, pp. 706-709, 2007.

[29] S. Ono, B. Wing, D. Johnston, J. Farquhar and D. Rumble, "Mass-dependent fractionation of quadruple stable sulfur isotope system as a new tracer of sulfur biogeochemical cycles," *Geochim. Cosmochim. Acta,* vol. 70, no. 9, pp. 2238-2252, 2006.

[30] J. Rufus, G. Stark, P. L. Smith, J. C. Pickering and A. P. Thorne, "High-resolution photoabsorption cross section measurements of SO2: 220 to 325 nm at 295 K.," *J. Geophys. Res.,* vol. 108, 2003.

[31] G. Stark, P. L. Smith, J. Rufus, A. P. Thorne, J. C. Pickering and g. Cox, "High-resolution photoabsorption cross-section measurements of SO_2 at 295 K between 198 and 220 nm," *J. Geophys. Res. Planets,* vol. 104, pp. 16,585-16,590, 1999.

[32] J. R. Lyons, "Mass-independent fractionation of sulfur isotopes by isotope-selective photodissociation of SO_2," *Geophys. Res. Lett.,* vol. 34, 2007.

[33] S. O. Danielache, C. Eskebjerg , M. S. Johnson, Y. Ueno and N. Yoshida, "High-precision spectroscopy of 32-S, 33-S, and 34-S sulfur dioxide: Ultraviolet absorption cross sections and isotope effects.," *J. Geophys. Res. Atmospheres,* vol. 113, 2008.

[34] S. Ono, A. R. Whitehill and J. R. Lyons, "Contribution of isotopologue self-shielding to sulfur mass-independent fractionation during sulfur dioxide photolysis," *J. Geophys. Res. Atmospheres,* vol. 118, no. 5, p. 2444–2454, 2013.

[35] M. W. Claire, J. F. Kasting, S. D. Domgal-Goldman, E. E. Stüeken, R. Buick and V. S. Meadows, "Modeling the signature of sulfur mass-independent fractionation produced in the Archean atmosphere," *Geochim. Cosmochim. Acta,* vol. 141, pp. 365-380, 2014.

[36] A. R. Whitehill and S. Ono, "Excitation band dependence of sulfur isotope mass-independent fractionation during photochemistry of sulfur dioxide using broadband light sources," *Geochim. Cosmochim. Acta,* vol. 94, pp. 238-253, 2012.

[37] B. C. Hathorn and R. A. Marcus, "An intramolecular theory of the mass-independent isotope effect for ozone I," *J. Chem. Phys.,* vol. 111, pp. 4087-4100, 1999.

[38] B. C. Hathorn and R. A. Marcus, "An intramolecular theory of the mass-independent isotope effect for ozone II," *J. Chem. Phys.,* vol. 113, pp. 9497-9509, 2000.

[39] Y. Q. Gao and R. A. Marcus, "On the theory of the strange and unconvential isotopic effects in ozone formation," *J. Chem. Phys.,* vol. 116, pp. 137-154, 2002.

[40] Y. Q. Gao and R. A. Marcus, "Strange and Unconventional Isotope Effects in Ozone Formation," *Science,* vol. 293, pp. 259-263, 2001.

[41] R. A. Marcus, "Theory of mass-independent fractionation of isotopes, phase space accessibility, and a role of isotopic symmetry," *Proc. Natl. Acad. Sci. U.S.A.,* vol. 110, no. 44, p. 17703–17707, 2013.

[42] D. Babikov, "Recombination reactions as a possible mechanism of mass-independent fractionation of sulfur isotopes in the Archean atmosphere of Earth," *Proc. Natl. Acad. Sci. U.S.A.,* vol. 114, no. 12, pp. 3062-3067, 2017.

[43] C. M. Western, University of Bristol, U.K., Private Communication, 2019.

[44] H. Lefebvre-Brion and R. W. Field, The Spectra and Dynamics of Diatomic Molecules, Elsevier Academic Press, 2004.

[45] J. M. Ricks and R. F. Barrow, "The dissociation energy of gaseous diatomic sulfur," *Can. J. Phys.,* vol. 47, pp. 2423-2427, 1969.

[46] M. E. Green and C. M. Western, "Upper vibrational states of the B" 3Πu state of $^{32}S_2$," *J. Chem. Soc. Faraday Trans.,* vol. 93, pp. 365-372, 1997.

[47] B. R. Lewis, S. T. Gibson, G. Stark and A. N. Heays, "Predissociation of the B $^3\Sigma_u^-$ state of S_2: A coupled-channel model.," *J. Chem. Phys.,* vol. 148, no. 23, 2018.

[48] G. Stark, H. Herde, J. R. Lyons, A. N. Heays, N. de Oliveira, G. Nave, B. R. Lewis and S. T. Gibson, "Fourier-transform-spectroscopic photoabsorption cross sections and oscillator strengths for the S_2 B $^3\Sigma_u^-$ -- X $^3\Sigma_g^-$ system.," *J. Chem. Phys.,* vol. 148, 2018.

[49] J. E. Meakin and R. F. Barrow, "The electronic spectrum of S_2," *Can. J. Phys.,* vol. 40, no. 3, pp. 377-379, 1962.

[50] P. Patiño and R. F. Barrow, "Observations on the B $^3\Sigma_u^-$ and B" $^3\Pi_u$ states of S2.," *J. Chem. Soc.,* vol. 78, pp. 1271-1282, 1982.

[51] M. Heaven, T. A. Miller and V. E. Bondybey, "Chemical formation and spectroscopy of S2 in a free jet expansion," *J. Chem. Phys.,* vol. 80, pp. 51-56, 1983.

[52] M. E. Green and C. M. Western, "A deperturbation analysis of the B $^3\Sigma_u^-$ (v'=0-6) and the B" $^3\Pi_u$ (v'=2-12) states of S_2.," *J. Chem. Phsy.,* vol. 104, pp. 848-864, 1996.

[53] D. A. McQuarrie, Statistical Mechanics, Mill Valley, California: University Science Books, 2000.

[54] P. F. Bernath, Spectra of Atoms and Molecules, Second Edition, Oxford, U.K.: Oxford University Press, 2005.

[55] R. N. Zare, Angular Momentum: Understanding Spatial Aspects in Chemistry and Physics, John Wiley & Sons, 1988.

[56] *Matlab 2017a,* Natick, Massachusetts: The Mathworks, Inc., 2017.

[57] E. E. Whitting and R. W. Nicholls, *Reinvestigation of Rotational-Line Intensity Factors in Diatomic Spectra,* 27: 1, 1974.

[58] J. T. Hougen, The Calculation of Rotational Energy Levels and Rotational Line Intensities in Diatomic Molecules, 1960.

[59] R. J. Le Roy, "RKR1: A computer program implementing the first-order RKR method for determining diatomic molecule potential energy functions," *J. Quan. Spectrosc. Ra.,* vol. 186, pp. 158-166, 2017.

[60] R. J. Le Roy, "LEVEL: A computer program for solving the radial Schrödinger equation for bound and quasibound levels," *J. Quant. Spectrosc. Ra.,* vol. 186, pp. 167-178, 2017.

[61] R. Shankar, Principles of Quantum Mechanics, New York: Springer, 1994.

[62] W. R. Anderson, D. R. Crosley and J. E. Allen Jr., "Franck–Condon factors for the B–X system of S_2," *J. Chem. Phys.,* vol. 71, no. 821, pp. 821-29, 1979.

[63] D. E. Pritchard, N. Smith, R. D. Driver and T. A. Brunner, "Power law scaling for rotational energy transfer.," *J. Chem. Phys.,* vol. 70, pp. 2115-2120, 1979.

[64] W. M. Gelbart and K. F. Freed, "Intramolecular perturbations and the quenching of luminescence in small molecules," *Chem. Phys. Lett.,* vol. 18, pp. 470-475, 1973.

[65] T. A. Brunner and D. Pritchard, "Fitting laws in rotationally inelastic collisions," in *Dynamics of the Excited State*, K. Lawley, Ed., New York, John-Wiley and Sons, 1982.

[66] T. A. Brunner, R. D. Driver, N. Smith and D. E. Pritchard, "Simple Scaling Law for Rotational-Energy Transfer in Na_2*-Xe Collisions," *Phys. Rev. Lett.,* vol. 41, pp. 856-859, 1978.

[67] T. A. Brunner, T. P. Scott and D. E. Pritchard, "Origins of power law behavior in rotationally inelastic collisions," *J. Chem. Phys.,* vol. 76, no. 11, pp. 5641-5643, 1982.

[68] C. R. Vidal, "Collisional Depolarization and Rotational Energy Transfer of the $^7Li_2$ ($B\ ^1\Pi_u$)-Li $^2S_{1/2}$ System Using Laser-Induced Fluorescene," in *Laser-Induced Processes in Molecules, Springer Series in Chemical Physics, vol 6.*, K. L. Kompa and S. D. Smith, Eds., Berlin, Springer, 1979, pp. 69-70.

[69] P. J. Dagdigian and M. H. Alexander, "Experimental and theoretical study of rotationally inelastic polar molecule collisions: ^{7}LiH–HCN," *J. Chem. Phys.,* vol. 72, no. 12, pp. 6513-6520, 1980.

[70] T. A. Brunner, R. D. Driver, N. Smith and D. E. Pritchard, "Rotational energy transfer in Na_2*-Xe collisions: Level to level dynamics," *J. Chem. Phys.,* vol. 70, no. 9, pp. 4155-4167, 1979.

[71] E. F. Jendrek and M. H. Alexander, "Rotationally inelastic collisions of LiH with He. II. Theoretical treatment of the dynamics.," *J. Chem. Phys.,* vol. 72, no. 12, pp. 6452-6461, 1980.

[72] R. Schinke, "On the validity of the power gap model in the strong coupling case," *J. Chem. Phys.*, vol. 75, pp. 5205-5207, 1981.

[73] N. K. Dabkara and P. M. Agrawal, "The maximum limit of rotational energy transfer in collisions of N_2 with Ne and the power-gap law," *Chem. Phys. Lett.,* vol. 299, no. 2, pp. 125-131, 1999.

[74] S. L. Dexheimer, M. Durand, T. A. Brunner and D. E. Pritchard, "Dynamical constraints on the transfer of angular momentum in rotationally inelastic collisions of I_2 ($B\ ^3\Pi$) with He and Xe," *J. Chem. Phys.,* vol. 76, pp. 4996-5004, 1982.

[75] S. Yang, M. R. Canagaratna, S. K. Witonsky, S. L. Coy, J. I. Steinfeld, R. W. Field and A. A. Kachanov, "Intensity Measurements and Collision-boradening coefficients for the oxygen A band measured by intracavity laser absorption spectroscopy," *J. Mol. Spec.,* vol. 201, pp. 188-197, 2000.

[76] C. Ottinger, R. Velasco and R. N. Zare, "Some Propensity Rules in Collision-Induced Rotational Quantum Jumps," *J. Chem. Phys.,* vol. 52, no. 4, pp. 1636-1643, 1969.

[77] C. W. McCurdy and W. H. Miller, "Interference effects in rotational state distributions: Propensity and inverse propensity," *J. Chem. Phys.,* vol. 67, no. 2, pp. 463-468, 1977.

[78] R. A. Gottscho, "Spin, orbit, and parity conservation in rotation changing collisions.," *Chem. Phys. Lett,* vol. 81, pp. 66-69, 1981.

[79] K. Bregmann and W. Demtroder, "Inelastic collision cross section of excited molecules. II. Asymmetries in the cross section for rotational transitions in the Na_2 ($B\ ^1\Pi_u$) state," *J. Phys. B,* vol. 5, no. 7, pp. 1386-1395, 1972.

[80] K. Bregmann, H. Klar and W. Schlecht, "Asymmetries in collision-induced rotational transitions," *Chem. Phys. Lett,* vol. 12, no. 3, pp. 522-525, 1972.

[81] B. Pouilly, J.-M. R. Robbe and M. H. Alexander, "Cross sections for collisional energy transfer between low-lying electronic states of Mg in collisions with N_2O," *J. Phys. Chem.,* Vols. 140-148, p. 88, 1984.

[82] M. H. Alexander, X. Yang, P. J. Dagdigian, A. Berning and H.-J. Werner, "Potential energy surfaces for the CN Ar system and inelastic scattering within the A state," *J. Chem. Phys.,* vol. 112, pp. 781-791, 1999.

[83] P. L. James, I. R. Sims, I. W. M. Smith, M. H. Alexander and M. Yang, "A combined experimental and theoretical study of rotational energy transfer in collisions between NO and He, Ar and N_2 at temperatures down to 7 K," *J. Chem. Phys.,* vol. 109, no. 10, pp. 3882-3897, 1998.

[84] J. S. Morrill and W. M. Benesch, "Auroral N2 emissions and the effect of collisional processes on N2 triplet state vibrational populations," *J. Geophys. Res.,* vol. 101, pp. 261-274, 1996.

[85] T. A. Caughey and D. R. Crosley, "Collision-induced transfer rates connecting fine-structure levels in S2($^3\Sigma_u^-$,v′=4)," *J. Chem. Phys,* vol. 71, pp. 736-734, 1979.

[86] W. A. Wensink, C. Noorman and H. A. Dijkerman, "Self-shifting of some rotational transitions of OCS and CH3CCH (propyne). A survey of measurements on shifting of rotational absorption lines of molecules," *J. Phys. B,* vol. 14, no. 16, pp. 2813-1821, 1981.

[87] M. J. Pilling and S. H. Robertson, "Master equation models for chemical reactions of importance in combustion," *Ann. Rev. Phys. Chem.,* vol. 54, pp. 245-275, 2003.

[88] N. Buchete and G. Hummer, "Coarse master equations for peptide folding dynamics," *J. Phys. Chem. B,* vol. 112, no. 19, pp. 6057-6069, 2008.

[89] N. Buchete and G. Hummer, "Peptide folding kinetics from replica exchange molecular dynamics," *Phys. Rev. E.,* vol. 77, 2008.

[90] J. R. Barker, "Energy transfer in master equation simulations: a new approach," *Int. J. Chem. Kinet.,* vol. 41, pp. 748-763, 2009.

[91] G. J. Rottman, T. N. Woods and W. McClintock, "SORCE solar UV irradiance results," *Adv. Space. Res.,* vol. 37, pp. 201-208, 2006.

[92] C. Sagan and G. Mullen, "Earth and Mars: Evolution of atmospheres and surface temperatures," *Science,* vol. 177, pp. 52-56, 1972.

[93] A. Ringwood, "Changes in solar luminosity and some possible terrestrial consequences," *Geochim. Cosmochim. Acta,* vol. 21, no. 3, pp. 295-296, 1961.

[94] C. Goldblatt and E. J. Zahnle, "Faint young Sun paradox remains," *Nature,* vol. 474, 2011.

[95] Y. Ueno, M. S. Johnson and S. O. Danielache, "Geological sulfur isotopes indicate elevated OCS in the Archean atmosphere, solving faint young sun paradox.," *Geophys.,* vol. 106, no. 35, pp. 14784-14789, 2009.

[96] C. Goldblatt and K. J. Zahnle, "Clouds and the Faint Young Sun Paradox," *Climate of the Past Discussions,* vol. 6, no. 3, 2011.

[97] D. C. Catling, "Planetary Atmospheres," in *Treastise on Geophysics, 2nd Ed. vol. 10*, G. Schubert, Ed., Oxford, Elsevier, 2015, pp. 429-472.